

Grazing Incidence X-ray Diffraction

- application on catalyst surfaces -

vorgelegt von

Michael Scherzer, MSc.

geb. in Graz/Österreich

von der Fakultät II – Mathematik und Naturwissenschaften

der Technischen Universität Berlin

zur Erlangung des akademischen Grades

Doktor der Naturwissenschaften

-Dr.rer.nat. –

genehmigte Dissertation

Promotionsausschuss:

Vorsitzender: Prof. Dr. Thomas Friedrich

Gutachter: Prof. Dr. Robert Schlögl (Fritz Haber Institut der MPG, Berlin)

Gutachter: Prof. Dr. Thorsten Ressler

Gutachter: Prof. Dr. Ullrich Pietsch (Universität Siegen)

Tag der wissenschaftlichen Aussprache: 19.6.2018

Berlin 2018

dedicated to
Prof. Dr. Viktor Obendrauf (†)
and
my family

„Labor omnia
vincit improbus“
(Vergil)

Acknowledgement

Herby, I would like to express my sincere gratitude to my supervisor and Director of the Department of Inorganic Chemistry at the Fritz Haber institute of the Max Planck Society, as well of the Max Planck Institute for Chemical Energy Conversion, Prof. Dr. Robert Schlögl for giving me the opportunity to follow my research interests and guiding my scientific education. He has been a continuous source of inspiration and contributing with numerous suggestions and advices throughout my work. The availability of high-end characterization techniques, as well outstanding discussions made this work exhilarating in his research group, as well being always in connection with state of the art experience.

I am very grateful to Prof. Dr. Ullrich Pietsch and Prof. Dr. Thorsten Ressler to invest their valuable time reviewing this work and to be part of the examination board. Prof. Dr. Thomas Friedrich I would like to thank to chair the examination board.

I would like to particular acknowledge the four group leaders I had during my work, Prof. Dr. Malte Behrens, Dr. Elias Frei, Dr. Marc Willinger and finally Dr. Thomas Lunkenbein for their patience and scientific discussions as well their valuable support.

I am greatly indebted and thankful to Dr. Frank Girgsdies. His support, our daily scientific discussions, as well numerous hours of technically and mechanistically tuning and adjustment has been extraordinary valuable for my work.

For additional help and contributions to my work I would like to thank (in alphabetical order): Adriana Bernal, Wiebke Frandsen, Adnan Hammud, Walid Hetaba, David Klein, Sven Kubala, Chinmoy Ranjan and Detre Teschner. Special thanks to my colleague from the Massachussettes Insitute of Technology, Dr. Charles Settens for our scientific discussions.

The monthly iridium coffee meetings have been source for deeply interesting discussions and exchange of scientific objectives within the Iridium project. Thanks to Dr. Verena Streibel and Dr. Cyriac Massué, for memorable hours.

A very special thank I would like to give to Jasmin Allan und Dr. Olaf Timpe. Their `chemical` humour and our work on developing new experiments lead to many exhilarating and memorable hours between the stressful scientific daily routine.

I also want to thank Paul Nieman for proof-reading my work.

Last but not least I would like to thank my family and friends for their unwavering and unconditional support.

Summary

The interest to study iridium electrocatalysts originates from their use in PEM electrolyzers, which are used to produce hydrogen from water splitting. The need to overcome the exploitation of fossil fuels and to promote the use of sustainable resources makes this a promising alternative. Usage of expensive and rare iridium additionally pushes research to find cost efficient alternatives, probably also dedicated highly active iridium oxide surface configurations. Thin film coatings of iridium render a likely promising system, as it is additionally economical. The use of thin film diffraction techniques becomes a powerful investigation strategy, since it can provide integral information over enormous length scales (angstroms to microns range). The lack of dedicated thin film studies on iridium based systems puts the focus of the present work into conducting such a study.

Establishing a thin layer model system for being studied under oxygen evolution reaction conditions is extended to two different deposition methods. These two intrinsically different films exhibit distinguishable surfaces and are differently active under OER conditions. These findings leads to the result of being dynamically instable since roughening as well smoothing and changes in the fractal parameter occur (as evidenced by XRR and XRDS). This is combined with electron microscopy results and X-ray photoabsorption spectroscopy supports the already proposed findings. In addition, the same surface morphology can react under different treatments to yield significantly different final structures and morphologies. Depth resolved XRDS parameter describe the kinetical different scenarios on nm scale. A detailed study on the electrochemical influence is executed and verified via peak width and intensity analysis of the Ir (111) reflection and reveals that just one cycle of cyclic voltammetry changes a thin and high dense Ir film considerably.

In contrast to the ex-situ investigation the possibility of in-situ studies was explored. Therefore a home-build in-situ setup for home laboratory use is developed and its working principle demonstrated, although with a simpler system than the complex case of iridium. A long-term oxidation of copper in alkaline media demonstrates the need of in-situ studies. During cyclic voltammetry, usual peak formation could be observed. Subsequent chronoamperometry revealed an interesting behavior towards a 20 h measurement. In connection with GIXRD measurements cuprite (Cu_2O) as intermediate could be identified and mechanistically integrated into a complex reaction network.

A final attempt has been made to implement the GIXRD technique also for powder samples by the use of pressed pellets and the surface oxidation of a high temperature alloy, as well as to provide a quick and practicable calibration technique via XRR for a home build LPCVD machine.

This thesis can provide a suitable insight into thin film diffraction (GIXRD), as well the use of X-ray reflectometry, for studying surfaces and interfaces. In addition to the general application the knowledge gained from the Ir electrode model system gives a contribution to the understanding of dynamical surface instability on the base of diffraction and reflectometry and demonstrates the unique capabilities of these methods in (electro-)catalysis.

Zusammenfassung

Das Interesse an Untersuchungen von elektrochemisch aktiven Iridium-Oberflächen resultiert aus deren Einsatz in PEM-Elektrolyseuren (Proton Exchange Membrane). Diese Technik wird als nachhaltige Alternative zur Wasserstoffgewinnung industriell immer interessanter, um von fossilen Rohstoffen Abstand zu nehmen. Die Verwendung des selten vorkommenden und extrem teuren Iridium-Metalls macht diesen Prozess sehr kostspielig und fordert die Erforschung von möglichen Alternativen. Diese könnten in dezidierten Iridiumoxid-Oberflächen gefunden werden, welche hohe katalytische Eigenschaften unter OER-Bedingungen aufweisen. Besonderes Augenmerk erhalten auch die Anwendung von dünnen Iridium-Schichten als Elektroden, welche einerseits ein Minimum an Iridium erfordern und andererseits ökonomischer einsetzbar sind. Die Anwendung von Dünnschicht-Beugungsmethoden hat im Zusammenhang mit ihrem integralen Charakter für solche Proben-Typen ein hohes Potenzial zur Charakterisierung, da herkömmliche Methoden entweder zu lokal oder zu unspezifisch sind. Diese Techniken können mikroskopische Änderungen mit makroskopisch messbare Größen in Zusammenhang setzen (Angström- bis zu Mikrometer-Bereich). Solche gezielten Studien für Iridium-basierte Systems unter OER-Bedingungen sind kaum dokumentiert, was zu dem Schwerpunkt der vorliegenden Arbeit wird, einen solchen Ansatz zu verfolgen und eine systematische Studie durchzuführen.

Die Entwicklung eines entsprechenden und anwendbaren Dünn-Schicht Modellsystems für OER-Studien wurde mit zwei unterschiedlichen Präparationstechniken erreicht. Diese beiden intrinsisch unterschiedlichen Schichten weisen vor und nach elektrochemischer Behandlung unterschiedliche Oberflächen-Morphologien auf, welche klar vom Ursprungszustand abhängen. Diese dimensionale Instabilität (Aufrauen und fraktale Änderungen) kann mit XRR und XRDS gezeigt und mit Elektronenmikroskopie, sowie XPS Ergebnissen unterstützend belegt werden. Umgekehrt kann auch der Einfluss von verschiedenen Behandlungen auf denselben Ursprungszustand gezeigt werden, welche ebenso zu deutlich unterscheidbaren resultierenden Schicht-Morphologien führt. Fraktale Parameter und Peak-Profil Analysen zeigen diese Änderungen im nm-Maßstab deutlich bis hin zur kompletten Amorphisierung. Eine gesonderte Studie an einer homogenen und dichtgepackten Iridium Schicht ermöglichen auch eine Studie des Ir 111 Reflexes in Abhängigkeit von der Eindringtiefe (veränderlicher Einfallswinkel), und zeigt bereits nach einem einzigen Zyklus in der Cyclovoltammetrie und nachfolgender Chronoamperometrie signifikante Änderungen am Ir 111 Reflex.

Parallel zu den ex-situ Untersuchungen wird auch die Möglichkeit zu in-situ Messungen durch die Konstruktion einer Zelle für Labor-Diffraktometer ermöglicht. Das Arbeitsprinzip der Zelle kann vorgestellt und ein Leitfaden zur Datenauswertung bereitgestellt werden. Als Test-Reaktion dient die Oxidation vom polykristallinem Kupfer in basischem Milieu. Während cyclovoltammetrischen Messungen konnten typische Kupfer Reaktionen beobachtet werden (Oxidation/Reduktion). Bei einem nachfolgendem 20 Stunden Experiment konnten im in-situ Aufbau bei gleichzeitig aufgezeichneten Beugungs-Pattern in zeitlicher Abhängigkeit eine Cuprit (Cu_2O) Zwischenstufe eindeutig nachgewiesen werden.

In einem zusätzlichem Ansatz wird versucht, Dünnschicht-Beugung auch auf andere Systeme auszuweiten, zum Beispiel auf gepresste Katalysator Pellets, welche oberflächlich reduziert wurden. Ebenso untersucht wurde auf eine Hochtemperatur-Legierung, die sich oxidativ entmischt, sowie die Kalibration eines selbst gebautem LPCVD-reaktors, um die lineare Anhängigkeit von Schichtdicke und Abscheidezeit mittels XRR zu bestimmen.

Die vorliegende Arbeit kann einen ausführlichen Überblick über die Anwendung von Dünnschicht-Beugungstechniken geben und durch die Untersuchungen an Iridium-Oberflächen einen Einblick in seine Dynamik ermöglichen. Die zusätzlich erarbeitete Lösung für In-situ Messungen zeigt nochmals mehr die weitreichenden Möglichkeiten dieser Methoden und ihre Einsatzmöglichkeiten in der Oberflächencharakterisierungen.

Table of contents

Chapter 1: Introduction

1.1	The energy challenge	1
1.2	Chemistry - the key tool	2
1.3	Water splitting for hydrogen production	4
1.4	Iridium as OER catalyst	5
1.5	The challenge of the structure	7
1.6	Scientific objective and outline of this work	8
1.7	References	10

Chapter 2: Thin film diffraction

2.1	Introduction	13
2.2	Theoretical background	14
2.2.1	Kinematic theory	14
2.2.2	Semi-kinematic theory	16
2.2.3	Dynamic theory	16
2.2.4	The q-space (reciprocal space)	17
2.3	Morphology testing techniques	18
2.3.1	X-ray Reflectometry (XRR)	18
2.3.2	X-ray diffuse scattering measurements (XRDS)	27
2.4	Structure testing techniques	30
2.4.1	Grazing Incidence X-ray Diffraction (GIXRD)	30
2.5	References	34

Chapter 3: Electrochemistry goes GIXRD – cell development and in-situ surface oxidation of copper

3.1	Abstract	37
-----	----------	----

3.2	Introduction	37
3.3	Electrochemical in-situ setup for out-of-plane GIXRD	39
3.3.1	Design of the in-situ setup	39
3.3.2	Operation modes	41
3.3.3	Experimental impact of the electrochemical setup on the peak intensity in GIXRD	42
3.3.4	Refraction shift correction for flat samples	44
3.4	In-situ electrochemical oxidation of copper in alkaline media investigated by GIXRD	45
3.4.1	Experimental	45
3.4.2	Cyclovoltammetry results and Interpretation	46
3.4.3	Surface oxidation (CA) and GIXRD results and interpretation	48
3.5	Conclusion	52
3.6	References	53

Chapter 4: Surface morphology change of iridium thin films during oxygen evolution reaction (OER) studied through X-ray reflectometry

4.1	Abstract	55
4.2	Introduction	55
4.3	Experimental	57
4.4	Results and Discussion	58
4.4.1	Electrochemical activity	58
4.4.2	XRR & EM results	60
4.4.3	XRDS results	64
4.4.4	XPS results	68
4.4.5	GIXRD results	69
4.5	Conclusion	70
4.6	References	72
	Appendix 1	74

Chapter 5: Iridium thin films under oxygen evolution conditions – influences on morphology and crystal lattice

5.1	Abstract	75
5.2	Introduction	75
5.3	Experimental	77
5.4	Results and Discussion	78
5.4.1	Morphological investigation by X-ray reflectometry, X-ray diffuse scattering and Scanning electron microscopy	78
5.4.2	Cyclic voltammetry	82
5.4.3	Cyclic voltammetry followed by Chronoamperometry	88
5.4.4	Higher numbers of CV cycles	92
5.4.5	Changes after the first cycle	97
5.5	Grazing incidence X-ray diffraction	100
5.6	Conclusion	103
5.7	References	105
	Appendix 1	107

Chapter 6: Thin film diffraction in extended use: three examples outside the box

6.1	Depth-sensitive phase analysis of surface layers	109
6.1.1	High temperature alloy	109
6.1.2	Sample comparison by similar probing depth	111
6.2	Surface sensitive reduction	113
6.3	Calibration of LPCVD process using X-ray reflectometry	117
6.4	Conclusion	119
6.5	References	119

Chapter 7: Summary and final conclusion

Appendix I	List of sample database numbers (FHI)	127
Appendix II	Information about the author	129

List of tables

Tab.3.1: Mass attenuation coefficients for Cu radiation	43
Tab.3.2: Calculated thickness values for the observed attenuation (in-situ-setup)	43
Tab.3.3: Fitted integral intensity, d-spacing and FWHM for Cu (111)	44
Tab.3.4: Observed results for the refraction shift correction	45
Tab.3.5: Fitted integral intensity and FWHM for Cu (111) and Cu (200)	50
Tab.4.1: Summary of the XRR evaluation of samples A to D	62
Tab.4.2: Obtained results from Rietveld refinement (TOPAS) of sample A and C	70
Tab. 5.1: XRR fit results obtained for samples A and E.	79
Tab. 5.2: XRR results obtained by fitting the measured data from sample B	85
Tab. 5.3: Fit results obtained from the XRR measurements of sample C.	90
Tab. 5.4: XRR fit results obtained from sample D.	94
Tab. 5.5: XRR fit results for sample F	98
Tab. 5.6: Obtained fit results for samples A to C (GIXRD)	101
Tab. 6.1: Summary of fit results from for the lattice constant a of Cu (brass)	117
Tab .6.2: Estimated layer thicknesses of deposited Si and the probable SiO ₂ top layer.	118

List of figures

Fig.1.1: World energy consumption by year in quadrillion Btu	1
Fig.1.2: World net electricity generation by electricity source	2
Fig.1.3: World energy supply by region	2

Fig.1.4: PEM electrolyser cell setup scheme	4
Fig.1.5: The negative theoretical calculated overpotentials versus the standard free energy	5
Fig.1.6: Potential cycling of a Ir foil in 0.5M H ₂ SO ₄	6
Fig. 2.1: Different types of XRD scans described in the reciprocal space.	17
Fig. 2.2: Geometrical view on a surface and constructed beam directions	20
Fig. 2.3: Penetration depth curve for Au, Pt, Ir	21
Fig. 2.4: Graphical summary of the parameters R, T and Λ	22
Fig.2.5: Beam path inside a thin layer.	23
Fig. 2.6: The Névot-Croce model of microscopic roughness	24
Fig.2.7: Representation of a rough surface	25
Fig.2.8: Measured XRR curve of a Si wafer coated with a 20 nm Pt layer	26
Fig.2.9: Rough and flat surfaces comparison	27
Fig.2.10. Fractal parameters; graphical representation	29
Fig. 2.11: ω -curve of a 50 nm Cu film	29
Fig.2.12: Intensity differences of an epitaxial GaAs/Al layer investigated by Marra	30
Fig. 2.13: in-plane and out-of-plane diffraction geometry	31
Fig.2.14: Standard out-of-plane setup	32
Fig.2.15: The refraction effect	33
Fig.2.16: The refraction effect dependence calculated for Ir	33
Fig.3.1: In situ XRD cell, optimized for Grazing Incidence diffraction (cross section view)	40
Fig.3.2: In situ XRD cell, optimized for Grazing incidence diffraction (side view)	40
Fig.3.3: Sample holder stamp (cross section view)	40
Fig.3.4: The in situ cell mounted on the diffractometer.	41
Fig.3.5: a) foil capping (FC) b) dome capping (DC) of the cell	42

Fig.3.6: Measured intensity of the Cu (111) reflection in the different steps of preparation	43
Fig.3.7: Four recorded cyclovoltammetry curves in 0.2M KOH	48
Fig.3.8: Chronoamperometry curve (20h @ -0.26V) of the polycrystalline copper	49
Fig.3.9: The polycrystalline copper electrode a) before and b) after treatment	50
Fig.3.10: In-situ GIXRD data recorded over time for the oxidation of polycrystalline Cu	50
Fig.3.11: In-situ GIXRD data recorded after 10 h exemplarily fitted	51
Fig.3.12: Graphical illustration of the assumed passivation layer formation	52
Fig.4.1: Cyclovoltamogram of sample A and B at different scan speeds	59
Fig.4.2: XRR data plots for all four samples A to D	61
Fig.4.3: HR-TEM image of Sample A and C	62
Fig.4.4: SEM images of the samples A to D.	63
Fig. 4.5: Diffuse penetration depth for iridium (scheme)	64
Fig.4.6: XRDS curved for samples A to D	65
Fig.4.7: Depth resolved XRDS parameter for samples A to D	66
Fig.4.8: XPS spectra for samples A to D	69
Fig.4.9: GIXRD pattern for samples A and C	70
Fig.4.A1: Hurst parameter over depth for samples A to D	74
Fig. 5.1: X-ray reflectometry curves and corresponding simulations for samples A and E	79
Fig. 5.2: SEM pictures of the sample surfaces of A and E in direct comparison	80
Fig. 5.3: Diffuse scattering measurements of samples A and E taken at various 2θ .	81
Fig. 5.4: Depth resolved XRDS parameter for samples A to E	82
Fig. 5.5: CV's of sample A in H_2SO_4 for 0.1 mV/s and 1 mV/s	83
Fig. 5.6: XRR curve of sample B	84
Fig. 5.7: Diffuse scattering measurements and data evaluation for sample B	86
Fig. 5.8: SEM image with corresponding EDX maps o sample B	87

Fig. 5.9: Close-up SEM image of sample B (compared to A)	87
Fig. 5.10: Results for the cyclic voltammetry of sample C	88
Fig. 5.11: Results for the chronoamperometry of sample C	88
Fig. 5.12: XRR curve of sample C	89
Fig. 5.13: Diffuse scattering measurements and data evaluation for sample C	91
Fig. 5.14: close-up SEM image of sample C (compared to A)	92
Fig. 5.15: SEM image with corresponding EDX maps o sample C	92
Fig. 5.16: CV curves of sample D	93
Fig. 5.17: XRR curve of sample D.	94
Fig. 5.18: Diffuse scattering measurements and data evaluation for sample D	95
Fig. 5.19: close-up SEM image of sample C (compared to A)	96
Fig. 5.20: SEM image with corresponding EDX maps o sample D	96
Fig. 5.21: CV and CA of sample F	97
Fig. 5.22: XRR curve of sample F.	98
Fig. 5.23: Diffuse scattering measurements and data evaluation for sample F	99
Fig. 5.24: SEM image with corresponding EDX maps o sample F	100
Fig.5.25: GIXRD pattern of samples A to D	101
Fig.5.26: GIXRD depth study of Ir (111) reflection	103
Fig.5.A1: Hurst parameter over depth for samples A to F	107
Fig. 6.1: SEM picture of the Ti-Al alloy (HT-alloy)	110
Fig.6.2: Depth sensitive GIXRD experiment of DP_1	111
Fig. 6.3: GIXRD patterns of differently treated Ti samples at identical incidence angles	112
Fig. 6.4: Cross-section TEM images and elemental composition (EDX) of sample IC-A and IC-B.	113
Fig.6.5: Temperature dependent reduction of the Cu/ZnO-based catalyst.	114

Fig.6.6: Hydrogen concentration dependent reduction of the Cu/ZnO catalyst	114
Fig.6.7: Activity data for the conversion to methanol for the temperature variation series.	115
Fig. 6.8: Lattice parameter changes Δa relative to pure copper	116
Fig. 6.9: Exemplary fit curves of the 400 °C/20% H ₂ treatment	116
Fig. 6.10: Exemplary reflectometry curves for of the LPCVD calibration	118
Fig. 6.11: Linear calibration curve for the LPCVD process of Si	119
Fig.7.1: Pictorial summary of the electrochemical behavior of sputter coated and e-beam evaporation prepared samples	123

Abbreviations

BESSY II	Berliner Electronenspeicherring für Synchrotronstrahlung
CA	Chronoamperometry
CE	Counter electrode
CV	Cyclovoltammetry
DWBA	Distorted Wave Born approximation
ED	Electron diffraction
FWHM	Full width half maximum
GIXRD	Grazing Incidence X-ray diffraction
HER	Hydrogen evolution reaction
OER	Oxygen evolution reaction
PEEK	Polyether ether ketone
PMMA	Poly(methyl methacrylate)
RE	Reference electrode
SEM	Scanning electron microscopy
TER	Total external reflection
TEM	Transmission electron microscopy
WE	Working electrode
XRD	X-ray diffraction
XRDS	X-ray diffuse scattering
XRR	X-ray reflectometry
XPS	X-ray photoemission spectroscopy

Chapter 1: Introduction

1.1 The energy challenge

Through the centuries, the development of human society was influenced by technological inventions. The availability of electricity, the glorious steam engine of James Watt and the development of computers which herald the digital century, are corner stones which have accelerated the changes in living technologies. Most daily used devices require energy and the world's consumption has increased enormously over the last decades. The energy demand of TVs, PCs, data storage systems, servers and the like already accounts for 8% of the world annual energy consumption (2008⁽¹⁾) and the prediction points towards even higher numbers in the near future. Fig.1.1 shows the world energy consumption by energy source since 1990 and a calculated prediction until 2040⁽²⁾. The trends seen can be separated into two categories: first, the positive increase of renewables and second, the still ongoing alarming increase in the use of fossil fuels like natural gas and coal to satisfy the world's energy demand.

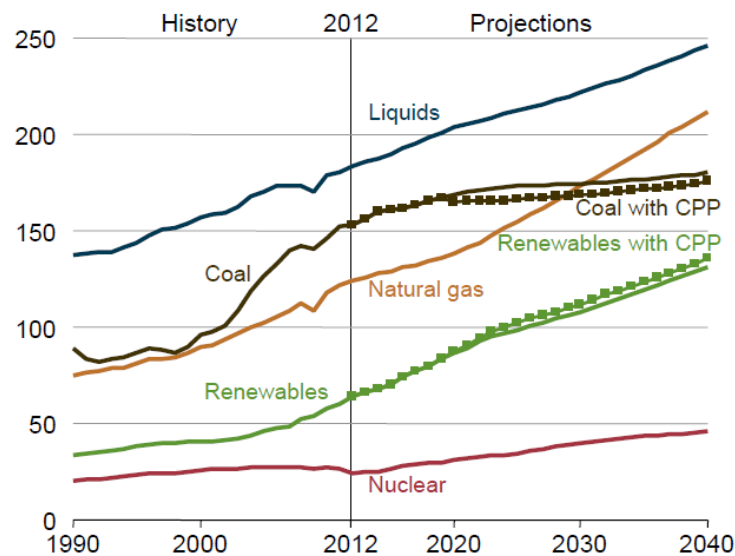


Fig.1.1: World energy consumption by year in quadrillion Btu (British thermal unit). CPP: clean power plan of the US government (prototyping). (graphic taken from⁽²⁾)

The latter trend represents a danger which is already visible and palpable today, the global warming connected with the greenhouse effect⁽³⁾. The necessary reduction of the CO₂ emission, the strongest origin of global warming, is strongly connected with the goal set on the Paris agreement to limit the global warming to 2.0 K⁽⁴⁾ (strong attempts to reach 1.5 K) compared to pre-industrial values. To achieve this ambitious goal, it requires a new industrial revolution to keep the frame and this small window open, in which it will be still possible to successfully reach it. Intertwine of politics, technology and industry is a mandatory step towards new possibilities to minimize the use of fossil fuels. This 2 K aim need on the one hand to achieve almost zero net CO₂ emission to be achieved between 2045 and 2060⁽⁵⁾, on the other hand the implementation of high efficiency low emission renewable resource technologies⁽⁵⁾. Nowadays, the term renewable energy sources includes bioenergy, geothermal energy, photovoltaics, wind energy and hydropower⁽⁶⁾. The electricity generation trend becomes the same than the above mentioned energy consumption in Fig.1.1, and is shown in Fig.1.2. Also in these graphs, the contribution of renewable energy sources becomes higher over decades beside a continuous use of fossil fuels for generating electricity.

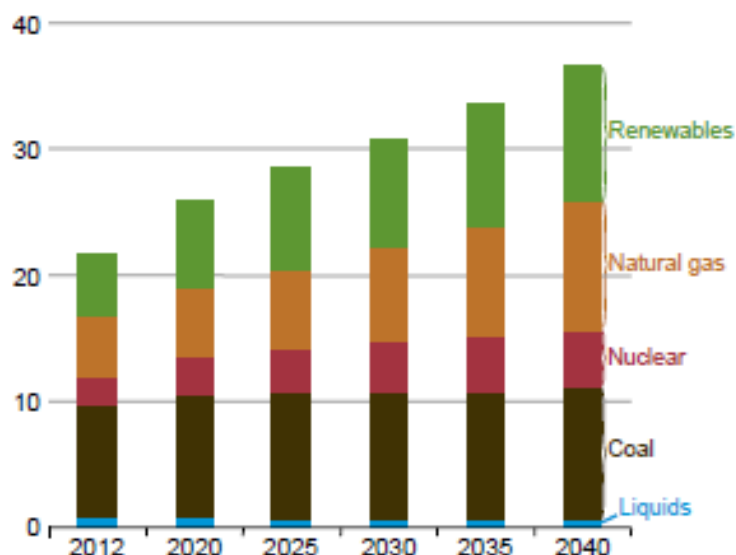


Fig.1.2: World net electricity generation by electricity source (year and trillion kWh). (graphic taken from⁽²⁾)

A last point of view on this increase in energy demand is a local perspective. Fig.1.3 displays the change in regional shares of the world energy supply from 1973 to 2014⁽⁷⁾. The total value (in Mtoe, Mega ton oil equivalent) has more than doubled within 40 years. One can clearly see also local changes, like the contribution of China which has become more than six times higher within this period. This opens the question of local infrastructure for the generation of renewable energy, as well the need to store energy excesses in an efficient and safe way next to agglomeration centres.

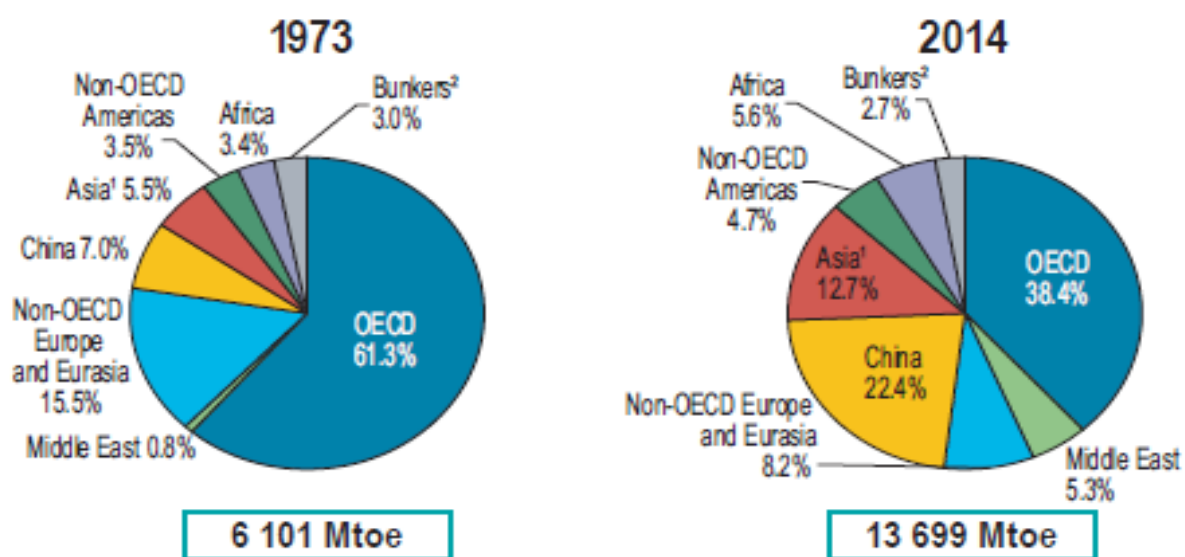


Fig.1.3: World energy supply by region (Mto : mega ton oil equivalent). (graphic taken from⁽⁷⁾)

1.2 Chemistry - the key tool

The conversion of excess energy into chemical compounds and bonds became a very interesting upcoming energy storage solution⁽⁸⁾. This offers the possibility to store very high energy densities in small energy rich molecules, like H₂, CH₄, CH₃OH or hydrocarbons⁽⁹⁾. The intermittency of wind and solar energy can be overcome by this solution and stored energy can be released on demand by

reconversion. Alternatively, the compounds can be further converted into desired products if not needed for energy generation. A drawback of this pathway is the low efficiency of converting energy into a chemical compound. Therefore, long term storage would be the primary use as rapid storage is hardly possible⁽⁹⁾. All of the above mentioned compounds are produced by reactions from hydrogen with carbon sources. Hydrogen received special attention as it seems to be the best compound for storage technologies due to its prominent properties like high storage density or reconversion possibility by fuel cells.

H₂ has the highest gravimetric storage capacity (33.3 kWh/kg) of all chemical compounds but the disadvantage of being gaseous^(9,10). In the conversion of hydrogen, no CO₂ emission occurs, just pure water is formed in case of O₂ as oxidant. Additionally, the use of hydrogen is widespread in many areas like industry, transport (fuel cells) or its further conversion to industrial base chemicals. One of the most promising ways to produce hydrogen is water electrolysis. This way of producing hydrogen just accounts for 4% of all hydrogen generation worldwide. The remaining 96% are made from coal and hence steam reforming^(10,11). This procedure yields low purity hydrogen with many impurities like CO, which need to be separated costly. The biggest challenge within the generation of hydrogen can be seen in the installation and development of highly efficient electrolyzers at low cost in the technology infrastructure⁽¹¹⁾. The great hope in this challenge relies on the possibility to overcome the intermittency effect of solar and wind energy and to store the energy with minimum loss as well high efficiency. Nevertheless, the use of hydrogen has also disadvantages. Since hydrogen is gaseous and hence has a low volumetric energy density, the efficient physical and chemical storage is an issue which is in the focus of investigation^(9,10). Additionally, the use of hydrogen and its transportation requires well developed safety standards, as it is a highly flammable compound.

One very promising technology among others, to reach an efficient H₂ production, is the water splitting process in PEM-electrolyzers. Fig.1.4 shows schematically a PEM cell setup. Proton Exchange Membranes (PEM) are semipermeable membranes, which let only protons pass through, while the gases stay separated. Nowadays the most widely used PEM material is Nafion® produced by DuPont⁽¹²⁾. Electrodes are very often made from platinum nanoparticles on carbon support, or other noble metals (Ir, Rh) or their oxides. One of the major advantages of this acid driven setup compared to other electrolyzers, like basic operating systems, is the very high purity of the produced hydrogen resulting from the very low cross-over rate during reaction^(11,13). This allows the PEM system to be very tolerant towards the input current and is related to the fact of very rapid transportation through the membrane almost without inertia of the protons. Achievable energy densities with this system reach values of 2 A/cm², which exceed the limits of many other possible electrolyser systems^(9,13). One disadvantage of the PEM-electrolysis are the very harsh operating conditions (acid electrolyte, pH < 4) and hence the resulting degradation of the materials used. Many materials suffer rapidly under these conditions and the system becomes deactivated. Only few noble metals are able to deal with the applied conditions. A second drawback are the costs and low abundance of the noble metals used in these electrodes. Many metals, metal oxides and supports have been tested and Ru and Ir based systems have been found to be the ones with highest stability and activity under OER conditions^(13,14). Unfortunately, the more active Ru based systems suffer from stronger corrosion than Ir⁽¹⁴⁾. Hence, Ir based systems are at the moment the only viable option in combination with PEM electrolyzers to offer an economical solution. However, the low abundance of Ir on the planet (<0.001 ppm⁽¹⁵⁾) represents a challenge for research to investigate the unique properties of iridium based electro-catalysts which are responsible for its excellent OER performance, in order to gain an understanding of key features to maybe be able to ultimately replace the expensive Ir.

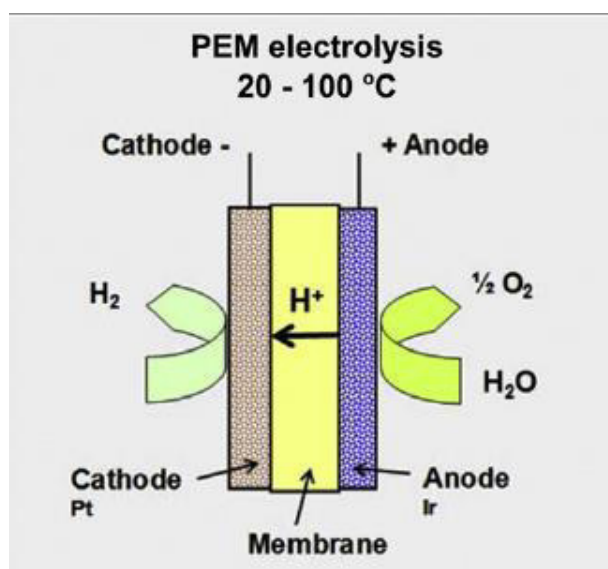
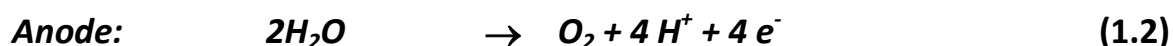
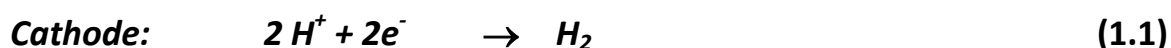


Fig.1.4: PEM electrolyser cell setup scheme (graphic taken from⁽¹³⁾)

1.3 Water splitting for hydrogen production

The water splitting reaction is already an “old” reaction and was first described by van Troostwijk in 1789⁽¹⁶⁾. He used a Leiden jar filled with water and two gold electrodes combined with an electrostatic machine to discharge the electrostatic potential difference between the two gold electrodes. As a result, he received hydrogen at one and oxygen at the other gold electrode. The following equations describe the overall process and the two half reactions^(13,17):



For the overall reaction, the reversible cell potential is 1.23 V (vs. SHE)⁽¹⁷⁾. Water splitting is an endergonic process ($\Delta G > 0$) and hence a driving force, in this particular case electrolysis, is needed to produce hydrogen. However, the value of 1.23 V is only valid for a perfect system. A variety of additional contributions needs to be considered which increase the cell potential, like ohmic losses, transport limitation by diffusion to the surface or slow electrolysis kinetics⁽¹⁷⁾. In case of the modern electrocatalysts like iridium the overpotential of the anodic oxidation (oxygen evolution reaction, OER) is much higher than the one for the cathodic reduction (hydrogen evolution reaction, HER). Exactly this OER overpotential makes the process energy consuming and not very economic for the desired hydrogen production. The understanding of the surface reaction of water splitting is a complex issue, since it requires the transfer of 4 protons and 4 electrons for one oxygen molecule (see Eq.1.1-1.3). Iridium exhibits one of the lowest overpotentials among the prominent OER catalysts, which, besides the mentioned stability, is another important reason for the increasing interest to study iridium surfaces under OER conditions.

1.4 Iridium as OER catalyst

The use of iridium surfaces as OER catalysts originates from the stability, low overpotential and high activity in the OER reaction after forming an active oxo-hydroxo layer on top of metallic iridium. If one takes a look on Fig.1.5, the theoretical overpotentials⁽¹⁸⁾. Man et al chose as descriptor $\Delta G^0_{O^*} - \Delta G^0_{HO^*}$, the difference in between the adsorption energy of bound O^* and OH^* . In the upper region, the noble metal oxides are located, indicating low overpotentials. The correlations between binding energies, enthalpy of transitions and activity are still a point of discussion in the literature^(19,20). In good agreement with experimental findings the most promising candidates for the desired OER are IrO_2 and RuO_2 . Even though RuO_2 has a lower overpotential than IrO_2 it suffers from some disadvantages. Weak O adsorption⁽²¹⁾, higher dissolution and formation of volatile Ru oxides in higher valent states are some crucial bottleneck properties in using Ru based OER catalysts^(21,22).

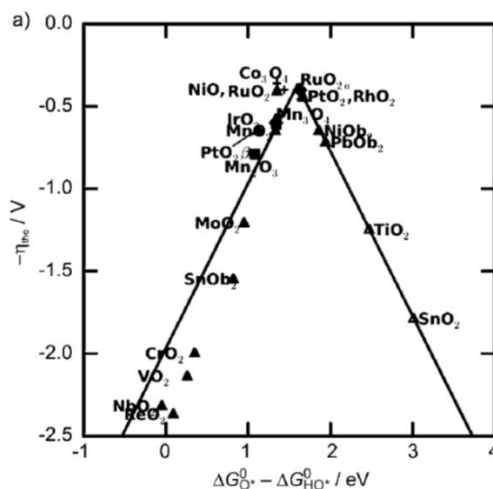


Fig.1.5: The negative theoretical calculated overpotentials versus the standard free energy of the $\Delta G^0_{O^*} - \Delta G^0_{HO^*}$ step (graphic taken from⁽¹⁸⁾).

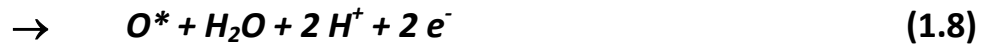
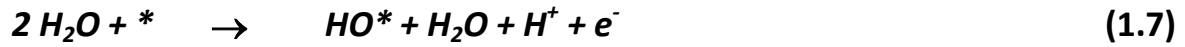
Efforts have been made in order to describe the OER mechanism^(23,24,25). Most of them are based on purely electrochemical observations with time dependent current potential measurements^(24,25). Bockris derived in 1956⁽²⁶⁾ a well-established and often referred to mechanism of the surface oxidation, in a dissociative oxide pathway:



The star (*) indicates the active site for oxygen evolution on the catalyst. The rate determining step in the work of Damjanovic⁽²⁷⁾ is shown in Eq. 1.5. and was proposed to be valid for iridium. A subsequent mechanistic step in the reaction scheme of Damjanovic and Bockris was derived by Fierro⁽²⁸⁾ to explain the activity also for active metal oxides.

Beside the mechanism proposed by Bockris, Nørskov⁽²⁹⁾ found out by using DFT calculations, that there is a possible second mechanism able to explain the OER, a recombination mechanism over a

peroxide intermediate. Eq.1.7-1.10 display the oxygen formation over a peroxo intermediate. The direct recombination of $-O-O-$ described by Bockris has, according to Nørskov *et al.*, a high activation barrier and thus is not likely to happen.



(*) again indicates the active site. In this mechanism, Nørskov assumed Eq.1.9 to be the rate determining step to form the high energy peroxo intermediate.

During potential cycling (cyclovoltammetry CV), iridium exhibits a unique behavior, the cyclovoltammogram changes remarkably in terms of increasing surface area⁽³⁰⁾. Fig.1.4 shows a classic current potential treatment (CV) on Ir. The initial stage of a reversible monolayer oxidation and the later turn into a multi-layer oxidation in connection with a significant change in conductivity rely likely to the later higher OER activity^(31,32). The bare metal, compared to the oxidized species on top formed during potential cycling, undergoes stronger dissolution during the treatment⁽³³⁾. The growth of the Ir-oxo-hydroxo layer on top of metallic iridium depends on many conditions like: the potential range⁽³¹⁾, the temperature or electrolyte concentration⁽³³⁾. Its formation is accompanied from a significant change in surface morphology⁽³²⁾.

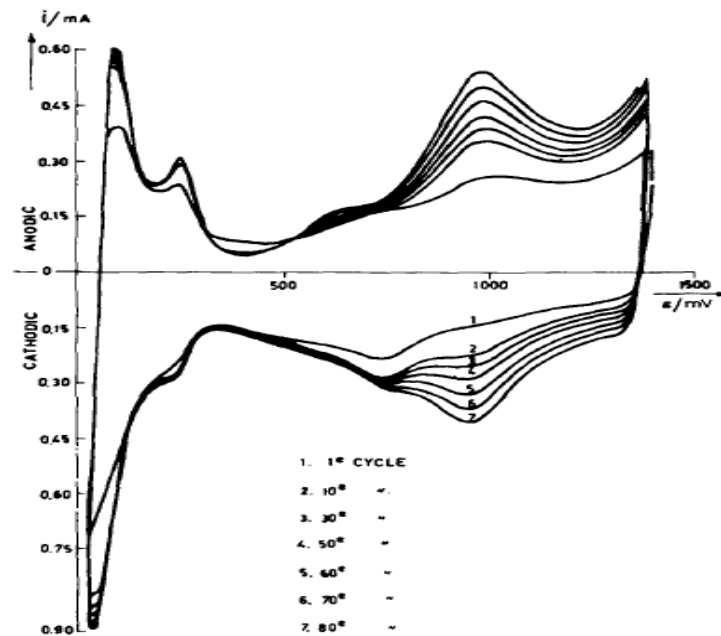


Fig.1.6: Potential cycling on Ir foil in 0.5M H_2SO_4 scan speed: 280 mV/s (80 cycles) (graphic taken from⁽³⁷⁾)

In Fig.1.6 it can be seen that with higher cycle numbers the oxidation peaks (around 1.0V vs. RHE) start to increase, and continue to grow^(30,34,35,36). Otten and co-workers^(37,38) were first reporting this phenomenon in detail. The interesting effect they observed was related to the fact, that only the

oxide peaks increase continuously whereas the hydrogen peaks (close to 0 V in Fig.1.4) converge after a few cycles at a constant value. This phenomenon lead according to Otten also to a surface smoothing^(33,37). The formation of this oxygen containing layer is nowadays known to be necessary and enhances the rate of OER⁽³⁹⁾. A second peculiar behavior of the iridium oxidation during cyclic voltammetry is its known electrochromism. The oxidation step is accompanied by a color change from shiny silver to bluish-black (depending if the CV is stopped before or after around 1V vs SHE) and according to Buckley⁽⁴⁰⁾ directly related to the formation of non-stoichiometric compounds, like oxides, hydroxides or hydrated oxides. Buckley *et al.* gave additional hints to a two-step model of conversion on the oxide layer, first from the metal to the hydroxide, than later *via* hydrated oxides to the surface oxide. Nevertheless, despite all these hints and pioneering work, the analysis of the layer and its composition remains a challenge for present-day analytical possibilities.

1.5 The challenge of the structure

Obtaining results indicating the structural change of the iridium surface under OER conditions is an elusive aim. To understand these changes, associated with electrochemistry is not straightforward. It is undoubtedly the key to understanding, to find direct hints for the atomic arrangement and the layer composition. Numerous attempts have been made to elucidate the nature of the oxo-hydroxo layer on top of metallic iridium. The work done so far can be roughly divided into two groups: First, the investigations on its electronic structure (including spectroscopic techniques) and second true crystallographic and microscopic investigations. One can find Raman spectroscopy⁽⁴¹⁾, DFT calculations⁽²⁹⁾, X-ray photoelectron spectroscopy^(42,43), ellipsometry⁽³⁷⁾ or electron microscopy⁽⁴⁴⁾ in the manifold pool of methods applied to study electrochemical oxidized iridium surfaces .

One of the major drawbacks of the before mentioned methods, is often their local character. Electron microscopy (especially Transmission electron microscopy) or X-ray Photoelectron spectroscopy have just small probing spots and therefore can only gain information on a very small length scale. Although often the integral characterization is of advance, since it statistically probe the whole surface area. The commonly most used integral technique is X-ray diffraction. It remains the most valuable and powerful method concerning structure determination. One of the greatest advantages compared to a method like electron microscopy relates to the non-destructive sample preparation and the ambient measurement conditions (as electron microscopy requires vacuum). The simplest way to perform an diffraction experiment is, absolute standard technique in a material characterization laboratory, the classic powder diffraction. Most of the early XRD works have been performed with this well-known Bragg-Brentano geometry⁽⁴⁵⁾ (reflection mode). The XRD testing in powder diffraction geometry of used electrocatalysts is often just applied as check for phase identification or to monitor lattice changes caused by the treatment^(46,47). One interesting insight by structural characterization was found by Michell⁽⁴⁴⁾ in 1977. With electron diffraction, they could derive a ring pattern indicating a hexagonal lattice of the likely formed oxo-hydroxo layer on top of a cycled Ir foil. Chabanier performed one of the first experiments for hydrogen adsorption on thermally prepared IrO₂ electrodes under in-situ conditions (electrochemical polarization) with X-ray diffraction⁽⁴⁸⁾. One of the major disadvantages of X-ray diffraction is the invisibility of amorphous or nanocrystalline phases. To make in such cases the X-ray diffraction technique applicable, one needs very dedicated setups. X-ray pair distribution function analysis would be one example. PDF describes the probability to find two atoms at a given interatomic distance. This technique is of special interest for samples which do not show a classical long range lattice periodicity. With this technique, some Ir-

O bridged rutile-typed structured were investigated⁽⁴⁹⁾. Today it is a well-accepted fact, that the oxo-hydroxo layer formed is X-ray amorphous but exhibits a better catalytic activity than the plain metal⁽³⁹⁾. The finding of the surface layer formed on an iridium substrate gave rise to the question of the surface sensitivity of diffraction methods. In general XRD is known as a bulk testing method and not to be very surface sensitive (nm scale). Since the pioneering experiment of Grazing Incidence X-ray Diffraction (GIXRD) in 1979 by Marra⁽⁵⁰⁾, the ability to study surface-near regions by diffraction became established. Additionally, the slightly older method of X-ray reflectometry (XRR) is also a very suitable tool for surface characterization. In contrast to GIXRD, XRR probes the electron density and not the crystal lattice, and thus can be applied also for amorphous layers. A few works with this elaborate technique are reported on thermally prepared iridium layers (as well electrochemically treated) and iridium oxide catalysts^(51,52,53). Nevertheless, these methods are found just in a few special cases in the field of electrochemistry to be reported in literature to the study of surface near phenomena, like catalysis. This originates from their delicate handling and elusive data evaluation in combination with many restrictions. So far, no real systematic diffraction/reflection studies of electrochemical treatments on iridium surfaces (e.g. thin Ir films) are reported in the literature.

1.6 Scientific objective and outline of this work

As stressed in the last section, integral methods are mandatory for a representative characterization of a sample surface. This is especially the case for layered systems. The need to do so for iridium samples originates from its use as electrocatalyst and the possibility to use it in lowest amount possible, coated on a conductive substrate. Studying such thin layered systems is a difficult goal to reach, since the problems of staying comparative with other works and published results start already in the early stage of sample preparation. The lack of dedicated studies on thin film electrodes, and the issue of comparability of the near-surface properties of iridium layers prepared with different deposition methods lead to the first two points of the basis of this work:

- Methodological development and application of the thin film diffraction techniques: GIXRD, XRR and XRDS on electrocatalytic systems.
- Establishing a very simple and applicable model system for demonstrating the influence of oxygen evolution reaction conditions on iridium thin film electrodes.

As both of these key points, the analytical/methodological and the sample side, represent explorative development work and need necessarily to go hand in hand to match each other, it should be self-evident that this road is highly iterative and anything but straight.

An additional very important field in connection with the study of thin film electrodes, as well electrochemistry in general, is to enable the possibility of in-situ experiments. This goal is even more difficult to reach, since many restrictions arise from making a reasonable compromise between the measurement techniques and the electrochemical requirements. Nevertheless the ultimate aim would be to get a direct structure-activity correlation under working conditions. Although this is probably not so easily achievable, a first attempt towards detectable changes can be made on well-known systems beside the very complex case of iridium. Thus, the third point of focus became:

- Development and establishing of a home laboratory in-situ setup for electrochemical surface investigations, especially enabling GIXRD studies.

In general the integral character of the thin film diffraction methods is in focus. Since many systems exhibit kinetically different intrinsic properties, e.g. defect density, the results after a certain treatment will be strongly influenced by them. In many reactions the process between bulk catalysts and their surface is different and often dedicated local sites play the key role. To give this a statistically lateral and vertical description on nm scale, GIXRD and related methods are likely a key tool, due to the reasons mentioned above. The present work can be seen as a three point attempt to establish thin film characterization in electrocatalysis.

Chapter 2 is dedicated to the theoretical background of the principle applied techniques in this work: X-ray reflectometry, X-ray diffuse scattering and Grazing Incidence X-ray diffraction. A short introduction on the theoretical background is given, followed by the description of the morphology testing techniques XRR and XRDS and subsequently the discussion of the structure testing technique GIXRD.

Chapter 3 focusses on the results of an electrochemical in-situ GIXRD experiment performed on polycrystalline copper. The development of an in-situ cell setup for use in the home laboratory and a guide for data treatment is presented. Oxidation of polycrystalline copper in alkaline media is used as test reaction to demonstrate the functionality of the in-situ setup. Cyclic voltammetry was used as characterization tool and chronoamperometry was applied for a 20 h study of oxidation activity. A multi-step surface passivation could be mechanistically deduced and described by the observed electrochemical as well diffraction data, resulting in clear evidence for a cuprite intermediate.

Chapter 4 gives a detailed study on the morphology of a thin Ir layer model system before and after exposure to oxygen evolution conditions. This study compares two differently prepared Ir-layers under identical electrochemical treatment. The chapter sheds some light on the question how the layer morphology influences the later activity under OER conditions. Cyclic voltammetry and chronoamperometry are used to treat the surfaces. The differences are monitored by XRR as well XRDS, Scanning electron microscopy (SEM) and Transmission electron microscopy (TEM). The electronic structure was checked by X-ray photoelectron spectroscopy and extracted lattice parameters were compared. This comparative study demonstrates that intrinsic differences in layer morphology are mirrored in the resulting electrochemical activity, hence pointing to kinetic differences. Additionally, the morphological characterization of a disturbed layer (probably the desired $\text{Ir}(\text{O})_x(\text{OH})_y$) formed on top of the metallic iridium highlights this chapter. Due to the integral characterization, nm scale changes can be connected to macroscopic measurable properties.

Chapter 5 intends to use the acquired knowledge from chapter 4 to illustrate the influence of the treatment on the morphology of identically prepared layers. Three scenarios to probe the dependencies are chosen: (i) slow speed cyclic voltammetry (CV) (ii) slow speed CV followed by chronoamperometry (CA) and (iii) high speed cycling. Again, the comparison of the morphological aspects was accomplished by XRR, XRDS and SEM. A dedicated two layer model is developed and allows separating the morphology of remaining and altered iridium regions. Here, it can be demonstrated that different treatments as well as different scan speeds do not result in the same final morphology. Fractal parameters are examined over depth and are in good agreement with electrochemical predictions. GIXRD finally completes the thin film investigation by observing peak shape changes. To perform verification for the sensitivity of the chosen measurement combination, one e-beam evaporation sample was cycled only a single time and shortly held at a low potential for chronoamperometry. This sample type, even though known to be less active from chapter 4, allows a more precise analytical data treatment. A detailed study on the intensity and peak width of the Ir 111

reflection is conducted and evaluated. This sample uncovers the changes which appear small in XRR and XRDS but obviously destroy the long range order already after one cycle. Due to the integral character of the applied X-ray diffraction and scattering methods the results illustrate the strong dependency of the resulting layer morphology and structure from the treatment. Due to the absence of massive bulk iridium, these experiments detect the lateral and structural changes on a very surface near level.

Chapter 6 sums up three examples of using GIXRD and XRR beside the common scope. The power of depth sensitive, qualitative phase analysis is performed at two samples, a high temperature alloy and a model system for lithium battery technology. The phase analysis is combined and verified with Scanning electron microscopy and Transmission electron microscopy. The second case 'outside the box' is related to powder samples. Dense pressed pellets of a catalyst, previously exposed to reductive atmosphere, were analyzed by GIXRD. A treatment-dependent shift could be identified due to alloy formation and connected to the deactivation of the catalyst. Finally, as third example, the calibration of a LPCVD process via XRR is presented.

Chapter 7 gives a conclusion and outlook about the present thesis and the answers obtained on the scientific questions.

1.7 References

- 1) M. Pickavet, W. Vereecken, S. Demayer, P. Audenaert, B. Vermeulen, C. Develder, D. Colle, B. Dhoedt, P. Demeester, IEEE ANTS, (2008 conference) 1-3
- 2) International energy outlook 2016, US Energy Information Administration, [www.eia.gov/forecasts/ieo/pdf/0484\(2016\).pdf](http://www.eia.gov/forecasts/ieo/pdf/0484(2016).pdf) , 18.10.2016
- 3) C. McGlade, P. Ekins, Nature 517 (2016) 187-190
- 4) The Paris agreement, <http://unfccc.int/resource/docs/2015/cop21/eng/l09r01.pdf>, 18.10.2016, see also: <http://unfccc.int/resource/docs/2010/cop16/eng/07a01.pdf>, 19.10.2016 see also: http://unfccc.int/files/essential_background/convention/application/pdf/english_paris_agreement.pdf, 19.10.2016
- 5) J. Rogelj, G. Luderer, R. Pietzcker, E. Kriegler, M. Schaffler, V. Krey, K. Riahi, Nature climate change, 5 (2015) 519-527
- 6) <http://www.bgbl.de/xaver/bgbl/start> , BGBl II, p.634-635, 20.10.2016
- 7) Key world energy statistics 2016, International Energy Agency, <https://www.iea.org/publications/freepublications/publication/key-world-energy-statistics.html>, 18.10.2016
- 8) R. Schlögl, ChemSusChem. 3 (2010) 209-222
- 9) F. Schüth, 1.2 Energy Storage Strategies in *Chemical Energy Storage*, R.Schlögl, (2013), de Gruyter
- 10) A. Ursua, L. M. Gandia, P. Sanchis, Proc. IEEE 100 (2012) 410-426.
- 11) B. Ulrich-Eberle, Energy & Environmental science 5 (2012) 8790-8798
- 12) <http://www.dupont.com/products-and-services/membranes-films/fluoropolymer-films/brands/naion-pfsa-membranes.html>, 20.10.2016
- 13) M. Carmo, D. Fritz, J. Mergel, D. Stolten, Int. J. Hydrogen Energy 38 (2013) 4901-4934
- 14) R. Kötz, S. Stucki, D. Scherson, D. Kolb, J. Electroanal. Interfacial Electrochem. 172 (1984) 211-219
- 15) Harry H. Binder: Lexikon der chemischen Elemente. S. Hirzel Verlag, Stuttgart 1999

- 16) A. Paets van Troostwijk, J. Deiman, *Obs. Phys.* 35 (1789), 369
- 17) C. H. Hamann, W. Vielstich, *Elektrochemie*, Wiley-VCH, Weinheim, 4th Edition, 2005.
- 18) I. Man, H. Su, F. Calle-Vallejo, H. Hansen, J. Martinez, F. Abild-Pedersen, J. Kleis, B. Hinnemann, J. Rossmeisl, *ChemCatChem*. 3 (2011), 1159-1165
- 19) S. Trasatti, *Electrochim. Acta*, 29 (1984) 1503-1512
- 20) J. Rossmeisl, Z. W. Qu, H. Zhu, G. J. Kroes, J. K. Nørskov, *J. Electroanal. Chem.* 607 (2007) 83-89
- 21) M. Wohlfahrt-Mehrens, J. Heitbaum, *J. Electroanal. Chem.* 237 (1987), 251-260
- 22) G. Beni, L. Schiavone, J. Shay, B. Schneider, *Nature* 282 (1979) 281-283
- 23) C. C. L. McCrory, S. Jung, J. C. Peters, T. F. Jaramillo, *J. Am. Chem. Soc.* 135 (2013) 16977-16987
- 24) J. Suntivich, K. J. May, H. A. Gasteiger, J. B. Goodenough, Y. Shao-Horn, *Science* 334 (2011) 1383-1385
- 25) M. Risch, J. Suntivich, Y. Shao-Horn, Oxygen evolution reaction, in R. Savinell, K. Ota, G. Kreysa, Eds., *Encyclopedia of Applied Electrochemistry*, Springer-Verlag, 2013
- 26) J. O. Bockris, *J. Chem. Phys.* 24 (1956) 817-827
- 27) A. Damjanovic, A. Dey, J. O. M. Bockris, *J. Electrochem. Soc.* 113 (1966) 739-746
- 28) S. Fierro, T. Nagel, H. Baltruschat, C. Comninellis, *Electrochem. Commun.* 9 (2007) 1969-1974
- 29) J. Rossmeisl, A. Logadottir, J. K. Nørskov, *Chem. Phys.* 319 (2005) 178-188
- 30) A. Capon, R. Parson, *J. Electroanal. Chem.* 39 (1972) 275-286
- 31) J. Mozota, B. E. Conway, *Electrochimica Acta* 28 (1983) 1-8
- 32) B. E. Conway, J. Mozota, *Electrochimica Acta* 28 (1983) 9-16
- 33) D. A. J. Rand, R. Woods, *J. Electroanal. Chem. Interfacial Electrochem.* 55 (1974) 375-381
- 34) S. Gottesfeld, J. D. E. McIntyre, G. Beni, J. L. Shay, *Appl. Phys. Lett.* 33 (1978) 208-211
- 35) E. Frazer, R. Woods, *J. Electroanal. Chem.* 102 (1979), 127-130
- 36) W. Böld, M. Breiter, *Electrochim. Acta*, 5 (1961), 145-160
- 37) J. Otten, W. Visscher, *J. Electroanal. Chem. Interfacial Electrochem.* 55 (1974) 1-11
- 38) J. Otten, W. Visscher, *J. Electroanal. Chem. Interfacial Electrochem.* 55 (1974) 13-21
- 39) Y. H. Hall, P. M. A. Sherwood, *J. Chem. Soc., Faraday Trans. 1*, 80 (1984) 135-152
- 40) D. N. Buckley, L. D. Burke, *J. Chem. Soc., Faraday Trans. 1*, 71 (1975) 1447-1459
- 41) Z. Pavlovic, C. Ranjan, Q. Gao, M. v. Gastel, R. Schlögl, *ASC Catalysis* 6 (2016) 8098-8105
- 42) R. Kötz, H. Neff, S. Stucki, *J. Electrochem. Soc.* (1984), 131, 72-77
- 43) V. Pfeifer, T. E. Jones, J. J. Velasco Vélez, C. Massué, R. Arrigo, D. Teschner, F. Girgsdies, M. Scherzer, M. T. Greiner, J. Allan, M. Hashagen, G. Weinberg, S. Piccinin, M. Hävecker, A. Knop-Gericke, R. Schlögl, *Surf. Interface Anal.* 48 (2016) 58-270.
- 44) D. Michell, D. Rand, R. Woods, *J. Electroanal. Chem.* 84 (1977) 117-126
- 45) J. Brentano, *Proc. Phys. Soc.*, 37 (1924) 184-193
- 46) A. Benedetti, S. Polizzi, P. Riello, A. Battisti, A. Maldotti, *J. Mater. Chem.* 4 (1991) 511-515
- 47) D. Abbott, D. Lebedev, K. Waltar, M. Povia, M. Nachtegaal, E. Fabbri, C. Copéret, T. Schmidt, *Chem. Mat.* 28 (2016) 6591-6604
- 48) C. Chabanier, D. Guay, *J. Electroanal. Chem.* 570 (2004) 13-27
- 49) J. Huang, J. D. Blakemore, D. Fazi, O. Kokhan, N. D. Schley, R. H. Crabtree, G. W. Brudvig, D. M. Tiede, *PCCP Communications* 16 (2014) 1814-1819
- 50) W. Marra, P. Eisenberger, A. Cho, *J. Appl. Phys.* 50 (1979) 6927-6933
- 51) S. Cherevko, S. Geiger, O. Kasian, N. Kulyk, J. Grote, A. Savan, B. Shrestha, S. Merzklin, B. Breitbach, A. Ludwig, K. Mayerhofer, *Catalysis Today* 262 (2016) 170-180
- 52) S. Kohli, C. Rithner, P. Dorhout, *Adv. X-ray Analysis* 45 (2004) 352-358
- 53) A. Bergmann, E. Martinez-Moreno, D. Teschner, P. Chernev, M. Gliech, J. Ferreira de Araújo, T. Reier, H. Dau, P. Strasser, *Nature Commun.* 6 (2015) 1-9

Chapter 2: Thin film diffraction

2.1 Introduction

Since the discovery of the diffraction condition in 1912 by Henry and William Bragg, the use of diffraction techniques has become a standard analytical tool in industry and research for structural investigations. The field of surface sensitive analytics has become one of major importance for the semiconductor industry due to the rise of microchip technology which has spawned an interest in investigating thin conductive layers and coatings on substrates (circuit boards) (hot topic: “FinFET Scaling to 10 nm Gate Length”⁽¹⁾). Furthermore, important optoelectronic layer materials like zinc oxide⁽²⁾, graphene oxide⁽³⁾ or tin oxide⁽⁴⁾ have moved into the focus of industrial research as they exhibit unique properties in photo- and electrochemical processes (OLEDs, phototransistors, solar cells,...). The behaviour of such thin layers is dependent on their composition and degree of order (single- vs. multilayer, degree of crystallinity) as well as their interface properties. The latter can enhance or suppress features like conductivity or resistance on the monolayer level. Magnetic and non-magnetic stacking⁽⁵⁾ in magnetic recording materials or the formation of quantum dots⁽⁶⁾ are two further examples of interesting information made accessible through X-ray diffraction techniques applied to thin films. Depending on the preparation process used, e.g. growth or deposition method, the layers exhibit different surface quality or smoothness. They may also show strain effects⁽⁷⁾ which lead to misorientation or unwanted island formation to achieve relaxation of the stress produced during the layer growth. Gaining knowledge and insight into microstructural contributions and the physical state of thin layers is of essential importance for industry to improve existing processes and targeting strategies for new processes.

Surface sensitive X-ray diffraction techniques are widely applied in material research. They offer the possibility of non-destructive analysis of samples for gaining insight into long range ordering (crystal lattice) for structural characterisation, as well as morphological characterisation. Areas like catalysis and electrochemistry have profited from the invention of thin film techniques, as they allow the study of interface phenomena (electrode-electrolyte, solid-gaseous) or surface reactions on a nm scale^(8,9). The characteristic extractable information, such as structure (phase) information or surface morphology parameters, provides the foundation for the mechanistic understanding of many reactions. The values obtained also offer the possibility of scaling between systems and allow predictions for process improvement. Therefore, surface X-ray diffraction provides a wide field of investigation possibilities and acts as a bridge for insights between macroscopic and microscopic changes.

To put the thin film diffraction methods used in this work into a larger context, a brief overview of the major surface sensitive X-ray techniques (XRR, XRDS and out-of-plane GIXRD) will be given later in this chapter. In placing them into a sequential order of a methodology “tree” one needs to consider the sample types to be investigated. First, one distinguishes between single crystal and powder X-ray diffraction. The former refers to single crystals with sizes usually larger than 0.1 mm, measured in transmission geometry for a complete structure characterization (atom positions, bond lengths and angles). The latter refers to the much more widespread analysis of polycrystalline powders. Nowadays, this is mainly divided into two sub areas, i.e. powder diffraction in the narrow sense and the field of layered materials. The first area has its focus on qualitative and quantitative phase analysis. Herein the lattice parameters (a , b , c , α , β , γ) as well as microstructural parameters like crystallite size and microstrain contributions of phases contained in a sample are can be and

determined. The most widely used measurement geometries are *Bragg-Brentano* (reflection mode) and *Debye-Scherrer* (transmission mode). With the aforementioned increasing interest in layered samples, dedicated X-ray diffraction techniques for their investigation have become more prominent as well. Depending on the question to be answered, different geometries and techniques are available within this area of diffraction methods. The most important ones are *Grazing Incidence Diffraction (GIXRD)* and *X-ray Reflectometry (XRR)*. Further methods are *X-ray Diffuse Scattering measurements (XRDS)*, *High Resolution X-ray Diffraction (HRXRD)* and *Reciprocal Space Mapping (RSM)*. For completeness, the reflection mode of Small Angle X-ray Scattering, termed *Grazing Incidence Small Angle X-ray Scattering (GISAXS)* shall be mentioned as well. The above mentioned techniques can be grouped as follows:

- Morphology testing techniques (XRR and XRDS) – they are ***electron density sensitive***
- Structure testing techniques (GIXRD and RSM (HRXRD)) – they are ***long range order sensitive (“lattice sensitive”)***

In general, all the above mentioned thin film techniques can be combined under the term *Grazing Incidence* as they all work at far lower incident or exit angles than common diffraction techniques. As the methods XRR and XRDS are the main focus of this work, they will be described in more detail in the following sections. Having used GIXRD in the experimental part of this thesis, the basic description for the out-of-plane geometry will be briefly given in addition. Reciprocal space mapping offers the possibility to measure in grazing-incidence or grazing-exit geometry also but this technique was beyond of the scope of this work and will not be discussed further.

2.2 Theoretical background

The theoretical considerations and theories behind X-ray scattering processes are very complex. Within this section, the theoretical background for XRR and XRDS shall be given in support of the overlaying interpretation and evaluation in the experimental parts of the later chapters.

2.2.1 Kinematic theory

X-ray diffraction is used as one of the best methods for structure determination, in terms of lattice parameter as well in the case of single crystal diffraction the atomic positions and angles. In the broad field of powder x-ray diffraction, the theory behind the scattering process is well described and very often the so-called kinematic approximation is used for reasons of simplification. The origin of this approximation is based on the assumption that for poly crystalline samples (powders) the scattering process can be seen as weak. This statement can be related simply to the imperfection of most crystals and crystalline samples. These crystals consist of a large number of slightly mis-oriented blocks (often referred to as mosaic blocks) and only a very small fraction of these blocks will be available for diffraction (-> Bragg condition). By averaging over the whole sample penetrated during a diffraction experiment (e.g. Bragg-Bentano geometry in powder diffraction) the intensity of a Bragg reflection is representatively measurable. The mosaic blocks can be seen as interruption of the “perfect” crystal and hence the dynamic effects do not occur. When multi-scattering processes appear (what most often happens in almost perfect crystals), the kinematic approximation breaks down and the interaction of the beam and matter becomes strong. For example, effects like multiple scattering, extinction or anomalous dispersion can then be only explained by considering the dynamic theory.

A very brief outline of the basic diffraction magnitudes, the intensity dependence and the peak position condition will be given in this short paragraph based on a classic physics textbook⁽¹⁰⁾. At first in modelling the measured intensity, the consideration on the scattering amplitude of a single atom, the so called atomic form factor f , needs to be taken:

$$f_0(Q) = \int \rho(r) e^{iQ \cdot r} dr \quad (2.1)$$

Herein the electron density distribution in the atom is evaluated. The integral over the electron density $\rho(r)$ is in turn equal to the total number of electrons Z . The volume weighted f_0 gives the distribution over the entire atom. This distribution can be extended to a molecule and is written as its sum over all apparent atoms (*1 to j-th atom*) within the molecule:

$$F_{mol}(Q) = \sum_j f_j(Q) e^{i(Q) \cdot r_j} \quad (2.2)$$

Since the scattering amplitude of a crystal is especially of interest, the definition of the contribution elements for F must be redone. Crystalline materials are described by their long range order (periodicity) as well their apparent translations symmetry. The combinatory description of the crystal lattice is based on the lattice and its basis. This means the lattice spans the spatial dimensions, whereas the basis represents the unit cell which corresponds atoms or molecules with each point of the lattice. This leads to an insufficient description of point r as mentioned in Eq.2.1, which defines the charge volume of electrons around point r with dr . Therefore r_j (Eq.2.2) becomes r_l via $R_n + r_j$. R_n represents a lattice vector and r_j the position of an j -th atom in the unit cell. With this new definition Eq.2.2 can be reformulated to average over all atoms in the crystal:

$$F_{cryst}(Q) = \sum_l f_l(Q) e^{i(Q) \cdot r_l} \quad (2.3)$$

Finally, to achieve a Bragg condition dependence, one needs to introduce the description of the lattice over the Miller indices (h,k,l) in connection with the reciprocal lattice vectors. This definition leads to an hkl dependent expression⁽¹¹⁾:

$$F_{hkl} = \sum_j^N f_j e^{[2\pi i(hx_j + ky_j + lz_j)]} \quad (2.4)$$

f_j ... atomic scattering factor of atom j

N ... number of atoms in the unit cell

h,k,l ... Miller indices

x,y,z ... coordinates of the j -th atom within the unit cell

Eq.2.1 reveals one very important statement of the kinematical scattering theory: the Fourier transformation of the electron density leads to the atomic scattering factor. This can be further extended to the structure factor F of a molecule or crystal and can become hkl -dependent. The second major statement of kinematic approximation becomes the intensity of the observed hkl reflection, which is simply related to the mean square of F_{hkl} :

$$I_{hkl} \propto |F_{hkl}|^2 \quad (2.5)$$

This relation describes also a fundamental problem of X-ray diffraction: the so-called phase-problem. Since only $|F_{hkl}|^2$ is available as measurement result (intensity) and not F_{hkl} directly, the information about the phase-shift and other phase-dependencies is lost. This is due to the overlapping of the scattered waves from all atoms (for a certain hkl reflection) within the unit cell and each has its discrete phase shift. To obtain the structure factor directly, this problem can only be solved either by so-called “direct methods” or the heavy-atom-method known as “Patterson-method”. These methods approximate analytically the phase shift and lead to the desired information and deliver F_{hkl} .

The second descriptor, the peak position condition is well known as a Bragg condition. This equation connects the constructive interference phenomenon of scattered waves (as prerequisite for Bragg diffraction) with the angular dependency of the lattice spacing. Only when n in the Bragg equation is an integer value, is the Bragg condition fulfilled and a diffraction peak appears.

$$n\lambda = 2d\sin\theta \quad (2.6)$$

n ... order of scattering λ ... wavelength d ... lattice spacing θ ... Bragg angle

The Bragg equation was developed using the kinematic scattering theory but is valid in both dynamic as well as kinematic theory. Ekstein⁽¹²⁾ has pointed out a generalized view on kinematic and dynamic theory defined by crystal size (von Laue⁽¹³⁾, Ewald⁽¹⁴⁾). They are treated as the two limiting cases of an advanced integral scattering equation based on von Laue's considerations of dynamic scattering.

2.2.2 Semi-kinematic theory

The description of grazing incidence measurements, due to consisting of refraction and diffraction events, does not allow the purely kinematic theory to be applied. The use of the highly complex dynamical diffraction theory overcomes this deficiency, but the complexity weighs against easy application to the problem at hand. It allows the use of kinematical approximations within dynamic diffraction problems. Here the Distorted Wave Born Approximation (DWBA) comes into play, as one of the most prominent examples of semi-kinematic theory. Its idea is based on the introduction of a second wave field of 'imaginary' scattering (the distorted wave) before hitting the real surface⁽¹⁵⁾. This pre-scattering happens at an assumed surface with a simpler distribution of material (scatterer). This formed wave field in return illuminates the true surface and this interaction is summed up over the whole surface. As a result, the reassembled scattering is now better described than by the simpler kinematic theory, since it covers the dynamic effects as perturbation. The idea was described first in detail by Vineyard in 1982⁽¹⁵⁾ for the use on Grazing angle measurements and significantly improved by Sinha in 1988⁽¹⁶⁾ for use in describing diffuse scattering events. Chapter 2.3.2 is especially based on semi-kinematic approaches.

2.2.3 Dynamic theory

Dynamic theory of diffraction⁽¹⁷⁾ was significantly developed and influenced by P.P. Ewald⁽¹⁴⁾ in 1917. The first publications and assumptions were made 1914 by Darwin⁽¹⁸⁾. In contrast to the kinematic theory, dynamic scattering corrects the kinematic description, e.g. for refraction, interference effects or extinction. The basic approaches in dynamic theories are based on either solving a set of differential equations of the Fresnel reflectance and transmittance of parallel atomic planes in a single layer (*Darwin approach*)⁽¹⁸⁾ or solving the eigenvalue problem of a diffracted wave in a periodic medium (*Ewald approach*)⁽¹⁹⁾. The latter approach requires special 'boundary conditions' for the exact treatment of the problem and its solution. The dynamic theory is very complex. Its equations are not practicable for daily use and are thus limited to the best case possible: a perfect crystal surface. The dynamic view on diffraction becomes important in describing thin film techniques at very low incidence angles (since kinematic or semi kinematic theory cannot fully cover the description of multi scattering events on perfect surfaces, e.g. standing waves). One example is the area around the critical angle where absorption and dispersion, as well complex phase shifts of the scattering waves, occur. Herein, the correct description of observable effects is mostly based and executed on dynamical theory (e.g. refraction shift).

2.2.4 The q-space (reciprocal space)

X-ray diffraction measurements are usually performed in angular space (2θ , ω , ...), whereas the analytical task of data evaluation is done in the reciprocal space. The conversion from real space (like the Bravais lattice) to the reciprocal lattice is done by a Fourier transformation. The obtained d-spacing from the Bragg equation is a vector pointing from the origin of the unit cell to the first hkl plane in the present lattice under an angle of 90° . The symmetry properties of the lattice in real and reciprocal space stay the same, whereas the reciprocal vector d^* is defined as $1/d$. Each hkl spot in the reciprocal space represent a set of Bragg planes as a vector.

From a practical point of view, the q-space provides an alternative way to represent scattering experiments. The coordinates used to describe the reciprocal space are usually Q_x and Q_z . The reciprocal space coordinate system is related to real space by placing its origin on the sample surface in the centre of the diffraction circle. The z direction projection represents the sample normal while the x direction runs across the sample surface along the projection of the beam path.

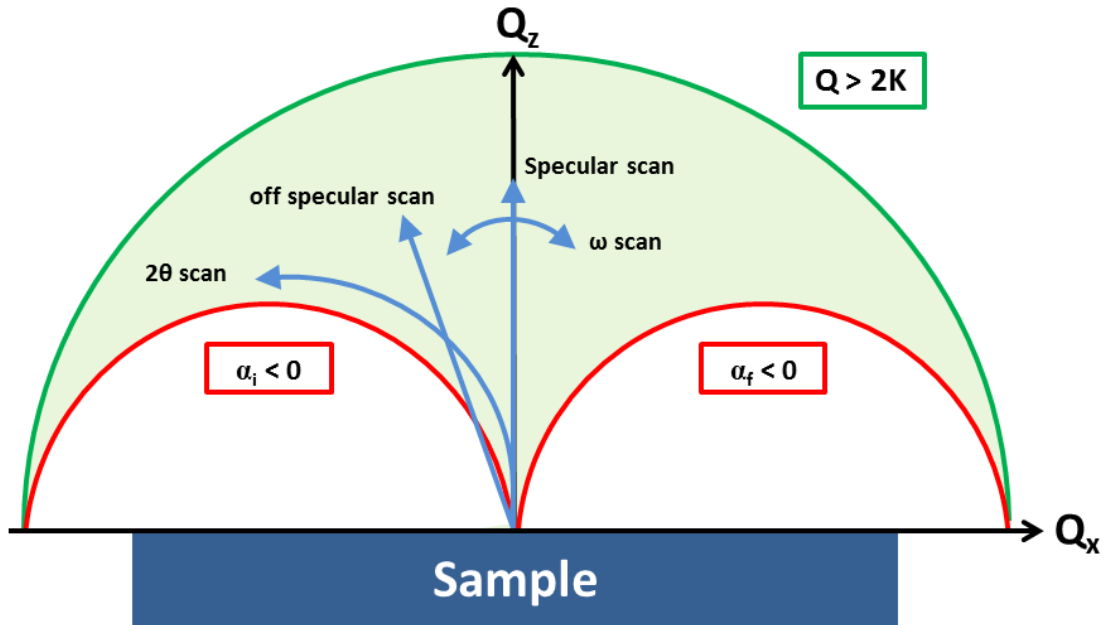


Fig. 2.1: Different types of XRD scans described in the reciprocal space. The green shaded area represents the region accessible for measurements. The white area is inaccessible due the incident or exit beam being below the sample surface.

Fig.2.1 schematically shows various types of scans in the reciprocal space. The accessible area is delimited by two restrictions. First, the wave vector defines the accessible reflections (green half sphere in Fig.2.1), so that using higher energies (lower λ) allows the measuring of more reflections. Second, the incident and exit beam define the area which is inaccessible for reflection measurements because either one beam or the other is below the sample surface. This is the area for transmission geometry, the Laue zone with radius $1/\lambda$ (red half spheres in Fig.2.1). K is defined as in eq.2.3 and Q_x and Q_z have the following definition with respect to the incident (α_i) and exit (α_f) angle⁽²⁰⁾:

$$Q_z = K(\sin\alpha_i + \sin\alpha_f) \quad (2.7)$$

$$Q_x = K(\cos\alpha_f - \cos\alpha_i) \quad (2.8)$$

Sometimes the definition is given in terms of q_x or q_z , which are derived by dividing Q_x and Q_z , respectively, by 2π . The important function represented by the reciprocal space construction is the scattering vector Q , a function of the scattering intensity. It is defined as $Q = K_i - K_f$, where K_i and K_f are the wave vectors of the incoming and outgoing beams, respectively. In reciprocal space, Q represents, by its intensity and angular distribution functions, the properties of a sample. In the case of co-planar Grazing Incidence X-ray Diffraction, K_i , K_f and the surface normal vector lie within a common plane, which is the only case covered in the present work. Non co-planar scattering, also called in-plane Grazing Incidence Diffraction, is not discussed here. The scans shown in Fig.2.1 are four prominent examples of the former. The specular (e.g. reflectivity) and off specular scan are at Q_z ($Q_x = 0$) or inclined to Q_z ($Q_x \neq 0$), respectively. This requires $\alpha_i = \alpha_f$ in the first case ($\theta/2\theta$ ratio exact) and $\alpha_i + \delta = \alpha_f$ in the latter. For an ω -scan (rocking curve), 2θ stays constant (α_i varies). For a 2θ scan (detector scan), the incident angle α_i stays fixed, thus the Q_x and Q_z components are varied simultaneously. For all scans the condition $\alpha_i + \alpha_f = 2\theta$ is valid.

2.3 Morphology testing techniques

2.3.1 X-ray Reflectometry (XRR)

This technique, when compared to GIXRD (introduced by Marra in 1979), is slightly older and has its origin in the early 1920s. Already by 1923 Arthur Compton⁽²¹⁾ had pointed out that at smooth surfaces the total external reflection at X-ray wavelengths should be possible. For glancing angle measurements, n (refractive index) becomes slightly less than unity. This originates from the fact that X-ray frequencies can be found to be higher than most electronic transition frequencies. With n being less than unity, the effect of Total External Reflection occurs. In 1931 Kiessig observed for the first time the oscillating behaviour at symmetric glancing angle measurements⁽²²⁾. He demonstrated that the appearing oscillations depend on the layer thickness (constructive interference at an observed fringe intensity maximum). One of the most detailed descriptions of this was given in 1954 by Parratt⁽²³⁾. He developed a recursive formalism for the Fresnel reflectivity of multilayer samples (several interfaces) and described the possible contributions of additional interface roughness. Nevót and Croce⁽²⁴⁾ were the first to give a comprehensive quantitative description of surface roughness contributions in 1980.

A complete overview on X-ray reflectometry can be found in various textbooks^(10,20,25). The following description shall give a basic understanding of the dependencies between layer thickness, roughness, density and the XRR curve appearance based on the aforementioned textbooks. XRR is in practice often described by basic optics knowledge and extended to refraction theory in dynamic and semi-kinematic content.

The most important value for XRR to describe in the behaviour of the X-ray beam at a certain interface is the refractive index n which consists of the dispersion (δ) and absorption (β) terms:

$$n = 1 - \delta + i\beta \quad (2.9)$$

The two terms are described by

$$\delta = \frac{r_0}{2\pi} \lambda^2 \rho \quad (2.10)$$

r_0 ... classic electron radius λ ... wave length ρ ... electron density

and

$$\beta = \frac{\lambda}{4\pi} \mu \quad (2.11)$$

λ ... wave length μ ... linear attenuation coefficient

The refractive index can be imagined by looking at the surface of water in a glass. The border of the bottom of the glass is seen to be at a slightly shifted position when compared to its real physical position. This is caused by the change in the direction of a wave of light upon entering a material with different refractive index than air (i.e. different optical density). This is commonly known as Snell's law. For X-rays the same consequence is valid, as has been pointed out by Arthur Compton. Since the deviation from unity is very small for X-ray wave lengths, refraction happens at far lower incident angles when compared to those of light. An incident wave and the wave formed by a point scatterer can be in or out of phase. In the first case, n becomes larger than unity, in the later, smaller. When n becomes smaller than unity, the effect of total external reflection occurs. Since the electron density ρ is not so practical for use in daily experiments, δ can be converted into the mass density with $\rho_m = \rho A / N_A Z$ (ρ : electron density; A : mass number; Z : atomic number; N_A : Avogadro number) which represents the density of the surface accessible with an XRR measurement. Dispersion is the main contributor to the effect of total external reflection. If absorption is neglected (which should be the case for angles at θ_c and beyond) the refractive index depends only on δ and hence the relation of the critical angle (θ_c) and density estimation at the surface can be derived simply. If one applies Snell's law ($\cos\alpha = n \cdot \cos\alpha'$) and set $\alpha' = 0^\circ$, one obtains a description for the critical angle of total external reflection:

$$\alpha_c = \sqrt{2\delta} \quad (2.12)$$

A rough practical definition of the critical angle α_c is the angle where the primary intensity (total reflection) of the beam decreases to 50% of its original value (since intensities in XRR plots are usually given on a log scale, this definition is more or less intuitive). The absorption term β describes the attenuation of the beam inside the material which it penetrates by a characteristic length $1/e$ (described by μ). It may be noted that β and δ can alternatively be derived from the anomalous dispersion of atomic scattering factors (f' and f'')⁽²⁶⁾. In the basic form using f' and f'' , the equations are valid only for mono-elemental layers, as for multi-element layers (e.g. SiO_2), the weighted sum over all contributing elements needs to be considered. For most calculations eq. 2.10 is a sufficient approximation, as the contribution of f' is usually very small.

The modification of the beam direction caused by n , leads now to the need of a geometrical view of the beam and its splitting on the sample surface as a consequence of interaction. In Fig.2.3 three wave vectors can be found: the incoming (k_i), the reflected (k_R) and the transmitted (k_T). The ratio of the two formed beams (k_R and k_T) is depending on n and α . With this figure the derivation of Snell's law and subsequently the Fresnel equation for transmittivity and reflectivity can be performed. Only by taking parallel components of k into account in combination with the boundary condition $a_i + a_R = a_T$, (corresponding amplitudes of the wave vectors k) does one yield $\cos\alpha = n \cdot \cos\alpha'$. The Fresnel equation can be found taking the components perpendicular to the surface and are displayed in Eq.2.13 und 2.14⁽¹⁰⁾:

$$r = \frac{\alpha - \alpha'}{\alpha + \alpha'} \quad (2.13)$$

$$t = \frac{2\alpha}{\alpha + \alpha'} \quad (2.14)$$

Their corresponding intensity related reflectivity (R) is the absolute square: $R = |r|^2$. Considering Snell's law again within the use of n it gives a complex expression:

$$\alpha^2 = \alpha'^2 + \alpha_c^2 - 2i\beta \quad (2.15)$$

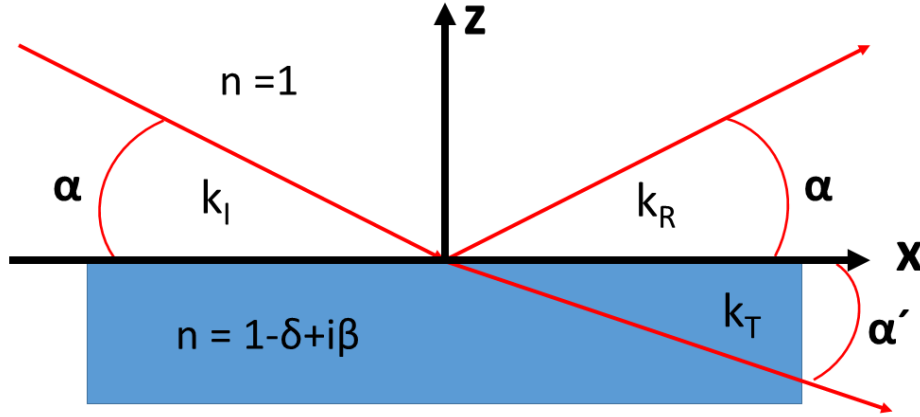


Fig.2.2: geometrical view on a surface and constructed beam directions (k_i : incident wave vector, k_R : reflected wave vector and k_T : transmitted wave vector)

This implicates the presence of the transmission angle α' as complex number under a given α . Since the imaginary part becomes dominant concerning the penetration depth (absorption dependent), one immediately sees that the intensity of the transmitted wave falls off with increasing depth⁽²⁵⁾

$$\Lambda = \frac{1}{2k \text{Im}(\alpha')} = \frac{\lambda}{2\pi(\Lambda_i + \Lambda_f)} \quad (2.16)$$

k ... wave vector transfer $\text{Im}(\alpha')$... imaginary part of α' $\Lambda_{i(f)}$... penetration depth of the incidence (i) or exit angle (f)

To arrive at a more useful description in connection to angular relation one can write also⁽²⁵⁾:

$$\Lambda_{i(f)} = \frac{1}{\sqrt{2}} \left\{ (2\delta - \sin^2 \alpha_{i(f)}) + \left[(\sin^2 \alpha_{i(f)} - 2\delta)^2 + 4\beta^2 \right]^{1/2} \right\}^{1/2} \quad (2.17)$$

δ ... dispersion term β ... absorption term $\alpha_{i(f)}$... incidence/exit angle

Figure 2.2 displays the sigmoidal penetration depth curve for the three noble metals, platinum, gold and iridium, depending on the chosen incidence angle (α_c calculated according to Eq.2.12 & 2.16 for Au: 0.57°, Pt: 0.60°, Ir: 0.62°). If the incidence angle exceeds the critical angle, the penetration depth significantly increases due to the formation of a transmitted wave, which is in contrast to the evanescent wave formed beyond α_c . Please note the normalisation of the x-scale by $c = \alpha_i/\alpha_c$ which allows for the comparison of the three curves on a scale relative to their α_c . The estimation of the penetration depth is essential information, since it allows for the tuning of the probing depth of the sample on demand. For small incidence and exit angles (like a rocking curve) Λ depends significantly on both angles. The higher the exit angle becomes (e.g. 2 θ measurement for GIXRD), the more it depends on the incidence angle only. Λ must be distinguished from the extinction length, since Λ determines the maximum penetration depth even without fulfilling the Bragg condition. In contrast, the extinction length depends on structure factor and hence on the Bragg condition⁽²⁷⁾.

To describe these dependencies more properly, regarding their appearance in the reciprocal space as wave vector transfers, one can refer back to Eq.2.7 and arrive at $Q(Q_c) = 2k \sin \alpha(\alpha_c)$. In addition, q can be expressed as Q/Q_c . With this redefined description, Eq.2.15 can be reformulated as:

$$q^2 = q'^2 + 1 - 2ib_\mu \quad (2.18)$$

q, q' ... wave vector transfer (α, α')

b_μ ... absorption parameter $= (2k/Q_c^2)\mu$

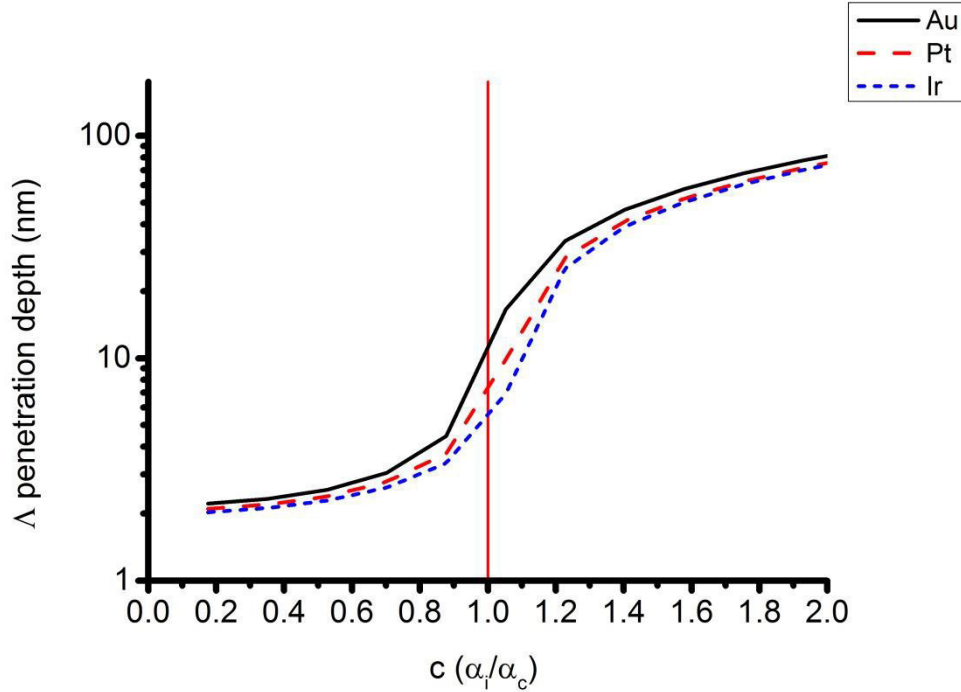


Fig. 2.3: Penetration depth of the incidence angle vs. $c = \alpha_i/\alpha_c$ for gold (black - solid), platinum (red - dash) and iridium (blue - dot). The vertical line at $c = 1$ represents incidence angle = critical angle

Eq.2.18 shows the common base for the calculation of reflectivity, transmittivity and penetration depth. Additionally, Eq.2.13 and 2.14 can be rewritten using the Q – Definition. Finally one can distinguish three cases for the order of magnitude for q in Eq.2.18, the incident angle, respectively⁽¹⁰⁾. For $q \gg 1$, the reflected wave is in phase with the incident wave and intensity drops as $R(q) \sim (2q)^{-4}$. It is a transmission case, where reflectivity is almost suppressed. With $q \ll 1$, the two waves are out of phase and transmission is not very significant. It's the case where $\alpha < \alpha_c$ and hence an evanescent wave is formed and travels parallel to the surface with very small penetration depth. The last case, where $q=1$, receives special attention for surface sensitive studies. Amplitude reflectivity becomes close to 1 (Δ is increased by $1/b_\mu$ to the asymptotic value of $1/Q_c$) and therefore the reflected and incident waves are in phase again and affect the evanescent wave to become stronger than the incident wave. All three cases require b_μ to be $\ll 1$ (absorption to be neglected). Fig.2.4 summarizes the three parameters and their development over increasing incidence angles (q respectively).

The knowledge gained so far can now be extended to the case where a thin layer is put on top of a substrate. By labelling the exterior (air) 0, the thin layer 1 and the substrate 2 (see Fig.2.5) and developing a geometrical series (which additionally eliminates the transmittivity term) one obtains an expression for the amplitude reflectivity of such a system:

$$r = \frac{r_{01} + r_{12}p^2}{1 + r_{01}r_{12}p^2} \quad (2.19)$$

with

$$p^2 = e^{iQ_L \Delta} \quad (2.20)$$

$Q_L \dots = 2k_s \sin \alpha_i$ $\Delta \dots$ phase difference (layer thickness)

This formula expresses the well-known oscillating behaviour of XRR curves known as Kiessig fringes⁽²²⁾. The maxima correspond to in phase scattering, the minima to scattering out of phase. The phase difference labelled Δ , directly corresponds to the layer thickness and the appearance of the fringes at always $2\pi/\Delta$.

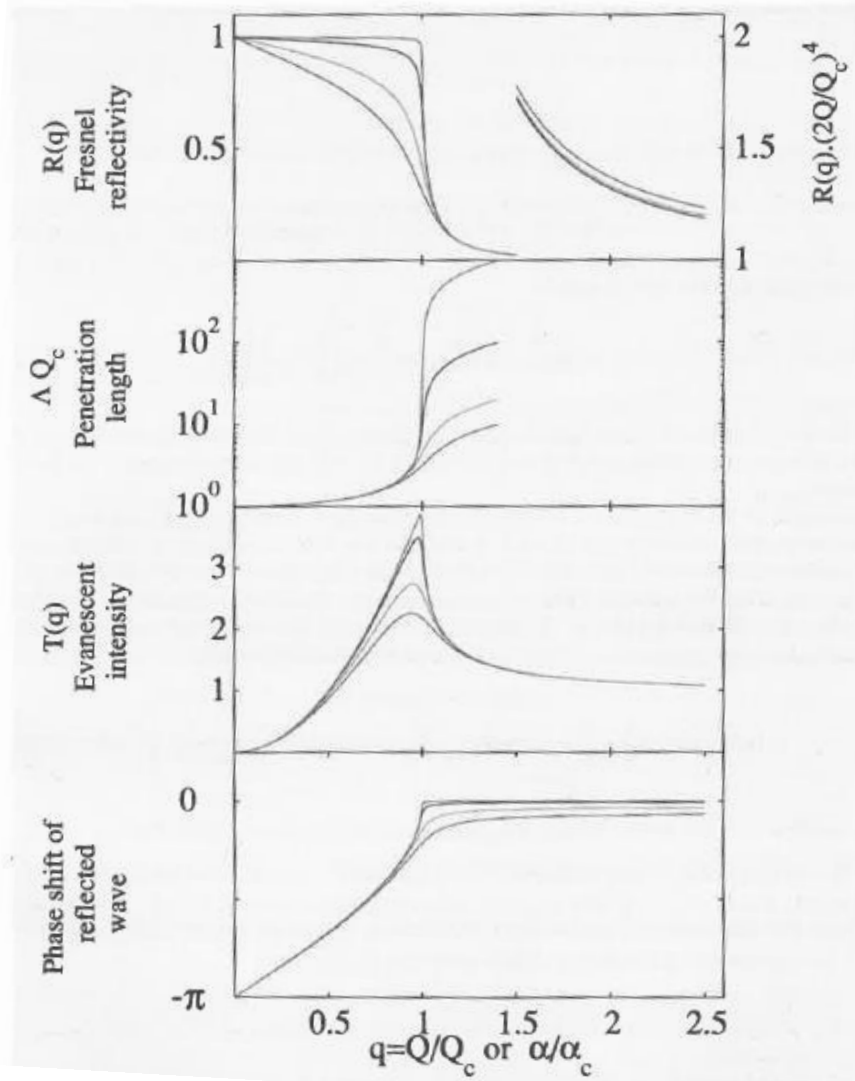


Fig.2.4: Graphical summary of the three beforehand discussed parameters R , Λ , T and additionally the proposed phase shift at various incidence angles normalized to the critical angle (x -axis). The four different lines correspond to varying b_μ : 0.001, 0.01, 0.05 and 0.1 (lower to higher absorption) and can be nicely followed at $R(q)$. The stronger the absorption gets, the less sharp the edge at the critical angle is defined. (picture taken from⁽¹⁰⁾)

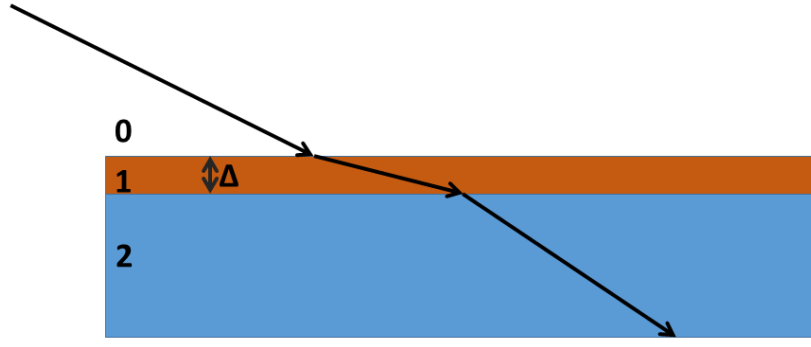


Fig.2.5: Beam path inside a thin layer (1) on top of a substrate (2). Appearing oscillations are the result of infinite numbers of reflections between substrate and layer of thickness Δ .

Equation 2.19 requires two boundary conditions. First, the layer is thin ($Q\Delta \ll 1$). Second, the angles are sufficiently high, so refraction can be neglected ($|r_{01}| \ll 1$). In other words, this formalism is only valid at angles above the critical angle, also called area of kinematic reflectivity.

Since often more than one layer is of interest, this formalism was extended to multilayer reflectivity by Parratt⁽²³⁾ by developing a recursive method. He imagined a stack of N layers sitting on a substrate of infinite thickness. As defined, the N th layer is directly on the substrate. The Parratt formalism can be written as follows for the reflectivity for the N th layer (so directly starting from the substrate):

$$r_{N-1,N} = \frac{r'_{N-1,N} + r'_{N,\infty} p_N^2}{1 + r'_{N-1,N} r'_{N,\infty} p_N^2} \quad (2.21)$$

It can be continued until the total reflectivity amplitude (uppermost layer to vacuum) is obtained. This method gives an exact treatment of the reflectivity for a multilayer system, also in the area close to the critical angle due to its being stepwise (recursively) solved from bottom to top. This formalism is also the basis for the data evaluation of the LEPTOS software^(28,29) and subsequently for the later data analysis of the XRR data in the experimental parts. Herein, the specular reflectivity (Fresnel reflectivity) is the experimentally accessible parameter and is consecutively and iteratively calculated over the Parratt formalism for each layer over the measurement range. To account for two important influences, namely graded interfaces (electron density gradient) and roughness, this modelling needs some modification and additional considerations.

These two effects can obviously be distinguished by the definition at the interface: roughness at a sharp interface (abrupt change in n) and grading, which does not show this sharp transition, but instead a smooth profile of n along z is observed. It can be modelled by considering thin slabs of varying homogeneous electron density at the depth of the interface summed up over all contributions. Introducing a description for grading, $f(z)$, requires obtaining a density profile change along z (depth) and fulfilling the condition if $f(z) \rightarrow 1$ than $z \rightarrow \infty$. In return, $f(z) \rightarrow 0$ if z goes to negative infinity. Amplitude reflectivity is modified by the function ϕ , which represents the convolution of electron density around the interface

$$r(Q) = r_{Fresnel}(Q) \phi(Q) \quad (2.22)$$

with

$$\phi(Q) = \int_{-\infty}^{\infty} f'(z) e^{iQz} dz \quad (2.23)$$

Remembering the condition at Fresnel reflectivity in Eq.2.15 to be $q \gg 1$, for the valid area of the model ($Q \gg Q_c$), one obtains the exact description for grading at an interface⁽¹⁰⁾:

$$\frac{R(Q)}{R_F(Q)} = \left| \int_{-\infty}^{\infty} \left(\frac{df}{dz} \right) e^{iQz} dz \right|^2 \quad (2.24)$$

For the description of grading for a multi-interface system, the summation over sample thickness needs to be taken into account. This immediately implies that for each interface, Eq.2.24 has to be solved separately, due to its dependence on α .

In the literature, various models for $f(z)$ exist. One of the most common is the so called error-function profile, which introduces the descriptor σ :

$$f(z) = \text{erf}\left(\frac{z}{\sqrt{2}\sigma}\right) \quad (2.25)$$

σ is a measure of the Gaussian width over the interface along z , which is graded (Fig.2.6). This model was derived by Névot-Croce⁽²⁴⁾ in a slightly different form to describe the reflectivity of a graded interface:

$$R(Q) = R_F(Q) e^{-QQ'\sigma^2} \quad (2.26)$$

with $Q(Q') = k \sin(\theta(\theta'))$, the incident and transmitted beams, respectively. LEPTOS offers four different profile models⁽²⁹⁾: tangential, sinusoidal, linear and error function. This description depicts also the method for obtaining σ : the actual reflectivity must be always normalized by the ideal Fresnel reflectivity. It originates from Eq.2.14 and $q \gg 1$. Here the intensity reflectivity R drops off by $1/(2q^4)$. In turn, this means that from the directly measured curve, the parameter is not accessible; only after renormalization is it.

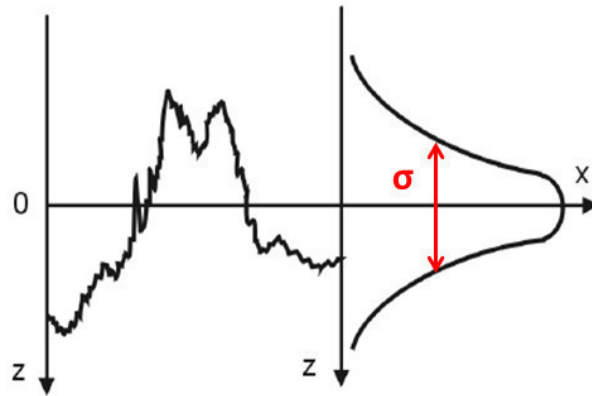


Fig. 2.6: The Névot-Croce model of microscopic roughness assumes that the “statistical assembly of interfaces” follows a Gaussian distribution (σ) concerning the depth coordinate z (picture taken from⁽²⁸⁾).

The last and quite important value one can obtain by analysing XRR is the surface and interface roughness. Reflectivity of a real sample always contains contributions from roughness. Small microscopic inclinations along the surface allow the description of the reflectometry to stay no longer purely specular. Roughness causes diffuse or off-specular contributions in reflectivity.

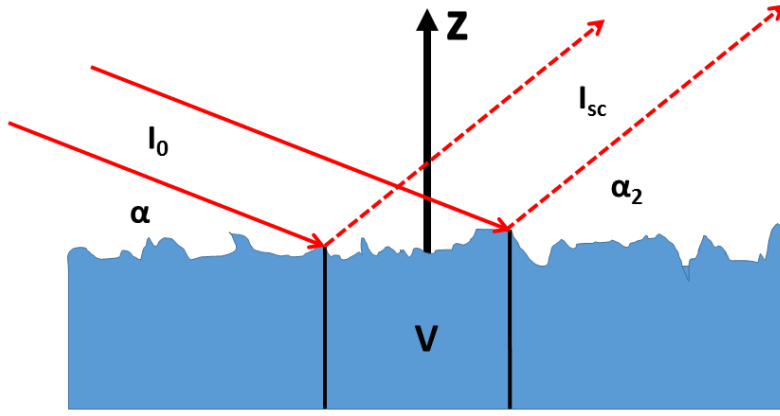


Fig.2.7: Representation of a rough surface. The scattering elements within the illuminated area V are considered as contributions.

Fig.2.7 shows the typical case for scattering at a rough surface. Scattering events are determined by the illuminated area, the probing depth (determined by μ) and the number of electrons in the volume element V. These elements are summed and represent the scattering amplitude r_v :

$$r_v = -r_0 \int_{\infty} (\rho d\mathbf{r}) e^{i\mathbf{Q} \cdot \mathbf{r}} \quad (2.27)$$

$-r_0$ is the Thompson scattering length of a single electron, $\rho d\mathbf{r}$ is the number of electrons around the position \mathbf{r} (electron density at \mathbf{r}) and $e^{i\mathbf{Q} \cdot \mathbf{r}}$ stands for the phase factor.

After some complex mathematical operations this volume integral r_v turns into a surface integral r_s and additionally the variation of the height at the surface is given by $h(x,y)$:

$$r_s = -r_0 \rho \left(\frac{1}{iQ_z} \right) \int_S e^{iQ_z h(x,y)} e^{i(Q_x x + Q_y y)} dx dy \quad (2.28)$$

The height differences $h(x,y) - h(x',y')$ are assumed to appear only on a relative scale and Eq.2.28 can therefore be simplified. It can be transformed into the differential cross-section (absolute square of the scattering amplitude), giving an exact description for the height differences over the illuminated surface area $(A_0/\sin\theta_i)^{(10)}$:

$$\left(\frac{d\sigma}{d\Omega} \right) = \left(\frac{r_0 \rho}{Q_z} \right)^2 \left(\frac{A_0}{\sin\theta_i} \right) \int e^{-Q_z^2 \langle [h(0,0) - h(x,y)]^2 \rangle / 2} e^{i(Q_x x + Q_y y)} dx dy \quad (2.29)$$

This derived formula is the basis for evaluating roughness for surfaces and interfaces. The height dependency introduced by h will be shown to have an additional influence on the so-called roughness correlation of surfaces. In this case, where the roughness is randomly oriented and not correlated, the function h can be simplified to:

$$\langle h(0,0) - h(x,y) \rangle^2 = 2\langle h^2 \rangle - 2\langle h(0,0) \rangle \langle h(x,y) \rangle = 2\langle h^2 \rangle \quad (2.30)$$

and Eq.2.29 becomes simply:

$$\left(\frac{d\sigma}{d\Omega} \right) = \left(\frac{d\sigma}{d\Omega} \right)_{Fresnel} e^{-Q_z^2 \sigma^2} \quad (2.31)$$

Where $\sigma = \sqrt{\langle h^2 \rangle}$ is the root mean square roughness (rms-roughness), a descriptor already seen in Eq. 2.26 and Fig.2.6. The derivation of Eq.2.31 shows that roughness contributions lower the ideal reflectivity (Fresnel reflectivity) and depend on Q_z (as a fluctuation component determined by the

angle of incidence) and σ . Eq.2.31 is identical to Eq.2.26, which implies that a unique solution can only be found if some pre-knowledge of the nature of the sample is known. XRR alone cannot give a unique solution.

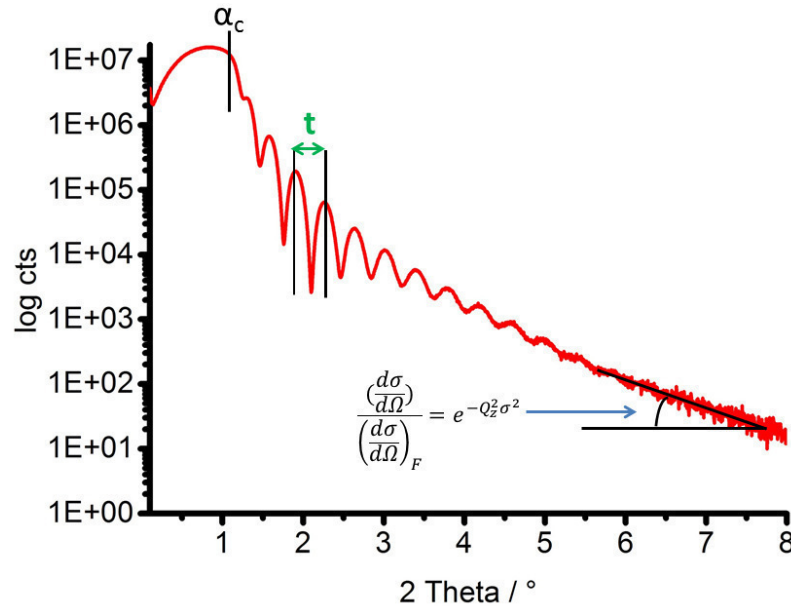


Fig. 2.8: Measured XRR curve of a Si wafer coated with a 20 nm Pt layer. Note the indications for the three parameters extracted from the reflectivity curve (α_c ... critical angle, $t(\Delta)$... layer thickness). The determination of σ over the slope of the curve can only be found after its normalization by Fresnel reflectivity, as seen in the inset equation.

Finally, some practical and helpful comments. A pitfall to be considered for the practical use of XRR (as well as for low angle diffraction experiments like GIXRD) is the footprint problem. The footprint is the illuminated area, i.e. the cross-section of the beam at the level of the sample surface, which depends on the incidence angle. Hence, at low incidence angles, it may easily become larger than the available sample surface. However, if the footprint is larger than the sample, then the sample area limits the observed intensity, which then will be smaller than theoretically anticipated based on the beam size. This change in the intensity scaling needs to be accounted for in order to calculate the correct α_c value. If the beam exceeds the sample size, the intensity needs to be corrected by multiplying by the sine of α_i ($I_0 = I_{\text{obs}} * \sin \alpha_i$). The footprint of the beam can be calculated with $d/\sin \alpha_i$ (d : slit width)^(20,28).

Through the estimation of α_c , the electron density is available. The accuracy of this estimation can be calculated as $2(\Delta \alpha_i / \alpha_c)$ and can be found in most cases to be between $\pm 1\%$ and 3% using the smallest step size for the measurement ($\Delta \alpha_i$ usually 0.001°)⁽²⁰⁾. Accuracy in layer thickness determination can be roughly estimated in the same way by $\Delta \alpha_i / \alpha_i$ and is about in the same range as that of the critical angle. Limiting factors for this technique can be separated into two groups. On the one hand, the resolution function of the setup. Thicker layers ($T > \sim 250$ nm) require a monochromator to separate the high frequency of appearing fringes. On the other hand, the sample itself. The roughness shouldn't exceed the limit of around 10 nm in order to be able to observe a reliable result. The XRR technique has the golden rule: you should be able to see your reflection on the surface of your sample. If this rule is kept in mind, XRR will work very well in most cases.

The two mentioned types of roughness, at surface and interface, can also cause different effects. Surface roughness causes the intensity of the specular reflectivity curve to decrease faster. Interface

roughness starts to smear out and dampen the thickness fringes⁽³⁰⁾. To distinguish between roughness and grading, the measurement of the diffuse scattering is necessary.

2.3.2 X-ray diffuse scattering measurements (XRDS)

In the previous paragraph, the discussion of the XRR parameters revealed that this technique when used as standalone method does not give a unique solution for the description of a surface and interface. Two discussed effects, roughness and grading, for example, cannot be distinguished by pure XRR measurements. It requires the measuring of off-specular reflectivity, in particular the diffuse scattered intensity distribution. Roughness causes higher intensity to be measured off-specular, whereas pure grading does not yield higher scattered intensity in XRDS. Fig.2.9 gives a pictorial view of a diffuse rocking scan and the observable artefacts in the resulting scan. Roughness, at the surface as well as the interface, shows correlations. The uncorrelated case was already discussed in the previous paragraph (Eq.2.29-2.31). Correlations are assumed to be isotropic and their behaviour can be separated into two cases depending on the behaviour of the function $g(x,y)$ which describes the length scale of the correlation on the surface: without and with cut-off length^(16,31,32,33,34). In the first case the function $g(x,y)$ is given by:

$$g(x,y) = \langle [h(0,0) - h(x,y)]^2 \rangle = Ar^{2H} \quad (2.32)$$

Here the description of the height fluctuations are described as fractal changes⁽³⁵⁾ along the surface where the exponent h describes the morphology. It is also known as Hurst parameter⁽³¹⁾ and defined as $0 < H < 1$. A value close to 1 describes a smooth surface, whereas around 0 the surface appears jagged. This case represents no limit in the height correlation along the surface. This allows Eq.2.29 to be modified according to the simplification of $y=0$ (since the resolution in Q_y is broad) and it becomes symmetric, since it depends on x ($|x|$) respectively to⁽¹⁰⁾:

$$\left(\frac{d\sigma}{d\Omega}\right) = \left(\frac{r_0 Q}{Q_z}\right)^2 \left(\frac{A_0}{\sin\theta_I}\right) \int_0^\infty e^{-AQ_z^2|x|^{2H}/2} \cos(Q_x x) dx \quad (2.33)$$

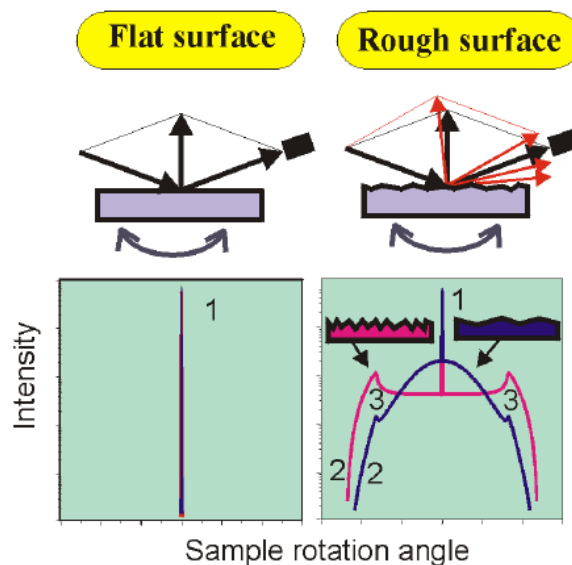


Fig.2.9: Pictorial view on the observable differences in a longitudinal rocking curve between flat and rough surfaces. Note the sample rotation angle corresponds to ω (sample tilt) and the differences in large and small ξ at rough surfaces (2,3 in the graphic)(taken from⁽³⁶⁾)

Eq.2.33 has to be evaluated numerically over the range of h , except for the exact solutions of $h = \frac{1}{2}$ or $h = 1$. They need to be analysed analytically and give, in the first case, a Lorentzian line shape and, in

the latter, a Gaussian shape^(10,16). The consideration that the g depends on r (the length of the isotropic correlation vector along the surface) quickly leads to the result that unbounded height correlations on a surface give purely diffuse scattering. Flat or uncorrelated surfaces in contrast give purely specular reflectivity. These surfaces are described as without cut-off length for height correlations. Far more interesting, and in many cases closer to reality, are surfaces with cut-off length, so that the height fluctuations along the surface are finite within $r \rightarrow \infty$. Such a case yields^(37,38,39,40,41):

$$g(x, y) = \langle [h(0,0) - h(x, y)]^2 \rangle = 2\langle h^2 \rangle - 2\langle h(0,0)h(x, y) \rangle \quad (2.34)$$

which can be further written as:

$$g(x, y) = 2\sigma^2 - 2C(x, y) \quad (2.35)$$

The term C is known as height-height correlation function and is most commonly written as^(38,42):

$$C(x, y) = \sigma^2 e^{-\left(\frac{r}{\xi}\right)^{2H}} \quad (2.36)$$

Here a new parameter is introduced: ξ , the so called lateral correlation length. It describes the length scale of the height-height correlation on the surface within r . It is also often referred to as the length of homogeneous roughness distribution (of a certain σ value). This form of $g(x, y)$ modifies Eq2.29 as follows⁽¹⁰⁾:

$$\left(\frac{d\sigma}{d\Omega}\right) = \left(\frac{r_0 Q}{Q_z}\right)^2 \left(\frac{A_0}{\sin\theta_I}\right) e^{-Q_z^2 \sigma^2} \int_0^\infty e^{Q_z^2 C(x, y)} e^{i(Q_x x + Q_y y)} dx dy \quad (2.37)$$

To make the connection to the purely specular reflectivity more clearly visible the formula can be split:

$$\left(\frac{d\sigma}{d\Omega}\right) = \left(\frac{d\sigma}{d\Omega}\right)_{Fresnel} e^{-Q_z^2 \sigma^2} + \left(\frac{d\sigma}{d\Omega}\right)_{diffuse} \quad (2.38)$$

with:

$$\left(\frac{d\sigma}{d\Omega}\right)_{diffuse} = \left(\frac{r_0 Q}{Q_z}\right)^2 \left(\frac{A_0}{\sin\theta_I}\right) e^{-Q_z^2 \sigma^2} F_{diffuse}(Q) \quad (2.39)$$

and:

$$F_{diffuse}(Q) = \int \left[e^{Q_z^2 C(x, y)} - 1 \right] e^{i(Q_x x + Q_y y)} dx dy \quad (2.40)$$

The expression in Eq.2.38 clearly shows that bounded height fluctuations on a surface always consist of two contributions: a specular component superimposed on a diffuse component. In Fig.2.10 the results for different ξ at constant h and vice versa display their physical appearance in a more pictorial way.

Diffuse scattering can be recorded in more than one way depending on the desired information. In general one can distinguish three types of diffuse scans^(20,34,37):

- symmetric with θ offset (off specular scan, longitudinal scan)
- ω scan at chosen 2θ point (transverse scan)
- 2θ scan (GID-geometry)

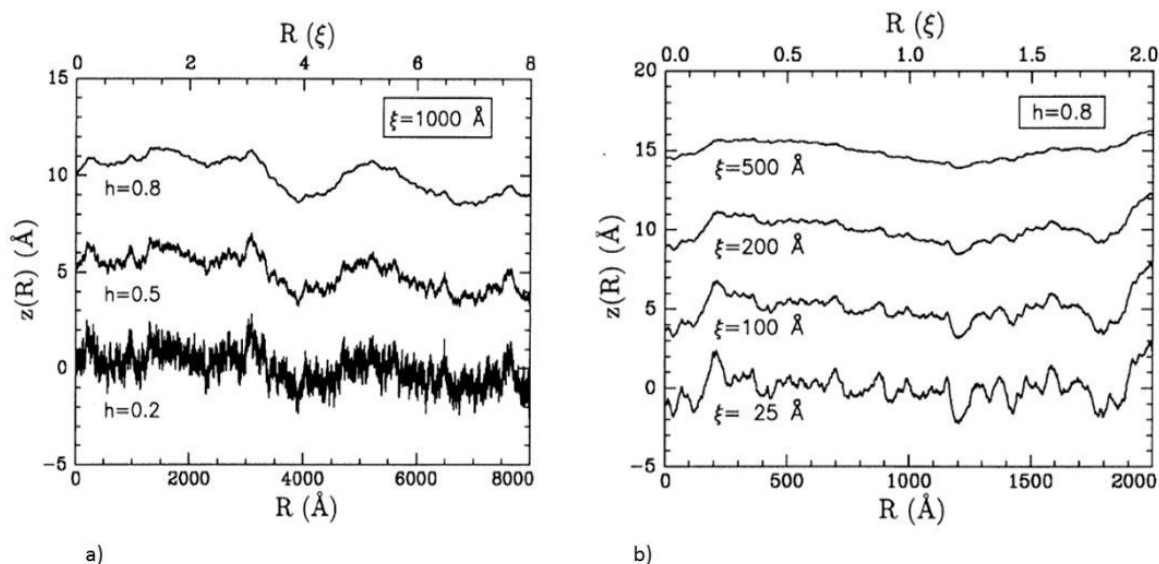


Fig. 2.10: The same surface (profile) at a) constant ξ , different h b) constant h and varying ξ (picture was taken from⁽³⁴⁾)

In symmetric mode with a small θ offset, the whole film is probed off-specular for roughness contributions. For well-defined and dense grown films with low roughness, it replicates the reflectivity curve with lower intensity due to its being off. Rocking curves (ω -scan) are performed at constant 2θ and hence at a constant probing depth. It is an almost pure q_x scan, as q_z at such low incidence angles is almost a straight line in reciprocal space. A GID scan (at constant θ) changes q_x and q_z simultaneously and also offers a constant probing depth. For example, vertical correlation can be monitored by 2θ scans, since varying the incidence angle leads to illumination of deeper interfaces also. In the present work we attempt to perform a depth resolved study of a thin iridium layer and therefore we chose ω -scans to investigate the changing morphology. A typical rocking curve recorded with our laboratory setup can be found in Fig.2.11.

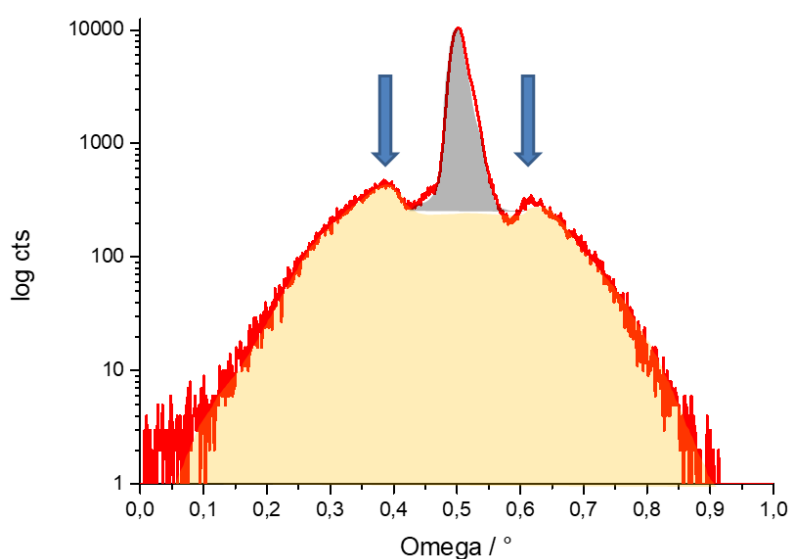


Fig.2.11: Measured ω curve of a 50 nm Cu film. The grey shaded area represents the specular contribution, whereas the light orange area displays the diffuse scattered intensity. The two blue arrows indicate the Yoneda wings.

A special feature which can appear in the 2θ -or ω -scans are the so-called “Yoneda wings”⁽⁴³⁾. They appear each time the incident angle α_i or exit angle α_f equals the critical angle α_c . These peaks are caused by the maxima of the electric field (twice of the incident field) on the surface (as transmission function of the incident/exit beam reaches a maximum, see Eq.2.18). The physical origin of this phenomenon can be simply regarded as the fact that at those angles the incoming and exit beam are in phase and enhanced. This leads to the increased intensity of diffuse scattering in this area⁽⁴¹⁾, as seen in Fig.2.11.

In the present work the data evaluation for XRR and XRDS was executed with the LEPTOS software (Bruker AXS). For the complete exact algorithms and functions used within this software, the reader is referred to the LEPTOS handbook⁽²⁸⁾ and monograph⁽²⁹⁾.

2.4 Structure testing techniques

2.4.1 Grazing Incidence X-ray Diffraction (GIXRD)

In the previous section the description and theoretical background for the surface sensitive technique XRR and XRDS was given. Nevertheless, one is not often only interested in the morphology and its changes. The structure of crystalline phases and their influences on physical properties of a thin film often shadow the ‘minor’ morphology task. The technique used for obtaining Bragg diffraction at surface layers and surface near regions is the explicit form of Grazing Incidence X-ray diffraction. This special diffraction technique was developed in the pioneering experiment of Marra, Eisenberger and Cho in 1979⁽⁴⁴⁾. They combined the idea of A. Compton (see 2.3.1, XRR) of total external reflection at X-ray wave lengths with Bragg-diffraction condition into a so-called “reflection-diffraction technique” to achieve ultimate surface sensitivity. Their effort has been concentrated in the study of the interface of epitaxially grown aluminum on a single crystalline GaAs substrate. It turned out that this specifically developed technique allowed them to observe the lattice mismatch of the growth of the Al on the GaAs substrate, as well as the domain sizes of the grown aluminum. Fig.2.12 shows the obtained results and layer sensitivity using the reflection-diffraction technique. Depending on the chosen interface, the intensity of either the Al surface or the GaAs interface is enhanced.

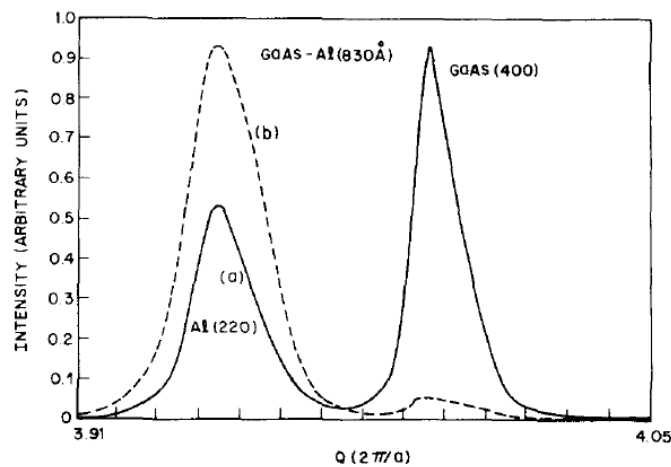


Fig.2.12: Intensity differences of a epitaxial Al layer grown on GaAs investigated by Marra⁽⁴⁴⁾. Depending at which interface the total reflection occurs, the signal of either the substrate or the layer becomes stronger (a ... α_c at the GaAs substrate; b ... α_c at the Al surface layer)

This combination opened the door to the (crystal) structural characterisation of surfaces and interfaces with X-rays on the nm scale. Nowadays this technique is widely applied in the semiconductor industry⁽⁴⁵⁾, battery research, and the study of surface corrosion in maritime applications⁽⁴⁶⁾, just to name a few prominent areas of GIXRD use.

Grazing Incidence diffraction can be nowadays separated into two types. First, the in-plane GIXRD (ip-GID)^(45,47) and second the out-of-plane geometry. The Marra-technique is currently known as the in-plane type, whereas out-of-plane GID is also referred to as asymmetric Bragg diffraction^(48,49). Which of these two methods one uses depends on the type of sample and more precisely its growth characteristics. If a sample is strongly textured (or epitaxially grown) the in-plane type is commonly used. For randomly oriented and polycrystalline samples the out-of-plane geometry is preferred. Since the small diffraction volume leads to very low diffracted intensities ($\sim 10^{-8}$)⁽⁴⁵⁾, the use of high-power sources is recommended. In addition the resolution in the reciprocal space depends on the geometry, collimation and beam conditioning (e.g. monochromators, analyser crystals,...). Fig.2.13 depicts the geometrical differences of the in-plane and out-of plane geometry. In the upper image it is referred to a horizontal goniometer and in the lower case to a vertical goniometer. ip-GID geometry is based on the almost full inclination (usually around $90^\circ \pm$ critical angle) of the sample surface along its z-direction⁽⁴⁷⁾. Its characteristic sample tilt results in the ability to test lattice planes normal to the thin film surface. The beam in the out-of-plane geometry hits the surface parallel to the planar direction (line focus) and probes the (randomly inclined) lattice planes in surface near regions. In case of the in-plane geometry the incidence angle cannot be adjusted simply by θ , it is a multi-parameter adjustment (χ, α, ϕ) which in turn is not the case for the out-of-plane geometry.

In the present work the attempt focuses on the out-of-plane geometry. Since the laboratory device is not explicitly dedicated to in-plane diffraction, this geometry will not be further discussed as it was not executed. The electrochemically treated samples which are investigated within this work tend to be better investigated in the out-of-plane direction with a minimum of additional requirements (e.g. in-situ cell) due to their being polycrystalline as well as randomly oriented. Fig.2.14 shows the used GID setup within the present work.

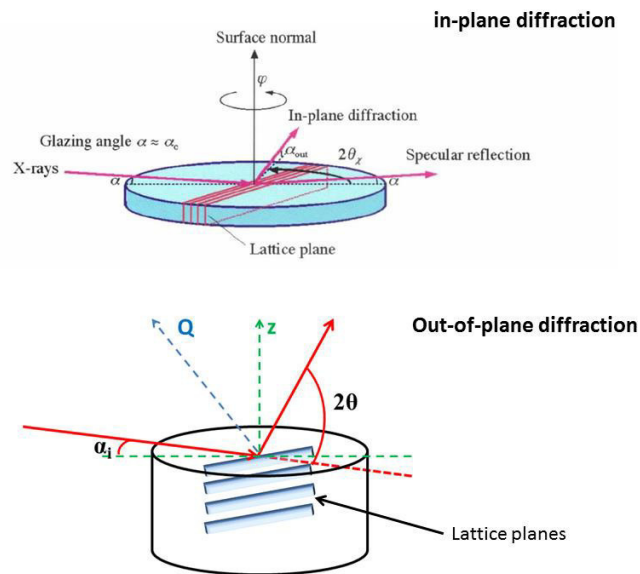
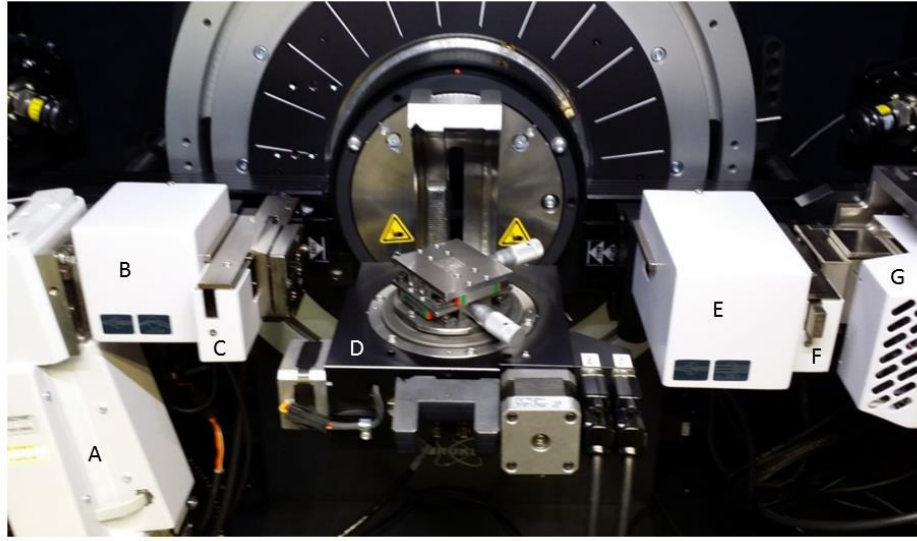


Fig.2.13: Graphical illustration of the geometrical difference between in-plane and out-of-plane Grazing incidence Diffraction. One shall notice the different orientation of the investigated lattice planes with respect to the geometry (the upper graphic was taken from⁽⁴⁷⁾).



A ... X-ray tube (Cu) D ... Eulerian cradle E ... Soller
 B ... Göbel mirror F ... Secondary slit
 C ... Primary slit G ... Detector (0-D)

Fig. 2.14: Standard out of plane GIXRD setup as used in this work

The characteristics which determine the GIXRD experiment are the penetration depth Λ (see Eq.2.16 & 2.17) and the Fresnel transmission function T . Varying the incidence angle α_i (in GID usually from $0.1-1^\circ$) allows the choosing of a proper penetration depth to suppress reflections from the underlying substrate. The power of Grazing Incidence lies in the formation of an evanescent wave^(10,50) travelling parallel to the surface (see Eq. 2.18 for $q \ll 1$) with minimum penetration depth. Exemplary Λ is shown in Fig.2.3 for three noble metals. The Fresnel transmission (T) represents the interaction of the beam with the air-sample interface and corrects the intensity by considering (including) refraction. If structure factors and form factors of the unit cell are ignored, the intensity variation of a Bragg reflection at given α_i is⁽⁴⁹⁾:

$$I(\alpha) \propto T^2(\alpha)\Lambda(\alpha) \quad (2.41)$$

The evolution of T by increasing α_i can be found in Fig.2.4 (evanescent wave intensity). The enhancement around α_c explains the surface sensitivity of this setup. A comprehensive and detailed evaluation of the GIXRD data in the present work was not executed due to the qualitative support of the surface investigation by the XRR and XRDS measurements. Exact GIXRD data evaluation becomes elaborate very quickly and results in the solution of various differential cross sections $d\sigma/d\Omega$. The combination of Bragg diffraction with reflection conditions requires dynamic theory elements in order to become applicable. This is beyond the scope of this work, since the phenomenological analytics of the morphological changes are in focus. A detailed crystallographic study is clearly the priority of the present work.

One element which also affected our qualitative analytics of the iridium layers was the so-called refraction shift. This effect strongly influenced the Bragg peak position when measured in GID-geometry, that is, at small incidence angles. The origin of this peak shift is the difference in refractive index n between two media (e.g. usually between air and sample). If the beam passes the boundary into the layer, then the transmitted beam changes its direction slightly due to refraction. This leads

to a positive shift of the diffracted beam towards higher 2θ values^(51,52,53). The illustration in Fig. 2.15 gives a pictorial view on the refraction shift.

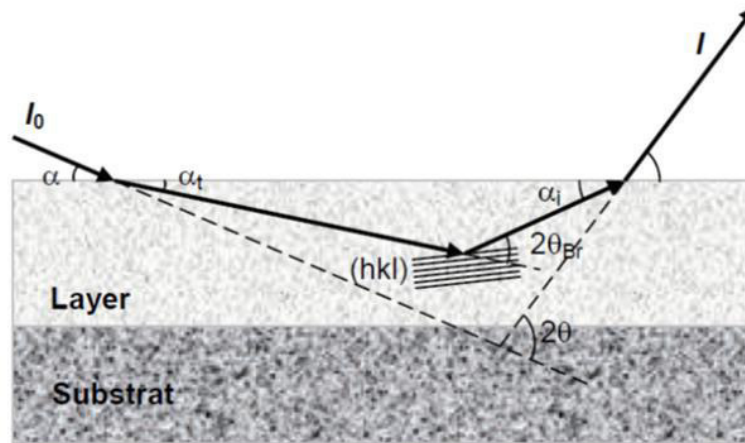


Fig. 2.15: The illustration describes the refraction effect. The incident beam gets transmitted (α_t) and reflected at the hkl plane. Due to the difference in n , the incident beam (α_i) for the diffracted beam becomes shifted (image taken from Bruker AXS Leptos Handbook⁽²⁸⁾)

The calculation of this shift is of essence in obtaining the correct Bragg angle and extracting the lattice parameter. It is based on the dynamic theory and follows^(17,55):

$$\Delta\theta = \theta - \theta_B = \frac{-\gamma_0 + \left[\gamma_0^2 - (\gamma_0 - \gamma_h)(1 - \gamma_0^2)^{\frac{1}{2}} \chi_0 / \sin 2\theta_B \right]^{1/2}}{(1 - \gamma_0^2)^{1/2}} \quad (2.42)$$

with

$$\gamma_0 = \sin \alpha_i \quad (2.43)$$

$$\gamma_h = \sin(\alpha_i - 2\theta_B) \quad (2.44)$$

$$\chi_0 = 2\delta \quad (2.45)$$

In Fig.2.16. the refraction shift for iridium is calculated according to Eq.2.42 from 0.6 up to 2.0° α_i ($\rho_{Ir} = 22.65 \text{ g/cm}^3$). The highest deviation can be found around α_c (for Ir = 0.62°) and its subsequent exponential decay with increasing incidence angle is shown. In return, the shift comes close to the value of the critical angle if α_i goes towards 0, which is caused by the dependence on δ .

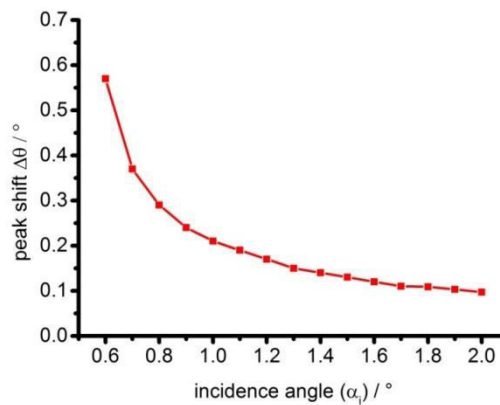


Fig.2.16: Refraction shift calculated for iridium from 0.6-2.0° θ

Correcting the refraction shift was executed in the experimental part of the present work when out-of-plane GID was performed. The diffraction peak fitting is discussed in each chapter separately, since the evaluation was not identical throughout the entire work and was not based on the elaborate semi-kinematic (dynamic) diffraction theory.

A further discussion of the related GIXRD topics and relevant insights is given in several textbooks^(10,17,22,55) and monographs^(32,33,39,48,49,50,56,57,58,59).

2.5 References

- 1) B. Yu H. Wang, A. Joshi, Q. Xiang, E. Ibok, M.-R. Lin, IEDM Tech. Digest (2001) 937-939
- 2) C. Jagadish, S. Pearton, Zink Oxide – Bulk, Thin films and Nanostructures (Elsevier), 2006
- 3) G. Eda, M. Chhowalla, Adv. Mater. 22 (2010) 2392-2415
- 4) E. Elangovan, K. Ramamurthi, J. Optoelectr. Adv. Mater. 5 (2003) 45-54
- 5) P. Dova, H. Laidler, K. O’Grady, M. F. Toney, M. F. Doerner, J. Appl. Phys. 85 (1999) 2775-2781
- 6) C. Murray, C. Kagan, C. Bawendi, Science 270 (1995) 1335-1338
- 7) L. Clevenger, A. Mutscheller, J. Harper, C. Cabral Jr., K. Barmak, J. Appl. Phys. 72 (1992) 4918-4924
- 8) F. Renner, A. Stierle, H. Dosch, D. M. Kolb, T.-L. Lee, J. Zegenhagen, Nature 439 (2006) 707-710
- 9) M. Samant, M. Toney, G. Borges, L. Blum, O. Melroy, J. Phys. Chem. 92 (1988) 220-225
- 10) J. Als-Nielsen, D. McMorrow, Elements of Modern X-ray Physics, (2nd edition, Wiley, 2010)
- 11) W. Massa, Kristallstrukturbestimmung (8th edition, Springer Verlag, 2015)
- 12) H. Ekstein, Phys. Rev. 62 (1942) 255-261
- 13) M. v. Laue, Ergebn. Exakt. Naturwiss. 10 (1931) 133-158
- 14) P. P. Ewald, Ann. Phys. 54 (1917) 519-597
- 15) G. Vineyard, Phys. Rev. B 26 (1982) 4146-4159
- 16) S. Sinha, E. Sirota, S. Garoff, H. Stanley, Phys. Rev. B 38 (1988) 2297-2311
- 17) A. Authier, Dynamic theory of X-ray diffraction (Oxford University Press, Oxford 2001)
- 18) C. G. Darwin, The Theory of X-ray Reflexion, Phil. Mag. 27 (1914) 315-333; 675-690
- 19) P. P. Ewald, Acta Cryst. A25 (1969), 103-108
- 20) U. Pietsch, V. Holy, T. Baumbach, High Resolution X-ray Scattering (2nd edition, Springer, 2004)
- 21) A. H. Compton, Philos. Mag. 45 (1923) 1121-1131
- 22) H. Kiessig, Ann. Phys. 10 (1931) 769-787
- 23) L. G. Parratt, Phys. Rev. 95 (1954) 359-369
- 24) L. Nevot, P. Croce, Rev. Phys Appl. 15, 1980, 761
- 25) H. Dosch, Critical Phenomena at Surfaces and Interfaces, (Springer-Verlag, 1992)
- 26) M. Toney, S. Brennan, Phys. Rev. B 39 (1989), 7963-7966
- 27) W. Bartels, J. Vac.Sci. Technol. B1 (2) (1983), 338-345
- 28) LEPTOS user manual, Bruker AXS Karlsruhe, DC-M88-EXX052, V7, (2009)
- 29) A. Ulyanenko, Adv. In Comp. Methods for X-ray and Neutron Optics, 5536 (2004) 1-15
- 30) G. T. Baumbach, P. Mikulik, X-ray Reflectivity of rough multilayers (in: X-ray and neutron reflectivity: principles and applications, ed. J. Daillant, Springer Berlin, 1999)
- 31) S. K. Sinha, J. Phys. III, 4 (1994) 1543-1557
- 32) A. Gibaud, S. Hazra, Current Science, Vol. 78 (2000), 1467-1477

- 33) J.Daillant, O.Belorgey, J.Chem.Phys., Vol 97 (1992), 5824-5836
- 34) J.-P. Schlomka, M. Tolan, L. Schwalowsky, O.H. Seeck, J. Stettner, W. Press, Phys. Rev. B 51 (1995) 2311-2321
- 35) B. Mandelbrodt, R. Voss, The fractal geometry of nature (Freeman New York, 1982)
- 36) S. Stepanov, Exploration of Subsurface Phenomena by Particle Scattering (Ed. N. Q. Lam, C. A. Melendres, and S. K. Sinha; IASI Press 2000) 119-137
- 37) V. Holy, J. Kubena, I. Ohlidal, K. Lischka, W. Plotz, Phys. Rev. B 47 (1993) 15896-15903
- 38) V. Holy, T. Baumbach, Phys. Rev. B 49 (1994) 10668-10676
- 39) D. Savage, J. Kleiner, N. Schimke, Y.-H. Phang, T. Jankowski, J. Jacobs, R. Kariotis, M. Lagally, J. Appl. Phys. 69 (1991), 1411-1424
- 40) S. Stepanov, E. Kondrashkina, M. Schmidbauer, R. Köhler, J.-U. Pfeiffer, Phys. Rev. B 11 (1996), 8150-8162
- 41) E. Spiller, D. Staerns, M. Krumrey, J. Appl. Phys. 74 (1993) 107-118
- 42) J. Als-Nielsen, D. Jacquemain, K. Kjaer, F. Leveiller, M. Lehav, Phys. Rep., 246 (1994), 251-313
- 43) Y. Yoneda, Phys. Rev. 131 (1963) 2010-2013
- 44) W. Marra, P. Eisenberger, A. Cho; J. Appl. Phys. 50 (1979) 6927-6933
- 45) U. Pietsch, Current Science 78 (2000), 1484-1495
- 46) D. Höche, C. Blawert, S. Lamaka, N. Scharnagl, Z. Mendis, M. Zheludkevich, Phys. Chem. Chem. Phys. 18 (2016) 1279-1291
- 47) K. Omote, J. Harada, Advances in X-ray Analysis 43 (2000), 192-200
- 48) B. Gilles, Grazing incidence diffraction: a review. No. LNF-IR--96-049. (1996)
- 49) R. Feidenhans'l, Surface Science Reports 10 (1989), 105-188
- 50) T. Baumbach, S. Tixier, U. Pietsch, V. Holy, Phys. Rev. B 51 (1995) 16848-16859
- 51) G. Lim, W. Parrish, C. Ortiz, M. Bellotto, M. Heart, J. Mater. Res. 2 (1987) 471-477
- 52) M. Toney, S. Brennan, Phys. Rev. B 39 (1989), 7963-7966
- 53) R. Goehner, M. Eatough, Powder Diffraction 7 (1992), 2-5
- 54) U. Pietsch, W. Borchard, J. Appl. Cryst. 20 (1987), 8-10
- 55) B.E. Warren, X-ray diffraction (Dover books on physics, 1991)
- 56) P.F. Fewster, N. Andrew, V. Holý, K. Barmak, Phys. Rev. B 72 (2005), (174105-01)-(174105-11)
- 57) T. Mitsunaga, Rigaku Journal 25 (2009), 7-12
- 58) I.K. Robinson, Phys. Rev. B 33 (1986), 3830-3836
- 59) D. Simeone, G. Baldinozzi, D. Gosset, S. Le Caer, J. Berar, Thin Soild Films, 530 (2013), 9-13

Chapter 3: Electrochemistry goes GIXRD – cell development and in-situ surface oxidation of copper

3.1 Abstract:

Grazing incidence X-ray Diffraction (GIXRD) can deliver integral information of the structure and chemistry of surface-near regions in a crystalline sample. Using this technology, we document and analyse the development of an in-situ and versatile, electrochemical GIXRD setup for surface studies at relevant conditions. The versatility of this setup can be expressed as: the possibility to investigate poly- and single crystalline samples, its operation at various pHs, and the accessibility to different scan modes, including glancing angle measurements. The oxidation of polycrystalline copper in an alkaline medium acts as an example of the functionality of the setup. The in-situ GIXRD results suggest a multi-step surface passivation that depends on the conditions of the experiment. Within cyclovoltammetric cycling, peak shifts were observed, which can be attributed to a surface smoothing of the Cu foil. Under chronoamperometric conditions the initial Cuprite phase (Cu_2O) transforms into a higher valent Tenorite (CuO) phase and $\text{Cu}(\text{OH})_2$ via a dissociation and precipitation mechanism. As the current decays over time leads to insulating surface properties, indicates the full passivation of the surface by a continuous formation of CuO and/or $\text{Cu}(\text{OH})_2$.

3.2 Introduction:

In-situ analysis of samples is the research subject of many sectors in materials science such as cancer research, metallurgy and catalysis. In catalysis research, for instance, this technique allows one to directly draw conclusions as per the modification of surface and crystalline bulk structures during their exposure to a catalyst in the reactive environment. Owing to the high coherency of crystalline samples, in-situ diffraction techniques are often applied at synchrotrons or in the laboratory^(1,2,3,4,5). As opposed to synchrotron radiation, laboratory X-ray sources are widespread. However, they are not always used for in-situ development. Synchrotron beam time is precious, and thus successful beam time applications require time, patience, and usually a good prior knowledge of the targeted reaction and sample. Consequently, laboratory in-situ setups need to be developed and used in parallel, either as a cheaper and more readily available alternative, or as a screening ground for exploring new approaches before they are then transferred to the synchrotron. Two significant drawbacks in using laboratory X-ray sources are their low photon flux and low collimated beam in comparison to a synchrotron source. When performing a high efficiency GIXRD experiment, these are necessary requirements since the intensity of a reflected-diffracted wave is in the order of 10^{-8} ⁽⁶⁾, especially at performed in-plane GIXRD measurements. With the development of modern X-ray optics like “Göbel mirrors”⁽⁷⁾ in 1995, flux density and coherency limitations of the X-ray beam of laboratory diffractometers could be decreased, thus paving the way for Grazing Incidence X-ray Diffraction (GIXRD) in the home lab. The power of this method lies in the precise depth control and the evanescent wave formed at the critical angle of total external reflection on the surface⁽⁸⁾. Thus, even monolayers on single crystal surfaces can be investigated^(9,10). Glancing angle X-ray diffraction techniques for thin film analytics, can be divided into two groups: in-plane, and out-of-plane measurements. The classical GIXRD experiment, starting with Marra’s experiment⁽⁸⁾ on epitaxial single crystal Al surfaces on a GaAs semiconductor substrate, is known as the in-plane type. This

method is based on the almost full inclination (usually around $90^\circ \pm$ critical angle) of the sample surface along its z-direction. Its characteristic sample tilt results in the ability to test lattice planes normal to the thin film surface. If the sample exhibits a strong texture (e.g. preferred orientation), this is the method of choice. Since this type of experiment can be seen as an advanced and very dedicated step in characterizing a sample surface, it requires a certain knowledge beforehand of the thin film. An X-ray diffraction depth profile can also be achieved from the out-of-plane geometry. In contrast to in-plane GIXRD, the tested lattice planes are then parallel to the sample surface. In the out-of-plane case, also called asymmetric Bragg diffraction, the penetration depth is controlled over the incidence angle (α , usually less than 1°) with respect to the sample surface, which is, in case of the in-plane type, a multi-drive parameter. This can be understood by imagining the scanning axis, which is in out-of-plane GIXRD simply 2θ , whereas in the in-plane case it is $2\theta\chi$ in connection with ϕ (sample rotation). As in-plane measurements in combination with an electrochemical in-situ setup are a challenge to realize in laboratory as well at synchrotron sources, we decided to focus on the easier out-of-plane direction for our experiment. Working with liquids in a vertical direction in an electrochemical environment as well raising attenuation problems during the adjustment (detection of surface layers with accessible reflections, attenuation due to electrolyte and capping,...) supported our decision to stay with the out-of-plane direction due to its higher tolerance in the development of the setup. The ability to switch quickly and easily between electrolytes, electrodes or conditions, as well the sufficient beam flux for random oriented samples in the out-of-plane geometry with laboratory X-ray sources, are strong arguments for increasing the number of (in-situ) surface diffraction experiments in the home laboratory. GIXRD provides an integral method for gaining surface structure information in contrast to high-end methods such as Transmission Electron Microscopy (TEM). The data of integral surface structures and their modifications are also the subject of electrochemistry. In electrochemistry, the surface is completely wetted by an electrolyte solution forming a solid-electrolyte interface. This interface is of special interest in electrochemistry as it is the border where the electron exchange happens and reactions on an atomic level (in electrochemistry referred to as inner and outer Helmholtz-layer⁽¹¹⁾) occur^(12,13). The structure of this double layer has a major impact on the electrode reaction and its kinetics. Depending on the strength of adsorption of the anion or cation, the rate can be enhanced or decreased for the electrode process. There are many influences which determine the structure of this double layer, ranging from the ordering by coulomb forces of adsorbed anions to disturbances of this ordering by temperature^(11,13). Recent results suggest that surface sensitive diffraction methods are capable of pinpointing the surface structures of electrode materials⁽¹²⁾. However, important insights into the relevant surface structure at the solid-electrolyte interface under working conditions are often missing. This information is fundamental in order to establish structure-activity correlations. In addition to this correlation, the influence of crystallinity on conductivity is also of strong interest. X-ray reflectometry (XRR) can be used as a complementary, morphological technique for understanding surface roughness, layer thickness and electron density⁽¹⁴⁾ but this, closely related to GIXRD technique, is not in the scope of this work.

Here, we report on the development of an in-situ electrochemical cell for laboratory GIXRD surface structure measurements focusing on the oxidation of polycrystalline copper in an alkaline medium. The formation of surface oxide layers on copper is known to change the environmental stability of copper and has been studied extensively since the first electrochemical work of Muller was published in 1907⁽¹⁵⁾. The use of copper as a material for electronic devices, wires and roofing covers more than 70% of its use. The electronic industry is especially interested in corrosion protection since copper oxide (CuO) has a significantly lower conductivity⁽¹⁶⁾. However, details on the electrochemical

oxidation mechanism of copper in alkaline media are still under discussion, hence the low number of in-situ measurements. In alkaline solutions copper forms surface oxides and hydroxides, whereas in acidic media it is known to undergo dissolution and require inhibitors^(17,18,19).

3.3 Electrochemical in-situ setup for out-of-plane GIXRD

3.3.1 Design of the in-situ setup

A schematic diagram of the design of the home-built in-situ cell is shown in Fig.3.1-3. The cell exhibits a total volume of approximately 7.5 mL and consists of three parts: a holding corpus, an electrochemical cell and the corresponding window cap. On top of the basal plate an aluminum corpus is mounted that hosts the electrochemical cell manufactured from PEEK (polyether ether ketone⁽²⁰⁾, Fig.3.1&2 A, B and C). PEEK exhibits a high chemical inertness that holds also for the majority of the acidic and basic electrolytes used and is therefore frequently chosen as the material to construct electrochemical devices⁽²¹⁾. The electrolyte inlet and outlet were also made from PEEK and were connected via Teflon hoses and PEEK ball-valves (Fig.3.4, part A). The Ag/AgCl reference electrode (Biologic RE-1S, Fig.3.1 D) is fixed by a PEEK inset and sealed with a Viton O-ring. In addition, a Pt counter electrode (1 mm diameter) was placed in opposite position to the reference electrode and sealed in an identical manner. The PEEK working electrode holder was tailor-made for the hat-shaped substrate (Fig.3.3, part E). A hat-shape substrate (with a step height of 0.7 mm, exposed surface diameter of 10 mm and a 13.5 mm rim at the bottom) ensures the benefit of having a greater mounting strength. The continuous rim provides a secure platform on which to clamp the sample and seal the cell, while the surface of the sample can easily be exposed to the electrolyte and the X-ray beam. The bottom of the sample is contacted by a copper stamp, which is tightened by a Viton O-ring to the inside of the PEEK housing (Fig.3.3, Part B). To obtain a three electrode setup a copper leakage was screwed through the aluminum corpus and connected to the copper stamp. The cell can be filled by an attached syringe (25 mL). The dead volume of the set-up is approximately 6.5 mL (Fig.3.4). When operating with a dome cap (caps are described in the following section), the volume increases to around 22 mL in total.

The setup of the in-situ cell was optimized for a Bruker D8 Advance diffractometer (da Vinci design) combined with the compact Eulerian cradle sample stage. An Eulerian cradle ensures the optimum alignment of the surface of the sample using the ϕ - and χ -circles. In addition, the cradle ensures the fine tuning of the sample height in the μm range. Similar results were obtained with an xyz-stage. However, the common xyz-stage offers fewer degrees of freedom, which can create a bottleneck during adjustment of the surface parallel to the X-ray beam. An easy to repair system ensures high versatility and simple exchange of the individual parts of the system. The requirement for GIXRD is to guarantee unimpeded accessibility to the sample surface in order to avoid any artifacts from the sample holder. Thus it is fixed at the highest point of the setup just below the cap of the cell. The most important part for X-ray diffraction in connection with electrochemistry, the cell cap, is discussed in the next section.

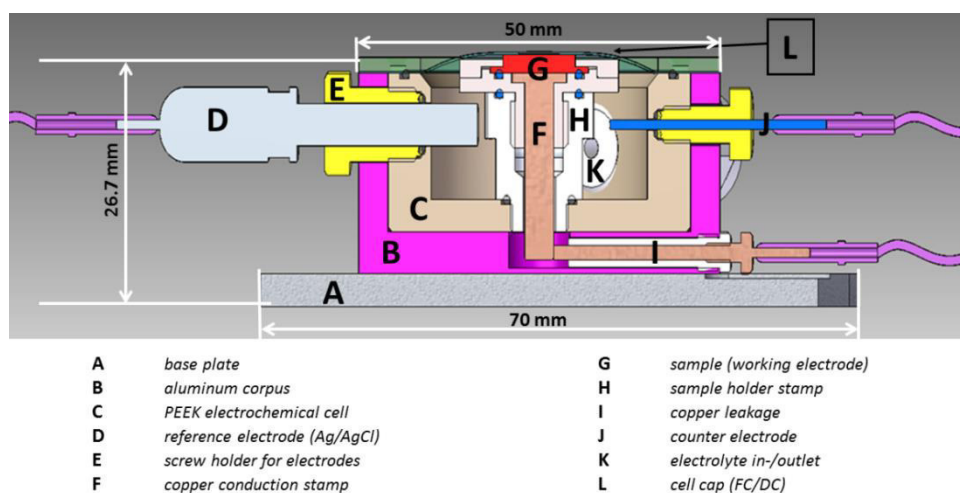


Fig.3.1: In situ XRD cell, optimized for Grazing Incidence diffraction (cross section)

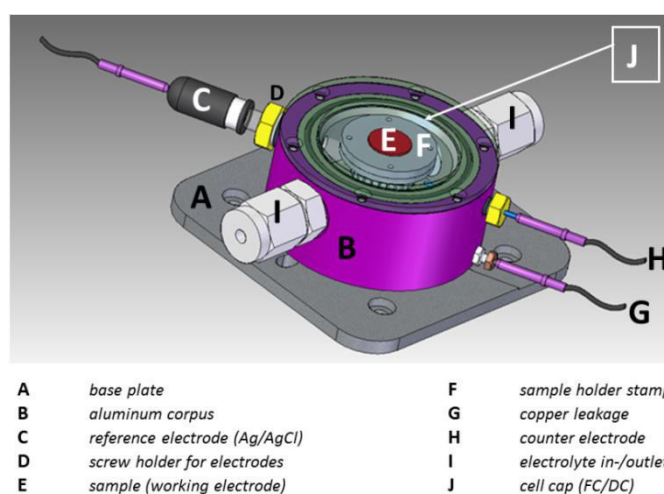


Fig.3.2: In situ XRD cell, optimized for Grazing incidence diffraction (side view)

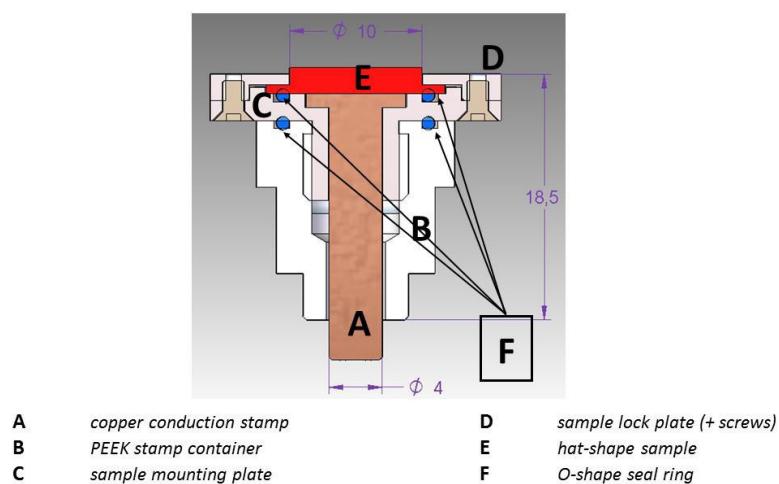
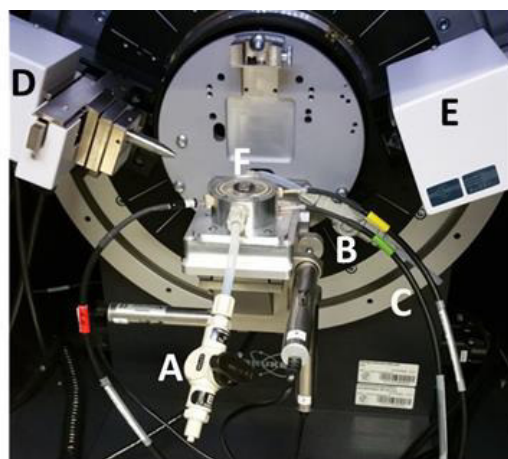


Fig.3.3: sample holder stamp (cross section view, lengths are in mm)



A	electrolyte inlet	D	Göbel mirror optic
B	electrolyte outlet	E	soller slit optic
C	potentiostat connections	F	in-situ cell

Fig.3.4: the in situ cell mounted on the diffractometer. Note the external setup

3.3.2 Operation modes

The in-situ cell can be operated with two different caps: foil capped (FC) or dome capped (DC). The foil cap is composed of Kapton (7.5 μm foil thickness) and screwed with a PMMA ring (polymethylmetacrylate) onto the PEEK cell. Kapton exhibits a very low linear absorption coefficient and chemical inertness. The 0.7 mm thick dome cap is made from PMMA and is precisely half-spherical shaped (32 mm diameter). PMMA was selected to guarantee the stability of the half-sphere shape. Figure 3.5 displays the two different types of caps. The main difference between these two caps is the amount of electrolyte on the surface of the sample. The FC is beneficial for polycrystalline samples since the material is exposed to a low amount of electrolyte ($\sim 300\text{-}500\ \mu\text{m}$). Owing to the small coherence length of the grains, polycrystallinity requires a high intensity of the X-ray beam on the sample. This can be ensured by a thin electrolyte layer. Thus, FC represents a reasonable compromise between optimized diffraction conditions and the quality of electrochemical measurements for polycrystalline materials. In DC the sample is exposed to a higher amount of electrolyte (Fig.3.5 b), which ensures a better electrochemical performance. The large amount of electrolyte prevents space limiting diffusion of the charge carriers. However, by using DC for diffractive measurements, the electrolyte content has to be lowered until a meniscus remains. Prior to experiments, blind tests have to be conducted with either a sample dummy or an inert liquid to empirically find the optimum meniscus level for each sample. The DC is considered for single crystalline samples or samples with a very defined and flat surface where the reaction shouldn't be suppressed by diffusion limitation. In many cases (but also depending on the desired reaction) polycrystalline surfaces are often more reactive than single crystalline surfaces, since the presence of different facets (e.g. 111, 110, 100, ...) and edge sites are more likely to offer active domains. The scan types available in the in-situ setup are (i) symmetric, (ii) GIXRD, and (iii) reciprocal space mapping. The last is exclusively for single crystalline samples or epitaxial grown layers in order to study in detail affected hkl planes. This scan type requires a highly dedicated beam optimization and resolution. Reciprocal space mapping by itself is a very elaborate technique and would exceed the scope of this work. Nevertheless, the design of the in-situ cell allows this measurement technique to also be performed. Since the surface sensitivity of Grazing Incidence X-ray Diffraction is the method of choice for studying surface-near structural changes, the present work restricts the use of the cell to FC in GIXRD geometry. In GIXRD, the roughness of the surface is important. The lower the surface

roughness the better the data analysis. For polycrystalline samples, the surface roughness is usually supposed to be approximately between 1-2 μm and, for single crystal samples, higher than 10 nm



Fig.3.5: a) foil capping (FC) Note the Kapton foil been pulled taut over the sample surface. b) dome capping (DC), the flooding of the whole cell is clearly visible.

Although GIXRD measurements reveal unique features of the surface composition, long penetration pathways arising from surface layers and/or the electrochemical set-up are limiting factors of this technique and lead to a reduction of the diffracted beam intensity. Owing to the low incidence angle, the Bragg angle is shifted to a higher 2θ value, which is physically induced by the so-called refraction effect at the interface of the solid and its environment.

While reflections in XRD are defined by their intensity, position and shape, GIXRD requires additional data treatment. In addition, for reciprocal space mapping geometrical considerations, such as symmetry, grazing incidence and/or grazing exit geometry have to be adjusted. As a result the evaluation and sample modelling become very time consuming⁽²²⁾.

3.3.3 Experimental impact of the electrochemical setup on the peak intensity in GIXRD

Focusing on the intensity, we demonstrate the pitfalls of investigating the influence of the foil cap and the electrolyte volume in the final diffractogram. Fig. 3.6 shows the influence of the electrochemical setup on the intensities of the Cu (111) reflection. Cap-free measurements on Cu foil reveal the highest intensity for the (111) reflection. The intensity decreases according to the following order: blank > cap > cap +electrolyte. In addition, changing the electrolyte, the type of the cap, the amount of electrolyte and/or the sample influence the intensity ratio.

A quantitative description of the intensity on the cap and electrolyte is presented below.

Initially the approximate thickness (Table 3.2) of the cap and electrolyte can to be evaluated over the mass attenuation coefficient (Table 3.1). Since the ratio of initial and measured intensity (the I/I_0 ratio) is known, the recalculation can be performed:

$$I = I_0 e^{-\left(\frac{\mu}{\rho}\right) \rho d} \quad (3.1)$$

I, I_0 ... Intensity μ/ρ ... mass attenuation coefficient cm^2/g ρ ... density (g/cm^3) d ... thickness (cm)

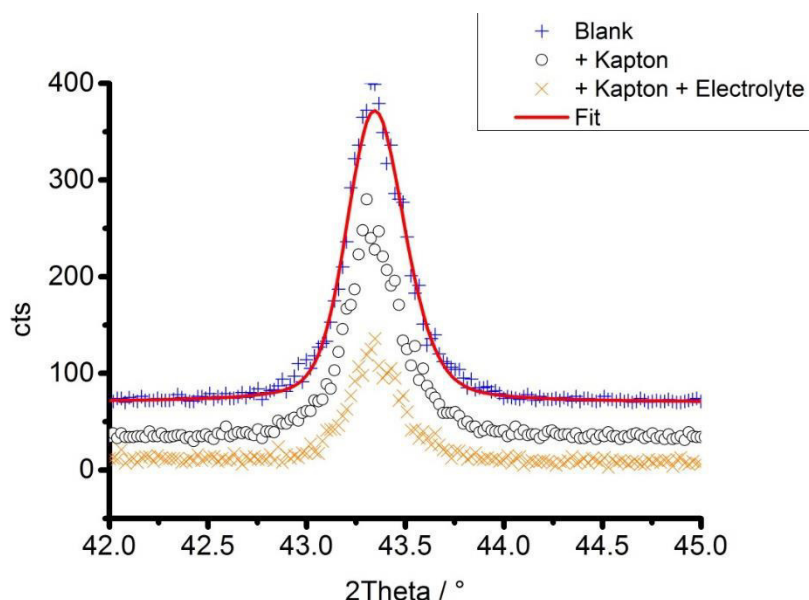


Fig.3.6: Measured intensity of the Cu 111 reflection in the different steps of the cell preparation. Please note the stacking of the three curves in y for better visibility. (in this case: 1° incident angle, 3s counting time/0.02° step size and slit size of 0.6 mm for the primary beam)

The mass attenuation coefficients for some materials are given in Tab 3.1:

Tab.3.1: Mass attenuation coefficients (from NIST⁽²³⁾) for Cu radiation (8.07 keV)

Material	μ/ρ (cm ² /g)	ρ (g/cm ³)
Mylar	6.75	1.38
PMMA	6.49	1.19
Prolene	3.97	0.91
Kapton	3.1 ⁽²⁴⁾	1.42
Water	10.37	1.00

Tab.3.2: calculated thickness values for the observed attenuation within the in-situ setup

	Intensity	Thickness (H ₂ O) (μm)	Thickness (Kapton) (μm)
Blank	330 cts	-	-
+ Kapton	260 cts	-	~275
+ Kapton + Electrolyte	130 cts	~350	~275

The large thickness values in Table 3.2 are relativized by considering a diameter of the studied surface of 1 cm (=10.000 μm) and an incidence angle of 1°. The value of the Kapton foil differs considerably from 7.5 μm and can be explained by that under GIXRD geometry the beam travels almost horizontally along the spanned foil instead of directly vertical. This also generates diffuse background scattered intensity. Owing to its having higher mass attenuation coefficient than the Kapton foil, the thickness of the water layer contributes more to the reduction of intensity. The calculated thicknesses of course cover both the incoming and the exiting beams. Since grazing incidence geometry is used, the incident beam counts much higher for attenuation than the exit beam (longer pathway through the electrolyte solution).

Altogether this study demonstrates that the sample surface hosted in an electrochemical relevant environment can be measured in-situ by GIXRD and at the same time the obtained diffractogram retains sufficient detectable intensity to be interpretable. The quantification of intensity can also be

obtained by refinement of the peak positions by Rietveld fitting (Fig.3.6, blank) that results in integrated intensity. In addition, the exact positions of the diffracted peaks and the full width at half-maximum (FWHM) are obtained (Table 3.3) for the Cu 111 reflection.

Tab.3.3: fitted integral intensity, d-spacing and FWHM for Cu 111 during the mounting sequence

	Integ. intensity	d (Cu) (Å)	FWHM (Cu 111) (°)
Blank	30.01	2.0858	0.25
+ Kapton	21.05	2.0861	0.25
+ Kapton + Electrolyte	10.08	2.0860	0.20

The tabulated values in Tab.3.3 are in excellent agreement with the trend from the previous attenuation calculation (Tab.3.2). Additionally, the FWHM and d-spacing remain almost constant during the mounting sequence. The intensity change can therefore be attributed purely to covering and flooding the cell.

3.3.4 Refraction shift correction for flat samples

The peak shift is caused by the so-called refraction effect that occurs at incidence angles below $<2^\circ$. When the incident beam passes through the boundaries of two different media with different refractive indices, the direction and wavelength is modified, resulting in a shift of 2θ towards higher scattering angles. For symmetric scans the effect is negligibly small, whereas in GI geometry the alterations can be in the order of 1/10 of a degree. To counterbalance this offset, several reports have suggested details on the correction of the refraction effect^(25,26). In particular for GIXRD, the correction factors may be used to estimate the actual $2\theta_{\text{Bragg}}$ values of thin films. Thin films often exhibit a significant strain that depends on the method of deposition or the growth mechanism. For these samples reference values obtained from bulk samples are often not accurate enough to estimate the exact d-spacings. Based on the equation given by Toney et al.⁽²⁵⁾ the refraction shift can be calculated for incidence angles smaller than 2° (see also chapter 2, Eq.2.38):

$$\Delta 2\theta = \alpha - \frac{1}{\sqrt{2}} \sqrt{\left\{ \sqrt{[(\alpha^2 - \theta_c^2)^2 + 4\beta^2]} - \theta_c^2 - \alpha^2 \right\}} \quad (3.2)$$

with: α ... incidence angle θ_c ... critical angle δ ... dispersion term of the refractive index n β ... absorption term of the refractive index n

The dispersion term δ , the absorption term β as well the critical angle can be calculated with Eq. 3.3-3.6:

$$\delta = \frac{r_0}{2\pi} \lambda^2 \rho_e \quad (3.3)$$

$$\rho_e = \frac{\rho_m N_A Z}{A} \quad (3.4)$$

r_0 ... classic electron radius λ ... wave length ρ_e ... electron density ρ_m ... mass density N_A ... Avogadro number Z ... atomic number A ... mass number

$$\beta = \frac{\lambda}{4\pi} \mu \quad (3.5)$$

λ ... wave length μ ... linear attenuation coefficient

$$\alpha_c = \sqrt{2\delta} \quad (3.6)$$

The refraction shift calculation is a mandatory correction for thin layer diffraction techniques. In contrast to purely bulk samples, as is the case in the present work, this shift has to be handled with care. Table 3.4 summarizes the result of the refraction shift correction of the copper sample for the Cu 111 reflection. The calculated value was obtained according to Eq. 3.2 and the experimental shift was measured at the blank sample against the copper 111 reference position (PDF 00-004-0836).

Tab.3.4: Observed results for the refraction shift correction on the adjustment of the in-situ setup

	δ	β	α_c	α
Cu 111	2.61×10^{-5}	5.13×10^{-7}	$0.414^\circ / 0.0072 \text{ rad}$	$1^\circ / 0.0174 \text{ rad}$
calculated $\Delta 2\theta$	0.089°			
experimental $\Delta 2\theta$	0.024°			

The experimental value is significantly smaller than the calculated one. This discrepancy can be explained mainly by the high deviation of the effective surface density from the nominal one. Polishing of the copper surface before its use in the experiment likely created a rough surface with ‘hills and valleys’. Penetration of the X-ray beam becomes inhomogeneous since the hills are hit before valleys, hence the electron density expressed by δ becomes lower than the nominal value due to ‘dilution’ with air. Refraction shift theory was derived for homogeneously flat surfaces and perfectly parallel interfaces. High roughness (μm - range) would not allow the beam to penetrate the surface homogeneously as pointed out before and therefore the refraction shift correction deviates from its ideal form. Effects of the coherent scattering domain sizes on the refraction effect also cannot be completely excluded⁽²⁶⁾. For all further evaluations the experimentally determined refraction shift was considered.

As opposed to the intensity attenuation for the in-situ electrochemical cell, the refractive shift is independent from the alignment procedure (Tab.3.3), but crucially depends on the incidence angle. The highest shifts can be observed around θ_c (for Cu $\theta_c = 0.41^\circ$). θ_c plays an important role for thin film diffraction and XRR measurements. Around this critical angle the sensitivity of the evanescent wave travelling parallel along the sample surface is highest for surface near regions. At this angle the information depth for copper is approximately 20nm. This quality and sensitivity of GIXRD measurements is limited to well-ordered homogeneous surfaces as they may occur in either single crystals or by using plane Si wafers as substrates. Common polycrystalline samples will suffer from the surface heterogeneities and the associated enhanced diffuse scattering. The full potential of GIXRD can therefore only be applied to a small fraction of homogeneous samples. Nevertheless, as we will demonstrate, this ultimate sensitivity is not always necessary to gain depth sensitive information and make our out-of-plane GIXRD setup a useful technique for polycrystalline surface studies.

3.4 In-situ electrochemical oxidation of copper in alkaline media investigated by GIXRD

3.4.1 Experimental

The copper sample was prepared by cutting it from a massive copper piece (hat-shape substrate with a step height of 0.7 mm, exposed surface diameter of 10 mm and a 13.5 rim) and subsequently polishing with SiC 2400 sandpaper to a shiny surface (10 mm diameter). Before measurement the electrode was kept for 10 min at -1 V to reduce already present surface oxides. **Electrochemistry:**

was performed in 0.2M KOH (ultrapure Merck) and purged with Argon before use. A Pt wire was used as counter electrode and an Ag/AgCl reference electrode. The electrochemical procedure was chosen as follows: the sample was cycled (cyclic voltammetry, CV) under constant scan speed of 20mV/s 4 times. Afterwards, the potential was held for 20 hours at -0.26 V (vs. Ag/AgCl) (chronoamperometry, CA). **X-ray Diffraction:** measurements were performed on a Bruker D8 Advance (Da Vinci design with LynxEye detector, Cu radiation), equipped with a Göbel mirror and Eulerian cradle. Measurement range was set from 25-70° 2θ, with 0.02° step size and 3s counting time per step. The primary slit was chosen to be 0.6 mm, a 0.2° secondary soller and the incidence angle to 1°. Primary beam alignment was performed on θ and 2θ scale before every measurement with glass-slit procedure. After 5, 10 and 15 hours the measurement was repeated under the same conditions in order to monitor the changes. The in-situ cell was used with foil cap (FC) with Kapton foil (7.5 μm thickness). The diffraction peaks were analyzed by full pattern fitting using the DIFFRAC.Topas software (V5, 1999-2015, Bruker AXS). Since the relative intensities of the crystalline phases are affected to some degree by the grazing incidence geometry as compared to conventional powder diffraction, a quantitative Rietveld analysis could not be performed. Instead, the main emphasis was put on qualitative phase analysis and extraction of peak shape and intensity parameters for of the main copper reflections.

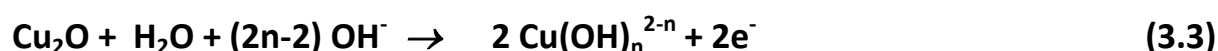
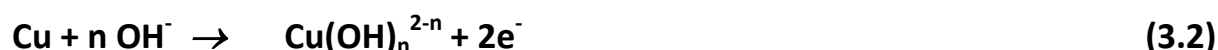
3.4.2 Cyclovoltammetry results and Interpretation

Since the first report on the electrochemical oxidation of copper in alkaline media by Muller, many different techniques have been applied to study this unexpectedly complex reaction^(27,28,29). There is great debate about the mechanism of the oxidation of copper at high pH values. Many intermediates, as well as mechanistic combinations are controversially discussed. He⁽³⁰⁾ and Ambrose⁽³¹⁾ introduced oxidative reaction steps that involve the interplay between copper, its cations and OH⁻ ions and are presented in the following:

(1.) Formation of Cu₂O:



(2.) Formation of a porous cuprite layer^(32,33) and subsequent oxidative metal and/or cuprite dissolution over:



(3.) Formation of a temperature dependent CuO and Cu(OH)₂ surface species⁽³⁴⁾:



It was proposed that the passivation layer forms via a precipitation/dissolution process of CuO accompanied by dehydration of Cu(OH)₂ and depends on the selected potential range and/or temperature⁽³²⁾. However published results differ, in particular for assigning the mentioned reactions to the corresponding cyclovoltagramms (CV) peaks. The initial step at -0.68 V serves as an example of this controversy. Ambrose⁽³¹⁾ reported the formation of soluble Cu(OH)₂ species since a pre-peak before the typical bulk Cu₂O formation potential appears. Fletcher⁽³⁵⁾ assigned it to dissolving Cu⁺, and Miller⁽²⁹⁾ mentioned that on rotating disc experiments no pre-film free dissolution of Cu₂O can be

observed. Finally, Droog⁽³²⁾ identified that the very first stage is the electrosorption of oxygen species which is represented by a very small double peak at lower anodic potential and happens in two stages. The broad distribution of opinions about this initial stage demonstrates the discrepancy in measurement, interpretations and sample treatments between the different groups.

In general, six peaks are situated between hydrogen and oxygen evolution on copper in the full range of cyclic voltammograms⁽³⁶⁾ in alkaline media. On the anodic side one can find four peaks, which can partially overlap. In the cathodic regime mainly two complex one are observed. The anodic reactions towards oxygen evolution reaction (OER) include electrosorption, formation of Cu_2O , and subsequent transformation into two Cu^{+II} species. In the cathodic regime two reactions dominate: the reduction of Cu^{+II} to Cu^{+I} and the complex and simultaneous reduction Cu^{+II} to Cu^0 and Cu^+ to Cu^0 ^(27,31,34). The observed peak positions and charges strongly depend on the electrolyte concentration, scan speed, the chosen potential range^(36,37) as well as the structure of the surface.

In Fig. 3.7 the recorded CVs obtained by our in-house built electrochemical set-up are shown. Four main peaks and two minor ones can be observed after the first sweep. They will be discussed in the following order: first the anodic and then second the cathodic regime. A pre-peak was found at -0.73 V. Droog⁽³²⁾ and Dong⁽³⁶⁾ attributed this pre-peak (0.68 V vs. Ag/AgCl in 1M NaOH) to the electrosorption of oxygen species. The absence of this peak in further cycles can be explained by the presence of nanostructured copper surfaces which remained after the pre-treatment (-1 V vs Ag/AgCl for 10 min). Owing to the higher surface area, the oxygen species can be more readily adsorbed. Two almost constant peaks at approximately -0.26 V and -0.06 V were ascribed to the formation of Cu_2O and CuO/Cu(OH)_2 , respectively.⁽³⁶⁾ A very broad peak located at approximately +0.32 V is assigned to a slow transformation of tenorite to Cu(OH)_2 . The peak is more pronounced in the first cycle and may point to the presence of initial surface nanostructure, which can be dissolved by the formation of Cu(OH)_4^{2-} species.

Corresponding reduction peaks are found at -0.28 V and -0.72 V, respectively. The peak at approximately -0.30 V corresponds the decomposition of dissolved Cu(OH)_4^{2-} species to surface deposited CuO ⁽³⁶⁾. It is often mentioned that a simultaneous reduction of Cu^{2+} to Cu_2O will also occur^(26,31,36). At more negative potential a complex reduction network involving the simultaneous reduction of Cu_2O and Cu^{2+} to Cu takes place^(31,37).

In the second cycle, the oxidation peaks in the anodic regime remain almost constant, whereas the reduction peaks become affected by a significant peak shift (to -0.55 V and -0.79 V respectively). The shift originates from a surface cleaning step after the 1st cycle removing possible surface Cu nanostructure. The initial surface cleaning process (i.e. the reduction of native surface copper oxide) causes the formation of metallic Cu surface nanostructures⁽³⁸⁾. The higher surface area of the nanostructured copper leads to a soluble Cu(OH)_4^{2-} species. Thus, reduction of the dissolved Cu^{2+} species may lead to a homogenous Cu deposition on the surface after the 1st cycle which causes flat low-surface area Cu surfaces. In the 2nd cycle there is almost no dissolution of Cu^{2+} and less surface hydroxide may be formed. Hence, the surface is enriched in CuO, which is energetically more difficult to reduce and the first reduction peak is shifted to a more negative potential. The reduction to only Cu_2O might be accompanying this process to a lesser extent^(31,37). The variation of the peak area between the first and the second scan is OH^- concentration dependent. From the 2nd to the 3rd cycle, no strong changes can be observed in the cathodic regime. Cycling may cause a surface annealing of metallic Cu that is formed via reconstruction and electrochemical deposition. The lower specific surface area does not likely favour the dissolution route (due to the need of higher potentials).

In the 4th cycle, another shift can be observed. Oxygen evolution is part of all cycles and thus small amounts of molecular oxygen are released. Its solubility and diffusivity have an essential influence and can be seen by a slight decrease of the oxygen reduction current. This effect changes the OH^- ion

concentration at the surface and the final shift of approximately 0.05 V appears^(36,37). This shift also affects the anodic regime responsible for oxidation. The in-situ setup influences the obtained CVs as well and may also contribute to the observed deviations. The unstirred/unpurged electrolyte will especially influence the result by means of local concentration gradients. Diffusion limitation may be caused by the taut foil spanning over the reactive surface.

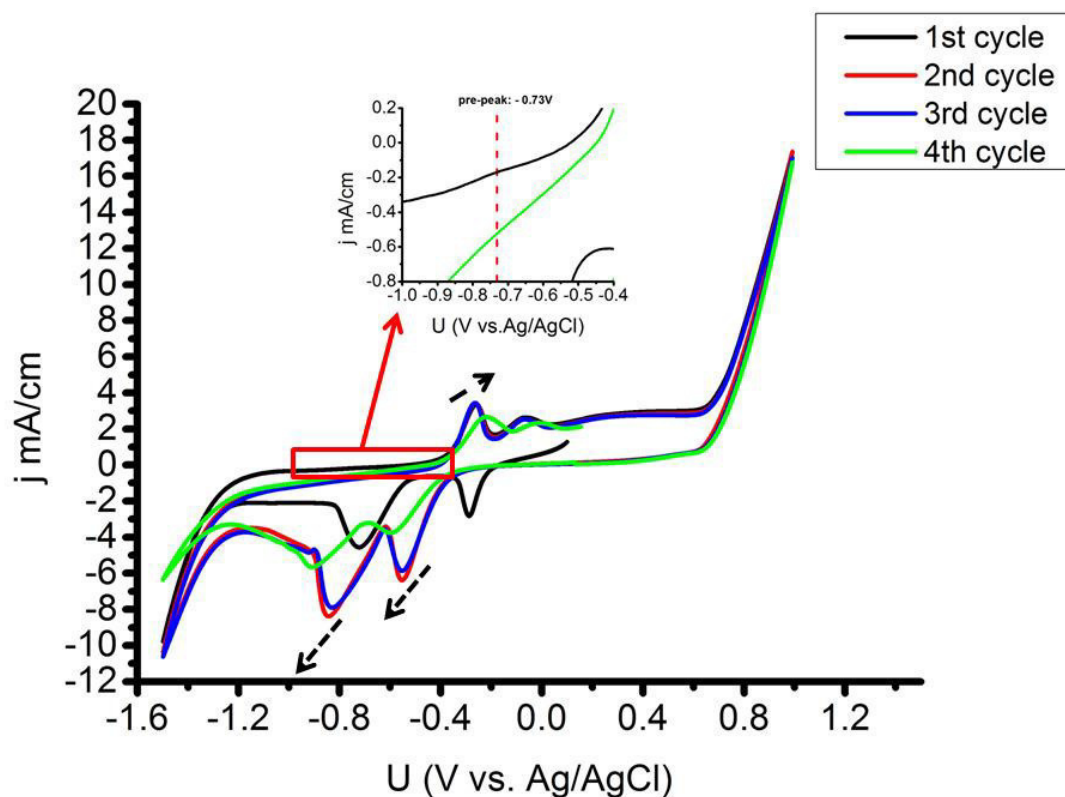


Fig.3.7: 4 recorded cyclic voltammetry curves in 0.2M KOH (Ar-purged) on the polycrystalline copper electrode (scanspeed: 20 mV/s).

3.4.3 Surface oxidation (CA) and Grazing Incidence X-ray Diffraction results and interpretation

After CV measurements, an isodynamic long-term experiment was conducted for 20 h at -0.26 V to study time-dependent details on the oxidation of metallic Cu. Fig.3.8 shows the corresponding chronoamperometric (CA) curve. The oxidation potential was set at the peak assigned to the Cu^+ species in the CV. The CA is the intended in-situ experiment to demonstrate activity of the oxidation over time by XRD scanning for transition states and species (Fig.3.10). Therefore the CA is discussed in connection with the GIXRD measurements and split into four areas: A to D. At the beginning of the CA curve the current is still in the cathodic regime indicating the presence of some X-ray amorphous oxidized species after the 4th cycle which were first reduced at this potential. They indicate the presence of $\text{Cu}(\text{OH})_2$ species formed after ORR on Cu surfaces. This leads to surface healing and the Cu domains become more defined. After approximately 2.5 h the current becomes positive indicating the oxidation of Cu surfaces, in which Cu is directly oxidized into Cu_2O . This oxidation can be discussed in two ways: first, the equilibrium of deposited surface $\text{Cu}(\text{OH})_2$ and soluble $\text{Cu}(\text{OH})_4^{2-}$ is disturbed and second, a likely local supersaturation drives the reaction towards the formation of Cu_2O and the direction oxidation of Cu (Eq. 3.1). Both findings are in agreement with GIXRD measurements. A stronger Cu 111 reflection was found along with the appearance of the cuprite phase (details can be found in the inset of Fig.3.10). The expectation to observe an intermediate

product, namely Cu_2O , was not made before the experiment. Its presence during potential cycling has already been proven in early work^(30,31,32). Oxidation of copper under constant conditions (constant potential) was expected to be ongoing until certain species are formed (preferred and stable at this potential) and due their presence the conductive properties become unfavourable for further conversion. The ongoing growth of the cuprite happens via the oxidation of underlying metallic copper and leads to the formation of a porous cuprite layer. Due to the high OH^- concentration ($>0.1 \text{ M}$) the surface can be partially converted and oxidized into $\text{Cu}(\text{OH})_2$ and soluble $\text{Cu}(\text{OH})_4^{2-}$ (Eq. 3.3) respectively. As a side reaction the dehydration of $\text{Cu}(\text{OH})_2$ arises, resulting in the formation of CuO , and solid CuO (Tenorite) begins to accumulate on the surface. This leads to the beginning of the surface passivation (area B in Fig. 3.8). Since the system is under constant potential, the conversion from copper over Cu_2O to CuO can probably be interpreted as the adaption of the system to more easily convert soluble species at the chosen potential rather than further oxidizing metallic copper or the cuprous oxide directly. The later conversion takes place at more positive potentials (in our CV assumed at $\sim -0.06\text{V}$). Therefore the observed formation of Cu_2O as intermediate under constant oxidation conditions and its subsequent (not direct) transformation into CuO is remarkable. The GIXRD scan after 10 h (area B) indicates the appearance of Tenorite peaks as well as a decrease in Cu_2O . At a certain point the concentration of dissolved $\text{Cu}(\text{OH})_4^{2-}$ decreases and the partial dehydration to X-ray amorphous $\text{Cu}(\text{OH})_2$ is preferred. This is reached after 10 h, as demonstrated by the decreasing current in Fig. 3.8 (area C) and shows the onset of surface passivation. After 15 h, GIXRD measurement indicates (Fig. 3.9, area C) that the Tenorite phase becomes more prominent and the Cuprite intensity decreases. The Cu_2O amount vanishes either via a hydroxide mediated pathway and dissolution, direct oxidation to CuO , or because the $\text{CuO}/\text{Cu}(\text{OH})_2$ is too thick to be penetrated by the X-ray beam. Finally, in area D the current drops to zero indicating a complete surface passivation. The formation of the oxidic surface layer can also be observed by a darkening of the sample that is typical for Tenorite (Fig.3.9).

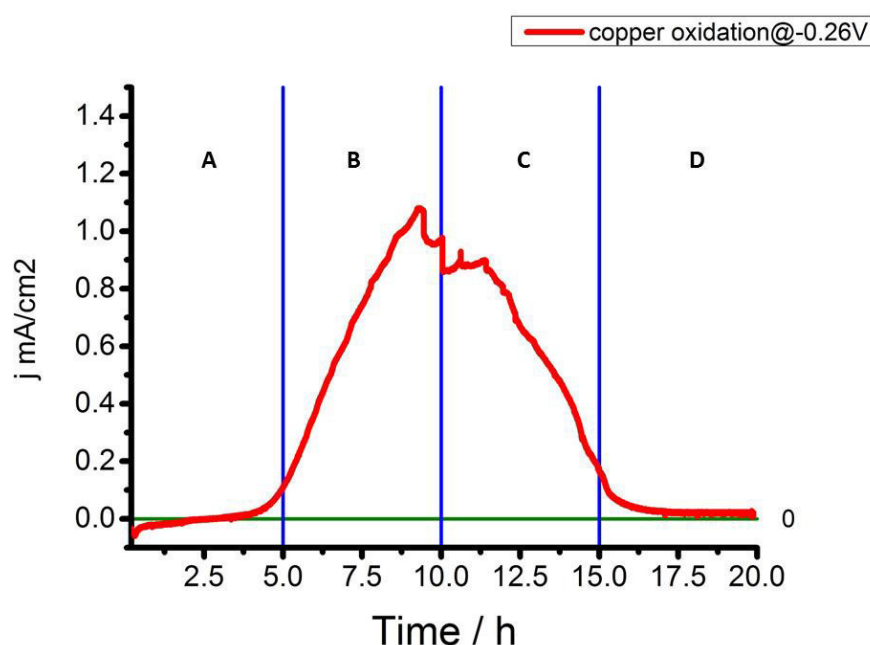
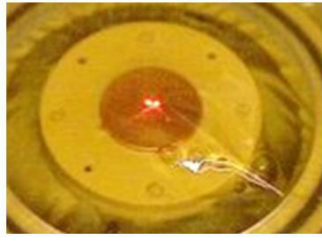
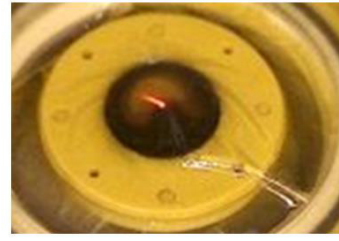


Fig.3.8: Chronoamperometry curve (20 h @ -0.26 V) of the polycrystalline copper electrode in 0.2 M KOH



a)



b)

Fig.3.9: The polycrystalline copper electrode a) before and b) after treatment. The different colour of the surface should be noticed (->foil capped).

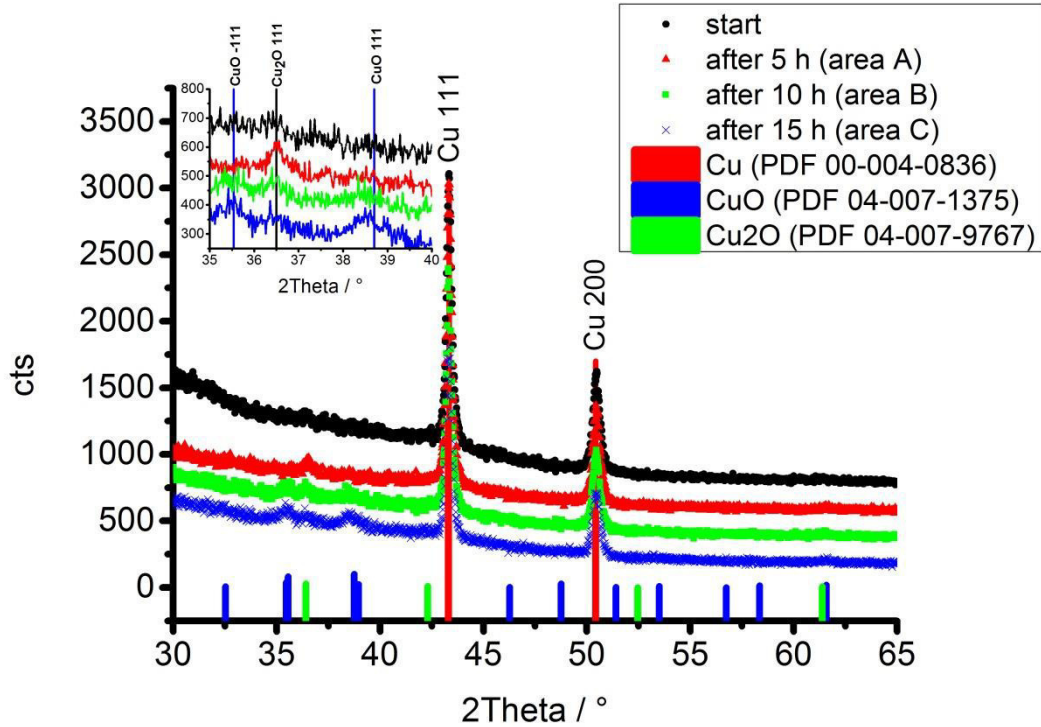


Fig.3.10: in-situ GIXRD data recorded over time for the oxidation of polycrystalline Cu in 0.2M KOH. Please note the stacking of the four curves in y for better visibility.

Tab.3.5: fitted integral intensity and FWHM for Cu 111 and Cu 200 during the chronoamperometric treatment

	Int(111)	Int(200)	FWHM(111) (°)	FWHM(200) (°)
Start	203.15	107.42	0.16	0.33
after 5 h	224.77	116.66	0.18	0.34
after 10 h	171.43	88.63	0.17	0.33
after 15 h	132.66	69.96	0.19	0.33

The above mentioned GIXRD results are in good agreement with expectations and in Fig.3.11 a fit of a refraction shift corrected GIXRD pattern of the in-situ measured copper oxidation is shown (after 10 h). Obtained pattern fit results are displayed in Tab.3.5. The intensity follows the predicted decrease during oxidation, whereas the FWHM remains constant within the estimated level of precision. The decrease in intensity for the sample after 10 h and 15 h is in line with the stepwise surface oxidation and the growth of the surface passivation layer. However, Shoesmith⁽³⁹⁾ and Ambrose postulated the formation of a $\text{Cu}(\text{OH})_2$ species⁽³¹⁾, which cannot be observed in our

measurement. The absence of $\text{Cu}(\text{OH})_2$ peaks suggest an amorphous or hydrated surface species, which is invisible for GIXRD. Ex-situ phase analysis reported by He⁽³⁰⁾ demonstrates that $\text{Cu}(\text{OH})_2$ is present on basic surfaces. Under the in-situ experimental basic conditions, $\text{Cu}(\text{OH})_2$ is soluble and may also be dissolved from the surface as a $\text{Cu}(\text{OH})_4^{2-}$ species⁽⁴⁰⁾. In addition, the weak intensity of the $\text{CuO}/\text{Cu}_2\text{O}$ peaks is related to a bifunctional surface layer that consists of amorphous compounds. Details on the film structure cannot be interpreted by the GIXRD measurements due to the suggestive presence of XRD invisible phases.

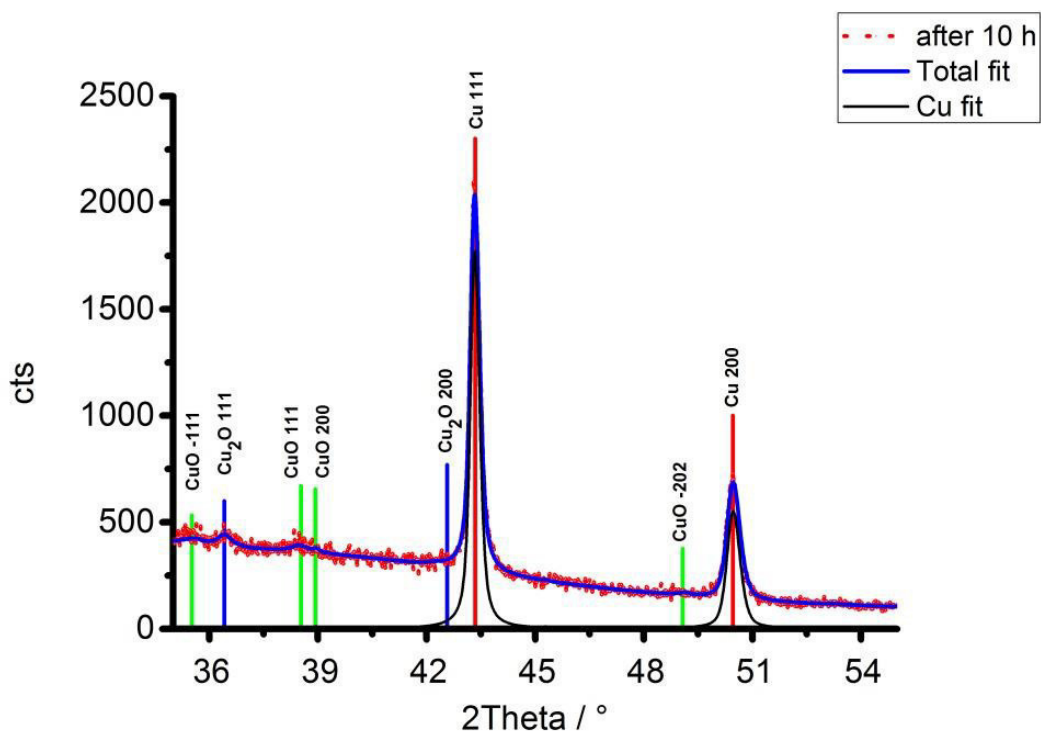


Fig.3.11: in-situ GIXRD data recorded after 10 h exemplarily fitted for integral intensity determination. The Cu 111 and 200 reflections are evaluated in detail.

The results gained by this in-situ out-of-plane GIXRD study clearly show that it's a feasible task yielding an impressive output. The combination of an oxidative treatment (CA) in connection with a diffraction study over time revealed details regarding the mechanism of Cu oxidation from the cuprite intermediate to the complete surface passivation. Observed peak shifts and likely OH^- concentration dependencies in the CV are in accordance with experiments done by Ambrose and Dong⁽³⁶⁾. The finding of crystalline Cu_2O as an intermediate and CuO as a component of the passivation layer highlight the importance of this in-situ characterization. Cuprite is formed and, under the reaction conditions, consumed, leading to the growth of CuO crystallites. Growth kinetics and super saturation drive the crystallization and oxidation process. $\text{Cu}(\text{OH})_2$ is invisible for GIXRD during our measurement, so we might conclude that due to its higher solubility at higher OH^- concentrations the degree of decomposition compared to dissolved CuO is smaller. A graphic summary of the proposed reaction pathway from origin to passivation is given in Fig.3.12.

These results observed with a simple out-of-plane diffractometer in home laboratory are an important basis for further investigations into the detailed surface passivation process. In terms of qualitative analysis, the developed investigation strategy provides sufficient resolution. If one wants to perform this with a high-resolution setup without intensity issues in order to enhance the sensitivity and precision for data analysis, one would then use the tool of choice: a synchrotron source. Nevertheless, the highlighted qualitative interpretation of in-situ diffraction- next to electrochemistry data in our laboratory source experiment with a simple home build cell is an

impressive example for gaining basic insights into a reaction. All prior information (phases, intensity, time scale,...) could be gained in our easy and multi-purpose in-situ electrochemistry cell and be used for further measurement planning and starting quantitative analytics (peak shape, potential-2 θ dependencies, ...).

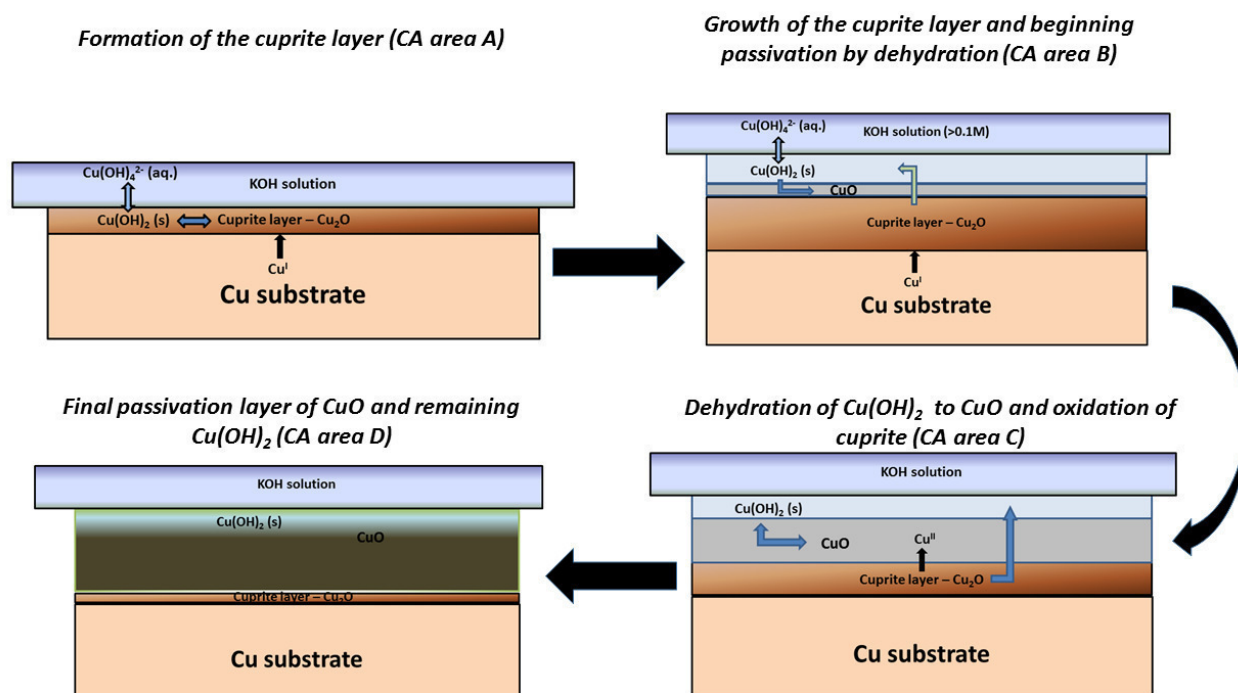


Fig.3.12: Graphical illustration of the assumed passivation layer formation by the proposed pathway.

3.5 Conclusion

The present work demonstrates the feasibility of in-situ electrochemical oxidation of polycrystalline copper in an alkaline solution with GIXRD. The combination of electrochemistry and integral structural characterization by GIXRD is powerful enough to monitor surface-near changes under reaction conditions. The ability of GIXRD to distinguish between bulk and surface-near regions facilitates its use in surface science.

The described considerations for the electrochemical cell render a common laboratory diffractometer into a powerful in-situ machine. The need to go to synchrotron sources for detailed and high resolution experiments is still an important step, nevertheless detailed prior insights could be already realised in a home laboratory. However, limitations arise due to the lower resolution and photon flux of the diffractometer as well as from the static measurement conditions. The static measurement conditions can be potentially overcome by implementing a special flow mode into the electrochemical cell.

The oxidation of copper in alkaline media (0.2M KOH) was chosen as a test reaction since the complexity of these reactions highlights the importance of an in-situ study of its mechanism. Combined CV, CA and GIXRD measurements revealed the stepwise formation of copper oxide films on the surface. The CV of the pristine copper electrode is in agreement with published reports. In-situ GIXRD experiments indicate the multi-step passivation of copper. The first step in the oxidation of Cu to Cu_2O could not have been detected without the use of an in-situ setup. The GIXRD results prove that a Cu_2O intermediate has to be considered in the passivation mechanism of Cu.

The results demonstrate the synergistic power of the combination of electrochemical setups with integral surface sensitive GIXRD measurements. It is expected that this combination can potentially be extended to investigate more complex surface modifications of electrodes during electrocatalysis and reactions such as oxygen evolution reaction.

3.6 References:

1. J. Zegenhagen, F. U. Renner, A. Reitzle, T. L. Lee, S. Warren, A. Stierle, H. Dosch, G. Scherb, B. O. Fimland, D. M. Kolb, *Surf. Sci.* 573 (2004) 67-79
2. A. Nikolaenko, M. Kovalchuk, Yu. Shilin, A. Ermolaev, S. Bobrovski, G. Chaplygin, *Physica B* 198 (1994) 228-230
3. F. Renner, Y. Gründer, J. Zegenhagen, *Rev. Sci. Instr.* 78 (2007), 1-8
4. A. Russell, S. Maniguet, R. Mathew, J. Yao, M. Roberts, D. Thompsett, *J. Power Sources* 96 (2001) 226-232
5. M. Samant, M. Toney, G. Borges, L. Blum, O. Melroy, *Surf. Sci.* 193 (1988), 29-36
6. U. Pietsch, *Current Science* 78, (2000), 1484-1495
7. H. Göbel, M. Schuster, *J. Appl. Phys.* 28, 1995, 270-275
8. W. Marra, P. Eisenberger, A. Cho, *J. Appl. Phys.* 50 (1979) 6827
9. K. Robinson, W. O'Grady, *Faraday Discuss.* 95 (1993), 55-64
10. O. Melroy, M. Toney, G. Borges, M. Samant, J. Kortright, P. Ross, L. Blum, *Phys. Rev. B*, 38 (1988), 10962-10965
11. Z. Stojek, "The electrical Double Layer and its Structure" in *Electroanalytical Methods – Experiments and applications*, Springer Verlag, 2002,
12. H. Keller, M. Saracino, H. Nguyen, P. Broekmann, *Phys. Rev. B* 82 (2010) 245425-1
13. O. M. Magnussen, *Chem. Rev.* 102 (2002), 679-725
14. C. Melendres, H. You, V. Maroni, Z. Nagy, W. Yun, *J. Electroanal. Chem.* 297 (1991), 549-555
15. E. Muller, *Z. Elektrochem.* 133 (1907), 13
16. B. N. Roy, T. Wright, *Cryst. Res. Technol.* 31 (1996), 1039-1044
17. H. Ma, S. Chen, S. Zhao, X. Liu, D. Li; *J. Electrochem. Soc.* 148 (2001) 482-488
18. S. Huemann, N. Hai, P. Broekmann, Klaus Wandelt, *J. Phys. Chem. B*, 110 (2006), 24955-24963
19. M. Vogt, R. Nichols, O. Magnussen, R. Behm, *J. Phys. Chem. B*, 102 (1998), 5859-5865
20. D. Parker et al., High temperature polymers, in „Ullmanns encyclopedia of industrial chemistry“, DOI: 10.1002/14356007.a21_449.pub3, 2012
21. A. Arun, C. Gupta, R. Howe, *ECS Solid State Letters* 4 (2015), P67-P71
22. P. Fewster, *Critical reviews in solid state and Material science* 22 (1997), 69-110
23. <https://www.nist.gov/pml/x-ray-mass-attenuation-coefficients>, checked: 03.10.2016, 19:56
24. M. Angelone, A. Esposito, A. Gentile, *Rad. Phys. & Chem.* 61 (2001) 547-548, **recalc. for Cu**
25. M. Toney, S. Brennan, *Phys. Rev. B*, 39 (1989), 7963-7966
26. G. Lim, W. Parrish, C. Ortiz, M. Belloto, M. Hart, *J. Mater. Res.* 2 (1987) 471-477
27. C. Pyun, S. Park, *J. Electrochem. Soc.* 133 (1986) 2024-2030
28. H. Strehblow, B. Titze, *Electrochimica Acta*, 25 (1980), 839-850
29. B. Miller, *J. Electrochem. Soc.* 116 (1969), 1675-1680
30. J.-B. He, D.-L. Lu, G.-P. Jin, *Appl. Surf. Sci.* 253 (2006), 689-697
31. J. Ambrose, R. Barradas, D. Shoesmith, *Electroanal. Chem. & Interfac. Electrochem.* 47 (1973) 47-64
32. J. Droog, C. Alderliesten, P. Alderliesten, G. Bootsma, *J. Electroanal. Chem.* 111 (1980) 61-70
33. M. Dignam, D. Gibbs, *Can. J. Chem.*, 48 (1969) 1244
34. D. Shoesmith, S. Sunder, M. Bailey, G. Wallace, F. Stanchell, *J. Electroanal. Chem.* 143 (1983) 153-165
35. S. Fletcher, R. G. Barradas, J. D. Porter, *J. Electrochem. Soc.* 125 (1978), 1960-1965
36. S. Dong, Y. Xie, G. Cheng, *Electrochimica Acta* 37 (1992), 17-22

37. S. Abd el Haleem, Badr Ateya, J. Electroanal. Chem. 117 (1981) 61-70
38. W.Zhank, X. Wen, S.Yang, Inorg. Chem 42 (2003), 5005-5014
39. D.Shoesmith, T.Rummery, D.Owen, W.Lee, J.Electrochem.Soc. 123 (1976), 790-799
40. S.Giri, A.Sankar, S.Mahajami, A.K.Suresh, ECS Transactions 75 (2017), 19-31

Chapter 4: Surface morphology change of iridium thin films during oxygen evolution reaction (OER) studied by X-ray reflectometry and Diffuse X-ray scattering

4.1 Abstract

The present work describes a dedicated approach to monitor, on a nm scale, electrochemically induced surface morphology changes in thin iridium films under oxygen evolution reaction conditions. The combination of electrochemistry with surface sensitive scattering by means of X-ray reflectometry (XRR), Grazing Incidence X-ray diffraction (GIXRD), as well as diffuse scattering measurements (XRDS) enables the study of potential induced effects on thin films in a non-destructive and direct way. X-ray Photoelectron Spectroscopy (XPS) and Electron Microscopy (EM) were used as complementary tools to assist the interpretation of the scattering data and to characterize the morphology and composition of the films. Two differently prepared thin films of Ir with intrinsic differences in their layer morphology were investigated under identical electrochemical treatment. Iridium deposited by sputter coating is characterized by a much rougher and porous film when compared to the more dense-packed and ordered iridium layer produced by e-beam evaporation. After electrochemical treatment by Cyclic voltammetry (CV) and Chronoamperometry (CA), the fractal parameters, for example, lateral correlation length as well the mass density of the iridium films, exhibited significant differences. Collected XRDS data were analyzed in detail over the depth of the iridium films and revealed its dimensional instability. Transmission electron microscopy and scanning electron microscopy confirmed the observed morphology changes of the iridium layer. Based on these observations, a possible growth mechanism was derived. Overall, we demonstrate that our developed investigation strategy, based on X-ray reflectometry, accompanied by GIXRD and XRDS is suitable for investigating electrochemical induced morphology changes on smooth electrode surfaces.

4.2 Introduction

Iridium and its oxides have received remarkable interest in research and industry over the last decades⁽¹⁾. The principle reason for this relates to the fact that iridium surface oxides (produced by, for example, CV) show promising performance as a catalyst for efficient electrochemical water splitting^(2,3). Their unique stability and activity under ambient temperature and in acidic media is shadowed by the sluggish oxygen evolution reaction (OER)⁽⁴⁾. Appearing to be an efficient catalyst, the high activity in producing oxygen with one of the lowest overpotentials makes it very worthwhile to look at them for mechanistic studies^(5,6). Once understood, the design of prospective water splitting catalysts can be done to replace the extraordinarily expensive and rare noble metal iridium. In addition, the economic viability of hydrogen production can therefore improve. Although the water splitting reaction itself is a rather “old” reaction and has been known since the 18th century, it is still not completely understood⁽⁷⁾. The OER taking part on the anode side involves the transfer of four protons as well four electrons⁽⁵⁾. The presently proposed mechanistic steps of the oxygen formation are based on either of two theories. The first, as postulated by Bockris⁽⁸⁾ and Damjanovic⁽⁵⁾, is via a direct recombination of O-atoms at the surface. The second, based on the DFT calculation of Nørskov⁽⁹⁾ and co-workers, is over a peroxo intermediate. Thus, the reaction network was found

already in the early purely electrochemical investigations to be quite complex due to unique behavior, for example, in cyclic voltammetry (growing OER-active oxide).

A variety of analytical methods were used to investigate the iridium surface oxide layer that is associated with the active phase. Electron microscopy⁽¹⁰⁾, X-ray photoelectron spectroscopy⁽¹¹⁾, X-ray diffraction, ellipsometry⁽¹²⁾ as well Raman-spectroscopy provided indirect insight into the composition and structure of the water splitting catalyst. Hence, direct information about the state of the active catalyst is largely absent due to challenges related to in-situ observations of the working electrode. Recent XPS and NEXAFS measurements have revealed clues about an active oxygen species on cycled iridium surfaces that is related to catalytic OER activity⁽¹³⁾. A spectacular effect of iridium during cyclic voltammetry is its known electrochromism (colour change depending on the potential regime). Depending on whether the applied potential is below or above 1 V (vs. SHE), the colour of the surface changes due to an oxidative step. This effect is discussed in literature and is related to the formation of an iridium oxo-hydroxo layer and proton exchange during hydration^(14,15,16). Currently it is an accepted finding within the electrochemistry community that the oxo-hydroxo layer formed on Ir surfaces is a better catalyst than that of pure iridium⁽¹⁷⁾. Its formation was already found in early investigations to occur through continuous potential cycling in a certain potential range⁽¹⁸⁾. Since this is supposed to be the active phase, we are especially interested in the formation of this surface layer on the metal substrate. Many of the past studies have mainly focused on the characterization of the formed surface oxide film. The transformation of the metallic iridium into the catalytically active phase, by means of studying the Ir metal degradation, has received less attention so far. From previous studies it is known that the formed surface layer exhibits no long range order and therefore becomes difficult to observe by methods such as X-ray diffraction⁽¹⁰⁾. Considering the fact that iridium belongs to the group of refractory metals, the question arises about how the oxidation of iridium takes place during electrochemical activation. Refractory metals generally exhibit a high resistance to heat and wear, and are known to be mostly inert against acids due to the formation of a stable surface oxide^(19,20). Since a stable oxide is most likely not very active, the question arises on the pathway and structural response during electrochemical formation of the active surface oxide.

In the present work we would like to follow the attempt made by Otten and Visscher^(12,18) and investigate the morphological changes of a thin Ir film induced by OER conditions using X-ray reflectometry. Accompanying Grazing Incidence X-ray Diffraction, as well as X-ray diffuse scattering measurements, are used to extend the surface characterization in terms of morphological parameters and contributions from roughness. In addition, we attempt to demonstrate the influence of surface consistency and the evolution of inhomogeneity (driven by potential cycling) on the electrochemical performance of iridium thin films. The electrochemically induced changes are expected to influence the surface morphology significantly which then lead to observable changes in specular contributions of the scattering signal. For comparison, two differently prepared thin Ir films are investigated to demonstrate the influence of the initial Ir film deposition and the associated growth mechanisms on its electrochemical activity. The microstructure of these thin films also plays also an important role in understanding their physical, optical and mechanical properties⁽²¹⁾. This study shall also demonstrate the difficulty of comparing results between differently prepared samples and the necessity of knowing the entire “curriculum vitae” of each sample. This latter attempt focuses on the great importance of the combination of *local* and *integral* methods. To analyze such complex reaction pathways always necessitates the application of various methods and perspectives.

4.3 Experimental:

The thin films were prepared on a Silicon (1 0 0) wafer after having been cleaned in an ultrasonic bath with isopropanol for 10 min and dried in a nitrogen flow. The wafers were broken into approximately 1.8 x 1.8 cm pieces for mounting in the holder of the deposition coater. **Sputter coater:** Ir films were deposited on silicon (1 0 0) wafers from metallic targets (Ir 99.99 %, Elektronen-Optik-Service GmbH) in 0.1 mbar Ar at plasma current of 40 mA using a Cressington 208HR sputter coater and a deposition time of 60s. **E-beam evaporation:** Ir films were deposited on silicon (1 0 0) wafers by electron-beam evaporation from a metal melt at room temperature. A Tungsten crucible was used to melt the Ir foil (99.99 % purity, GoodFellow). The base pressure of the chamber was 8.10E^{-10} mbar. However, the desired thickness could not be achieved. The high melting point of iridium and low evaporation rate set a limit to the obtainable thickness in our e-beam sputter device. Therefore, only a thickness of 5 nm was achieved. **Electrochemistry:** was performed in 0.1M H_2SO_4 (ultrapure Merck) and a three electrode glass cell (Cyclovoltammetry-setup, BioLogic potentiostat) was used. Purging with nitrogen during reaction was done. Clamp holders were used to mount the sample in the electrochemical cell and to contact the Ir film. A Pt wire and a saturated calomel electrode (SCE) were used as counter electrode and reference electrode, respectively. The electrochemical procedure was chosen as follows. The samples were cycled under constant scan speed of 20 mV/s for 24 cycles. Afterwards the potential was held for 1 h at 1.1 V (vs. SCE) on the onset of the OER region in the anodic regime to equilibrate for the desired OER- and oxidation conditions and growth of the oxide layer. This procedure is similar to the one used for continuous cyclic voltammetry by Otten⁽¹²⁾. Since higher potentials (>1.3 V vs. RHE) give rise to the extensive formation of O_2 bubbles which can burst the thin film quickly and lead to detachment, milder oxidation conditions were chosen. For simplification, the investigated samples were labelled according to the following abbreviations:

iridium deposited by sputtering, as is	->	Sample A
iridium deposited by e-beam evaporation, as is	->	Sample B
iridium deposited by sputtering, oxidized	->	Sample C
iridium deposited by e-beam evaporation, oxidized	->	Sample D

X-ray photoelectron spectroscopy: XPS spectra were recorded using a laboratory XPS machine at room temperature, using non-monochromatized Al $\text{K}\alpha$ (1486.6 eV) excitation and a hemispherical analyzer (Phoibos 150, SPECS). The binding energy scale was calibrated by the standard Au4f(7/2) and Cu2p(3/2) procedure. **Scanning electron microscopy:** was performed on a Helios NanoLab G3 UC, and a Hitachi S4800 instrument. EDX spectra and elemental maps were acquired with a Bruker XFlash energy dispersive X-ray detector (EDX). **Transmission electron microscopy:** a FEI Talos F200X equipped with a SuperX EDX system was used for TEM and STEM imaging as well as acquiring EDX line-scans. Cross-section samples for TEM were prepared by mechanical polishing and subsequent ion-milling using a GATAN PIPS. **X-ray reflectivity and diffraction:** measurements were performed on a Bruker D8 Advance (Da Vinci design with LynxEye detector, Cu radiation), equipped with a Göbel mirror and eulerian cradle. The measurement range was chosen between 0.1 to 10° 2θ with a step size of 0.005° and counting time of 1s, with a double slit assembly on the secondary beam path to avoid background scattering. Diffuse scattering was measured by rocking curves at a chosen 2θ position on the reflectivity curve to gain depth resolved parameter evolution (scan range: $0-2\theta$). GIXRD measurements were performed at the critical angle of each sample and done between 10 and

65° 2Theta with step size of 0.02° and counting times of 2s before and 10s after reaction (higher counting time was needed due to the poor diffraction signal with 2s counting time). A 0.2° soller was used instead of the double slit assembly on the secondary beam path for GIXRD. XRR and XRDS were analyzed using DIFFRAC.Leptos (V7.8 Bruker AXS)⁽²²⁾. For a detailed description of the methods and algorithms used for XRR and XRDS data evaluation, please refer to chapter 2. The diffraction peaks were analyzed by full pattern fitting using TOPAS software. The peak positions were coupled to represent a common lattice parameter which was refined together with a zero error (which also includes the refraction shift).

The original state of the freshly prepared electrodes was measured for each method before the electrochemical treatment and will be discussed in comparison with each oxidation result.

4.4 RESULTS AND DISCUSSION

4.4.1 Electrochemical activity

The growth of an Ir-oxide surface layer is known to be observable by continuous potential cycling (growing peak area at ~+1.0V vs. SHE) from already early electrochemical works. Otten⁽¹²⁾ reported the growth to be dependent on oxidative as well as reductive environment. Therefore the attack appears to happen layer by layer. This statement opens the question of oxidation behaviour of different intrinsic layer morphologies. Porosity, layer density and homogeneity are crucial parameters that determine the electrochemical behaviour of thin layer surfaces⁽²³⁾. The differently prepared electrodes were exposed to identical electrochemical treatment in order to enable comparison. Fig.4.1a shows the cyclovoltammogram of sample A recorded at three different scan-speeds. As can be seen, characteristic features due to iridium are largely missing in the cyclovoltammogram and do not appear at high scan speeds (see chapter 1 for a comparison to a defined Ir CV). At speeds lower than approximately 5 mV/s the CV curve becomes more structured. This influence of the scan speed may be due to various reasons. The broad double layer regime indicates a higher charge capacity, which leads to changed adsorption behaviour. Since the curve with a scan speed of 20 mV/s exhibits the worst resolved shape, one can conclude that at higher scan speeds the reaction rate is limited by the diffusion of the anions at the surface. With a higher scan speed the electron transfer inside the layer becomes very fast and hence the double layer capacity increases. The slower the scan speed gets, the more time the counter ions have to diffuse away. This finding is clearly seen in Fig.4.1. Another contribution might be the intrinsic resistance of thin metal films⁽²⁴⁾. Film thickness and surface roughness are known to strongly influence the film's resistance. They are known to have higher resistance values than corresponding bulk material. It depends on their higher defect density (compared to the film volume) within the films, as well as on the deposition technique used (e.g. a less dense film with higher resistivity can be observed). One more important influence on the less structured cyclovoltammograms is the likely arising potential difference within the double layer formed on such thin films⁽²⁵⁾. This strongly influences its kinetic behaviour and enhances or hinders the reaction and can also be further influenced by covered and uncovered parts of the electrode surface. Sulfate anions on iridium surfaces will not always absorb the same way and through resistivity can local charge differences arise and hinder oxidation taking part homogeneously. This finding is also reflected in the later paragraphs (e.g. XPS-results) and may explain the differences between found morphology and electronic structure. The CV of the e-beam evaporation prepared sample exhibits a slightly different look. A scan speed of 20 mV/s gives already

a partially structured CV curve which, in contrast, is not the case for the sputtered sample. A broadened double layer regime is also visible at sample B, indicating an increased charge capacity. This structured CV gives a clear hint as to the much better defined layer formed by e-beam evaporation. It seems that the film is more continuous as well as homogeneous over the entire sample surface when compared to sample A, although it is much thinner (thickness). Therefore, these factors give an explanation for the better CV curve; additionally mirrored by a defined hydrogen adsorption area (0 to -0.3 V).

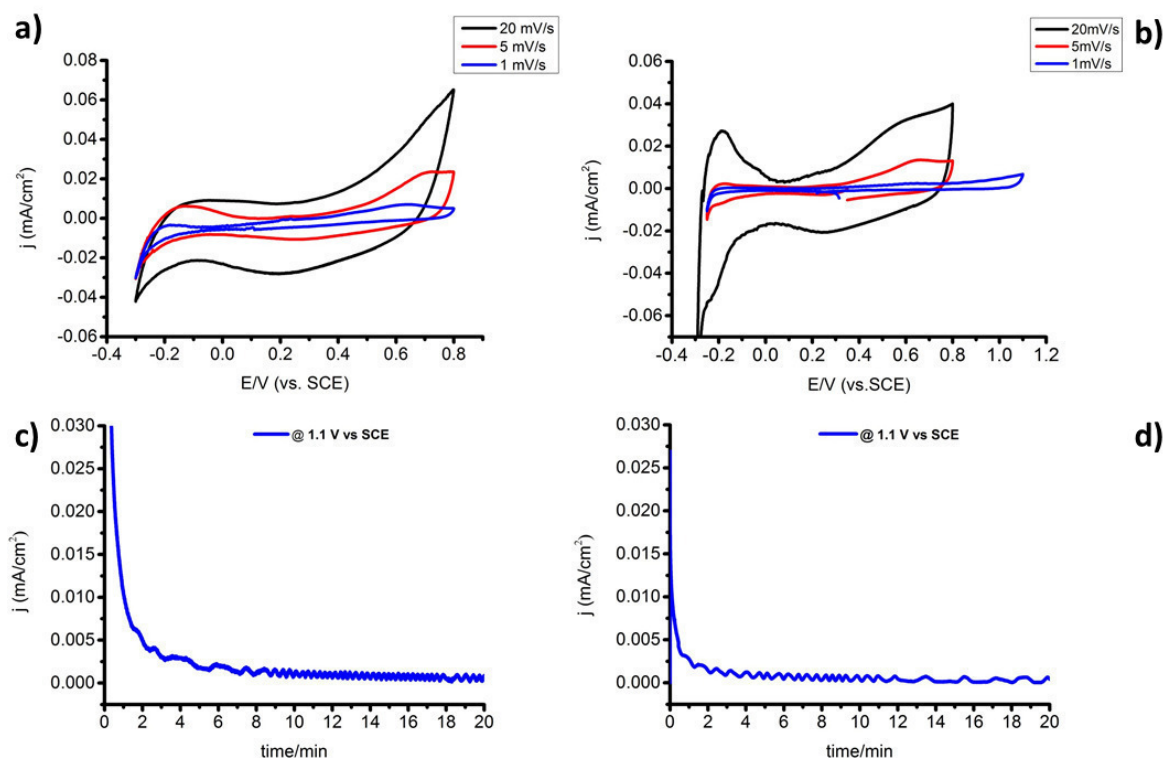


Fig.4.1: a) Cyclovoltamogram of sample A at different scan speed. b) Cyclovoltamogram of sample B at different scan speed. c) Chronoamperometry of sample C. d) Chronoamperometry of sample D

After 24 activation cycles, both samples are held at 1.1 V (vs. SCE, OER onset) for one hour for chronoamperometry. This test should demonstrate possible long term activity of the two oxidized samples. Fig.4.1c and d show the plotted CA curves. The CA graphs exhibit small fluctuations which are defined as measurement artefacts caused by the potentiostat. The deactivation of samples A and B appears to be obviously different: sample B degrades approximately twice as fast as sample A. Intensity drops very quickly after the stop at 1.1 V which indicates an immediate change in conductivity (e.g. starting of passivation or formation of an undesired by-product). Another reason might be the permanent adsorption (sticking) of oxidation products of iridium or sulfate (since the chosen potential is far into the OER regime) on the electrode surface. The longer activity of sample A likely originates from the surface morphology and reflects its higher surface area, which is probably transformed into a iridium-oxo-hydroxo layer in small areas. The more dense packed film of sample B appears, due to its structural inflexibility, to be less active, although it was more conductive in potential cycling. Referring to the influences on the CV curves discussed in the last paragraph, this finding is in agreement and supports the assumption of less ordered surfaces being the better choice. It simply takes longer to introduce defects into the iridium surface of sample B and to destroy its dense packing and become more flexible for further oxidation. The obtained morphology and fractal

parameters which describe these changes are also depth resolved, before and after electrochemistry, and will be discussed in following sections in detail. Both sample surfaces have a slightly greyish-blue blurry colour after oxidation. This phenomenon has already been documented⁽¹⁴⁾.

4.4.2 XRR & EM results

X-ray reflectometry (XRR) is one out of just a few integral methods with which one can determine morphological changes in a non-destructive way and on a nm-scale. Therefore XRR has become an accurate and well established method for the characterisation of thin layers. The extractable parameters are: layer thickness, roughness and electron density. These are obtained via a symmetric scan at very low incidence and exit angles (grazing angles) and evaluated via LEPTOS software which is based on the Parratt recursive algorithm⁽²⁶⁾. The fit model was assumed as a single layer (Nevot-Croce⁽²⁷⁾) of iridium on a SiO_x/Si substrate (Si 100 wafer). Substrate values were determined independently on a blank sample and kept as starting parameter for every sample fit curve (SiO_x, thickness: 2.5 +/- 0.1 nm; roughness: 0.3 +/- 0.05 nm; density: 2.4 +/- 0.3 g/cm³). χ^2 values (goodness of fit) for each fit curve are given in the summary of obtained layer parameters in Tab.4.1. The measured XRR curves and results of the XRR analysis of samples A to D are shown in Fig.4.2.

The higher electrochemical activity of sample A as compared to sample B is also mirrored in the parameters obtained by XRR. From the chemical point of view, the most interesting changes are the loss in density and surface roughening. The transformation of sample A into C is accompanied by a decreasing layer thickness as well as an increasing surface roughness. The value of the thickness loss is almost identical to the roughness gain, so one can assume this is no true loss in thickness. The increase in surface roughness from sample A to C originates likely from the crack-like surface structure (as seen in the SEM images Fig. 4.4). The TEM image (Fig.4.3) of sample A displays the pillar-like growth of iridium on the silicon wafer. One can clearly see the discontinuity of the iridium layer prepared by sputter coating. In this arrangement of nanoparticles within one pillar, loosely bound surface-near particles might become quickly and easily oxidized and are probably washed away. This would on the one hand explain the loss in layer thickness and on the other hand the decreasing mass density of the iridium. These parameters give another hint as to the cause of the widened cracks and inhomogeneous penetration of the beam into the layer. The roughening of the Ir surface leads to the decrease of specular reflected intensity (the “knee” seen in Fig.4.2 left, green curve) and the interface roughening is reflected by the damping of the Kiessig fringes⁽²⁸⁾. As seen in the SEM images shown in Fig.4.4, only larger cracks appear on the surface of sample C. The channel-like cracks of the layer allow the electrolyte to also reach the substrate and react between the pillars of iridium and as well account for a higher accessible surface area than in sample B. They are also responsible for the higher flexibility of the iridium film and likely tend to dampen the volume expansion of the film during oxidation and gas evolution. Changes on the iridium surface layer are accompanied by a slight change on the underlying SiO_x interface; it becomes obviously affected by electrochemical treatment. Changes in interface roughness are likely due to the electrolyte contacting the interface through the cracks. Remaining electrolyte or gas evolution on the interface (Ir-side) could influence the determination of this parameter. The aforementioned surface cracks also lead to the lower observed critical angle of iridium; it is affected by roughness and porosity (“dilution with air”), reflecting approximately 80% of its nominal value^(29,30) of 0.62°. Hence the critical angle does not allow any conclusion in the present case for an occurring oxidation. In corroboration with the electrochemical data, CV and CA, we can conclude that the presence of larger numbers of nucleation areas (rougher surface) and less ordered surface morphology (low ξ as seen later, and

mass density) are the key features for higher activity in the OER reaction (both reflected by the roughening and the decrease in mass density).

The less active but much higher ordered samples B and D exhibit a different look under XRR. Here, the effects are not nearly as visible when compared to A and C. Mass density, layer thickness and roughness remain almost constant within the error margins. Transforming sample B into D gives a different result according to its intrinsically different layer morphology. This extremely dense and continuous film cannot be oxidized so easily under the chosen treatment method and remains almost unchanged. Due to a lack of flexibility, low number of present defects and the likelihood of residual stress, this transformation takes much longer to attain the same state than does sample C. Taking the SEM image of Fig. 4.4 into account, the result can be only seen at lower magnification. Sample D exhibits a breakup of the surface into large compartments and hence detaches more easily because of its residual stress and becomes less conductive over the entire sample surface. Interface roughness changes cannot be observed for the e-beam prepared samples. One of the most obvious differences in the sample with the sputtered Ir film is the much stronger absorption feature in the XRR of the e-beam deposited iridium layer. This effect is manifested by the absence of a sharp edge of total external reflection. Instead, it slowly decreases with increasing incidence angle. Strong absorption hints of a closely packed highly dense layer of iridium. The value of θ_c matches almost perfectly the nominal value of 0.62° . Due to this, even with a thickness of approximately 5 nm, the reflection interference between the substrate and the layer (electron density of Ir is approximately 10 times higher than for Si) becomes much stronger when compared to sputtering.

The obtained XRR data requires careful interpretation. Data quality for this highly dynamic system is not the best and not every parameter could be estimated with sufficient accuracy in order to determine the underlying physical/chemical processes. This is reflected by the size of the error margins. The number of contributions (electrolyte, completeness, homogeneity, potential range, conductivity, resistivity,...) to produce the desired oxidized state, are too numerous to be precisely controlled on a 10 and 5 nm layer. Therefore the obtained results by XRR always need to be taken with caution and not over-interpreted. The more complex and detailed depth resolved fractal parameters are discussed in the next section.

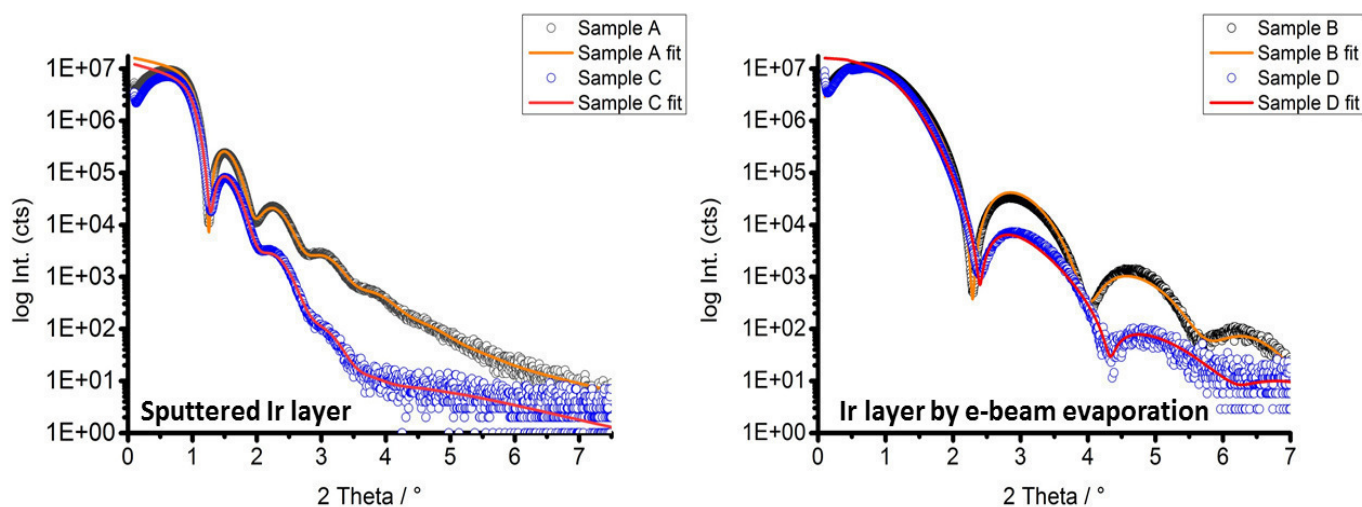


Fig.4.2 XRR data plots for all four samples (A to D)

Tab.4.1: Summary of the XRR evaluation of the 4 investigated samples

	layer	thickness (nm)	roughness (nm)	density (g/cm ³)	α_c (°)	χ^2
A	Ir	10.0 ± 0.1	1.1 ± 0.1	12.3 ± 0.2	0.48	0.028
	SiO _x	2.1 ± 0.1	0.5 ± 0.1	1.2 ± 0.2		
B	Ir	4.7 ± 0.1	0.5 ± 0.1	22.8 ± 1.3	0.60	0.020
	SiO _x	0.9 ± 0.2	0.7 ± 0.1	1.0 ± 0.6		
C	Ir	9.3 ± 0.1	1.7 ± 0.1	11.4 ± 0.1	0.47	0.030
	SiO _x	2.1 ± 0.3	1.0 ± 0.1	1.4 ± 0.3		
D	Ir	4.2 ± 0.6	0.4 ± 0.1	21.7 ± 3.2	0.60	0.059
	SiO _x	1.1 ± 2.0	0.6 ± 0.3	1.2 ± 9.1		

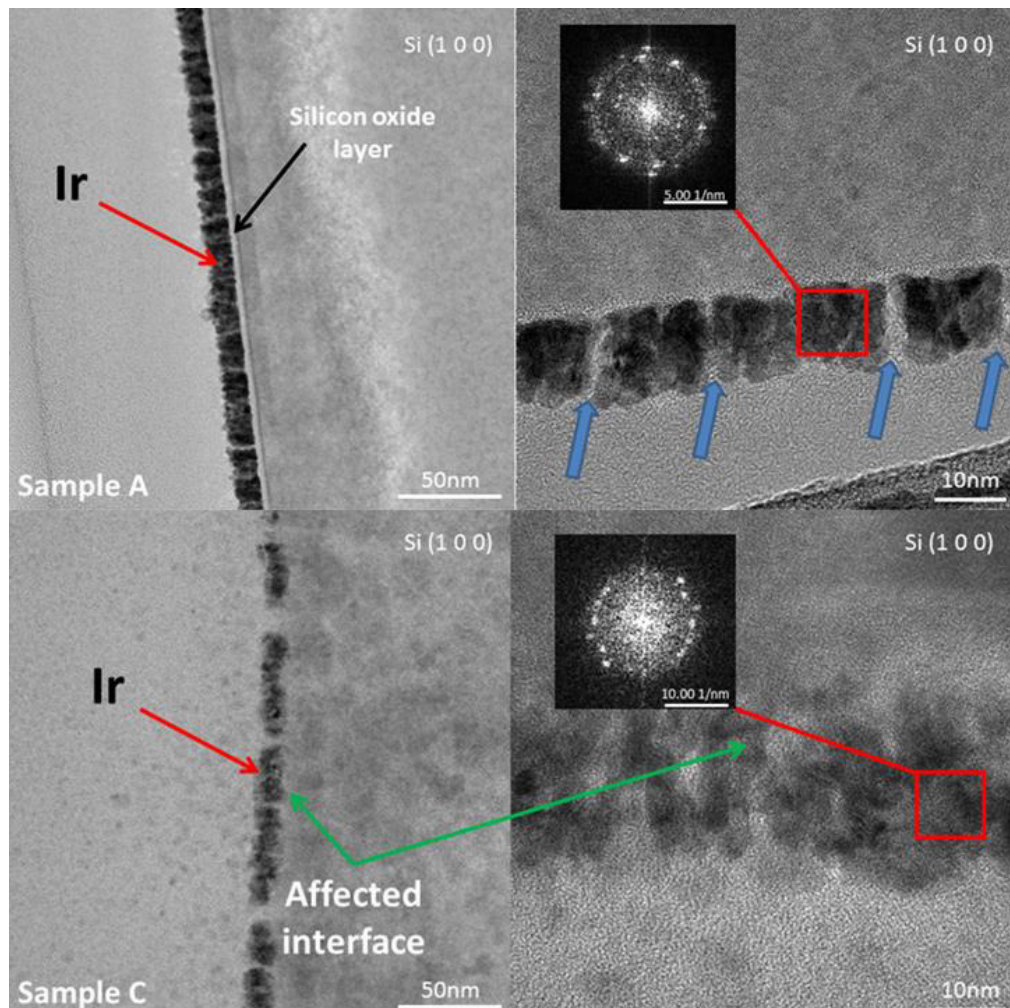


Fig.4.3 HR-TEM image of Sample A and C: left sides show the overview, right side a close up. The insets at right hand side display Fourier transformed electron diffraction pattern. The channels (blue arrows) between the iridium columns and the pillar-like growth of iridium on the substrate are visible. In the case of sample C, the channels are not clearly visible anymore, and the SiO_x-Ir interface is also strongly affected. The whole iridium layer gets after reaction also in TEM much more difficult to investigate compared to A.

The observed effect of roughening the interface is supported by the TEM images of cross-sections prepared from the samples before and after electrochemical testing (see Fig.4.3.). The TEM images of the as prepared films show that the Ir films grow in a columnar or pillar-like structure (dark line) with randomly appearing channels between the pillars. Individual pillars consist of defective crystalline domains. The thickness of the film is in agreement with the value extracted from the XRR fit. After electrochemistry, the morphology drastically changed for sample C. Incompleteness of the layer, as well the influence on the SiO_x/Si interface becomes obvious. The detached layer seen in the TEM image of sample C cannot exclusively be attributed to the electrochemical treatment. This gap maybe was widened during cross-section preparation as well. Some influence on the interface appearance was already visible by XRR (for a discussion see XRR data), which was measured before TEM. Cyclovoltammetry as “oxidizing” treatment for the activation of the iridium surface, is assumed to destroy the ordering of the iridium layer and to form an X-ray amorphous oxygen containing surface layer^(31,32). Electron diffraction reveals that the layer remains crystalline after oxidation, the appearing diffraction spots can in both cases be assigned as the 111 and 200 planes of the cubic Ir lattice (black insets in Fig.4.3). The GIXRD results shown in Fig. 4.8 also support this finding.

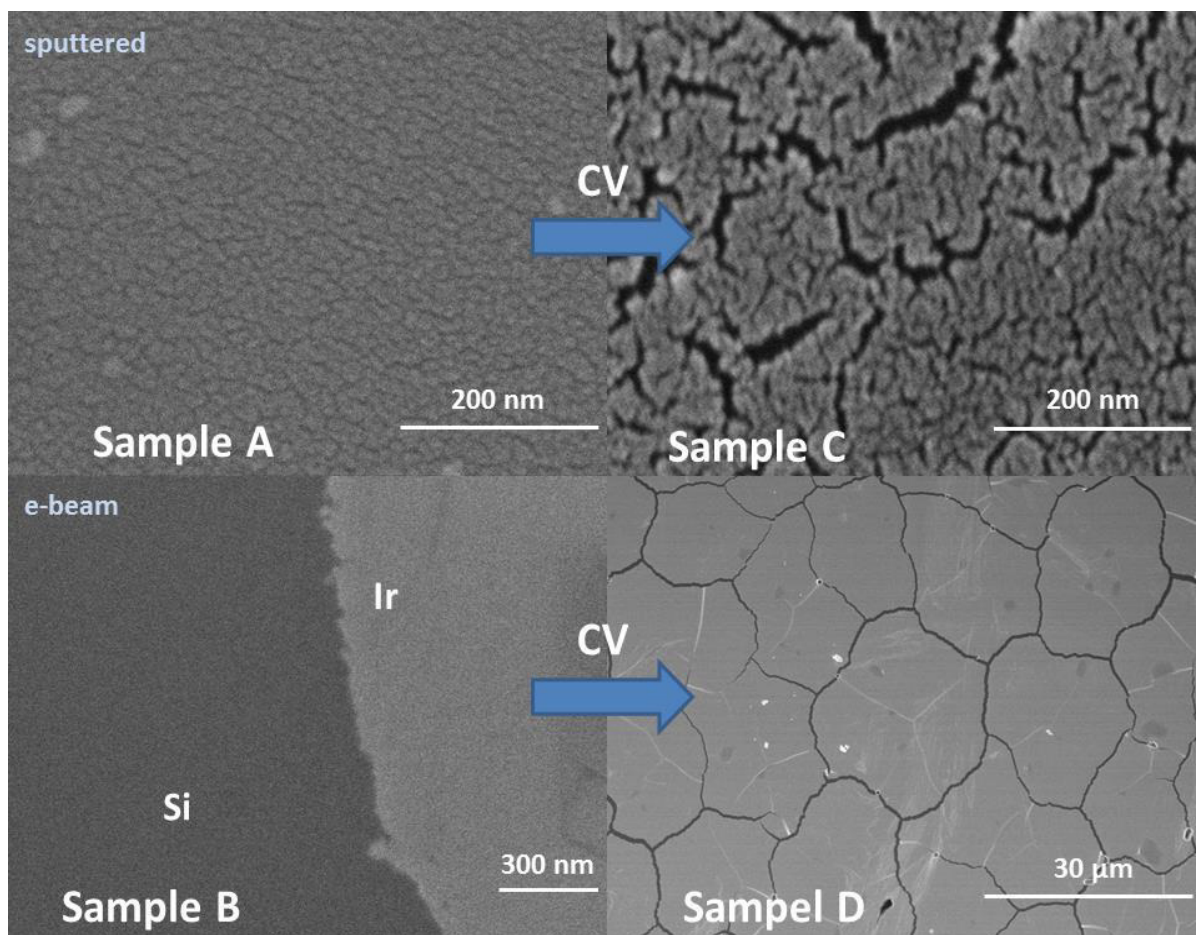


Fig.4.4: SEM images of the samples A to D. One notices the bigger cracks appearing at sample C after cyclic voltammetry. In contrast, the break-up of the surface on large scale shall be noticed in the case of e-beam evaporation prepared samples (30 μm scale)

By looking at the SEM images in Fig.4.4, one can see the higher homogeneity of the layer (absence of large surface cracks), as well the breakup of the layer after electrochemistry of samples B and D. One can notice that the higher magnification of the SEM image of sample D demonstrates the breakup of the layer. Electrochemically induced stress formation during the reductive and oxidative steps (cyclic voltammetry) leads to a detachment of the layer and forces it to break up in many islands of similar size and shape. This denser structure does not offer flexible channels as does the case of sputter deposition. Due to the higher layer density, more activation cycles are needed to increase the oxidation of this iridium surface. The obtained effects of the transformation from sample A to C are displayed in the upper part of Fig. 4.4 and are in good agreement with the above discussed results of sample C by XRR.

4.4.3 XRDS results

The finding of electrochemically induced roughening of the thin sputtered iridium film under OER conditions leads to the fundamental question of its stability in three dimensions for long term applications of this system. The thin coating as well as the absence of massive bulk iridium make our samples an adequate model system to study very near to surface changes. To gain additional parameters to quantify the dimensional instability (fractal changes) caused by electrochemistry, X-ray diffuse scattering measurements are applied. The basis of these measurements are the XRR curves recorded earlier. At various points along the 2θ scale, transverse rocking scans were performed⁽³³⁾. Ω -scans (rocking curves) represent a cut through the reciprocal space at constant 2θ (in other words: the sample is tilted around the specular reflection condition, see chapter 2). One of the most important details connected with these measurements is the corresponding penetration depth at each chosen 2θ . Rocking curves do not have linear penetration depth or a sigmoidal curve as in GID geometry (see Chapter 2). This is displayed in Fig.4.5.

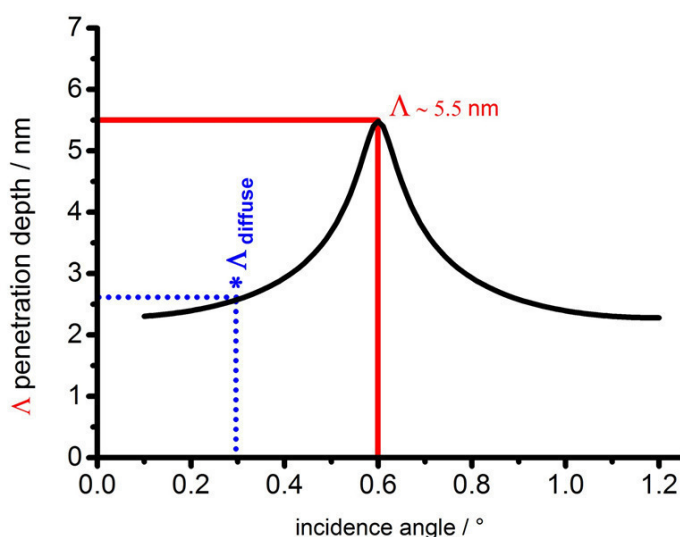


Fig.4.5: Calculated penetration depth of the rocking curve for $\alpha = \alpha_c$ for sample B. The red Λ represents the maximum penetration depth at $\alpha_i = \alpha_f$ (the specular range). Blue Λ here indicates exemplarily the penetrated depth at diffuse profiles (->Yoneda wings).

The penetration depth calculation is based on the samples' critical angle (δ) and absorption (β) as well on α_i and α_f , the incidence and exit angles respectively. This shape reflects the changing penetration depth during a rocking scan. If the incidence and exit angles are equal, the penetration becomes maximal due to it being in the specular range (red Λ in Fig. 4.5 at the peak maximum). This

is in many cases not directly representative for diffuse contributions since they are not likely to appear homogeneously along the entire penetrated depth. To account for their surface (interface) near character, the appearance of diffuse profile features (\rightarrow Yoneda wings) was chosen as a prerequisite for further analysis. For samples A and C this was only the case for 2θ values higher than 1.20° and for samples B and D for 2θ values higher than 1.80° . The position of the maximum (on the θ -scale) of the Yoneda wings (blue stars in Fig. 4.6) was determined and the corresponding depth (x-axis in the parameter plots in Fig. 4.7) estimated on each depth curve (as shown in Fig. 4.5, blue Λ_{diffuse}). One should notice that the angular scale used for Fig. 4.6. is defined relative to the specular angle, while Fig. 4.5 uses the absolute scale for the depth estimation. Fig. 4.7 shows the three parameters of each sample: surface roughness, lateral correlation length and mass density with corresponding error margins. Hurst values were left out due to their being almost constant and for simplification (plots can be found in Appendix 1). With this set of data a depth resolved analysis of parameter evolution can be realized. The refinement of the simulation curves was executed with LEPTOS software by using the semi-kinematic DWBA concept^(34,35). The parameters obtained from XRR were used as input; all four parameters were refined together. The sample model was assumed to be fractal and uncorrelated in the vertical direction, while the iridium surface was evaluated as single layer model only. Fig. 4.6 displays the measured XRDS curves with corresponding fits.

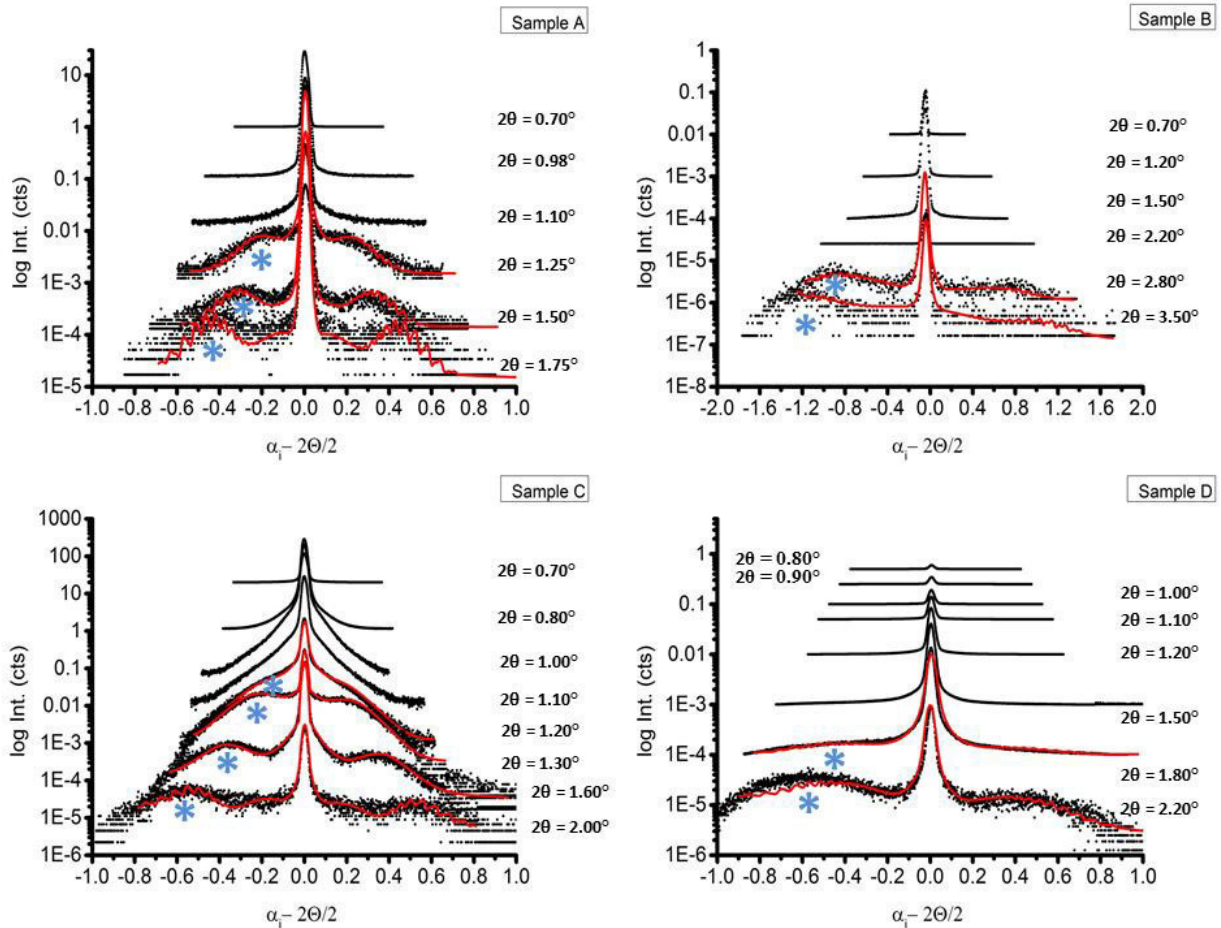


Fig. 4.6: XRDS curves of the four samples. The measurements were taken at various 2θ values shown next to the curve. Only curves which exhibit diffuse profiles (indicated with blue asterisk at the Yoneda wing maximum position) were further analysed by simulation (red curves). Please note the stacking of the curves in y for better visibility.

One important effect, which one can distinguish with the observed XRD curves, is roughening versus grading. As has been earlier pointed out, a higher degree of intensity scattered off-specular (diffuse) after reaction means the surface becomes rougher. From samples A to C we see an intensity increase in diffuse scattering, whereas for B and D it stays comparable. This gives a clear hint that A is truly roughened, whereas B appears graded (no sharp electron density change over depth between two layers) during the electrochemical treatment. The morphology change which the electrochemical treatment causes the two intrinsically different morphologies can also be found in the XRD parameters, which are plotted in Fig.4.7. Surface roughness of samples A and C is consistent with values obtained by XRR. The transformation of sample A into C leads to a clearly visible roughening of the layer, although in the very surface near region the trend seems to become inverted. Otten and Visscher observed a similar behaviour in oxidized iridium surfaces and found a smoothing by approximately 20-25%^(12,18).

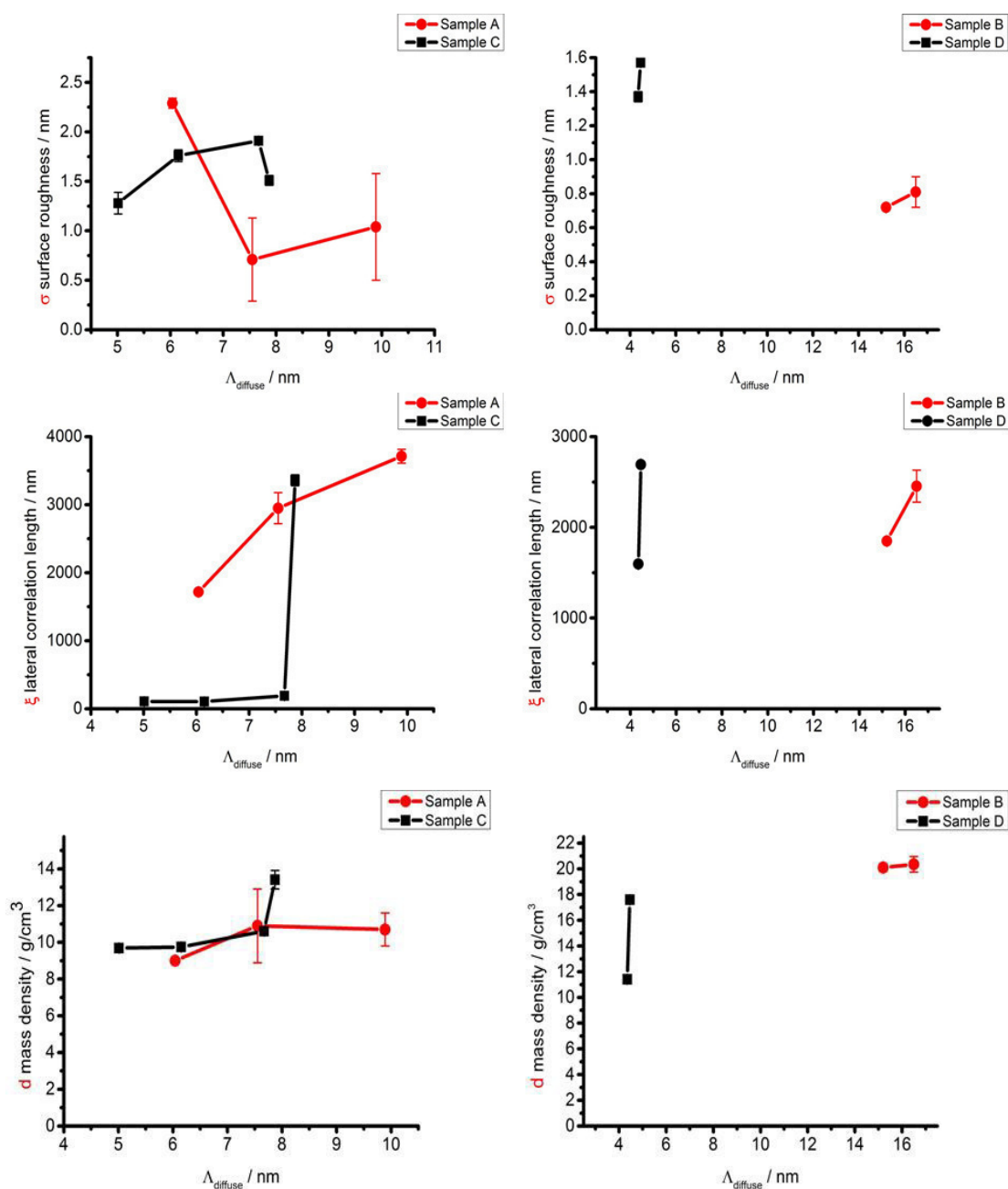


Fig.4.7: Obtained XRD parameter from Fig.4.6 plotted over corresponding penetration depth for samples A&C (left) and B&D (right).

Nevertheless, in our measurements their statements cannot be clearly supported. The integral trend over depth points towards higher roughness for the oxidized state. For samples B and D this trend can also be found but since only two data sets exhibit a diffuse profile, we do not interpret any evolution in the σ -parameter. Additionally, the appearance of diffuse profiles in the rocking curves only at high 2θ values in the case of sample B hampers the interpretation, since the thickness of the layer is significantly exceeded. A tentative interpretation of this observation could be that it indicates a strong correlation between the layer and the substrate. The lateral correlation lengths of samples B and D show no significant differences, with values between 1500 and 2700 nm depending upon the penetration depth. The lateral correlation length (ξ) describes the length scale on which the surface appears smooth at a corresponding roughness value. Only for sample D, the drastic jump between the two closely spaced measurement points could hint at the interface between Ir and SiO_x . This probably represents the transition between iridium and the SiO_x/Si interface (i.e. the higher correlation length is not representing the iridium but rather the native oxide and silicon wafer as it is almost exactly at the end of the iridium layer). In contrast to this morphology, the sputter coated samples A and C are significantly different in lateral correlation. ξ is found to be far smaller after oxidation than in the untreated case and this is over an almost constant length of approximately 7.5 nm. Cyclic voltammetry and chronoamperometry lead to an opening of the cracks, which has already been discussed for XRR results and supported by SEM data. The sharp edge of ξ found in Fig.4.6 for sample C stems from hitting the unaffected rest of the initial iridium layer. Lengths around 8 nm have been disturbed by electrochemistry and 2 nm remain in their original state (which was 10.0 nm). This finding proves the morphological trend already obtained by XRR: the surface cracks allow the oxidation to take place to a better degree than a fully closed and densely packed layer such as sample B. Oxidative treatment as postulated by Otten and Visscher is occurring in pits on the surface and, after about 80 cycles, around 3 nm of a smooth iridium foil are disturbed^(12,18). In our case we have no continuous surface and only 10 nm of a porous iridium deposition. The surface cracks allow the electrolyte to also reach the inner layer very easily and hence the observations in the present work are comparable to their work. Surface near ξ -values can be nicely compared with the SEM images in Fig.4.4 and are in good agreement within its order of magnitude. In the last row of Fig. 4.7 the mass density evolution over depth can be found. In case of e-beam evaporation the obtained densities of samples B and D point towards a slight affection during the electrochemical treatment. The jump between the two data points of sample D likely originates from the same reason as ξ ; the iridium layer is close to the surface of the SiO_x/Si interface and better ordered than in the higher levels of the layer. A corresponding jump from 12 to 18 g/cm³ is also observed in the mass density. Finally, the density evolution seen for samples A and C also fits into the line of already discussed reasons and findings. The overall change is not in the significant range and no special trend can be observed. However, if one considers the trend of ξ and σ , the increase of the last point of sample C towards a higher density and reflects the postulated model of the disturbed layer again. Roughness decreases, lateral correlation as well as mass density increases; this identifies a transition between a morphologically disturbed layer and its underlying origin leftover. All three parameters exhibit a change at the same depth of approximately 7.5 nm. Oxidative and reductive (stress induced) detachment, as well its discontinuity determines the behaviour of the sputter coated layer. Reactive areas on top as well as between the pillars take part in the oxidation and start to change the morphology of the layer. Since these are inhomogeneous conditions and obviously potential gradients (-> quick deactivation in the CA curve) within the cracks and discontinuous parts are present, the treatment fails to modify the surface homogeneously. Nevertheless, the disturbed morphology can be easily monitored, especially in the case of sputter coated samples. In contrast,

the inflexibility of a highly dense and closely packed layer could be demonstrated also to be unfavourable for OER conditions and for iridium as an electrode material.

All data obtained by XRDS are in good agreement with XRR data and demonstrate the complementary character of these methods. The sample model might need to become adapted to match both techniques more properly (e.g. extended to a two-layer model). XRR and XRDS should always be used together for surface morphology studies, since important knowledge might be missed by just using one of them. For example, the depth resolved analysis of the fractal parameters would not have been available, since XRR measures symmetrically ($\rightarrow \theta/2\theta$) and integrates over the whole surface and depth of the sample. The detection of the disturbed layer made this combination an outstanding choice for investigation of thin surface layers.

If one considers the values observed from XRDS and XRR, one can carefully derive a growth model for the two deposition methods. As the density in the sputtered samples is lower, as well as the lateral correlation length is decreasing towards the top of the layer, this can be seen as indicative of an island growth mechanism. The TEM picture (Fig.4.3) confirms this statement. In comparison, the e-beam evaporation prepared film shows a high density and high lateral correlation length over depth, pointing towards a layered growth mechanism, which in turn explains the differences in the electrochemical behaviour.

4.4.4 XPS results

To verify if an oxidation process took place and the iridium surface composition changed, laboratory XPS was measured on samples A to D. Ir 4f core level spectra as well O1s spectra were measured. Figure 4.8 a-d depicts the XPS comparison of the four samples. It can be seen that in the iridium 4f core spectra, the iridium peaks exhibit very slight changes (a shift towards higher binding energies) in the shape (a small shoulder on the left side of the Ir 4f spectra). These changes can be attributed to the likely arise of an additional component, probably Ir^{3+} species as discussed by Pfeifer et al.⁽¹³⁾. Nevertheless, the metallic character is still widely present (metallic Ir at 60.8 eV)^(36,37). In Fig. 4.8c, the reference spectra of IrO_2 (rutile-type) as well as metallic iridium are plotted for comparison to the untreated samples. If an Ir^{3+} species is considered as a contribution, the Ir double peaks are found at 62.3 and 65.3 eV⁽³⁸⁾ as seen in Fig.4.8 c. From the O1s spectra (O1s mainly at 531 eV) one can observe the presence of different contributions. Due to the chosen electrolyte, H_2SO_4 , the sulfate anion as well OH groups on the metal surface are contributors. A partial oxidation of iridium and lattice oxygen are two additional contributions which need to be considered. The partial loss of the iridium layer (caused by layer detachment and small gas evolution) also makes the underlying substrate visible ($\text{SiO}_x\text{-Si}$) in some areas. This also likely contributes to the O1s spectra. Molar ratios for the composition O/Ir were estimated (peak area and cross-section values)⁽³⁹⁾ for samples A and C (0.83 \rightarrow 1.52) and for samples B and D (0.66 \rightarrow 0.87). The strongest O1s signal from sample C also indicates the higher activity as already pointed out above. These changes can be regarded as small but they indicate that the surface changes due to the electrochemical treatment, for example, the break up and make the underlying Si-O layer visible (also in comparing the two preparation techniques). Nevertheless, the changes observed with XPS are not significant enough to postulate any successful oxidation of the thin iridium layer. In contrast, the changes observed in the morphology (XRR/XRDS) are stronger, as the physical state of the layer is already affected by a low number of cycles in cyclic voltammetry.

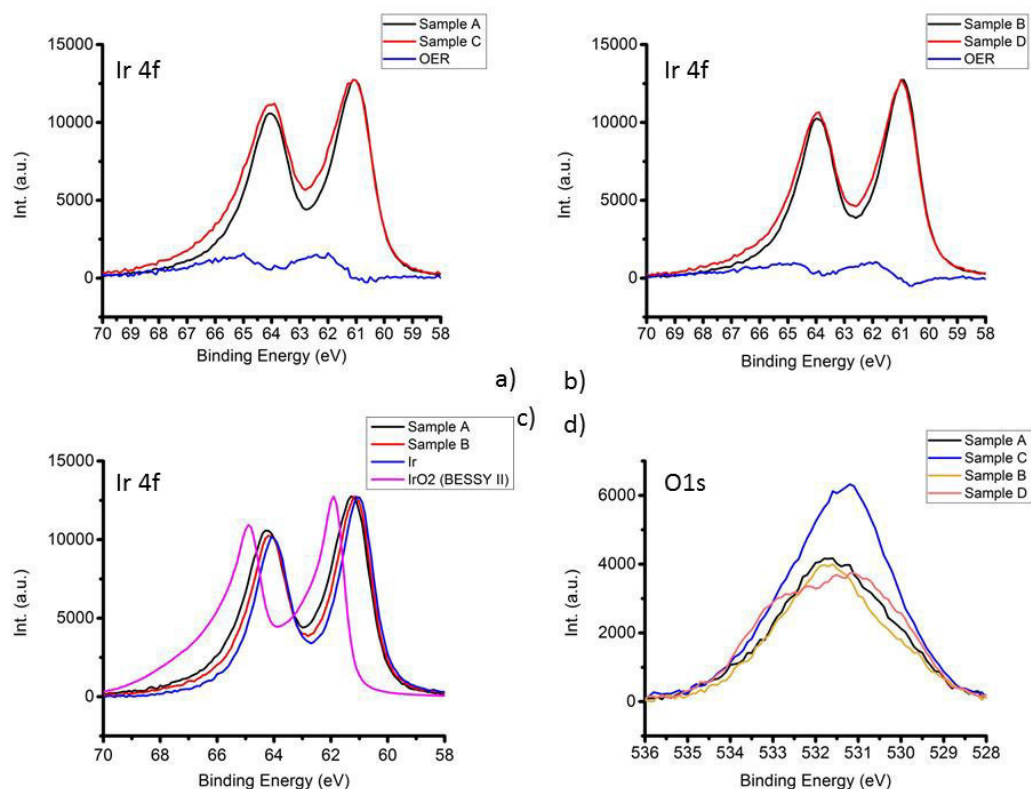


Fig.4.8: a) Ir4f XPS spectra of sample A and C (also differential curve) b) Ir4f XPS spectra of sample B and D (also differential curve) c) Ir4f spectra of A & B in comparison with metallic iridium and IrO₂ (rutile-type). d) O1s XPS spectra of A,B,C and D. The higher oxygen signal in sample C should be noticed.

4.4.5 GIXRD results

Finally, Grazing Incidence Diffraction (GIXRD) was applied. However, as a diffraction based method, further insights can be only expected in the case of the presence of crystalline phases. The higher active samples (A & C) were measured. The GIXRD results are plotted in Fig.4.9. The measurements before and after reaction were performed over the 2Theta range of the most intense iridium peaks, namely Ir 111 and 200. The rescaled plots (due to the bad intensity with the same counting time as the scan before treatment, the scan was repeated with 10 s/step and therefore appears smoother) show well the presence of the Ir peaks in addition to Si 311. As we chose a very low incidence angle of 0.55° (Ir: α_c : 0.62°, see chapter 2) the measurement is expected to be very surface sensitive. The appearance of Si 311 in the scan of sample C is a well-known reflection in this area, as it has GID-geometry. The sharp reflection next to the bump of Si 311 is a known diffraction phenomenon. The sharp peak corresponds to the Si 311 reflection from the edge of the wafer; the broad bump to the surface diffraction of Si 311. The appearance of the Si reflection is an indication of the partial loss of the iridium layer on the surface (edge) during the reaction, so the Silicon substrate begins to appear, which is not the case in the untreated sample. Older and recent studies show the behaviour of dissolution of metallic iridium^(40,41) to be more prominent than for iridium oxides. The intensity decrease of the Ir 111 reflection may either indicate a possible loss of iridium (dissolved or transformed into its oxo-hydroxo surface layer) or a degradation of the scattering coherency (defect formation). Since the FWHM of Ir 111 and 200 become larger after oxidation (smaller average crystallite domain sizes), underlying nano-crystalline contributions cannot be completely excluded.

The fit shown in Fig. 4.9 exhibits a discrepancy concerning the shape of the 200 reflection. While the effects look like a peak shift to higher angles combined with an additional overlapping peak on the lower angle side, it may also be interpreted as pronounced peak asymmetry of the 200 reflection. Similar effects are known from other fcc metals, especially in Cu and Ag catalyst samples, and are suspected to be caused by hexagonal stacking faults in the cubic lattice⁽⁴²⁾. Tab 4.2 summarizes the fit results. GIXRD proved the presence of crystalline Ir before and after the reaction. The data are in good agreement with TEM results and additionally allow the extraction of crystal lattice parameters. Although the data needs to be treated carefully, no result of a newly formed phase was found. Since the active hydrous iridium oxide layer is assumed to be amorphous, crystallographic hints can be only derived indirectly over the substrate on which it is grown, in this case metallic iridium.

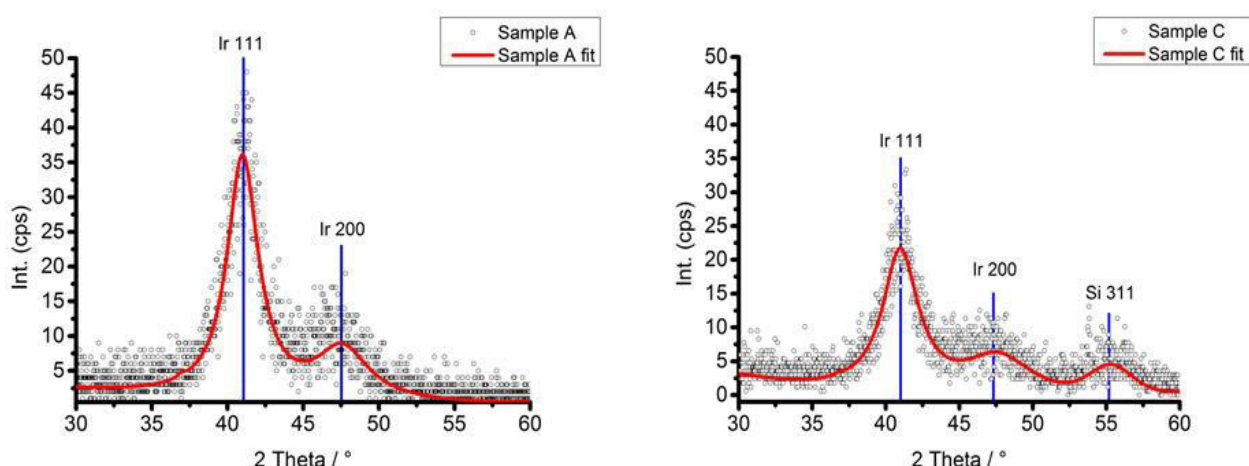


Fig.4.9: GIXRD pattern of sample A and C (PDF: Ir 06-0598, Si 27-1402)

Tab.4.2: obtained results from Rietveld refinement (TOPAS) of sample A and C

	a (Ir) (Å)	FWHM (Ir 111) (°)	FWHM (Ir 200) (°)	I(111)/I(200)
Sample A	3.869(7)	2.26(9)	3.9(3)	2.19
Sample C	3.845(9)	2.69(14)	5.2(4)	1.50

4.5 Conclusion

With this work we could demonstrate that the combination of X-ray reflectometry and X-ray diffuse scattering measurements provide a valuable tool for the investigation of electrochemically induced surface morphological changes. They can be used to gain insight into the nanostructure of the films and their changes through potential cycling. Furthermore, geometrical features such as correlation length and fractal parameters are accessible. They show, in three dimensions, the induced changes and the dimensional instability of the system under electrochemically induced transformation. Some limits and assumptions need to be considered for each type of sample, for example, completeness of layer, stress (reductive and oxidative stress, etc.) resistivity, etc. Additional applied methods, especially electron microscopy, helped to prove the results of XRR and XRDs. The crystallographic investigation by GIXRD is of additional value since the extraction of a lattice constant could be performed, even though no new phases were observed.

The strategy of choosing a thin film rather than massive bulk iridium relates this work as model study for real applications. In the design of electrodes, and due to the high costs of iridium, thin layers are favourable for water splitting. The results gained from this work lead to the conclusion that for the

design of iridium coated electrodes one needs to strongly consider the morphological state and the microstructure of iridium for optimum electrochemistry. Reaction sites, meaning the accessible iridium area of the surface, depends likely on the preparation method and the growth of the layer. In the case study of samples prepared by sputtering and e-beam evaporation, we could demonstrate that the less ordered sputter sample is more active. This could be connected to the morphology of the layer and demonstrates the kinetically different influence depending on, for example, defect density. The expected behaviour of the surfaces (roughening, lowering mass density, etc.) was proven by the examination of the fractal parameters in a detailed depth profile after the integral study by XRR. The degradation of ordered iridium (sputter coated samples) through cyclovoltammetry as a conditioning step for the desired OER-behaviour could be proven by its transformation into a thick disturbed layer (with different morphology parameters) on top of the remaining unaffected metal. Although there was no crystalline phase (e.g. oxide, ...) found on the surface, the breakdown of the scattering coherency reveals the impact of the morphological change on the crystallinity as well. SEM images showed the different surface morphologies of the samples: on the one hand growing surface cracks for sputtered samples, and on the other hand a complete breakup of the highly dense iridium film prepared by e-beam evaporation. Within this investigation, we could derive a growth mechanism for the two deposition types (island vs. layered growth). The HR-TEM image also showed the channel type structure of the grown iridium film by sputtering, as well the conserved crystallinity of the layer even after cycling. Pillars, visible in the HR-TEM image (Fig.4.3) of the iridium layer, explain the higher surface area on the reaction site as they reveal the interaction not only at the iridium surface as it's likely to happen, but also between the pillars. Therefore, one needs to consider not only the reaction of atoms at the surface, but also redox centres in the channels, which are connected to the surface and accessible for the electrolyte. The highly dense e-beam prepared film is inflexible, becomes too strained (due to lack of the channels) and breaks up into compartments to compensate for the applied stress due to the electrochemical treatment. Another reason for sample B's lower activity might be the lower defect density compared to sample A, which in return requires a far higher number of cycles to reach the same state as sample A. XPS showed that under the chosen conditions the electronic structure was not significantly altered.

The entire work contributes important insight into the morphologic behaviour of very thin iridium layers under OER conditions. The most important outcome is the understanding that the same treatment on differently prepared samples, by means of their morphological state, (even consisting of the same material) does not always give the same results. In our case, the most promising insight was the detection of the transformation of the iridium layer into a partially disturbed layer. This revealed the difficulty in comparing results between different samples (or treatments) undergoing the same reaction. This finding gives the very important indication that when samples are compared, their entire "curriculum vitae" needs to be known. This work also demonstrates the necessity of both local and integral methods. Though local investigations are important in understanding phenomena on an atomic scale, an integral look at a sample's surface offers understanding as well on the macroscopic scale. In the present work we could obtain results through X-ray reflectometry (mass density, roughness, layer thickness) and XRDS (lateral correlation length, roughness, mass density, Hurts parameter) created on a nanometric scale integrated over the whole sample surface (-> current density), which is in the cm range and therefore statistically representative. This combination allowed us a three-dimensional insight into a sample's nature. In contrast, transmission electron

microscopy can only give a local view of a sample in the range of tenths of nanometres. To acquire an encompassing knowledge, both microscopic as well macroscopic views are necessary.

4.6 References

- 1) C. McCrory, S. Jung, J. Peters, T. Jaramillo, J. Am. Chem. Soc. 135, (2013) 16977-16987
- 2) J. P. Barton, D. Infield, IEEE T Energy Conver 19 (2004), 441-448
- 3) I.C. Man, H. Su, F. Vallejo, J. Rossmeisl, ChemCatChem, Vol.3 (2011), 1159 – 1165
- 4) I. Katsunobaru, S. Cherevko, A. Zeradjanin, K. Mayrhofer, Angew. Chem Int. Ed 53 (2014), 102-121
- 5) A. Damjanovic, A. Dey, J. O. M. Bockris, J. Electrochem. Soc. 113,(1966) 739ff
- 6) B. Conway, J. Mozata, Electrochimica Acta 28 (1983), 9-15
- 7) A. Paets van Troostwijk, J. Deiman, Obs. Phys., 35 (1789), 369
- 8) J. O. Bockris, J. Chem. Phys. 24, (1956), 817
- 9) J. Rossmeisl, A. Logadottir, J. K. Nørskov, Chem. Phys.,319 (2005) 178-188
- 10) D. Mitchell, D. Rand, R. Woods, J. Electroanal. Chem. 84 (1977) 117-126
- 11) R. Kötz, H. Neff, S. Stucki, J. Electrochem. Soc. (1984), 131, 7
- 12) J. Otten, W. Visscher, Electroanal. Chem & Interfac. Electrochem., 55 (1974), 1-11
- 13) V. Pfeifer, T. Jones, J. Velasco, C. Massue, M. Greiner, R. Arrigo, D. Teschner, F. Girgsdies, M. Scherzer, J. Allan, M. Hashagen, G. Weinberg, S. Piccinin, M. Hävecker, A. Knop-Gericke, R. Schlögl, PCCP, 18 (2016), 2255-2287
- 14) D. Buckley, L. Burke, J. Chem. Soc., Faraday Trans. 1, 71 (1975), 1447
- 15) A. Cruz, L. Abad, N. Carretero, J. Moral-Vico, J. Phys. Chem, 116 (2012), 5155-5168
- 16) S. Ito, Y. Abe, M. Kawamura, K. Kim, J. Vac. Sci. Technol. B, 33 (2015), 041204-1 - 041204-5
- 17) Y. Hall, P. Sherwood, J. Chem. Soc., Faraday Trans. 1, 80 (1984), 135
- 18) J. Otten, W. Visscher, Electroanal. Chem & Interfac. Electrochem., 55 (1974), 13-21,
- 19) E. Ohriner, Platinum Metals Rev., 52 (2008), 186-197
- 20) H. Jehn, J. of the Less-Common Metals, 100 (1984), 321-339
- 21) Y.G. Shen, Y.W. Mai, Q.C. Zhang, D.R. McKenzie, W.D. McFall, W.E. McBride, J. Appl. Phys. 87(2000), 177-187
- 22) A. Ulyanenko, Adv. In Comp. Methods for X-ray and Neutron Optics, Vol. 5536 (2004) 1-15
- 23) H. Ma, Science Rep. 6, (2016), 2-11
- 24) G. Reeves, M. Lawn, J. Vac. Sci. Technol. A, 19 (1992) 3203-3206
- 25) B. Timmer, M. Sluyters-Rehbach, J.H. Sluyters, Surf. Sci. 18 (1969), 44-61
- 26) L.G. Parratt, Phys. Rev. 2, Vol.95, (1954) 359-369
- 27) L. Nevot, P. Croce, Rev. Phys Appl. 15, (1980), 761
- 28) H. Kiessig, Annalen der Physik 10 (1931), 769-87.
- 29) S. Kohli, C. Rithner, P. Dorhout, Adv. X-ray Analysis, Vol 45 (2004), 352-358
- 30) M. Elvis, D. Fabricant, P. Gorenstein, Appl. Optics, 27 (1988), 1481-1485
- 31) S. Gottesfeld, S. Srinivasan, J. Electroanal. Chem., 86 (1978),89-104
- 32) E. Frazer, R. Woods, J. Electroanal. Chem. 102 (1979), 127-130
- 33) J. Schlomka, M. Tolan, L. Schwalowsky, O. Seeck, J. Stettner, W. Press, Phys. Rev. B, (Vol.51) 1995, 2311-2321
- 34) S. Sinha, E. Sirota, S. Garoff, H. Stanley, Phys. Rev. B, (Vol.38) 1988, 2297-2311
- 35) V. Holy, T. Baumbach, Phys. Rev. B 15, 49 (1994), 10668-10676
- 36) R. Kötz, H. Neff, S. Stucki, J. Electrochem. Soc. (Vol 131), 1984, 72-77

- 37) R. Kötzt, H. Lawrence, P. Brüesch, S. Stucki, J. Electroanal. Chem. & Interfacial Electrochem. 150 (1983) 209-2015
- 38) V. Pfeifer, T. Jones, J. Velasco, C. Massue, M. Greiner, R. Arrigo, D. Teschner, F. Girgsdies, M. Scherzer, J. Allan, M. Hashagen, G. Weinberg, S. Piccinin, M. Hävecker, A. Knop-Gericke, R. Schlögl, Surf. Interfacs Anal., 48 (2016), 261-273
- 39) J. J Yeh, At. Data Nucl. Data Tables 32 (1985) 1-155
- 40) S. Cherevko, S. Geiger, O. Kasian, N. Kulyk, J. Grote, A. Savan, B. Shrestha, S. Merzklin, B. Breitbach, A. Ludwig, K. Mayerhofer, Catalysis Today 262 (2016), 170-180
- 41) M. Wohlfahrt-Mehrens, J. Heitbaum, J. Electroanal. Chem 237 (1987), 251
- 42) T. Kandemir, I. Kasatkin, F. Girgsdies, S. Zander, S. Kühl, M. Tovar, R. Schlögl, M. Behrens, Topics in catalysis, 57 (2014), 188-206

Appendix 1

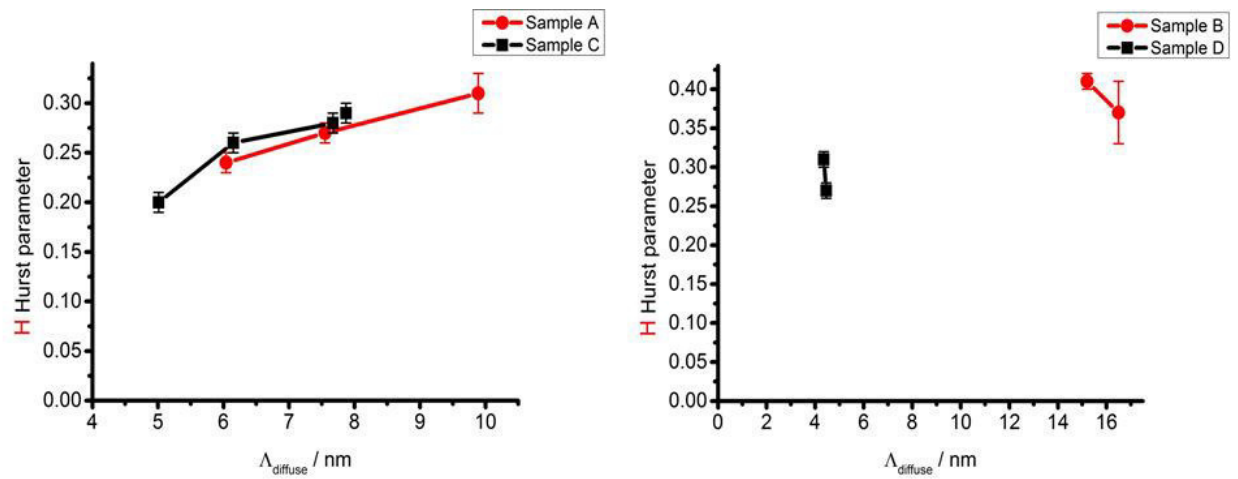


Fig.4.A1: Hurst parameter plotted over diffuse penetration depth for samples A to D

Chapter 5: Iridium thin films under oxygen evolution conditions – influences on morphology and crystal lattice

5.1 Abstract

The present work describes the morphological investigation of thin polycrystalline Ir films which have been under oxygen evolution reaction (OER) conditions in combination with varying electrochemical treatments. X-ray reflectometry (XRR), X-ray Diffuse Scattering (XRDS) as well as Grazing Incidence X-ray Diffraction (GIXRD) were used for surface sensitive structural and fractal analysis of the iridium metal layer before and after electrochemical reaction. Three different electrochemical scenarios have been applied to monitor resulting layer structure and morphology: i) slow speed cyclic voltammetry (CV) ii) slow speed CV followed by chronoamperometry (CA) and iii) high speed cycling. The observed results depict the influence of the electrochemical conditions on the resulting layer morphology and follow the trend already mentioned in chapter 4. The slower scan speed clearly shows the influence of kinetics on the dynamic surface transformation indicated by strongly changing fractal parameters. The original metal layer is transformed into a two-layer system (IrOx/Ir) and in addition a local anion (SO_4^{2-}) accumulation on Ir layer fragments can be observed. Scanning electron microscopy (SEM) was applied to confirm the fractal changes deduced from the XRR/XRDS results. Finally, to prove the sensitivity of our measurement strategy we used a homogeneous, high density Ir layer and followed the depth dependence of the Ir 111 reflection profile before and after one CV cycle and a short CA. Already after one cycle the original layer lattice is strongly affected. Although our chosen sample model does not completely reflect real-life electrode tailoring, the gained insights demonstrate the valuable use of integral characterization methods GIXRD and XRR for studying dynamic reactions and their unique capabilities for electrocatalysis.

5.2 Introduction

The study of iridium and its oxides in the oxygen evolution reaction under acidic conditions has become a prominent topic in the context of today's energy economy. The necessity to replace fossil fuels has also created the need for finding new ways of storing the energy from sustainable sources. Hydrogen production by water splitting is a promising candidate for achieving this goal⁽¹⁾. While the hydrogen evolution reaction (HER) is the actual target, the economical use of the water splitting reaction is limited by the large electrode overpotential of the concurrently sluggish oxygen evolution reaction (OER). The most promising candidates for achieving sufficiently low OER overpotentials are IrO₂⁽²⁾ and RuO₂⁽³⁾. Testing these two examples showed the complexity of mechanistic studies. The oft simplified model systems, such as rutile typed IrO₂, only partially satisfy the reaction description. Determining the real composition and structure of the active surface layer is a much more elusive goal. The use of RuO₂ however, suffers, for example, from weak O adsorption⁽⁴⁾ and the formation of volatile higher valent Ru oxides⁽³⁾. Although studies on these oxides are widespread, recent publications have paid more attention to the metallic surface itself on which the OER active layer is formed by continuous cyclic voltammetry (CV). One of the most notable differences between oxide and metal catalysts lies in the instability^(5,6) of the former, as metallic catalysts degrade much faster and have a slightly higher overpotential than their corresponding oxides⁽⁴⁾. The pioneering work of

Fierro⁽⁷⁾ extended the basic mechanistic description^(8,9) of metal oxides MO_x in the water splitting reaction and showed by isotope labeling experiments that only the outer sphere of the IrO_2 crystal lattice participates in the oxygen evolution reaction. This points to the fact that an ordered monovalent compound like IrO_2 is probably not the active phase in the oxygen evolution reaction. Furthermore, recent studies show a discrepancy in the activity of a chosen catalyst depending on whether it is present as bulk material or as nanoparticles⁽¹⁰⁾. As long-term stability under acidic oxidizing conditions is a necessary prerequisite for an OER electrode catalyst to be used within a proton exchange membrane cell (PEM-electrolyzer⁽¹¹⁾), noble metals like gold, platinum and iridium have been studied extensively in this context. In contrast to its thermal stability against oxidation, platinum has been shown to be oxidized under OER conditions⁽¹²⁾. However, the oxides formed are instable and start to decompose upon removal from the electrolyte, thereby making Pt an unfavorable choice as OER catalyst. In contrast, iridium forms a very stable amorphous oxide which suffers less from degradation, making it an interesting candidate as an OER catalyst^(13,14). The formation of oxidized, active surface species on iridium metal under OER conditions has been evidenced by several analytical methods^(7,12,15,16,17,18,19).

Besides the change of the electronic state of the iridium under OER conditions, the transformation into the active oxo-hydroxo layer on top of the metal is accompanied by a significant alteration of the surface morphology. Michell⁽¹⁷⁾ and co-workers were one of the first to report on these morphology changes by electron microscopy (roughening, induced strain) and showed an electron diffraction pattern indicating a hexagonal structure for the formed surface layer. A second important work, connecting the formation of the OER-active layer with switching conductivity, was made by Conway and Mozota in 1983^(20,21). This work was based on the study previously performed by Capon and Parsons⁽²²⁾ in trying to obtain a stable monolayer oxide on the Ir surface. This deep electrochemical work also provided insights into switching conductivity and mono- to multilayer oxide formation for IrO_x electrocatalysis. The first attempts to study dependencies, such as conductivity, layer thickness and oxygen coverage, were already made in the early 1970s by Otten and Visscher^(23,24), who used ellipsometry to detect changes while growing an oxide film on the surface of an iridium foil. They found the iridium layer to be changed by pitting corrosion and that changed the metal substrate significantly- 80 cycles introduced an approximately 2-3 nm thick disturbed layer on top of the iridium. Additionally, they found two types of oxygen species covering the surface (ellipsometry results) depending on the chosen potential switch. Nowadays there is an accepted agreement in the scientific community that a metallic Ir surface is a poorer OER catalyst in comparison to samples containing an amorphous oxo-hydroxo Ir layer on their surface⁽²⁵⁾. Previous work showed that formed oxo-hydroxo layers on OER-active metals do not exhibit long range order, hence explicit results of an integral characterization method like X-ray diffraction are largely missing or became very difficult to interpret⁽²⁶⁾.

Since in electrochemistry the solid-electrolyte interface is of particular interest, special integral methods are needed. The principal techniques for doing so are Grazing Incidence X-ray Diffraction⁽²⁷⁾ and X-ray Reflectometry⁽²⁸⁾. These techniques deal with restricted penetration depths and became therefore extremely valuable for investigating surface-near regions compared to classical Bragg diffraction (powder diffraction). The field of X-ray reflectometry (XRR) is a well-known and established technique for characterizing thin layers (crystalline and amorphous). It offers parameters such as: layer thickness, roughness and electron density. In addition, monitoring the diffusely scattered intensity of the X-ray beam (XRDS)⁽²⁹⁾ on such surfaces extends the characterization to the fractal parameters of samples (e.g. to distinguish roughness and electron density grading). This

combination of XRR and XRDS can describe the morphology of a surface on the nm scale over enormous integral length scales (angstroms to microns). GIXRD, as well as XRR and XRDS offer integral insights into the microstructure of the samples and are complementary to local methods like X-ray Photoelectron Spectroscopy (XPS) and Transmission Electron Microscopy (TEM). Various in-situ studies can be found elsewhere^(30,31,32,33). The microstructure of thin films plays an important role in understanding physical, optical and mechanical properties⁽³⁴⁾.

Within this work we would like to demonstrate the power of combining XRR and XRDS (as well as GIXRD) to monitor the electrochemically induced changes in the morphology and structure of a thin Ir layer model system. Although X-ray diffraction is known as the most powerful tool for structure determination (Bragg-diffraction), we will demonstrate that testing electron density without long-range order can reveal valuable insights into a thin surface layer. The model system consists of iridium deposited on a commercial Si wafer substrate. The use of thin film electrodes has the economic benefit of using a small amount of iridium for coating and therefore becomes more affordable on an industrial scale. We will focus on the impact of three scenarios on the layer: i) low number of cyclic voltammetry (CV), ii) low number of cyclic voltammetry followed by subsequent chronoamperometry (CA) and iii) high cycle numbers. These three scenarios are each kinetically different and this is revealed in the final state of the Ir layer (e.g. changing fractal parameters, intensity drop,...). Finally, to prove the sensitivity of our method, a fourth treatment (only one cycle of cyclic voltammetry and short chronoamperometry) is applied to a homogeneous, highly dense Ir layer prepared by e-beam evaporation. Here a depth sensitive diffraction study is executed and shows the electrochemical impact over layer depth. This study shall: demonstrate the need and value of integral characterization methods like XRR and XRDS, and expose both the difficulties in comparing differently treated samples that were prepared in an identical way and the delicate impact of the electrochemical parameter.

5.3 Experimental

The thin films were prepared using pre-cleaned Silicon (100) wafers (ultrasonic bath and isopropanol for 10 min, dried in nitrogen flow and stored under N₂ until coating) as substrates. The native SiO₂ layer was not removed but for further analysis considered in the fit model. The wafers were broken into approximately 1.8 x 1.8 cm pieces (for mounting in the coating holder) before coating. **Sputtering:** Ir films were deposited from metallic targets (Ir 99.99 %,Elektronen-Optik-Service GmbH) in 0.1 mbar Ar at 40 mA using a Cressington 208HR sputter coater. The deposition time was 60s (desired thickness: ~ 20 nm). **E-beam evaporation:** Iridium was deposited by electron-beam evaporation from a metal (99.99 % purity) melt using a tungsten crucible. The base pressure of the chamber was 8.10e⁻¹⁰ mbar, the substrate was kept at room temperature. **Electrochemistry:** All experiments were performed in 0.1M H₂SO₄ (ultrapure Merck) and a three electrode glass cell (cyclovoltammetry-setup, BioLogic potentiostat). Purging with argon during reaction was done. Clamp holders of the substrate were chosen to only contact through the iridium deposited site. A Pt wire was used as the counter electrode and a saturated calomel electrode (SCE) for the reference. The samples were removed from electrolyte at Open Circuit Potential (OCP). For simplification, the investigated samples are labelled with the following abbreviations:

Iridium deposited by sputtering, as is	->	Sample A
Iridium deposited by sputtering, cyclic voltammetry	->	Sample B

Iridium deposited by sputtering, CV + chronoamperometry	->	Sample C
Iridium deposited by sputtering, 220 CV cycles	->	Sample D
Iridium deposited by e-beam evaporation, as is	->	Sample E
Iridium deposited by e-beam evaporation, 1x CV + 1h CA	->	Sample F

Scanning electron microscopy: was performed on a Hitachi S4800 for imaging and necessary EDX spectra. The Hitachi S-4800 FEG is equipped with a Bruker XFlash detector and an energy dispersive X-ray spectroscopy (EDX) system Quantax. **X-ray reflectivity and diffraction:** measurements were performed on a Bruker D8 Advance (DaVinci design with LynxEye detector, Cu radiation), equipped with a Göbel mirror and Eulerian cradle. The measurement range chosen was between 0.1 to $8^\circ 2\theta$ with a step size of 0.005° and a counting time of 1s/step, with a double slit assembly on the secondary beam path to avoid background scattering. All XRR curves were additionally measured with an off-set of 0.1° in θ and corrected for the longitudinal direction to obtain the true specular contribution. Diffuse scattering was measured with the same setup by transverse rocking curves (at α_c). GIXRD measurements were performed close to the critical angle of each sample ($0.4^\circ \theta$) and done between 10 and $70^\circ 2\theta$ with a step size of 0.02° and counting time of 3s. A 0.2° equatorial soller was used instead of the double slit assembly on secondary beam path for GIXRD. Depth profile for samples E and F were taken from 0.4 - 1.5° incidence angle (with 0.11° and 0.1° step size, respectively). XRR and XRDS were analyzed using DIFFRAC Leptos (V7.8, Bruker AXS)⁽³⁵⁾. The GIXRD peaks were analyzed using the Topas software (version 5, 1999-2014, Bruker AXS). The sample contribution of the peak profiles was described using pseudo-Voigt functions, from which the integral intensity (area) and the full width at half maximum were extracted.

5.4 Results and Discussion

5.4.1 Morphological investigation by XRR, XRDS and SEM of the untreated samples

The untreated pieces, samples A and E, were analyzed first. Here one develops the sample model (layer stack) and fit parameters before electrochemical treatments are applied and define the parameter pool for the later refinement strategy. In the previous chapter, the model was kept simple to gain the description of the morphology with minimum variables. In the present chapter, this strategy does not hold for the entire sample convolute. In the following paragraphs the model will be significantly modified and extended to a multilayer system. Up until this point the discussion has been based on the morphological differences between sputtered and e-beam evaporation prepared samples, and this has revealed the need of structural flexibility (less densely packed) for certain activity in the OER. The results of samples A and E are basically comparable with data in chapter 4 before oxidation. Fig. 5.1 shows the reflectometry curves obtained for samples A and E, together with the corresponding XRR fit curves.

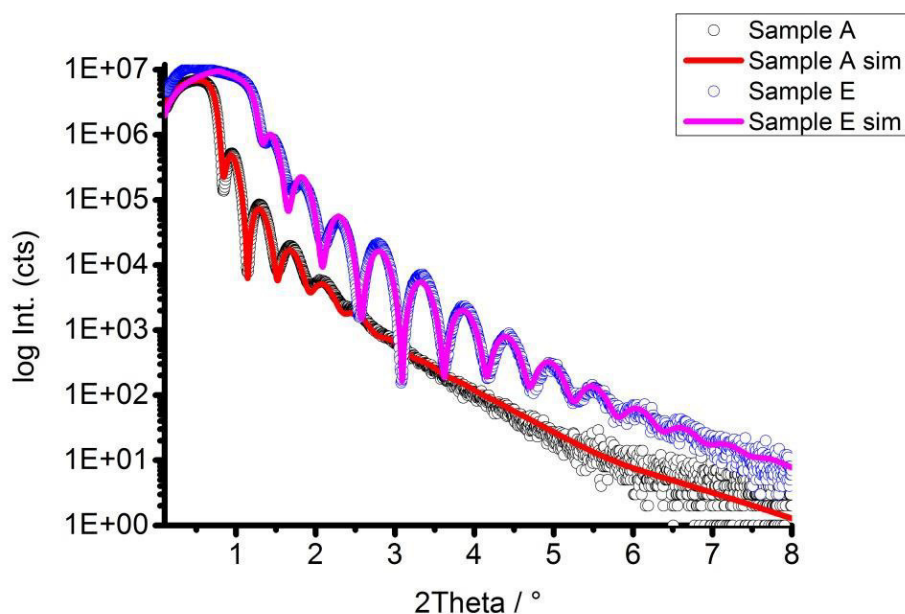


Fig. 5.1: X-ray reflectometry curves and corresponding simulations for samples A and E.

Tab. 5.1: XRR fit results obtained for samples A and E.

	layer	thickness (nm)	roughness (nm)	density (g/cm ³)	α_c (°)	χ^2
A	Ir	19.5 ± 0.2	1.6 ± 0.1	8.2 ± 0.2	0.37	0.026
	SiO _x	1.5 ± 0.2	0.5 ± 0.3	2.0 ± 0.6		
E	Ir	15.5 ± 0.1	0.5 ± 0.1	22.5 ± 0.7	0.60	0.021
	SiO _x	1.1 ± 0.5	0.7 ± 0.4	1.9 ± 0.7		

Parameters were derived by the following XRR simulation model: The starting values for the substrate parameters used in the fits were obtained from a blank substrate sample (SiO₂, thickness: 1.7 +/- 0.3 nm; roughness: 0.3 +/- 0.2 nm; density: 1.6 +/- 0.5 g/cm³; Si, roughness: 0.3 +/- 0.2 nm). The stacking order was assumed to be Si/SiO₂/Ir in order to keep the system as simple as possible. The interface was modeled as Névot-Croce type (abrupt)⁽³⁶⁾. In the previous chapter the morphology investigation after electrochemistry showed that the underlying SiO_x can also be affected. Therefore, we tabulate and monitor the values in XRR for the SiO_x layer here as well.

While the similar oscillation frequency results from comparable layer thickness, both the critical angle and the amplitude dampening are vastly different for samples A and E. These are tabulated in Tab. 5.1. The dampening seen in sample A points to a higher surface roughness compared to sample E. Furthermore, the very low critical angle α_c of A corresponds to a surprisingly low electron density. These two effects have already been discussed (see above: chapter 4) and explain the difference in appearance of the XRR curves. Again, both effects can be understood in connection with the SEM evidence given below. The crack-structured surface of sample A explains to the low α_c . The dilution with air between the cracks as well the appearance as nanoparticle arrangement (the pillars) need to be taken into account in comparison to sample E. In addition, incomplete coverage of the surface of sample A with iridium might be considered as contribution for the low α_c also. The two deposition methods likely follow a different growth mechanism and hence exhibit distinct morphologies. The

finding of a higher degree of packing and layer quality of sample E as compared to sample A is also reflected by oscillations still appearing at quite high 2θ values. X-ray reflectometry measurements are performed over the entire surface (illuminated sample surface) at a small and very low angular fraction of 2θ . The results are an average over the contributions on the layer.

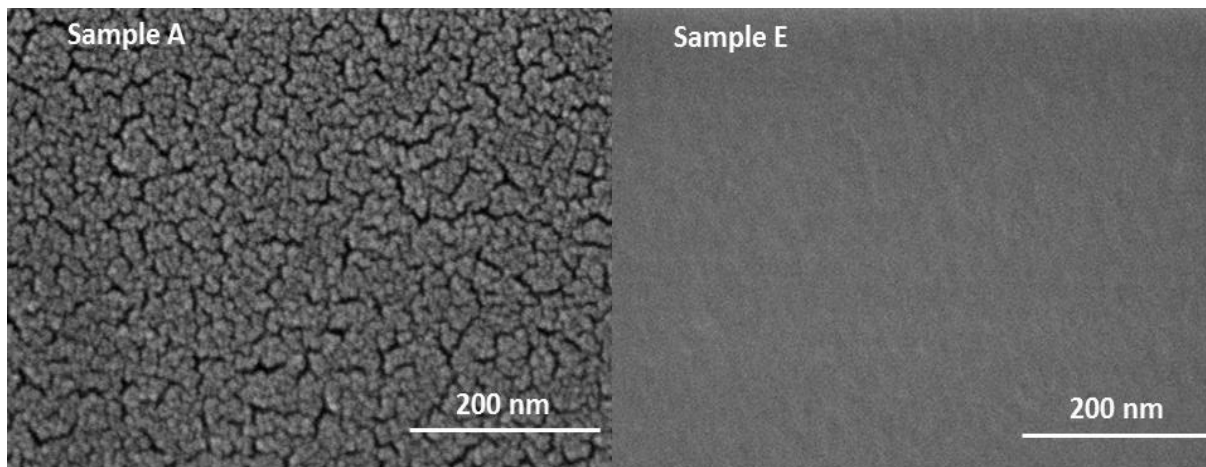


Fig. 5.2: SEM pictures of the sample surfaces of A and E in direct comparison. The strong difference in surface roughness and homogeneity depending on the chosen deposition method should be noted.

In addition to X-ray reflectometry, diffuse scattering measurements were recorded. The evaluation of the rocking curves was already described in chapter 4 (4.4.3, Fig.4.5). This strategy was kept and used for the current investigation. This technique allows the determination of a samples fractal parameter⁽³⁷⁾: the Hurst value (h) and lateral correlation length (ξ). The Hurst value describes the jaggedness of an interface (its texture), whereas ξ is a parameter describing the length scale of correlation of homogeneous roughness laterally. In the present work, the data treatment of XRDS curves was chosen to be executed for four parameters: the roughness, Hurst value, lateral correlation and mass density. These parameters are connected over the height-height correlation function C (see chapter 2), excepting mass density. H and ξ are not strictly independent from each other and since H does not exhibit any significant changes, it was refined but taken out of the interpretation for the sake of simplification (plots can be found in Appendix 1). The decision to also refine mass density originated from the expected necessity of splitting later into a two-layer model for oxidized samples. Since the obtained penetration depth (q_z restriction) depends on the dispersion and absorption terms of the refractive index n of a layer, this decision is justified and allows for a sufficient description. Fig.5.3 shows the measured rocking curves at corresponding 2θ (chosen at each samples XRR curve) for sample A and E. Only curves which exhibit a diffuse profile (\rightarrow Yoneda wings, see chapter 2) were further analyzed. The position of the maximum of the Yoneda wings is indicated by a blue asterisk and taken for the estimation of the penetration depth (Λ_{diffuse} , see chapter 4). For the later two layered system, we set the requirement to obtain the whole penetration depth profile according to the XRR stacking, so that the lower depth is expressed as a sum of the calculated upper and lower depth. The refinement of the simulation curves was executed with LEPTOS software by using the semi-kinematical DWBA concept^(35,37). The parameters obtained from XRR were used as input All four parameters (H, σ, ξ, d) were refined together. The sample model was assumed to be fractal and uncorrelated in the vertical direction, while the iridium surface was evaluated as single layer model only. Fig. 5.4 displays the extracted XRDS parameter for samples A and E over depth next to one other. The obtained differences can be explained with arguments already described in chapter 4.

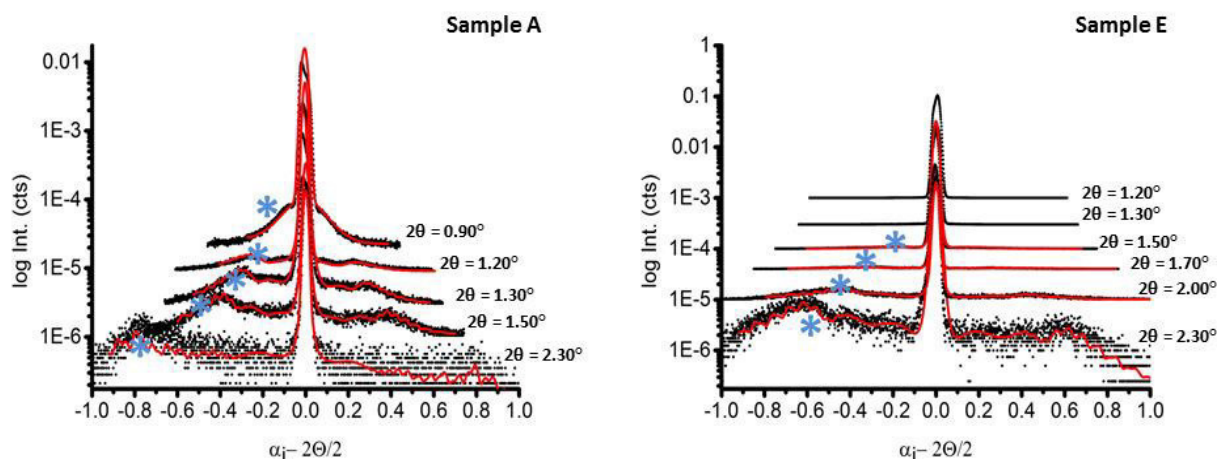


Fig. 5.3: Diffuse scattering measurements (including fit curves) of samples A and E taken at various 2θ . Please note the stacking of the curves in y for better visibility (log scale).

Initially the XRDS curves appear quite similar but upon close inspection the differences become visible. Samples A and E exhibit a difference in off-specular scattered intensity by one order of magnitude, which is caused by sample E's layer mass density (and corresponding lower surface roughness). The strong homogeneity of the iridium film in sample E does not allow to compensate the electrochemical induced stress like sample A does (stress-free layer islands), due to missing surface cracks. Like it was discussed in the previous chapter, strong local orientation differences in e-beam evaporation grown samples compensate the stress by a complete surface breakup. The obtained information depth profile in XRDS of samples A and E exceeds, in both cases, the layer thickness of 19.5 and 15.5 nm respectively. This finding can maybe be explained considering dynamical scattering events. When the beam becomes scattered internally, between the layer and the substrate, this cross-correlation might act as origin for obtaining exceeding penetration depths. Therefore, the exceeding penetration depth represents the correlation still between the iridium and the underlying wafer substrate. Interference between the upper (air-Ir) and lower interface (Ir-SiO_x) becomes stronger when both are hit by the beam. This explains the differences between the first and later data points along the probing depth. XRDS data needs always to be seen and interpreted in connection with the XRR results. The chosen penetration depth (Δ_{diffuse} , see chapter 4) represents, in a more dedicated way, the surface near character of the diffuse profile. Distinct from using the specular depth (symmetric case, maximum depth, see chapter 4). The evaluation based on purely specular calculated penetration depth becomes unreliable, since the obtained depth does not reflect useful data and falsifies them. Considering their intrinsic morphology, the following trends can be summed up: The different density of sample A is caused by surface cracks and the smoother surface of sample E is due to its homogeneous dense layer growth. The aforementioned layer growth mechanism is also depicted in the ξ -trend of samples A and E: layer growth for sample E (almost constant ξ), pillar like growth for sample A (increasing from top to bottom). The density evolution again follows the growth mechanism trend as well as packing density discussed above. By looking at the SEM image in Fig. 5.2, the differences in ξ can be clearly observed and are of comparable orders of magnitude to the XRDS results.

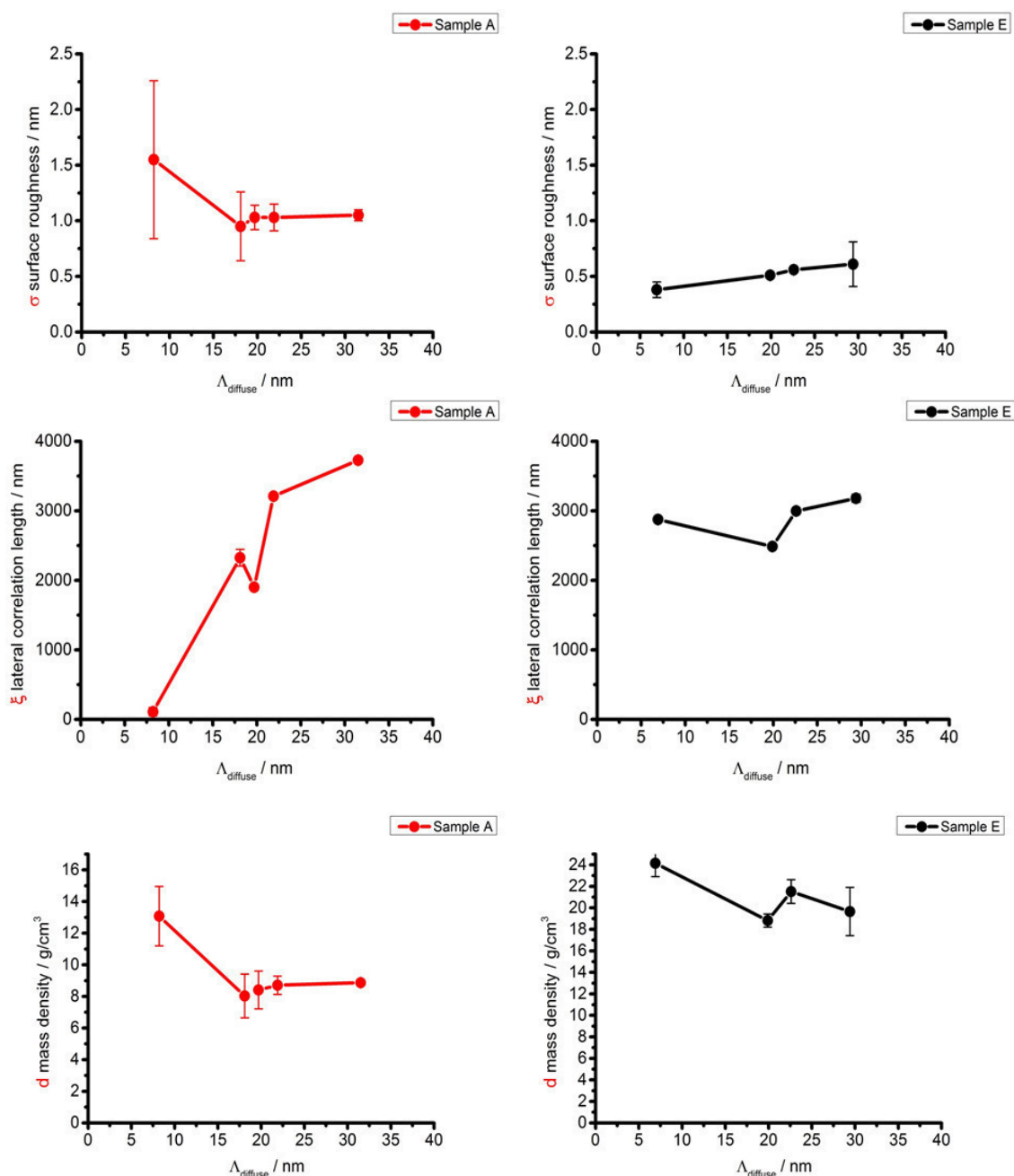


Fig. 5.4: Fractal parameters over depth extracted from the fits of the XRD curves of samples A and E.

This pre-investigation of the untreated samples is in good agreement with results obtained already in chapter 4. In addition, XRR and XRD support each other; they give essentially the same results and trends. The depth-resolved view of the untreated samples elegantly depicts the differences in layer quality laterally as well as over depth. This intrinsic difference will play a major role for the later electrochemical induced change in morphology as well as crystal lattice.

5.4.2 Cyclic voltammetry

It is known that pristine iridium metal is less active in OER than iridium which has already formed a thick oxohydrate layer^(25,26) on top. We attempted to gain an insight into the first steps of this layer formation and wanted to monitor the morphology changes of the iridium substrate within a very soft treatment by slow speed cyclic voltammetry. Six cycles with 1 mV/s followed by five cycles at

0.1 mV/s were chosen as the probing scenario. The results of the cyclic voltammetry can be seen in Fig. 5.5.

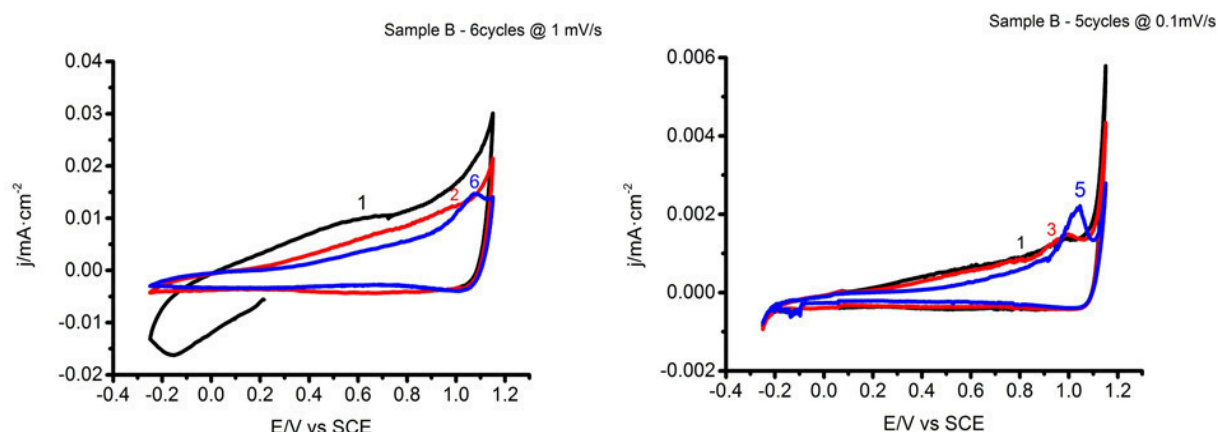


Fig. 5.5: CVs of sample A in 0.1M H₂SO₄ with 1 mV/s (left) and 0.1 mV/s scan speed (right) Labeled numbers display the shown cycle number.

CV curves exhibit quite an interesting shape, which is, upon first viewing, not very closely related to a classical bulk Ir cyclovoltammogram. As compared to chapter 4 (Fig.4.1), the shape appears more structured with a more compact double layer regime (lower capacity). The low scan speed (1m V/s versus 20 mV/s) explains this phenomena. The diffusion control on the surface, as well as the electron transfer inside the layer, becomes moderate and place exchange (e.g. O to Ir) can take place in a controlled manner. These samples are only very thin layers (XRR: 19.7 nm) of iridium and hence a very well-defined iridium curve is not to be expected (also due to the absence of massive bulk iridium). The morphology of this layer strongly influences the electrochemical behavior and was previously discussed in chapter 4. Considering the work of Gottesfeld^(38,39), our chosen potential range (-0.25 up to 1.20 V) is known as the range of slow growth of Ir-oxide films. In combination with the slow scan speeds ($\leq 1\text{mV/s}$) the conditions are mild and are assumed to lead to a slow and homogeneous growth of the surface layer. In Fig.5.5 only two prominent peaks can be found in the CVs, at 0.6 V and 1.05 V respectively. The first vanishes during continuous cycling, whereas the later becomes more prominent. We assume the first peak to be part of a cleaning step on the surface, whereas the second is likely the indicator for the oxide-layer growth in our treatment. Compared to well-known electrochemical works on Ir, the peak position is close to the onset peak of the OER reaction ($\sim 1.21\text{ V vs. SCE}$). In the work of Conway, this peak is associated with the under potential deposition of $-\text{OH}$ groups within the monolayer oxide formation process. It appears reasonable to us, that on our very thin layers the transformation takes place but the appearance of the CV becomes distorted due to the absence of massive bulk iridium as well by the accompanied thin film morphology effects. The resulting oxide layer formation is also confirmed by the absence of the hydrogen adsorption after the first cycle in the 1 mV/s treatment. Iridium is known to have a low overpotential for the production of hydrogen and, as discussed by Gottesfeld^(38,39) and co-workers, H-adsorption at the oxidized surface is unlikely. In addition, the sulfate anion adsorption ("sticking") might play a role in this potential range. Since there is no corresponding reduction peak observed, the reaction taking place at 1.05 V is irreversible. The position of this peak is also comparable with the appearance of an oxidation peak on well-defined Ir (111) surfaces⁽⁴⁰⁾ cycled with H₂SO₄. Hence, it potentially indicates the presence of a preferred attacking site in combination with the use of sulfuric acid. One more effect which might be attributed to adsorbed anion species is the shrinking of the double layer regime^(41,42). It is a known effect that in the double layer regime no electrochemical

reactions happen since it is a charging area. In our case it is decreasing during cycling, which leads to the assumption that the charge carrier density (so the double layer capacitance) gets lower and the double layer is influenced by the adsorbed/formed species (e.g. $\text{SO}_4^{2-}-\text{H}_3\text{O}^+$)⁽⁴¹⁾ during cycling. Decreasing activity in the range of 1.1-1.2 V points additionally towards the reasonable assumption that there is a layer formed which covers the metallic iridium surface but does not catalyze the OER in this potential regime. Higher OER activity of the oxo-hydroxo-layers can be seen usually at higher potential ranges (1.5-1.6 V). The time scale for our scenario became rather long; 43.4 h in total (4.6 h at 1 mV/s + 38.8 h at 0.1 mV/s). Reported thickness values for over-night experiments by Gottesfeld⁽³⁸⁾ are approximately 250 nm after 15 h (scan speed 100 mV/s). We expect to possibly achieve one tenth of this value, based on our chosen treatment.

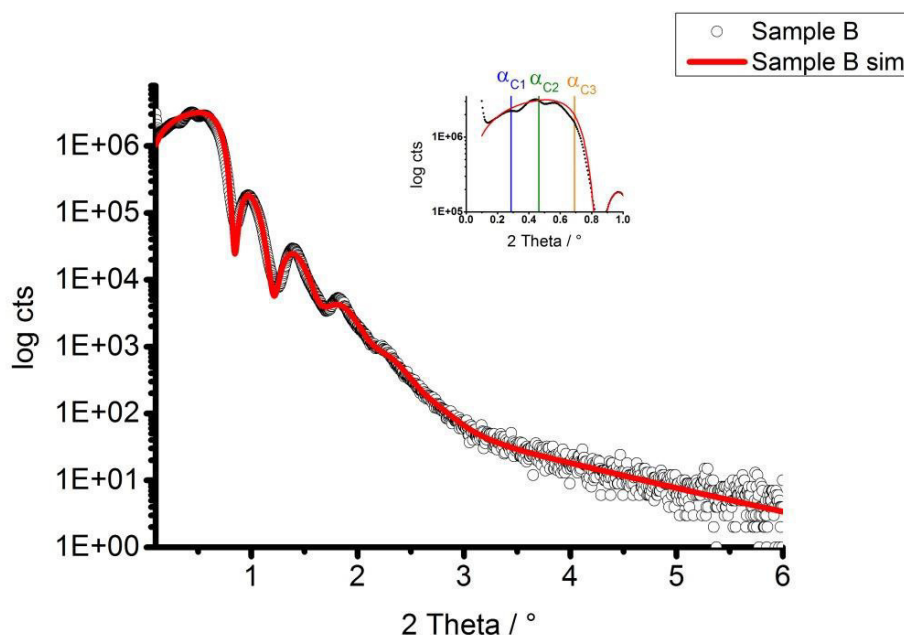


Fig. 5.6: XRR curve of sample B. The inset indicates the three critical angles found ($\alpha_{c1}= 0.30^\circ$ 2 θ , $\alpha_{c2}=0.47^\circ$ 2 θ , $\alpha_{c3}= 0.69^\circ$ 2 θ)

Morphology characterization after the eleven slow voltammetry cycles was started again with XRR. The results are summarized in Fig. 5.6 and Tab. 5.2. The already aforementioned modification of the sample model now becomes now effective. The appearance of more than one critical angle in the inset of Fig.5.6 necessitates this treatment. Appearing oscillations do not directly reveal this problem but fitting the data with the same model as sample A fails completely. The modification was executed as per the following: the layer was split into two parts, the upper and lower regions (layers) as well the electron density were allowed to change with an exponential electron density gradient over depth. Top and bottom density values of each Ir-layer are tabulated in Tab.5.2. This change in fitting strategy makes the data treatment significantly more time consuming and elaborate as well more challenging to interpret. Increased surface roughness becomes quickly apparent from the XRR curve in Fig.5.6 beside the three α_c 's. Introducing the separate upper part of the iridium layer, which is significantly different in density from the lower region, enable this model to be far more tailored to real life (as compared to chapter 4). The three critical angles gave recalculated densities of $\alpha_{c1} = 1.3 \text{ g/cm}^3$, $\alpha_{c2} = 3.2 \text{ g/cm}^3$ and $\alpha_{c3} = 7.1 \text{ g/cm}^3$. Since we allowed the system an internal electron density grading (in order to keep the model as simple as possible) we used only the lowest and highest α_c as start for the XRR refinement. The final obtained layer parameters are summed in Tab.5.2. The loss in

thickness in the underlying metallic Ir layer clearly shows that a detectable amount of the layer has been transformed into the expected oxo-hydroxo surface layer.

Tab. 5.2: XRR results obtained by fitting the measured data from sample B.

	layer	thickness (nm)	roughness (nm)	density top (g/cm ³)	density bottom (g/cm ³)	α_c (°)	χ^2
B	Ir (upper layer)	36.3 ± 0.6	3.5 ± 0.8	0.6 ± 0.1	1.3 ± 0.1	0.15	0.007
	Ir (lower layer)	17.1 ± 0.1	1.1 ± 0.2	5.4 ± 0.2	9.6 ± 0.2	0.34	
	Si-O	1.9 ± 0.2	1.0 ± 0.1	2.5 ± 0.2	-		
comp. to A	Ir	19.7 ± 0.1	1.7 ± 0.1	7.7 ± 0.1	-	0.37	0.011
	Si-O	2.3 ± 0.8	0.6 ± 0.2	2.2 ± 0.4	-		

The effect of smoothing the iridium surface itself (lower layer) was already pointed out by Otten⁽²³⁾. A smoothing of approximately 20 % was measured after 80 cycles on a bare Ir foil. The density obtained by the XRR fit is surprisingly extremely low for the upper layer and significantly graded for the lower region of sample A. Reasons for the morphology of the upper layer can be found in its probable chemical origin, a hydrated oxo-hydroxide. It contains larger amounts of water and appears as a significantly crack-structured layer, as has already been pointed out in very early works. Therefore, it appears as a barely absorbing and low dense film (its found density is indeed close to the value of water). In the case of the underlying layer, the grading indicates the opening of the cracks of the original iridium; making it continuously more porous. A higher degree of porosity also lets the electrolyte react inside the layer and the remaining underlying metallic iridium. Since α_c estimation suffers from already mentioned reasons, this value needs to be viewed carefully and on relative scale. The estimated layer thickness of ~ 36 nm for this layer is likely a result of the extremely long lasting treatment (-> ~ 44h) and fits our expectations of ~ 10 % of reported values. It is safe to assume that the formed layer is at least partially the desired product. In the next paragraph, we will come back to this statement when we test its long term OER activity. Splitting the original Ir layer into two separate layers appears, as per the already discussed assumptions, reasonable and also reflects the expectations drawn from electrochemical treatment. Even though the potential range applied barely reached the OER regime (> 1.4 V), the layer morphology and transformation of the metallic iridium was significant. The difficulty in detecting the upper layer in XRR originates essentially from two reasons. First, its' very low mass density. XRR is very sensitive to thickness changes since it probes the electron density. Kiessig fringes only appear when two layers with different electron densities are present. This means that interference only takes place where layers are present, even though the whole surface is not homogeneously covered by them. Iridium and silicon have a difference in electron density of approximately one order of magnitude, which leads to a very strong interference phenomenon. Between the upper layer and the lower layer, the contrast is much less and hence the interference is weaker. Second, its' high roughness accompanied by the layer thickness. XRR probes the specular direction only and hence the results are an average over the entire sample depth. If such a low dense layer is present on top of a strongly reflecting substrate (lower Ir layer), the upper layer becomes hardly visible since the reflectivity is determined by the heavier layer (by means of mass density). The resulting XRR curves often exhibit the oscillating frequency of the under-dense layer 'riding' on the dominant one. In the present case, due to the low density and high surface roughness, these oscillations are hardly visible. The three TER-edges (critical

angles) are a direct indication of this layer stack. In the Fourier-transformation of the pure XRR curve, the layer contributions become unfolded and more clearly visible (not separately shown here). The crystallographic results from Grazing Incidence X-ray Diffraction will be discussed in a separate section below.

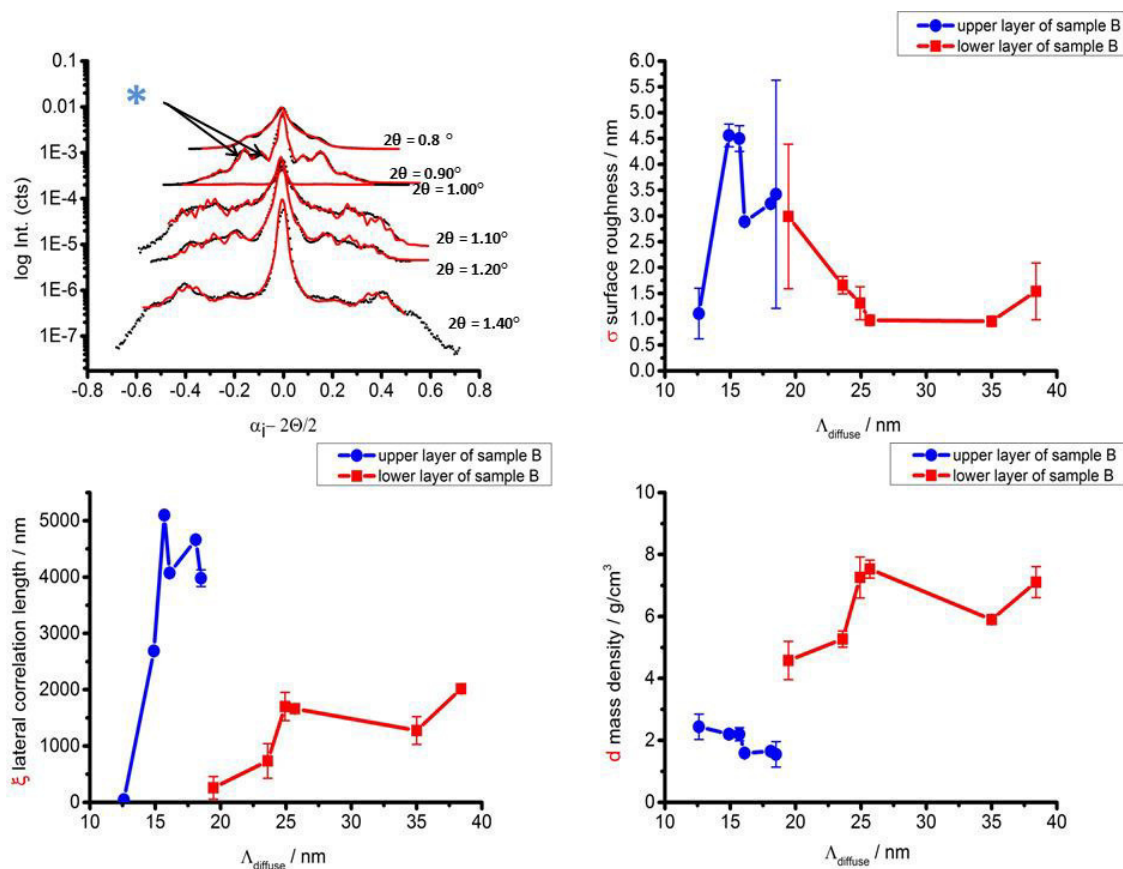


Fig. 5.7: Diffuse scattering rocking curves taken at various 2θ for sample B with corresponding extracted fractal parameters.

Fig. 5.7 shows the XRDS investigation results of sample B. XRDS rocking curves appear quite structured when compared to chapter 4, pointing towards significant contributions in off-specular direction. Fig. 5.6 (upper left) depicts the evolution of the rocking curves over depth in connection with the position of the Yoneda peak maximum (shown for one set with the blue asterisk). Though our system has been redefined as two-layer system now, surprisingly there are two sets of wings found in the rocking curves, what somehow proves our statement. Yoneda wings (see chapter 2) appear always whenever the incidence or exit angle is equal to a critical angle of the sample. The recalculated density values from the Yoneda wings almost coincide with obtained XRR values (for the upper layer: $\sim 2.1 \text{ g/cm}^3$ and for the lower: $\sim 7.7 \text{ g/cm}^3$). Taking a look at the three refined parameters over depth, the trends clearly point towards a completely different morphology formed on top of the original iridium substrate. Starting with the evolution of mass density over depth, the finding can be easily compared to the XRR results. The upper layer again exhibits the low density up to approximately 20 nm when the density then starts to significantly increase to the expected values for the underlying Ir layer. Roughness and lateral correlation length for the upper layer correlate well, probably indicating a strong break up (cracking) of the oxo-hydroxo layer surface. This process must occur quite homogeneously across the surface since the lateral correlation for the rough surface appears to be very large before it breaks down to far lower values on top of the metallic iridium underneath. The very surface-near values also appear lower, which may show a flat surface

as a 'reaction front' followed by a disturbed layer and a rearrangement of the inner layer of the oxo-hydroxo film. Inner reordering or transformation of the oxidized surface film has already been extensively discussed in literature. The already aforementioned smoothing of the Ir substrate can also be found in the XRDS curves.

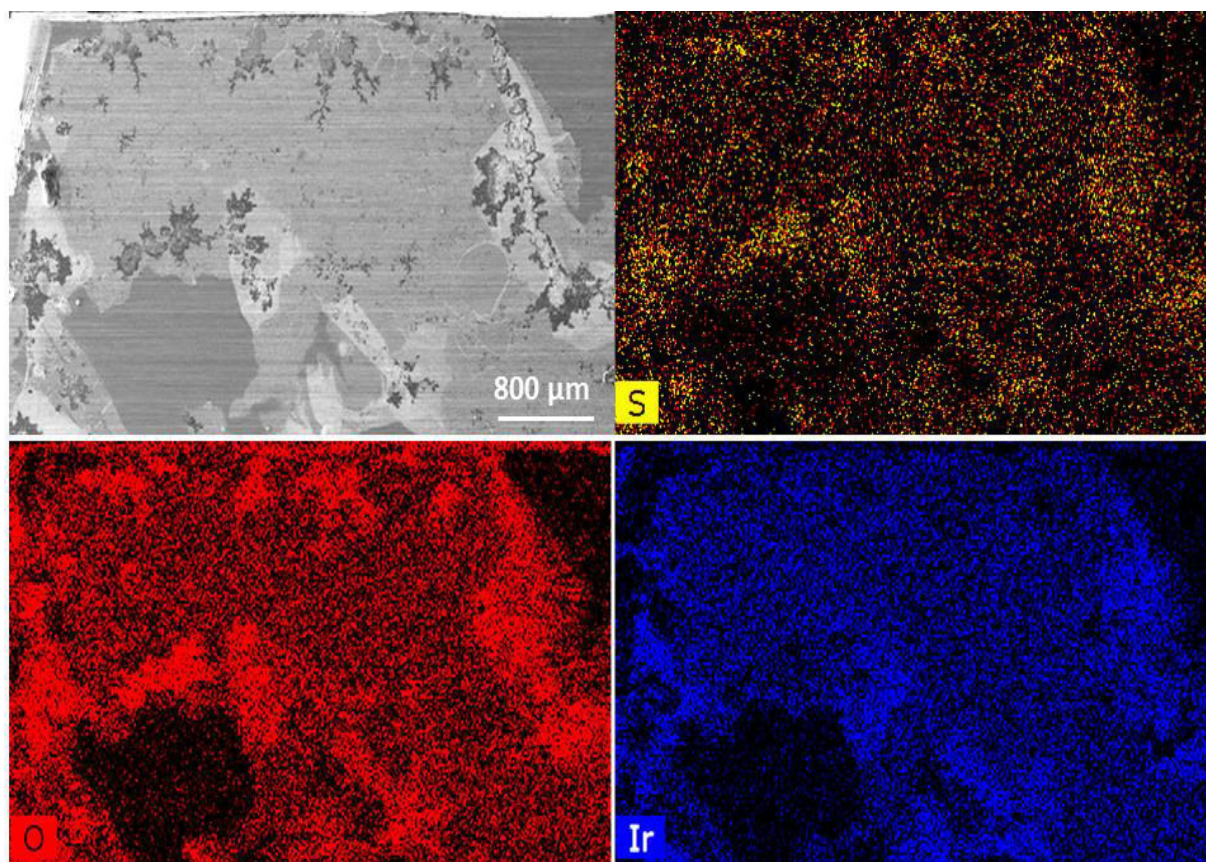


Fig. 5.8: SEM image and corresponding EDX maps of sample B. One can clearly see the accumulation of oxygen at the borders of the layer.

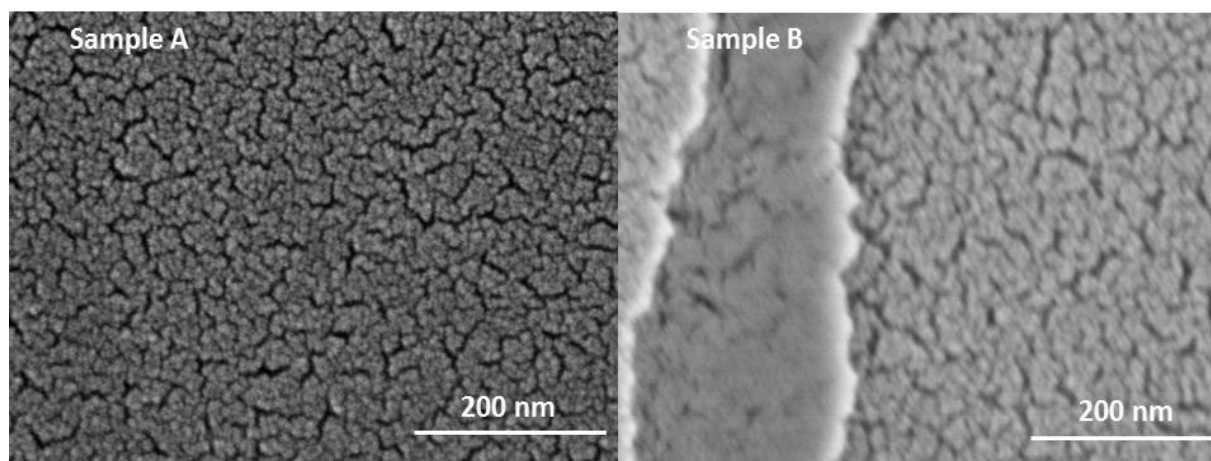


Fig. 5.9: SEM close-up image of the surface cracks at sample B

If one finally looks at the SEM pictures of sample B (Fig. 5.8), the above discussed results from XRR and XRDS can be graphically observed. Corresponding EDX spectra indicate the accumulation of oxygen and sulfur (probably as sulfate) along the borders of the iridium layer. In addition, one can find many areas of different image contrast along the surface. In connection with the iridium EDX

spectra, one can clearly see the heterogeneity indicating varying iridium accumulation. Another finding, which can be seen on the taken SEM image, is the partial incompleteness of the layer. Even after a few (eleven) cycles the deposited layer starts to break up at areas where it's very loosely bound to the substrate; either through becoming relaxed by reductive and oxidative detachment or through gas evolution (partial oxidation). Fig. 5.9 displays the crack-structured surface after the slow cyclic voltammetry at a higher magnification. Smoother areas and a less prominent crack-like surface structure can be observed. This supports the findings by both XRR and XRDS that the surface becomes smoother and, on larger length scales, more homogeneous (high ξ values). An electrochemical treatment based on potential cycling alone starts to modify the surface as already described in previous literature. The layer growth can be monitored by XRR and more deeply evaluated with XRDS with the smoothing of the metallic surface being proven by our investigative strategy. Details, such as the vastly different lateral correlation between the ground state and the oxidized state, become interesting and are likely key features in understanding the morphological transformation and could become the focus of further analysis which is beyond the scope of the present work.

5.4.3 Cyclic voltammetry followed by Chronoamperometry

In the preceding paragraph, the influence of pure potential cycling on a metallic iridium surface was investigated. In order to study the longterm activity on a CV-pretreated surface, a subsequent two-step chronoamperometric treatment was applied. This should give a direct indication of the long-term activity of the oxidized surface as well reveal the influence of a constant potential on the resulting layer morphology. The three-step treatment (CV + CA + CA) is summed up in Fig. 5.10 and Fig. 5.11.

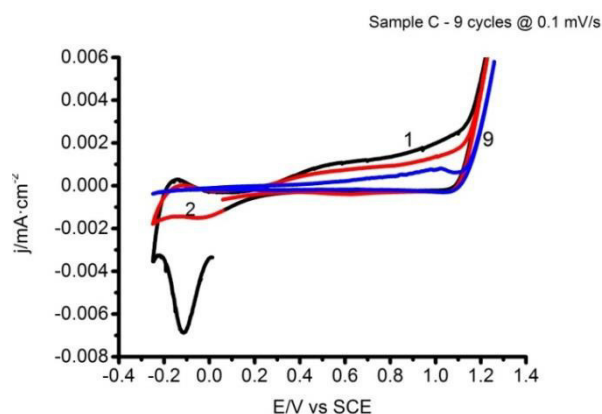


Fig. 5.10: Cyclic voltammetry of sample C

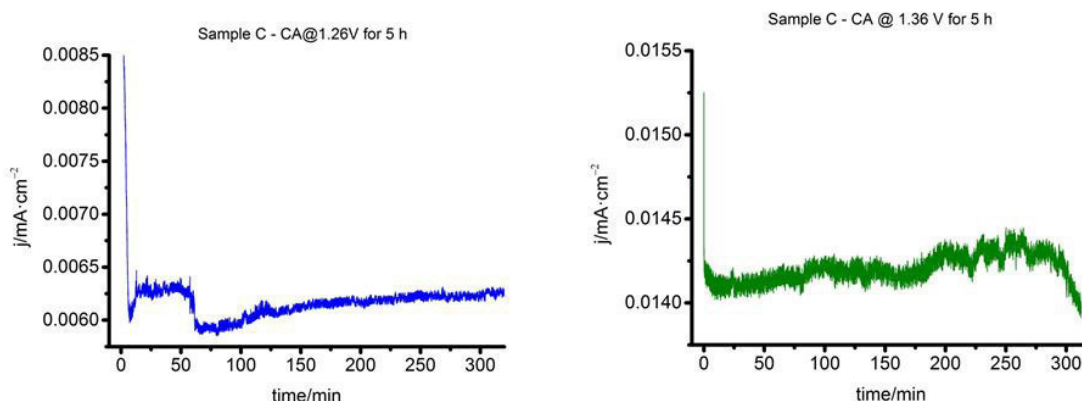


Fig. 5.11: Results for the chronoamperometry of sample C (left: 5 h at 1.26 V; right: 5 h at 1.36 V)

To remain comparable to the former analysis the scan speed was again set to 0.1 mV/s. Time dependent measurements (CA) were chosen to be performed over 5 h for each potential in order to obtain statistically time-representative activity. The cyclic voltammetry curves of sample C show basically the same results as for sample B; as discussed in the above paragraph. The two noisy chronoamperometry curves displayed in Fig. 5.11 result from the activity of the already formed oxo-hydroxo layer through potential cycling. It has been pointed out already in an early work on iridium electrochemistry by Stonehart^(43,44) that applying a constant potential to metallic iridium surfaces does not change them, as would be the case for Pt or Rh. Hence our interpretation focuses on the alteration of the oxidic surface formed by CV itself. A most significant effect can be found at the beginning of the blue curve where an area of higher activity between its start and approximately 50 minutes appears. This likely indicates a further oxidation of a pre-formed species (during CV treatment) which is limited in availability. Considering the pre-formed layer, a rearrangement or a healing of a perhaps not completely oxidized (or reduced) layer seems reasonable. Conway and Mozota^(20,21) have also explained the growth of the layer by accumulation of incomplete reduced oxides after each cathodic sweep. Since, in the present case the potential stop is far in the anodic regime, we assume this first activity in the blue curve to be connected to this step. The subsequent increase in activity, after a potential drop, now represents the activity of the fully oxidized surface. This observation is continued without further salience over both potential steps (at 1.26 V as well at 1.36 V). We expect that the OER activity of this very thin Ir film is accompanied by metal dissolution which would also partially account for layer loss in the weakly attached Ir layer on top of the Si wafer substrate. Mayerhofer and co-workers^(45,46) described clearly, in various experimental approaches, the correlation between OER activity and metal dissolution in detail. Focusing on the XRR results obtained from the fit curve in Fig. 5.12, they basically support the electrochemical interpretation; though nevertheless with two surprising outcomes.

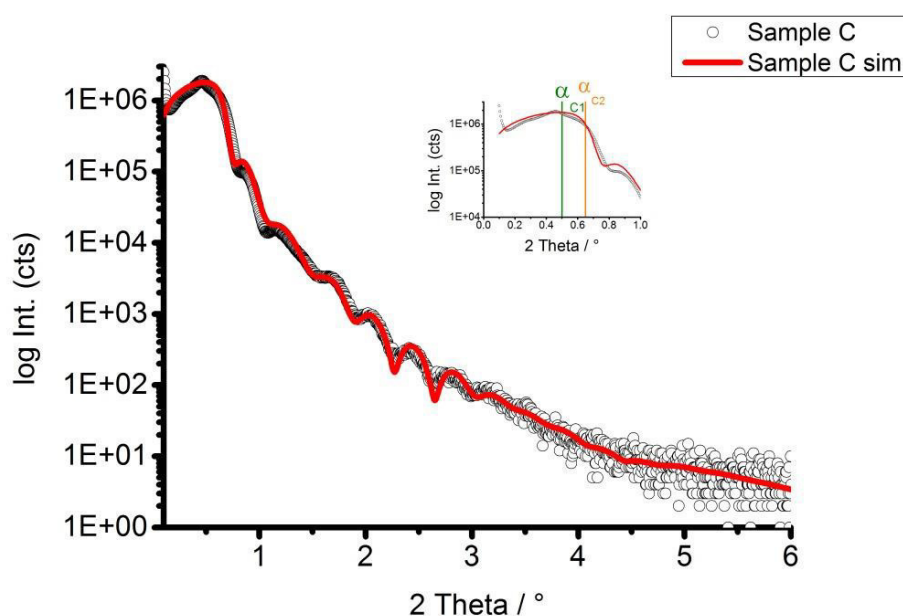


Fig. 5.12: XRR curve of sample C. ($\alpha_{C1} = 0.48^\circ$ 2 θ , $\alpha_{C2} = 0.65^\circ$ 2 θ)

By comparing the XRR curve of sample B with the one of sample C, one can immediately see the oscillations of sample C continuing to appear at higher incident angles. This finding proves the statement about the smoothing the surface which in turn means that the quality of the layer becomes enhanced. We see this also in the extracted surface roughness which displays a very

smooth surface for the metallic iridium, as well as for the formed oxo-hydroxo layer on top. The thickness of the upper layer, which was found to be approximately 20 nm was somewhat surprising. Although the cycling time was almost doubled (~ 76 h), the layer appears thinner.

Tab. 5.3: Fit results obtained from the XRR measurements of sample C.

	layer	thickness (nm)	roughness (nm)	density top (g/cm ³)	density bottom (g/cm ³)	α_c (°)	χ^2
C	Ir (upper layer)	19.6 ± 0.6	1.0 ± 0.7	0.87 ± 0.1	2.2 ± 0.1	0.14	0.011
	Ir (lower layer)	20.3 ± 0.4	0.3 ± 0.1	7.4 ± 0.2	4.4 ± 0.7	0.32	
	Si-O	1.3 ± 0.2	0.2 ± 0.1	2.5 ± 0.2	-	-	
comp. to A	Ir	19.7 ± 0.1	1.7 ± 0.1	7.7 ± 0.1	-	0.37	0.011
	Si-O	2.3 ± 0.8	0.6 ± 0.2	2.2 ± 0.4	-		

In relation to the obtained mass density values, the picture becomes even more complex. Now only two pronounced critical angles can be obtained for certain. The upper layer's bottom density becomes higher than for sample B, whereas the bottom density of the remaining metallic iridium is halved. Chronoamperometry seems to form an intermediate morphology between the two original layers (formed by CV) as the mass density (in turn the electron density) accumulates at this point. Recalculating the mass loss within the metallic layer reveals, although it still appears as 20 nm in thickness, that the material transformation becomes almost one third of the original layer. In relation to the electrochemical procedure, this means an increasing porosity of the iridium substrate layer. Taking a look at the XRDS data, the interpretation becomes even more complex concerning the parameter evolution over depth. Fig.5.13 does not reflect the trend observed from XRR completely. The re-calculated density values from the Yoneda wings almost coincide with obtained XRR values (for the upper layer: ~ 1.5 g/cm³ and for the lower: ~ 6.0 g/cm³). The intensity observed for sample C in off-specular direction is increased by around one order of magnitude. This clearly indicates a roughening of the thin iridium film. This is also supported by the obtained roughness values. The upper region becomes strongly roughened, whereas the lower region stays comparable to sample A. XRR, in contrast, indicates smoothing rather than roughening. We assume that the origin of the discrepancy between these two measurements can be found in the strongly different orientation of the probing direction (specular vs. off-specular) relative to the final morphology. ξ of the upper layer shows a large jump between 15-20 nm below the air-surface interface, whereas the lower layer exhibits small ξ values. This gives a direct hint that porosity is likely present in the metallic substrate and plays a major role during the electrochemical transformation. The ξ -jump in a depth of ~ 17 nm is possibly representing a homogeneous orientation of roughness in this region, which could point towards some tilt against the specular direction of the lattice planes. However, if this connected to the already mentioned deviation between XRR and XRDS cannot be resolved with the present data. Finally, also the XRDS mass density differs slightly from XRR. It stays for both layers approximately constant (upper: ~ 4.0 g/cm³; lower: 7.5 g/cm³). Continuing from the former observations, these values also do not match the XRR trend. Compared to sample B, this indicates what was already indicated by the XRR of sample C, that the morphology and layer transformation under CV with CA appears to be completely different from the pure CV. Since we cannot provide data for lower 2θ rocking curves, the behavior of the upper most area remains undescribed. With such low incidence angles, many difficulties arise, for example, the specular peak broadening and lower resolution due

to the beam footprint. Giving an explanation for the observed deviation between XRR and XRDS is not a simple matter. On the one hand, the assumed layer stack could be far more complex than expected and underestimated with our two-layer model. Since absorption and dispersion factors for the two layers are calculated on the basis of XRR fit results, the obtained penetration depth might not be correctly represented. A deviation from the model under the given refinement strategy for chronoamperometric treatment cannot be excluded. Sticking to a strict two-layer model might also contribute to this contradiction. Finally, also the contributions of the two layers are different. As depicted in Fig.5.13, only the last three XRDS curves exhibit significant contributions from the lower layer and could be evaluated. Hence, to resolve the properties of both layers in more detail, a further study based on e.g. smaller 2θ steps would be required. The true origin of this deviation remains at the moment unknown. In addition to XRR and XRDS, SEM images with corresponding EDX spectra can be found in Fig. 5.14. Sulfur containing areas are rarely present and oxygen can again be found along the borders of the remaining iridium layer. Compared to sample B, these pictures can be understood as per the above mentioned considerations. The lower amount of sulfur found on the surface might also be related to the chronoamperometric procedure. It is simply either oxidized or adhesion on the oxidized surface becomes less and anion interaction is too weak. In forming a smooth surface, as well as some intermediate layer, the structure appears again, unsurprisingly, to easily become partially detached. The image taken at the higher resolution in Fig. 5.15 depicts clearly a different surface morphology compared to sample A. The surface appears more homogeneous and surface cracks appear to become 'closed' after chronoamperometry. One should also notice the difficulties of taking electron microscopy pictures of these oxidized samples since they are very sensitive to a vacuum and as well undergo various charging effects next to (likely) beam induced changes (carbon deposition). Altogether this supports our theory for CA that the layer becomes compacted and surface gets likely roughened, although the exact representation of the XRR-XRDS deviation remains slightly nebulous.

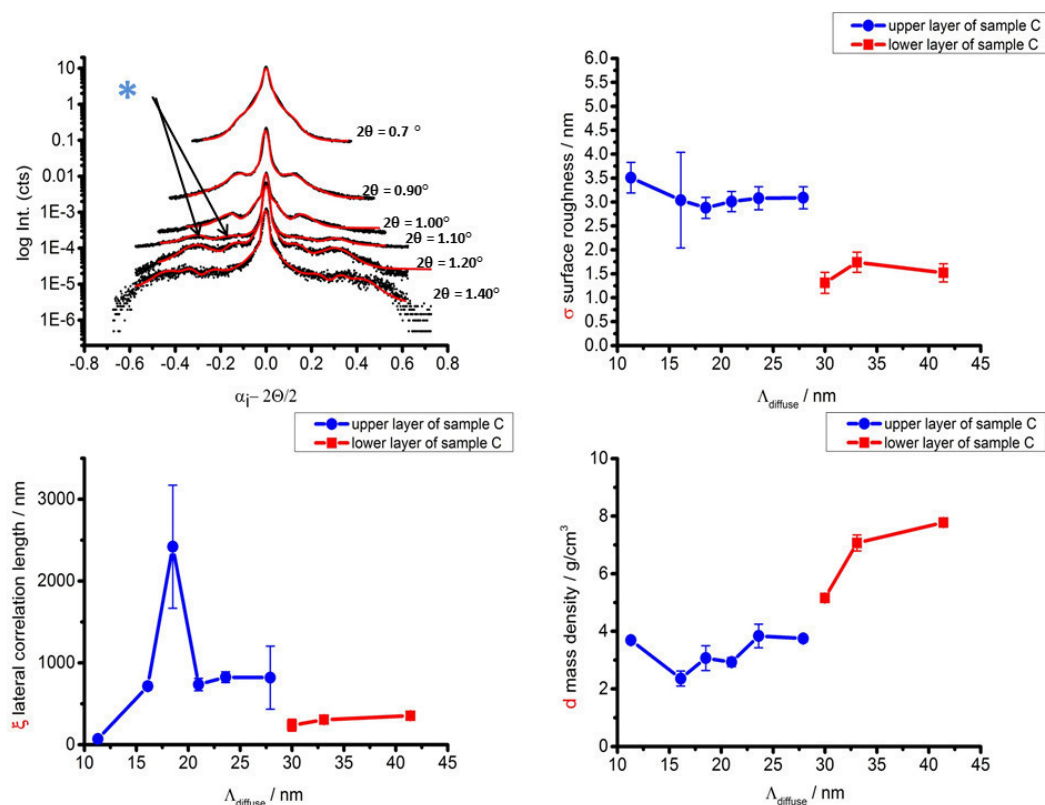


Fig. 5.13: Diffuse scattering rocking curves taken at various 2θ for sample C with corresponding extracted fractal parameters

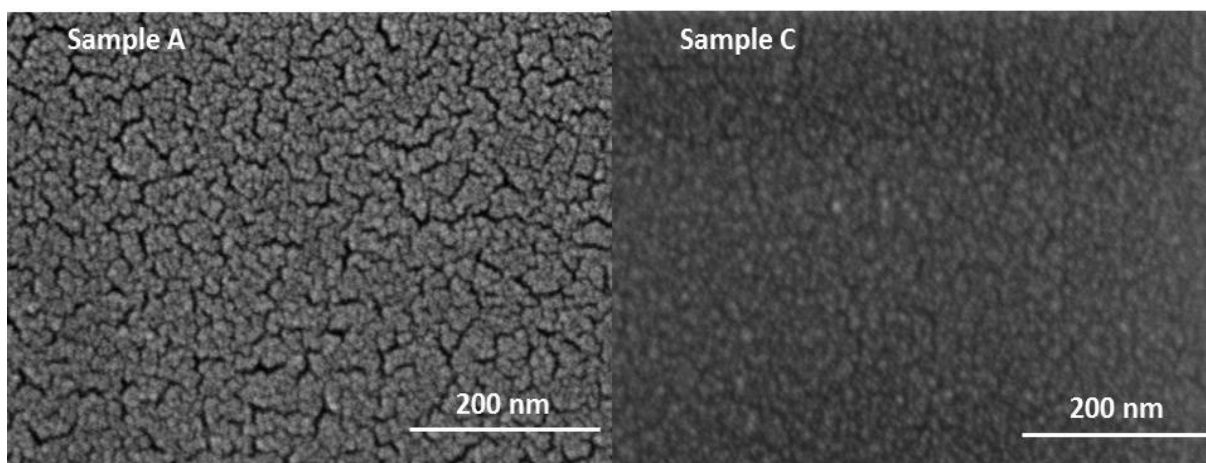


Fig. 5.14: SEM image in higher magnification. The more homogeneous surface in addition to almost no big surface cracks compared to sample A should be noticed.

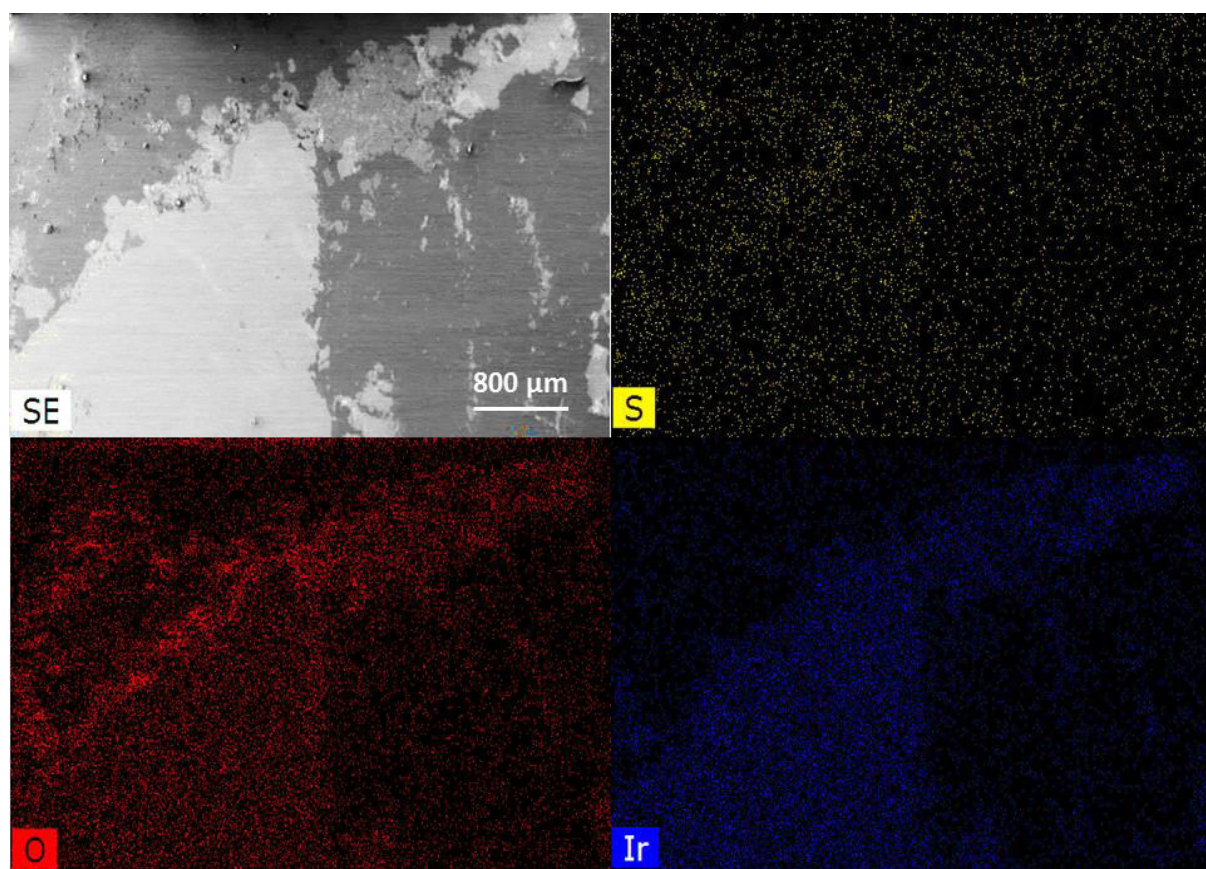


Fig. 5.15: SEM image and corresponding EDX maps of sample C.

5.4.4 Higher number of CV cycles

In the third experiment, the sample was exposed to higher cycle numbers. This treatment represents the classic growth of iridium oxides on the surface of a metallic iridium substrate. All well-known work regarding iridium in combination with the OER reaction is based on this technique for growing the active surface film. A continuous increase of the peak currents in the oxide region of the CV is accompanied by a cycle by cycle growth of the oxide layer. The exact description of this layer growth is still under discussion in the literature. Otten^(23,24) and co-workers proved first that the earlier postulated layer-by-layer oxidation and reduction is not the true origin since ellipsometry results did

not indicate a stoichiometric change within the layer. They claimed that the film formed on the surface appears to have a metallic character and is formed within pits on the original surface. Another interesting fact is the change of the oxidation state of the iridium itself within the layer during this treatment. Since we are dealing with the morphology and crystal-lattice, the examination of the electronic structure can be found in various papers^(15,19). In a possible contribute to the investigation of the layer formation and resulting morphology, we decided to apply 208 cycles (4 slow – 200 fast – 4 slow) to allow a thick oxide layer grow on top of our sputtered iridium layer. The electrochemical treatment is shown in Fig. 5.16. The first four and last four cycles were measured with 1 mV/s while the remaining cycles were scanned with 20 mV/s to gain a high number of cycles within a reasonable amount of time. Again, the shape and observed effects in the slow scan curves are comparable with those discussed for samples A, B and C. Additionally, one can observe that resistance and diffusion control play a role at higher scan speeds. The CV becomes less defined and peaks become very broad. One can conclude that capacitance is significantly affected at a higher scan speed for such thin layers and that the diffusion of counter ions at the interface becomes rate determining. The transport of the electrons inside the oxidized surface, and probably inside the double layer itself, becomes very fast in comparison to the ion diffusion. Interestingly, the faster CVs show a reduction at approximately 0.82 V in the cathodic regime over approximately the first 50 cycles. In the anodic regime the same effect can be observed and hence be identified as a reversible process. This might be explained by the following: since the first cycles were done with a very slow scan speed, a homogeneous thin oxide surface layer was formed. Since we discussed the diffusion limitation induced by the higher scan speed in the following cycles, this layer might play the key role. As long as the layer can handle this quick scan speed, a higher activity at the onset before the OER region (0.8-1.3 V) can be found. As the layer grows thicker, the conductivity and hence the diffusion of charge carriers at the surface changes^(20,22,23). It seems that as long as this reversibility continues, the oxygen evolution activity is also higher^(22,22, 42). The last cycles don't show reduction or significant OER activity, hence the reaction might have reached a steady state and the remaining cycles don't seriously affect the layer anymore. An "ageing" of the Ir/Ir-O interface over the last cycles is also a possible explanation. In the slow speed cycles one can clearly see a peak shift from the known peak at around 0.96 V (red curve) towards more positive potentials after the 200 fast cycles (Fig. 5.16, blue curve) to 1.08 V (ΔV : 0.12 V). This shift is likely a consequence of the thicker oxide layer on the surface. It changes conductivity and for a further oxidation of the surface a more positive potential is needed.

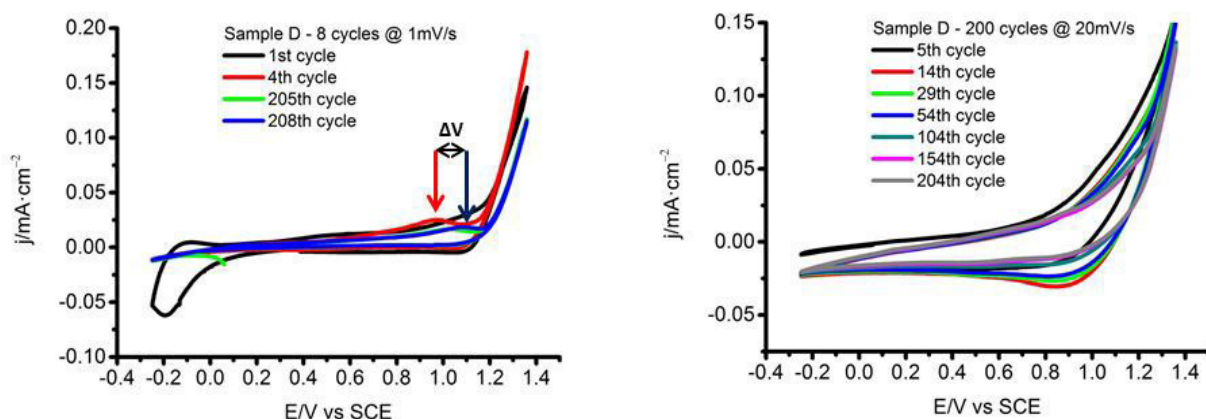


Fig. 5.16: CV curves of sample C, left: 8 cycles at 1 mV/s; right: 200 cycles at 20 mV/s.

Fig. 5.17 and Tab. 5.4 summarize the results from modeling the XRR curve of sample D. Our expectations were fulfilled since the obtained layer parameter appears similar to sample B, which

indicates that our sample model is satisfactory. Only the roughening of the upper layer does not appear to be that precisely determined, which is likely caused by the low interference and heterogeneity of the surface layer. Additionally, the three critical angles were found to be present and fit again to observed density values, comparable to sample B. Surprisingly, the layer thickness seems thin for a number of 208 cycles. We consider the treatment to be ineffective to the thin Ir film, with 200 cycles at 20 mV/s. The scan speed is likely too fast to let the film grow homogeneously as well to apply favorable oxidative conditions on such a thin film. Since massive bulk iridium is not present and the metal substrate is limited in availability, the transformation might stop at a certain point due the metallic film to become discontinuous or to be passivated by aging of the surface. For the other parameters, the same explanations are valid as for sample B.

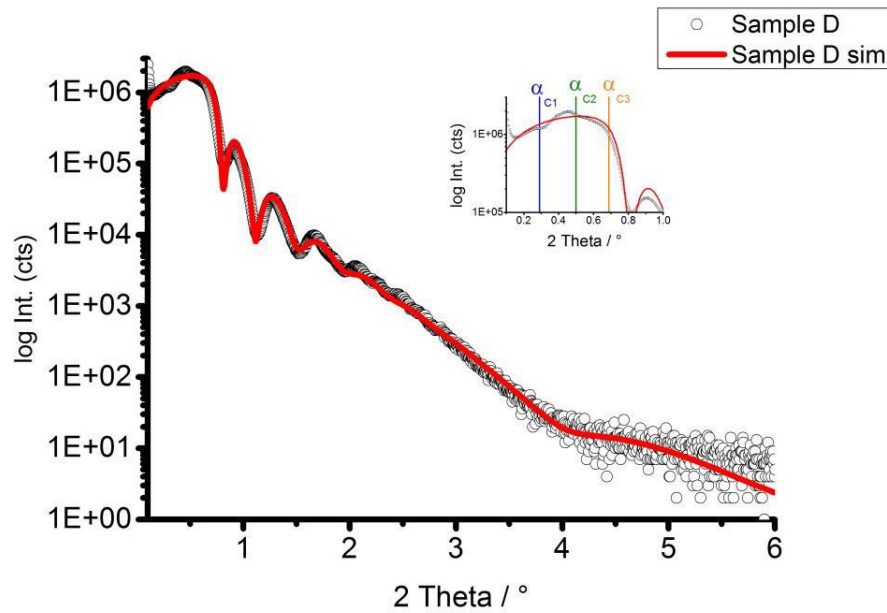


Fig. 5.17: XRR measurement of sample D with corresponding fit curve. The inset indicates the three critical angles found ($\alpha_{C1} = 0.29^\circ$ 2 θ , $\alpha_{C2} = 0.50^\circ$ 2 θ , $\alpha_{C3} = 0.69^\circ$ 2 θ)

Tab. 5.4: XRR fit results obtained from sample D.

	layer	thickness (nm)	roughness (nm)	density top (g/cm ³)	density bottom (g/cm ³)	$\alpha_c (^\circ)$	χ^2
D	Ir (upper layer)	33.8 ± 3.9	1.1 ± 1.1	0.5 ± 0.1	0.7 ± 0.1	0.14	0.008
	Ir (lower layer)	17.7 ± 0.4	1.8 ± 0.1	8.2 ± 0.2	7.2 ± 0.3	0.34	
	Si-O	1.3 ± 0.2	0.2 ± 0.1	2.7 ± 0.2	-		
comp. to A	Ir	19.7 ± 0.1	1.7 ± 0.1	7.7 ± 0.1	-	0.37	0.011
	Si-O	2.3 ± 0.8	0.6 ± 0.2	2.2 ± 0.4	-		

For the investigation of the fractal parameters, the XRDS rocking curves were measured again and displayed in Fig. 5.18 along with the according extracted parameters over penetration depth. The similarities are closely related to sample B. Higher off-specular intensity in the rocking curves, as found in sample C, points again towards a roughening of the surface. XRDS examines the roughness distribution in particular and therefore describes it more precisely than pure specular XRR (as the

XRR σ value exhibits a 100% error margin in this case). The resolution of the peaks appears broad and the XRDS curve less structured, which also indicates the strong heterogeneity of the surface. The roughness evolution can basically be described along the whole penetrated depth as continuously rough over both layers. ξ starts with low values and increases to a depth of approximately 15 nm, before it drops again. The very first data point for the lower Ir region within the layer appears to be very low. The entire curve indicates a nice trend, which might label this point as outlier. On the other hand, if the trend is assumed to be correct there is again a layer formed with defined interfaces. Neither σ nor density values directly support this assumption as they don't show any significant changes at this depth. The density evolution appears similar to sample B and since these two samples were exposed solely to potential cycling, the similarities are not surprising. The recalculated density values from the Yoneda wings do not completely coincide with obtained XRR values (for the upper layer: $\sim 1.8 \text{ g/cm}^3$ and for the lower: $\sim 7.26 \text{ g/cm}^3$).

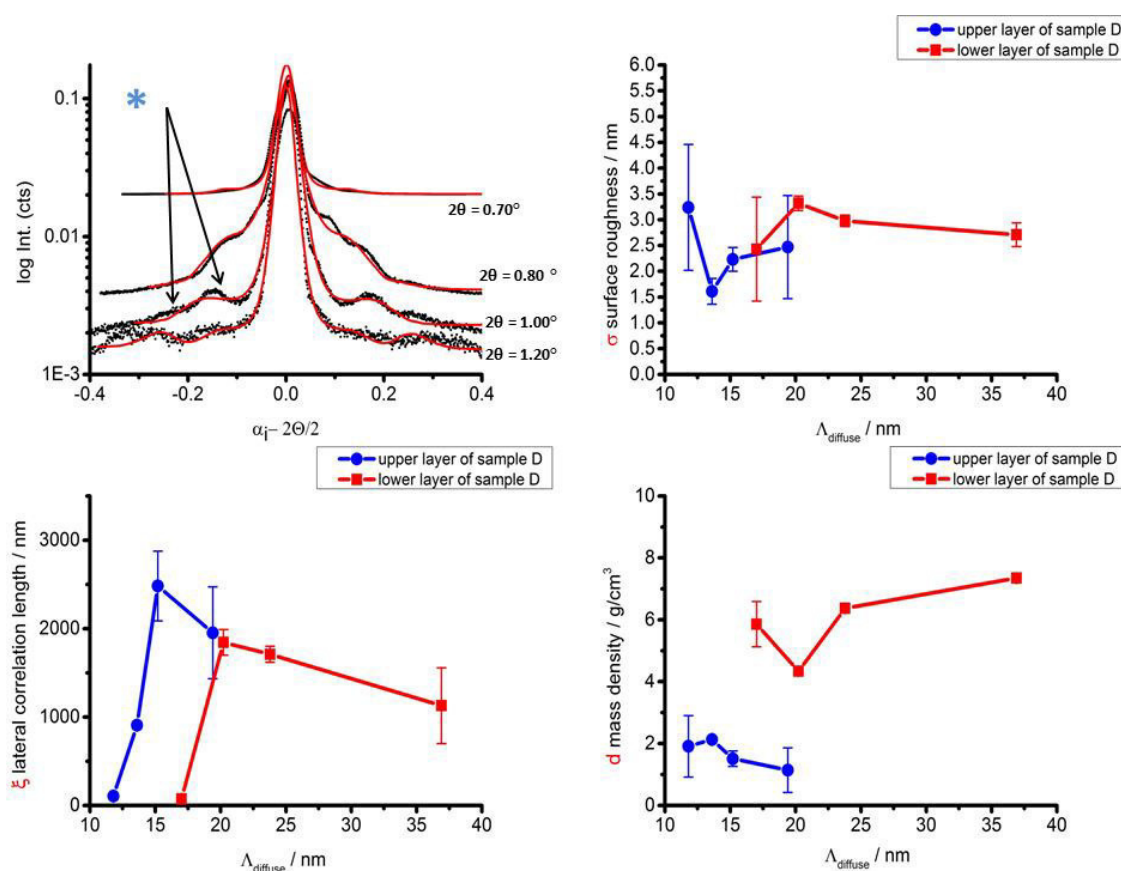


Fig. 5.18: Diffuse scattering rocking curves taken at various 2θ for sample D with corresponding extracted fractal parameters

The SEM image and EDX map of sample D reveal again the partial loss of the iridium layer due to the higher cycle number (Fig. 5.20). In the oxygen EDX map, one can find a strong accumulation of oxygen in two rows in the lower left image part, whereas the sulfur content is hardly visible. The height contrast in the image points to a possible particle growth. The greatly magnified image in Fig. 5.19 clearly depicts the case of a surface breakup and the layer arrangement does not look homogeneous as both coarsely and finely structured areas are visible. XRR and XRDS values are again in good agreement with each other. In addition, the lateral correlation can be compared to SEM images on similar length scales. For this very rough treated sample the model does not perfectly describe the correlation anymore. This can be seen in the deviation from the fit curves and the measured ones. Also, the extremely heterogeneous surface and incompleteness exacerbates the

measurement as well as data interpretation. It is still sufficient to draw conclusions regarding trends, especially for XRR, and would probably request a further improvement for the XRDS scans. Nevertheless, we are able to describe three completely different scenarios with one developed morphological model. The interesting finding during Grazing Incidence X-ray Diffraction is described separately in a later paragraph.

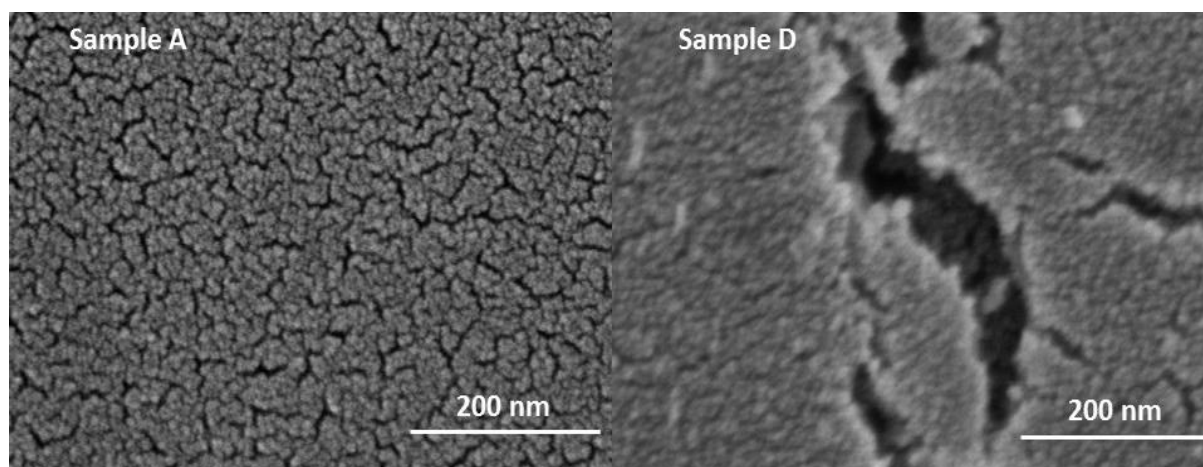


Fig. 5.19: SEM image of sample D. One notices the coarse- and fine grinded areas beside the opened surface cracks.

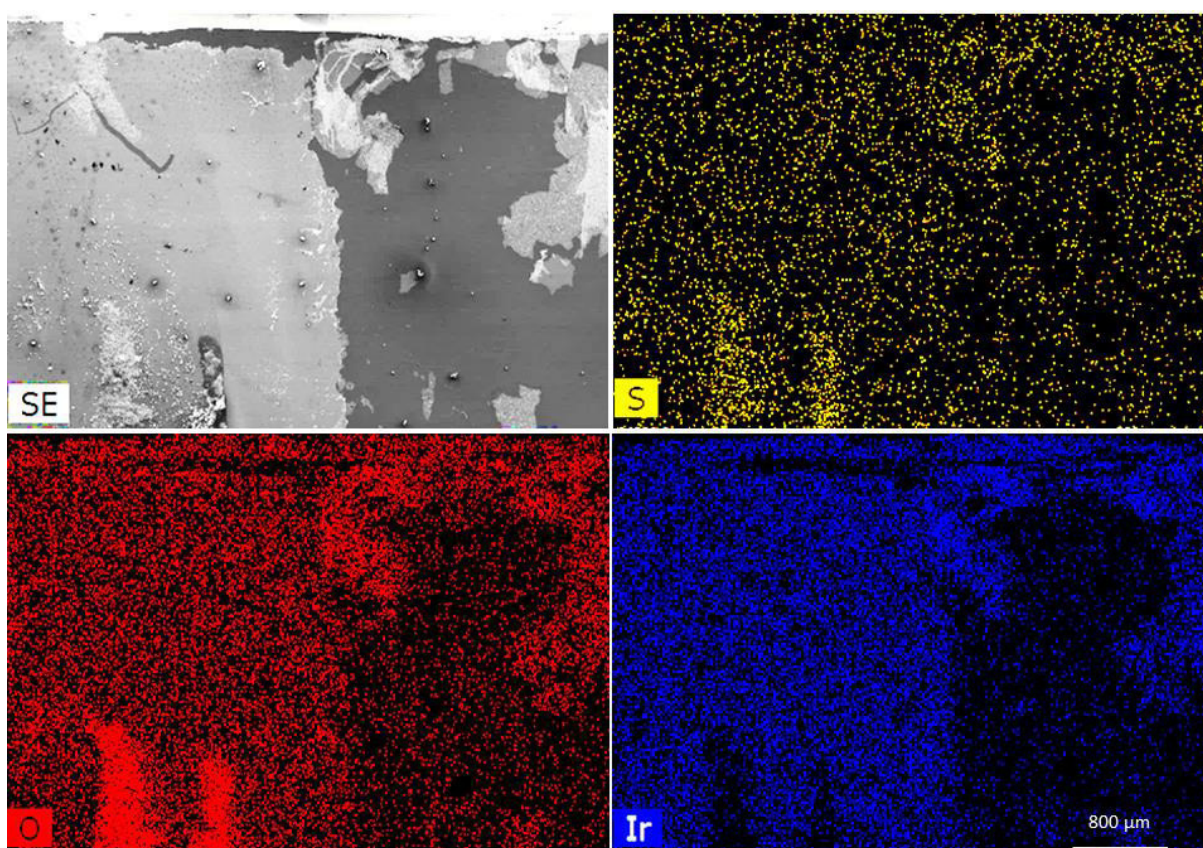


Fig. 5.20: EDX map of Ir and O of sample D. The likely particle formation in the two “fingers” containing oxygen on the lower left side image can be clearly seen.

5.4.5 Changes after the first cycle

In all three samples discussed above there was one very interesting observation: the complete inhibition of hydrogen adsorption after the first cycle of cyclic voltammetry. As stated above, we hypothesize that this inhibition might be caused by the depositing of a sulfate layer or a thin layer of oxide formed on the sample surface. Since the roughness of the sputtered samples hinders the use of X-ray methods in finding corroborative structural evidence for this hypothesis, samples prepared by e-beam evaporation were utilized instead. This preparation method provides a very well ordered and dense Ir layer with a high surface quality, low roughness and sharp specular reflections compared to those of the sputtered samples. Fig. 5.21 displays the first cycle and the LSV (linear sweep voltammetry) up to 0.609 V before a 1 h CA was started at that point. The electrochemical data are better defined and appear smoother compared to those of the sputter coated samples. Already in this first cycle, the hydrogen adsorption and HER are pronounced, and only one additional peak appearing around +0.06 V (~ 0.304 V vs. RHE) can be found. This peak can be attributed to the desorption of hydrogen from the metallic surface^(21,41). With the second half cycle (LSV), this peak becomes smaller and is shifted to lower potentials. This can be rationalized as the surface termination being altered by the first cycle due to sulfate coverage, hence less hydrogen can be adsorbed⁽³⁸⁾. Whether this is the case due to the formation of a monolayer oxide or from a simple blocking effect of the sulfate cannot be exactly distinguished after one cycle. It is likely a combination of both. The subsequent CA proceeds as expected, with an almost immediate deactivation and a very slow decrease in the current over time.

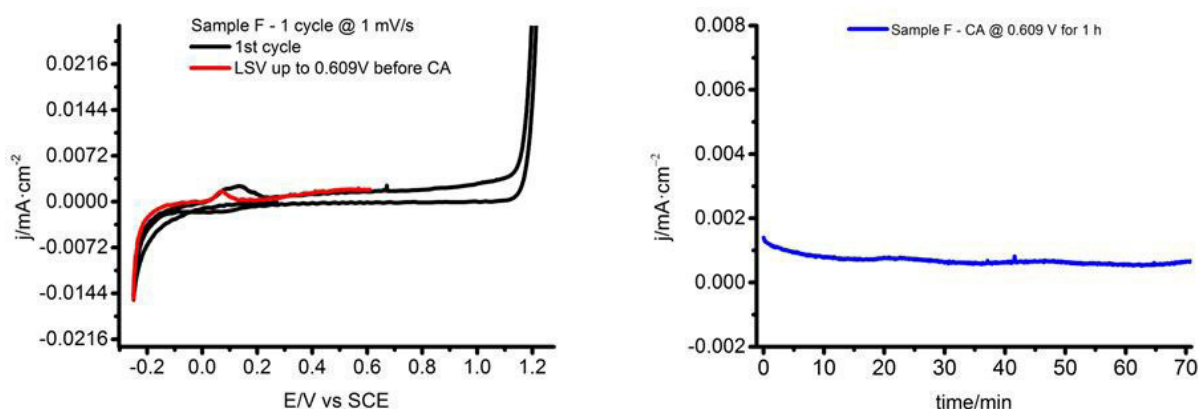


Fig. 5.21: One cycle cyclovoltammetry and half LSV (left), subsequent chronoamperometry for 1 h (right) of sample F.

The reflectometry results are represented in Fig. 5.21 and Tab. 5.5. Between the two measurements before and after the treatment, only very small changes can be noticed. The reflectogram is well pronounced due to the very homogeneous and dense layer structure. Consequently, it can be assumed that a much stronger treatment, such as running a much higher number of CV cycles, would be necessary in order to cause noticeable changes. The assumption made already in chapter 4, the activity dependence on the morphological appearance of the layer, is also proven here. The inflexible structure generated by e-beam evaporation is not very active under OER conditions and probably requires a much longer conditioning time to break up the crystalline in order to become an efficient electrode. In contrast to the XRR, the SEM images shown in Fig. 5.24 clearly depict a strong modification of the surface by this very moderate treatment. The break up into smaller and larger compartments of the Ir layer can be well observed, as is the full coverage of the remaining part by SO_4^{2-} .

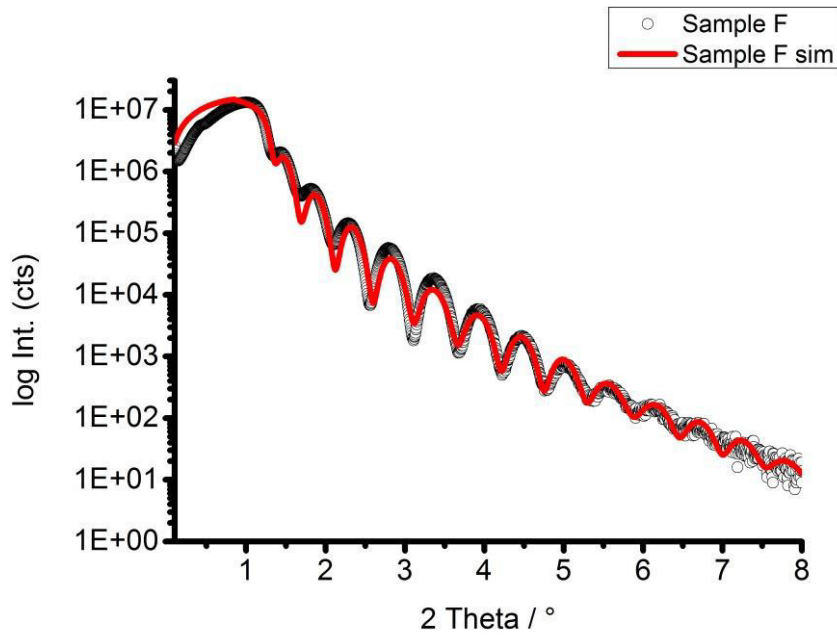


Fig. 5.22: XRR and corresponding fit curve of sample F.

Tab. 5.5: XRR fit results for sample F.

	layer	thickness (nm)	roughness (nm)	density ³ (g/cm ³)	α_c (°)	χ^2
F	Ir	15.4 ± 0.1	0.3 ± 0.1	21.9 ± 0.1	0.60	0.010
	SiO _x	1.7 ± 0.5	0.4 ± 0.1	2.6 ± 0.5		
E	Ir	15.5 ± 0.1	0.5 ± 0.1	22.5 ± 0.7	0.60	0.010
	SiO _x	1.1 ± 0.5	0.7 ± 0.4	1.9 ± 0.7		

Fig. 5.23 summarizes the results of the diffuse scattering. Recorder rocking curves appear almost like a text book example. Most surprising, the intensity scale of the oxidized sample in diffuse scattering is about six orders of magnitude higher than before. In case of such a dense film, this can be due to one reason primarily: the film was extremely stressed. Higher intensity in off-specular direction means usually higher roughness values. In the present case, this is unreliable. XRR curves before and after electrochemistry are on very similar scales and such a high deviation cannot be observed. Since XRR probes exclusively the specular direction and in XRDS the surface is tilted around the specular area, this explanation becomes reasonable. We didn't observe this behavior for samples described in chapter 4, which we believe is related to the different sample thickness (5 vs. 15 nm). The trends found for the extracted parameters are unsurprisingly very homogeneous and almost constant. Roughness as well lateral correlation lengths do not show any considerable changes, neither does the density. Except that their scale has shifted slightly, as ξ is now at ~ 2000 nm (instead of 3000 nm originally) and density becomes 14 to 18 g/cm³. The decrease in ξ is probably caused by the breakup of the almost completely closed surface (see SEM image and EDX mapping in Fig. 5.2). This also counts for the lower density found, since the layer becomes discontinuous in larger parts. Small irregularities, such as defects and small holes, probably act as nucleation points for the partial destruction of the Ir layer already during the first cycle of the OER. In addition, the e-beam evaporation causes a very dense and therefore likely extremely stressed layer. The applied potential allows the surface to break up in order to relax the layer. One finds very sharp edges along the

border of the remaining iridium (see SEM Fig. 5.24, Ir-free areas) we count this as strong evidence for the previous statement. The formation of a sulfate layer next to a possible formed monolayer oxide would also explain the effect observed in the first three samples. The loss of the hydrogen adsorption capacity is caused in this case simply by the presence of stronger binding sulfate in the selected potential range. Single crystal studies revealed a clear difference between different electrolyte anion adlayers, such as SO_4^{2-} and ClO_4^- (21,40). The very well-defined e-beam surface makes the attack more homogeneously possible than on the crack-structured surface of the sputtered Ir layer. In contrast, the columnar growth of the sputtered samples makes the transformation of the iridium lattice into its oxo-hydroxo layer easier.

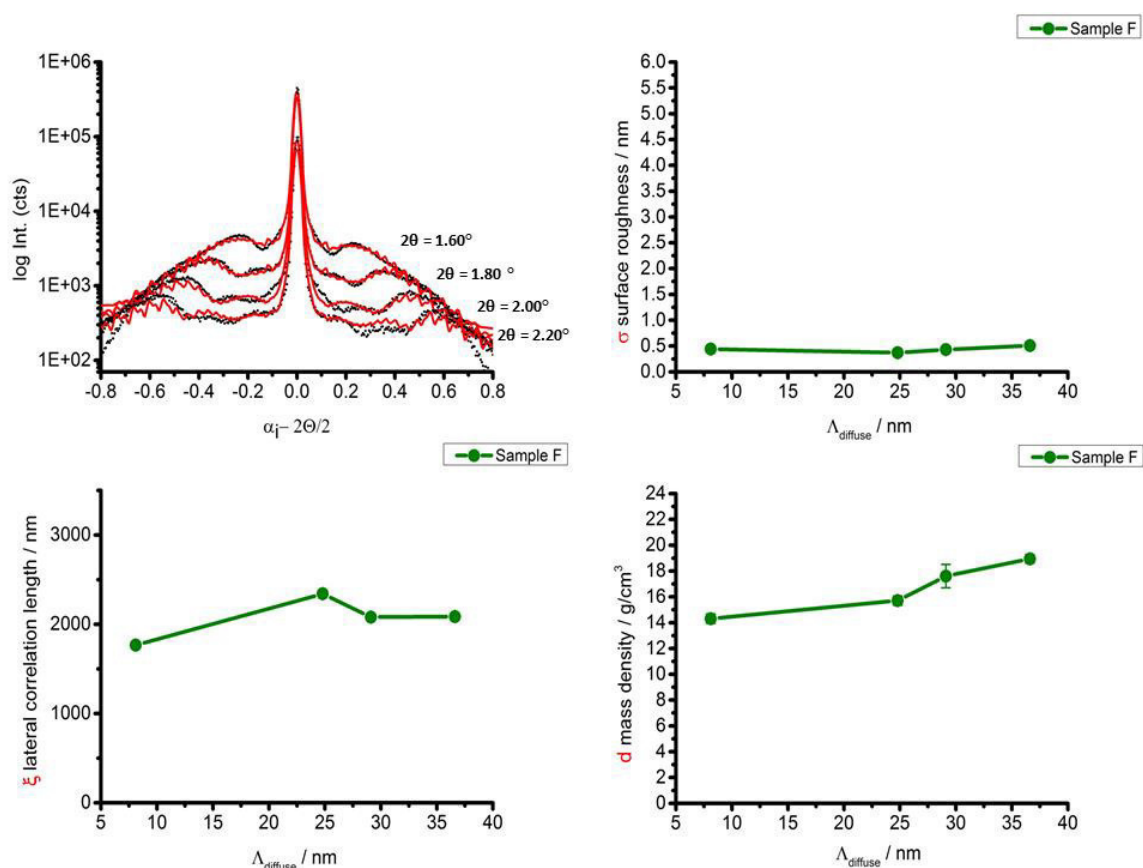


Fig. 5.23: Diffuse scattering rocking curves taken at various 2θ for sample F with corresponding extracted fractal parameters

This section follows the electrochemical degradation of iridium by four different treatments. The observed morphology changes are clearly different in each case and could be analyzed by X-ray Reflectometry as well X-ray Diffuse Scattering, supported by scanning electron microscopy. Nevertheless, as has already been pointed out several times, the destruction of the ordered iridium lattice is a strong prerequisite for higher activity in OER by forming the oxo-hydroxo surface layer which catalyzes oxygen evolution. The next section focuses on the Grazing Incidence X-ray Diffraction results in order to demonstrate the application of this very sensitive technique on our electrocatalytic surface.

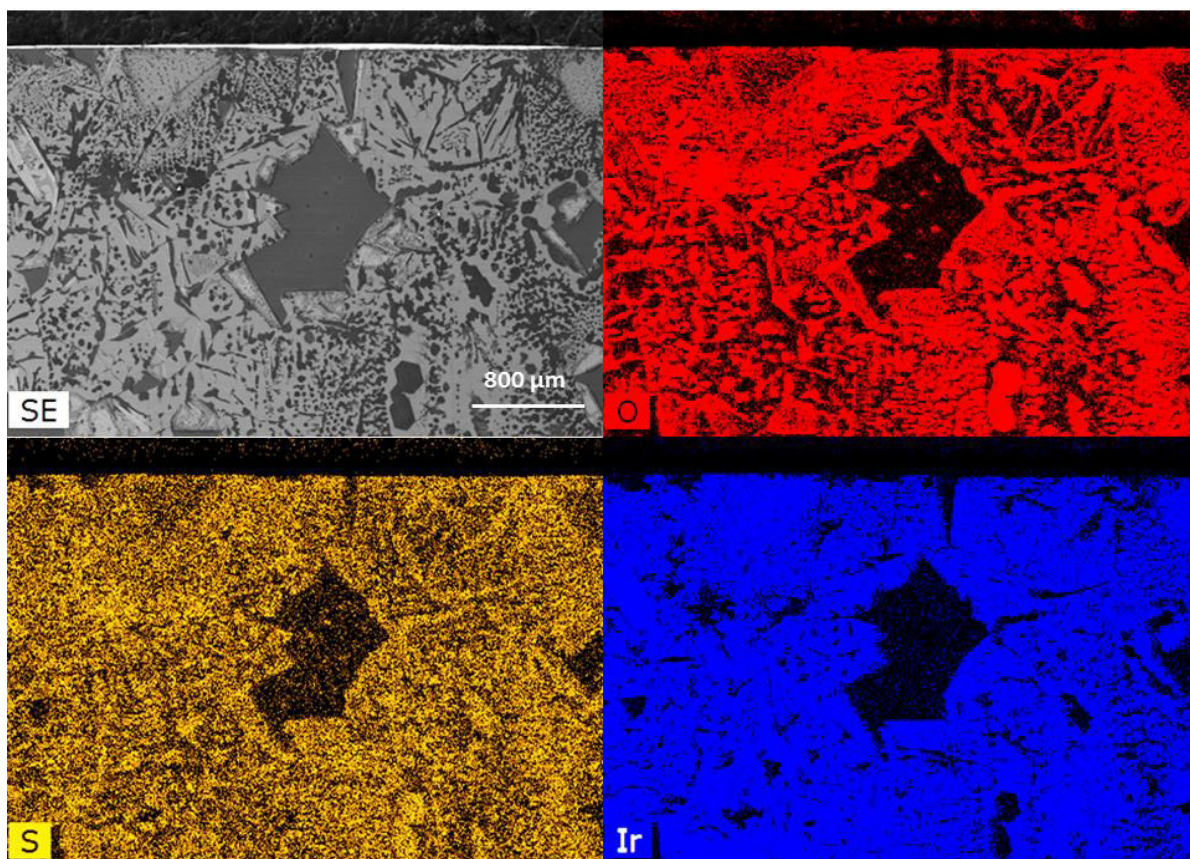


Fig. 5.24: SEM surface image of sample F with measured EDX elemental mapping.

5.5 Grazing incidence X-ray diffraction

The GIXRD measurements^(47,48) were taken at $0.4^\circ \theta$ which is slightly above the critical angle of each sample in order to ensure approximately the same penetration depth (~ 10 nm, calculated for the corresponding α_c , not the nominal value, see chapter 2). Results for samples A and D and the corresponding fit curves are represented in Fig. 5.25. Already executed morphological investigations revealed significant changes on the surface for each chosen scenario. Structural investigations by GIXRD also reveal an interesting behavior, which one can follow up by extracting the parameters for the 111 reflection of the iridium lattice. Table 5.6 sums up the refinement results for the four samples. For the slowly cycled sample B, the intensity of the 111 reflection is significantly decreased. It also exhibits a broadening. A correct meaningful interpretation is difficult to obtain, since there exists more than just one possibility which might lead to this observed effect. In principle, one can point out that the very slowly performed cyclic voltammetry gives the layer the opportunity to transform slowly, and thereby well equilibrated to the applied conditions, into the amorphous iridium-oxo-hydroxo surface layer. The rise of an unidentified shoulder on the left side of the 111 reflection in sample B might also support this assumption. Since in case of the three oxidized samples two layers of different density could always be identified, as well morphology, this supports the finding of this shoulder. In addition, one needs to keep in mind the layer loss by detachment and that dissolution can also account for this. A very small peak of Si 311 appearing at $\sim 55.1^\circ 2\theta$ indicates the latter postulated effect; therefore it is likely a combination of both these reasons. Sample C, in contrast, is obviously again higher in intensity and the two before mentioned peaks (the left hand-side shoulder to Ir 111 as well the Si 311 reflection) became more pronounced. As we concluded

from XRR and XRDS for CA that a concentration of density between the two layers is found, we tend to believe this is reflected in this result also. The growth of the amorphous phase is probably preferred by chronoamperometry (noted as “unidentified” in Fig. 5.24). The higher intensity found for C supports our finding of a more homogeneous layer formed by CA and this enhances diffraction signals. Nevertheless, the dissolution plays a role in the OER regime as well and follows almost exactly the OER-activity trend⁽⁴⁹⁾. Hence the origin of the unidentified phase remains unknown.

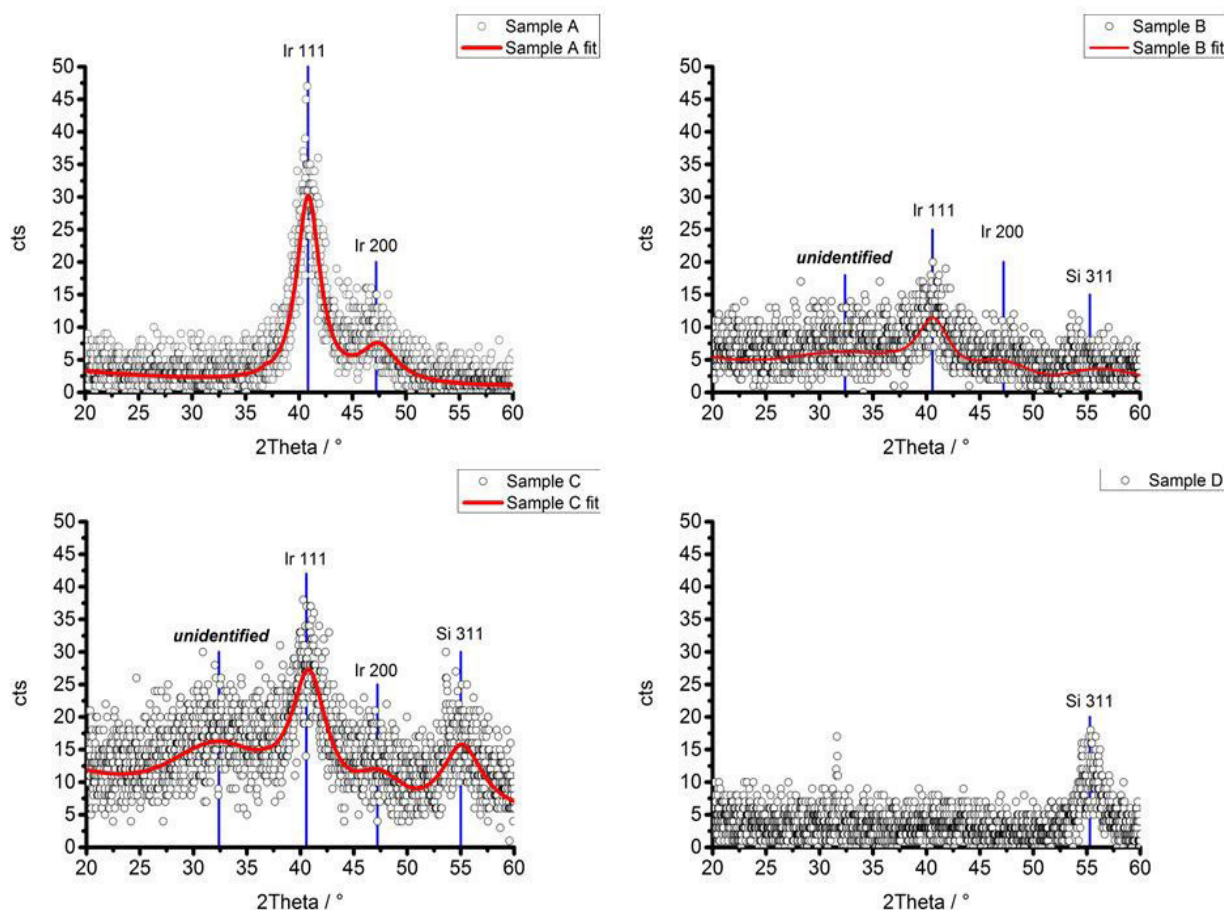


Fig. 5.25: GIXRD patterns of samples A to D

Tab. 5.6: Obtained fit results for samples A to C

	2θ (Ir 111) (°)	FWHM (Ir 111) (°)	Integr. Intensity (Ir 111)
Sample A	40.98 ± 0.09	2.60 ± 0.26	14.48 ± 1.71
Sample B	40.44 ± 0.29	2.92 ± 1.17	7.04 ± 0.20
Sample C	40.70 ± 0.21	3.35 ± 0.82	20.11 ± 3.75
Sample D	-	-	-
Ir (PDF 06-0598)	40.663	-	-

The expected trend of degradation of the Ir metal itself is in accordance with the successive 111 peak broadening observed for each treatment. In close relation, the peak position is shifted with every treatment to lower 2θ values. 208 cycles of cyclic voltammetry completely destroys the surface near the iridium lattice. Sample D exhibits no detectable Ir reflections anymore, only Si 311 is visible. Taking a look at the XRR (Fig. 5.17) of sample D, Kiessig fringes are still present, thereby indicating the presence of a different electron density on the surface as compared to the substrate in our two-layer model. The disappearance of the diffraction signals can be, in this case, the probable reason for the transformation of the surface-near Ir lattice of the metallic layer into amorphous phase by

oxidation. The 0.4° incidence angle allows a penetration depth of roughly 10-12 nm, whereas the layer thickness is almost 20 nm and, even though the electron density is diluted by oxidation, the full layer thickness will probably not be penetrated by the beam at this angle. The resulting diffractogram for sample D can also be seen as the result of restricted penetration depth and the underlying non-oxidized iridium is either still present or became either nanocrystalline or very porous as indicated by the XRD parameter. The 2θ position of the Ir 111 reflection for the face-centered cubic Ir cell has a nominal value of 40.663° (PDF 06-0598). According to the extracted fit parameters, none of the samples exhibits this value. All of them have a larger value and so can be seen as either strained or that some intercalation has taken place and the unit cell became expanded. Since in sample D, the longest cycled sample, the lattice has completely disappeared, one can conclude that the loss of the diffraction signal for Ir is very likely an indication of the structural change within the unit cell of iridium. The broadening of the 111 reflection can have many reasons and therefore cannot be attributed exclusively to one source. Concentration gradients (as we expect a non-stoichiometric compound to be formed on surface), structural defects (point defects, strain, dislocations...) and of course changing crystallite size are just a small fraction of the possible influences for the observed Ir 111 broadening.

To verify the sensitivity of our measurement strategy, the e-beam evaporation prepared samples E and F were analyzed in more detail. With these samples, a full depth-profile over the range from 0.4° up to 1.4° was recorded to monitor the changes before and after electrochemistry on a well ordered and homogeneous Ir layer. Since only one cycle of cyclic voltammetry was performed in connection with a short chronoamperometry, the differences can be expected to be very small. In Fig. 5.26 the integral intensity profile over depth is shown for the Ir 111 reflection (left hand side). It depicts an extreme loss in diffraction intensity of the Ir 111 reflection before and after electrochemistry. The principle shape of the intensity curve is a very complex issue and can be explained by the dynamical theory of diffraction^(47,48). Basically, one can find the highest intensity around α_c . This fact is attributed to the incident and exit wave field being in phase exactly at that point, thereby enhancing each other. This dependence can be approximately understood as $I(\alpha) \sim T^2(\alpha)\tau(\alpha)$ (without considering structure factors, T: transmission coefficient, τ : penetration depth). In addition, the increasing penetration depth and thereby the diffraction cross section are changed with increasing incidence angle. The difference in scattering intensity can be explained by the alteration of the surface as mentioned above, either by detachment/dissolution (less Ir available) or by the transformation of the surface through oxidation or sulfate adsorption. In the range $\alpha < \alpha_c$, the penetration depth is very small and does not vary too strongly between the two samples. At $\alpha > \alpha_c$, the cross-section of the diffracting volume is continuously changing and shows an exponential decay. At approximately 0.7° incidence angle the 15 nm Ir layer is completely penetrated by the X-ray beam. The constant diffraction volume above this point is then mostly influenced by photo absorption. In the right-hand side image in Fig. 5.26, the evaluation of the peak width (FWHM) of the Ir 111 reflection over depth is shown. A remarkably high difference in the observed width between samples E and F can be found. The shape obviously follows the penetration depth and can be again separated into areas before and after α_c . At incidence angles lower than α_c , the effective diffraction volume is smaller than usual domain sizes in the layer and the additionally lower transparency of the sample (as it is the area before the beam can consequently penetrate the material) leads to a broadening of the Ir 111 peak in this regime.

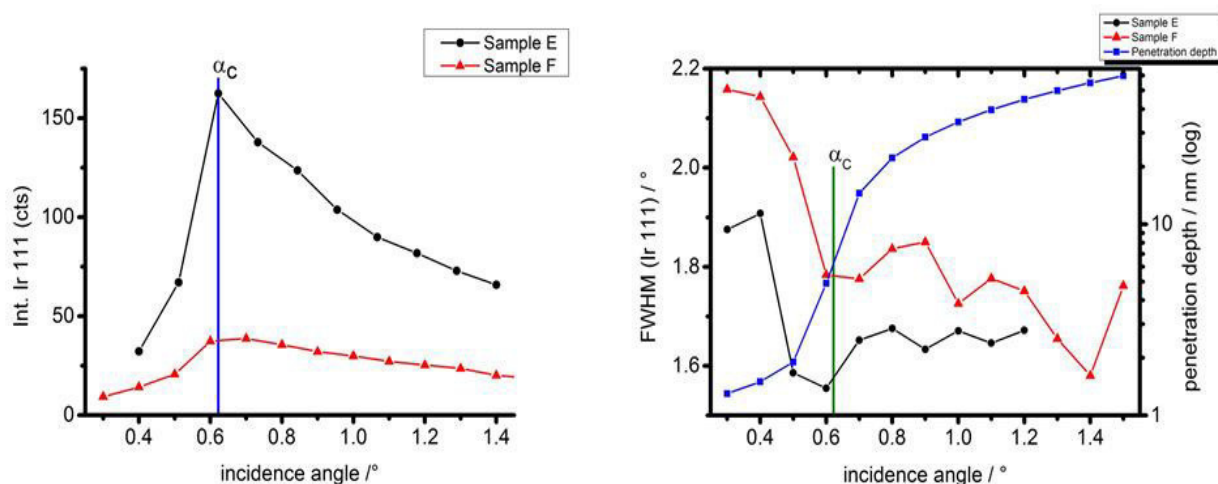


Fig.5.26: left: Intensity depth profile of Ir (111) right: FWHM depth profile of Ir (111) for samples E and F

Above α_c the variation of the cross-section becomes dominant and the FWHM is affected. The curves exhibit fluctuations in the higher incidence angle range, which might be related to the already illuminated underlying substrate. Sample F specially seems to be affected more strongly in this area. The origin of the difference between samples E and F is likely a complex interplay of multiple factors. First, as already mentioned, the changing cross section contributes significantly. Second, the crystallite size over depth will probably be not uniform and therefore influence the width. Third, the adsorption of sulfate on the surface within the CV cycle might introduce a higher number of point defects in the surface-near region and increase the peak width additionally. Finally, the presence of structural defects might become a contributing factor in broadening the Ir 111 reflection after electrochemistry. At the same incidence angle (e.g. 0.6°) the difference in peak width is almost 0.24° (0.235° exact). This is significant evidence for a strong influence after just one cycle of cyclic voltammetry and a short chronoamperometry on the iridium lattice. This demonstrates the ultimate sensitivity of our chosen measurement strategy on a well-defined surface. The effects are clearly visible and detectable, nevertheless the detailed origin could not be uncovered and would require a more dedicated electrochemical treatment and specific sample preparation, as well as an extended series of measurements for further analysis.

5.6 Conclusion

Iridium surfaces and their transformation under OER conditions are of tremendous interest for research and industry due to their great ability to produce hydrogen⁽⁵⁰⁾. It is mainly the OER reaction which makes the whole process energy intensive. With the present work we could demonstrate the unique capabilities of thin film diffraction methods Grazing Incidence X-ray Diffraction, X-ray Reflectometry and X-ray Diffuse Scattering. The use of scanning electron microscopy supported the results in a more visual manner.

The three different treatments applied on the sputtered deposited iridium layer revealed their influence on the Ir lattice. In contrast to the former chapter, the model could be improved (2 layer) and allowed to separate the contributions of the surface and remaining metallic substrate. Cyclic voltammetry, at slow scan speeds, leads to the formation of a ~ 30 nm layer on the surface with a high roughness and a high lateral correlation length. The same treatment followed by a

chronoamperometric procedure lets the layer become smoother and as well decreases ξ drastically, which is indicated by closed cracks in SEM. Interestingly, a CA seems to form an intermediate layer between the two original ones formed by CV, which is indicated somehow by higher density and some ξ -jump in depth found in XRDS. This finding is contradictory to the obtained XRR curve and the reason for it remains unresolved for now. High speed cycling revealed a very similar result as slow speed CV, but with higher porosity as well as very low surface mass density. Although some effects remain not completely explained, one can draw three very important conclusions from this comparison: First, the type of treatment significantly changes the morphology transformation. Pure cycling or a CV followed by CA do not lead to the same morphology. This means that, depending on the desired transformation, the treatment must be considered carefully. Second, kinetics is seriously influencing the morphology. We could demonstrate that a higher scan speed does not yield the same result as a slow speed cycling. The cyclovoltammograms become distorted and strongly controlled by diffusion on the surface, which leads to capacitance as well as to strong resistance effects on such thin films⁽⁵¹⁾. Third, the intrinsic morphology (also in comparison to chapter 4) determines the electrochemical behavior. For the desired reaction, the oxygen evolution, a flexible as well as less densely packed film is of great benefit. Higher surface area as well as a more defective morphology type becomes favorable. Partial detachment, metal dissolution, as well as stressed layers are additional difficulties one needs to consider when handling such thin films in connection with electrocatalysis. In the slow as well as higher cycled sample, the formation of an approximately 30 nm oxidic film influences the diffracted intensity at the Ir layer as well as the peak profile. After more than 200 cycles no diffraction signal could be obtained, indicating a finite oxidation possibility for such thin layers. Chronoamperometry changes the morphology by reconstructing homogeneous on the surface and between the two layers (although higher roughness is detected). GIXRD could detect as well an increasing hump of an amorphous phase, indicating the probable presence of the postulated OER-active oxo-hydroxo iridium species. Electrochemical data are not very characteristic as compared to bulk iridium, and in all samples only one peak could be observed and this was attributed to early stages of sulfate anion transition as well as the blocking H-adsorption by the oxide formation. Both causes will probably contribute to the finding. The absence of massive bulk iridium might lead to this deviation in behavior from classical bulk iridium samples since we dealt with a thickness in the lower nm range.

The test for our technique was performed on a well ordered and highly dense layer deposited by e-beam evaporation and treated with just one cycle of CV. Sensitivity and changes larger than expected were found in the extended data evaluation. As predicted by GID theory, the observed peak intensities and widths show a depth dependency with a pronounced change around the critical angle which proves the sensitivity of the method. The origin of the observed differences between the data before and after electrochemistry can probably be attributed to: the introduction of defects, an (Ir-) concentration gradient due to oxidation or surface inhomogeneities and possibly the loss of material due to detachment. The extreme increase of diffuse scattered intensity for the oxidized e-beam sample revealed another influence: the deposited film was highly stressed, which led to the cracked mirror like SEM image.

Integral methods are important in revealing the connections between microscopic changes and macroscopically measurable parameters and properties, as in the present case, the effect of current density on nm scale roughening and long-range order changes in diffraction. The sensitivity of Grazing Incidence X-ray Diffraction demonstrated here makes this technique a promising candidate for the study of dynamic systems on an integral scale. Still, the importance of the complementary

application of local methods also needs to be acknowledged. This preliminary study shows the necessity of investigating the entire lifecycle of a sample from preparation to treatment under various conditions. It turned out that the nature of the selected model systems has a more pronounced influence on the morphological changes caused by the different electrochemical experiments than expected. Thus, comparability between different model systems, as well as between model and real-life systems, remains an issue. The strong influence of kinetic parameters on the defect formation for different samples and treatments is also an important outcome which can be attributed to the sensitivity and integral nature of GIXRD, XRR and XRDs.

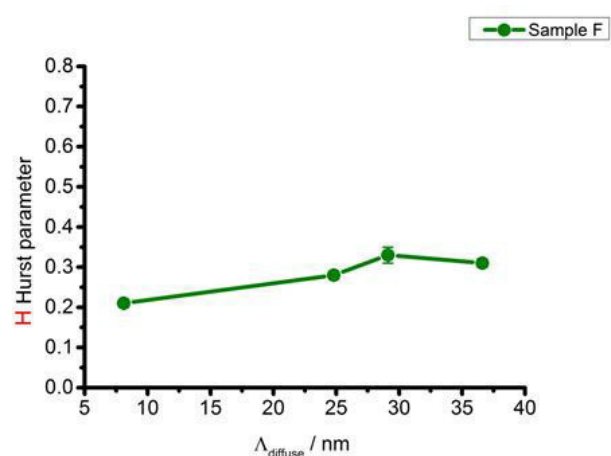
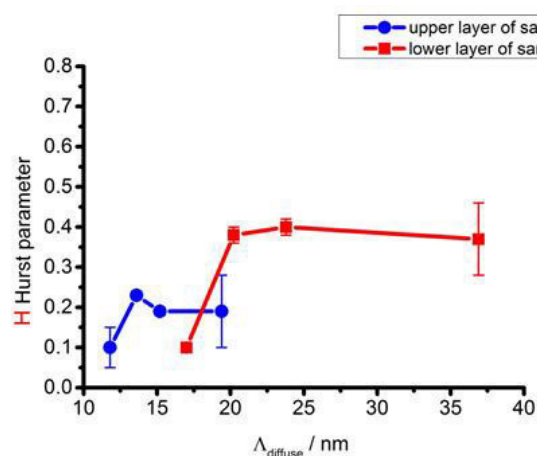
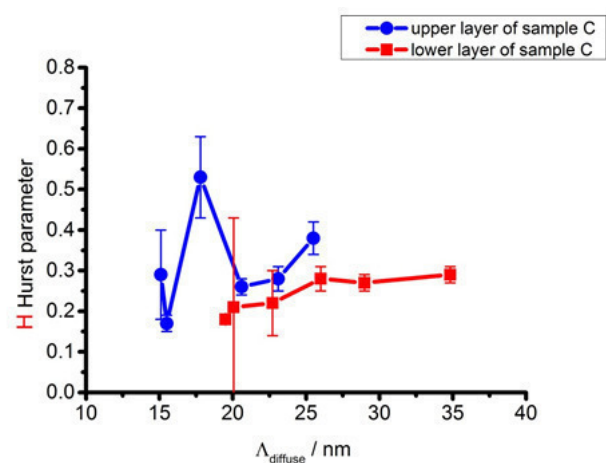
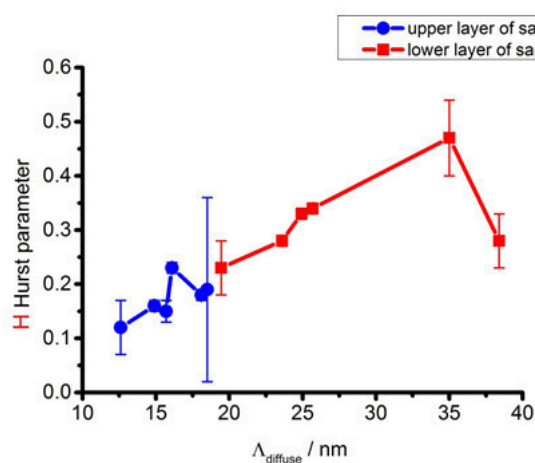
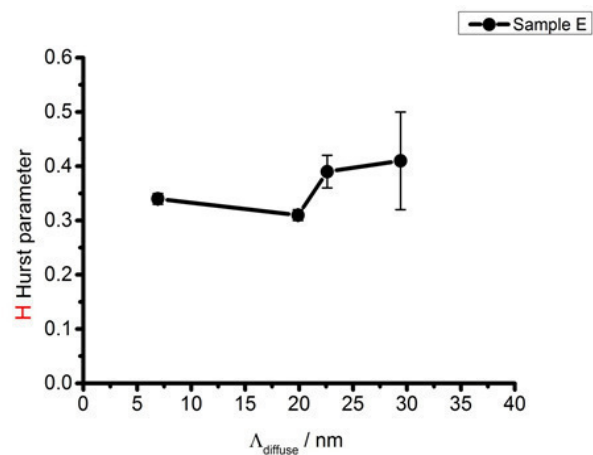
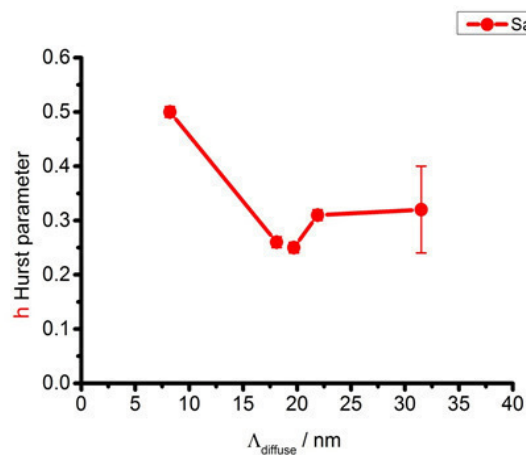
5.7 References

- 1) R. Schlögl, *ChemSusChem* 3 (2010) 209-222
- 2) I. C. Man, H. Su, F. Calle-Vallejo, H. Hansen, J. I. Martinez, N. G. Inoglu, J. Kitchin, T. F. Jaramillo, J. K. Nørskov, J. Rossmeisl, *ChemCatChem* 3 (2011) 1159-1165
- 3) É. A. Paoli, F. Masini, R. Frydenda, D. Deiana, C. Schlaup, M. Malizia, T. W. Hansen, S. Horch, I. E. L. Stephens, I. Chorkendorff, *Chem. Sci.* 6 (2015) 190-196
- 4) J. Rossmeisl, Z.-W. Qu, H. Zhu, G.-J. Kroes, J. Nørskov, *J. Electroanal. Chem.* 607 (2007) 83-89
- 5) M. Wohlfahrt-Mehrens, J. Heitbaum, *J. Electroanal. Chem.* 237 (1987) 251-260
- 6) G. Beni, L. Schiavone, J.-L. Shay, W. C. Dautremont-Smith, B. Schneider, *Nature* 282 (1979) 281-283
- 7) S. Fierro, T. Nagel, H. Baltruschat, C. Comninellis, *Electrochem. Commun.* 9 (2007) 1969-1974
- 8) J. O'M. Bockris, *J. Chem. Phys.* 24 (1956) 817-827
- 9) A. Damjanovic, A. Dey, J. O'M. Bockris, *J. Electrochem. Soc.* 113 (1966) 739-746
- 10) T. Reier, M. Oezaslan, P. Strasser, *ACS Catalysis* 2 (2012) 1765-1772
- 11) M. Carmo, D. L. Fritz, J. Mergel, D. Stolten, *Int. J. Hydrogen Energy* 38 (2013) 4901-4934
- 12) B. Johnson, C. Ranjan, M. Greiner, R. Arrigo, M. E. S. Chuster, B. Höpfner, M. Gorgoi, I. Lauermaun, M. Willinger, A. Knop-Gericke, R. Schlögl, *ChemSusChem* 9 (2016) 1634-1646
- 13) S. Hackwood, L. M. Schiavone, W. C. Dautremont-Smith, G. Beni, *J. Electrochem. Soc.* 128 (1981) 2569-2573
- 14) Y. Lee, J. Suntivich, K. J. May, E. E. Perry, Y. Shao-Horn, *J. Phys. Chem. Lett.* 3 (2012) 399-404
- 15) R. Kötz, H. Neff, S. Stucki, *J. Electrochem. Soc.* 131 (1984) 72-77
- 16) D. F. Abbott, D. Lebedev, K. Waltar, M. Povia, M. Nachtegaal, E. Fabbri, C. Coperet, T. J. Schmidt, *Chem. Mater.* 28 (2016) 6591-6604
- 17) D. Michell, D. A. J. Rand, R. Woods, *J. Electroanal. Chem.* 84 (1977) 117-126
- 18) Z. Pavlovic, C. Ranjan, Q. Gao, M. v. Gastel, R. Schlögl, *ASC Catalysis* 6 (2016) 8098-8105
- 19) V. Pfeifer, T. Jones, J. Velasco, C. Massue, M. Greiner, R. Arrigo, D. Teschner, F. Girgsdies, M. Scherzer, J. Allan, M. Hashagen, G. Weinberg, S. Piccinin, M. Hävecker, A. Knop-Gericke, R. Schlögl, *PCCP* 18 (2016) 2255-2287
- 20) J. Mozota, B. E. Conway, *Electrochimica Acta* 28 (1983) 1-8
- 21) B. E. Conway, J. Mozota, *Electrochimica Acta* 28 (1983) 9-16
- 22) A. Capon, R. Parsons, *J. Electroanal. Chem.* 39 (1972) 275
- 23) J. Otten, W. Visscher, *J. Electroanal. Chem. Interfacial Electrochem.* 55 (1974) 1-11

- 24) J. Otten, W. Visscher, J. Electroanal. Chem. Interfacial Electrochem. 55 (1974) 13-21
- 25) Y. H. Hall, P. M. A. Sherwood, J. Chem. Soc, Faraday Trans. 1 (1984) 135-141
- 26) D. Michell, D. A. J. Rand, R. Woods, J. Electroanal. Chem. 89 (1978) 11-27
- 27) W. Marra, P. Eisenberger, A. Cho; J. Appl. Phys. 50 (1979) 6927-6933
- 28) L. G. Parratt, Phys. Rev. 95 (1954) 359-369
- 29) J.-P. Schlomka, M. Tolan, L. Schwalowsky, O. H. Seeck, J. Stettner, W. Press, Phys. Rev. B 51 (1995) 2311-2321
- 30) C. Chabanier, D. Guay, J. Electroanal. Chem. 570 (2004) 13-27
- 31) K. M. Robinson, W. E. O'Grady, Faraday Discuss. 95 (1993) 55-64
- 32) M. Samant, M. F. Toney, G. L. Borges, L. Blum, O. R. Melroy, J. Phys. Chem. 92 (1988) 220-225
- 33) C. Cao, H.-G. Steinrück, B. Shyam, K. H. Stone, M. F. Toney, Nano Lett. 16 (2016) 7394-7401
- 34) Y. G. Shen, Y. W. Mai, Q. C. Zhang, D. R. McKenzie, W. D. McFall, W. E. McBride, J. Appl. Phys. 87 (2000) 177-187
- 35) LEPTOS user manual, Bruker AXS Karlsruhe, DC-M88-EXX052, V7, (2009)
- 36) L. Nénot, P. Croce, Rev. Phys. Appl. 15 (1980) 761
- 37) S. Sinha, E. Sirota, S. Garoff, H. Stanley, Phys. Rev. B 38 (1988) 2297-2311
- 38) S. Gottesfeld, S. Srinivasan, J. Electroanal. Chem. 86 (1978) 89-104
- 39) S. Gottesfeld, J.D.E. McIntyre, J. Electrochem. Soc. 126 (1979), 742-750
- 40) L. Wan, M. Hara, J. Inukai, K. Itaya, J. Phys. Chem. B 103 (1999) 6978-6983
- 41) O. M. Magnussen, Chem. Rev. 102 (2002) 679-725
- 42) D. A. J. Rand, R. Woods, J. Electroanal. Chem. Interfacial Electrochem. 55 (1974) 375-381
- 43) P. Stoenhart, H. A. Kozłowska, B.E. Conway, Proc. Roy. Soc. A. 310 (1969), 541-563
- 44) R. Woods, Electroanal. Chem and Interfac. Electrochem. 49 (1974), 217-226
- 45) S. Cherevko, S. Geiger, O. Kasian, A. Mingos, K. J. J. Mayrhofer, J. Electroanal. Chem. 773 (2016) 69-78
- 46) S. Cherevko, S. Geiger, O. Kasian, A. Mingos, K. J. J. Mayrhofer, J. Electroanal. Chem. 774 (2016) 102-110
- 47) B. Gilles, Grazing incidence diffraction: a review. No. LNF-IR--96-049. (1996)
- 48) A. Gibaud, S. Hazra, Current Science 78 (2000) 1467-1477
- 49) S. Cherevko, S. Geiger, O. Kasian, N. Kulyk, J.-P. Grote, A. Savan, B. Shrestha, S. Merzkin, B. Breitbach, A. Ludwig, K. J. J. Mayrhofer, Catalysis Today 262 (2016) 170-180
- 50) I. Katsunobu, S. Cherevko, A. Zeradjanin, K. J.J. Mayrhofer, Angew. Chem. Int. Ed. 53 (2014) 102-121
- 51) G.K. Reeves, M.W. Lawn, R.G. Elliman, J. Vac. Sci. Technol. A 10(5) (1992), 3203-3206

Appendix 1

Corresponding evolution of the H-value (Hurst parameter) for samples A to F:



Chapter 6: Thin film diffraction in extended use: three examples outside the box

The application of Grazing Incidence Diffraction and X-ray reflectometry is widespread in many areas of material research, but is also gaining importance in catalysis. This chapter gives a short overview of three examples for its use besides the classical application of thin film diffraction in semiconductor research and industry. The first example follows a materials science approach and deals with depth-sensitive phase analysis of the passivating oxide layer on the surface of a high-performance titanium aluminium alloy. The second case comes from the field of heterogeneous catalysis and tries to investigate the role of surface-near brass formation in Cu/ZnO-based methanol synthesis catalysts. Finally, the third example exploits X-ray reflectometry as a reference-free method to calibrate the deposition rate of a low-pressure chemical vapour deposition (LPCVD) process developed in-house to produce electrode materials.

All these examples in their respective research fields have in common that the characterization of surfaces on the morphological and chemical structural level is a prerequisite to understanding their reactivity, which in turn is of essential importance for the development and design of new materials.

6.1 Depth-sensitive phase analysis of surface layers

6.1.1 High temperature alloy

In GIXRD, the low incidence angle is exploited to artificially enhance the “surface sensitivity” of a bulk sensitive method. Thus, a variation of the incidence angle can also yield depth-dependent information in the case of layered systems. It can be used to investigate effects like intermixing⁽¹⁾, impurities, thickness⁽²⁾, blocking layers or other important effects at interfaces^(3,4,5).

There is more than one way to perform a depth sensitive experiment. In the case of uniform, homogeneously layered sample systems, one can study the electron density variations with depth by X-ray reflectometry, or perform in-plane Grazing Incidence Diffraction as a highly sensitive measurement for observing possible Bragg shifts (preferably on single crystalline substrates). For more heterogeneously composed layered samples, however, the best way to record depth-dependent information is to measure at different incidence angles over the same 2Theta range and compare the patterns. The latter strategy shall be briefly demonstrated here.

While GIXRD may be considered to be a surface- or depth-sensitive variant of conventional powder diffraction, it needs to be noted that this ‘additional dimension’ of information comes at the cost of further limitations. In powder systems, the Rietveld method may be used to quantify phase mixtures, provided that the phases under consideration have been identified and suitable structure models exist to calculate the theoretical reflection intensities. However, this will only work if the mixture is homogeneous, i.e. if the absorption of the matrix is the same for all phases. In layered systems, in contrast, the absorption of each layer will reduce the signal intensity of all layers below it. While it is exactly this factor which provides the depth sensitivity, at the same time it prevents a quantitative analysis. Finally, the angular dependence of relative intensities in the strongly asymmetric measurement geometry of GID differs significantly from conventional symmetric diffraction, which is

why the Rietveld method fails to accurately model the intensity distribution. In other words, the analytical problems of depth profiling and phase quantification interfere with each other and hence cannot be solved simultaneously.

The investigated sample (DP_1) is a high performance alloy provided by the DLR (Deutsches Zentrum für Luft- und Raumfahrt, Dr. N. Laska) and consists of titanium-aluminium with traces of chromium and yttrium (Ti-60Al-13Cr-Y(Zr), given in at.%). The sample was heated for 1000 h at 900 °C in synthetic air (80% Ar, 20% O₂) to form a protecting oxide layer at the surface (passivation). As can be seen in the SEM cross section view (Fig. 6.1), the oxide layer exhibits an average thickness of 1 to 3 µm and is inhomogeneous not only in thickness, but also in composition, as evidenced by the contrast variations.

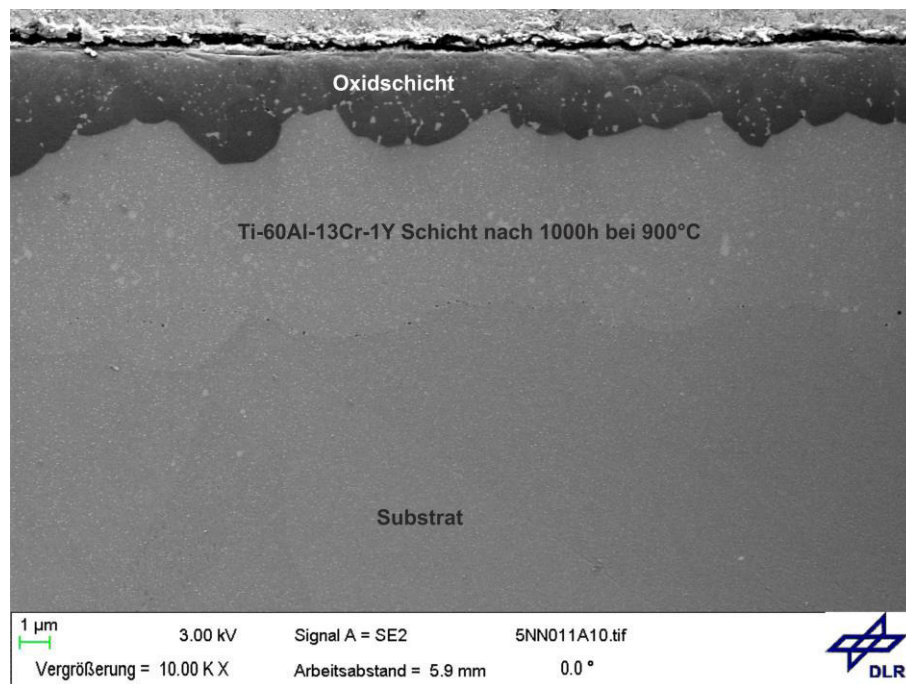


Fig. 6.1: SEM picture of the Ti-Al alloy (DP_1). The oxide layer on top can be clearly seen.

The question of interest was to elucidate the identity and depth distribution of phases occurring at the surface. The GIXRD experiment was performed with incidence angles between 0.5° and 2.5° in 0.4° steps (6 measurements). The results are shown in Fig. 6.2. The phase analysis of DP_1 shows α -Al₂O₃ (corundum) and a hexagonal Cr-based metal alloy as the two main phases. Some further peaks can be attributed to a mixed oxide Y₄Al₂O₉, while several other reflections could not be assigned even with the latest version of the PDF-4+ database. An attempt to do a Rietveld-based analysis of the patterns failed due to the unusual intensity distributions resulting from the strongly asymmetric GID geometry, probably combined with preferred orientation effects. An alternative quantification approach via single peak fits was prevented by the complexity of the pattern with its extensive peak overlap and incomplete peak assignment. Thus, only a semi-quantitative assessment by comparing the trends in the main phases was possible. Relative to the corundum reflections, the intensities of the Cr-alloy reflections increase with increasing incidence angle (and thus penetration depth), meaning that corundum is closer to the surface than the alloy. Also, when compared to the corundum signal, the Y₄Al₂O₉ intensity appears constant. However, the Cr-alloy is also expected to

have small contributions in the same positions, making conclusions difficult. In summary, the results indicate that the most electropositive metals Al and Y are oxidised and move to the surface, while Cr aggregates and combines with the remaining metallic elements in an Al-depleted layer below the oxide layer.

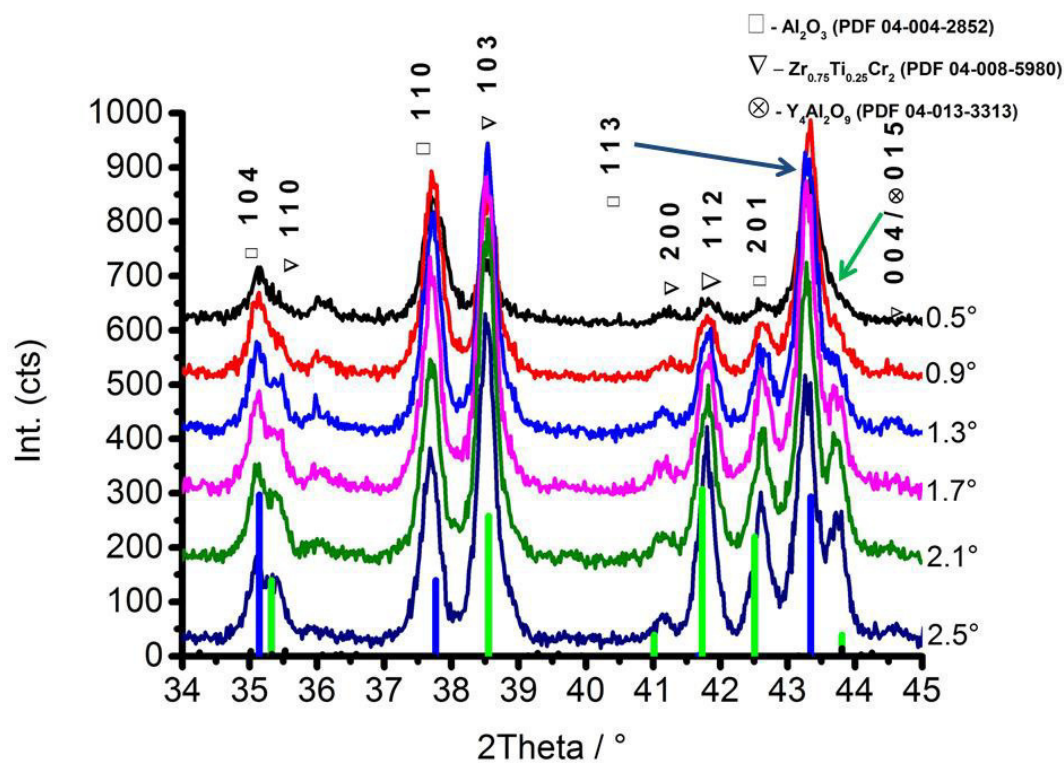


Fig.6.2: Depth sensitive GIXRD experiment of DP_1 with variable incidence angles (indicated right on hand side).

6.1.2 Sample comparison by similar probing depth

Depth sensitive measurements can also be used with a constant information depth (constant incident angle) as a method to compare the effects of different treatments in a series of samples. This shall be demonstrated with a nitriding process of a titanium layer, which is a prominent example for corrosion inhibition and blocking layer formation on substrates^(6,7,8). The substrate was chosen to be a silicon (100) wafer coated with titanium (by magnetron sputtering, ~ 450 nm). On the Ti layer an additional silicon layer was deposited using Low Pressure Chemical Vapour Deposition (LPCVD; 50sccm (SiH₄/H₂:20%/80%), 100 sccm Ar, 1 mbar, 550 °C), which is assumed to be amorphous (sample IC-A). Compared to sample IC-A, a second sample was prepared with the same stacking order, but the titanium layer was nitrided by high temperature treatment in an ammonia atmosphere (700 °C, 100 mbar, 50sccm NH₃, 100sccm Ar) before the silicon top layer was deposited (sample IC-B) with the same treatment as in sample IC-A. To monitor the differences caused by the nitridation, GIXRD was performed for both samples at 0.6° incidence angle. The surface sensitivity and precise control of the penetration depth are the key features of GIXRD in studying interfaces and their changes. Fig. 6.3 sums up the observed results. Due to layer complexity, a complete assignment of all phases was not achieved (IC-A, ~ 36.6° 2θ). In the case of the untreated sample, the deposited silicon appears to be polycrystalline. In addition, the formation of TiSi species, namely TiSi₂ can be observed. In contrast, sample IC-B shows only 2 amorphous humps (at ~ 28.5° & 47.3° 2θ), and

therefore indicates an amorphous or nano-crystalline state of the silicon on the nitrified sample (IC-B). The nitride layer is also found in the patter, however with just very weak peaks (e.g. $\text{Ti}_2\text{N} \sim 36.7^\circ 2\theta$). An interesting observation is that the TiSi_2 phases formed differ in the two samples. While the crystal lattice in both cases is orthorhombic, the lattice parameters and space groups are different. The TiSi_2 phase in sample IC-A has the space group *Cmcm* (63), in IC-B it is *Fddd* (70). It should be noted that the nitrated sample was heated twice to different temperatures. A possible explanation for this difference might offer the consideration of the Ti-N layer formed. While the penetration depth stays approximately constant between 300-350 nm (for both samples, $\rho \sim 4.0 \text{ g/cm}^3$ ($\text{TiSi}_2\text{:Si}$ 1:1) assumed, 63% absorption), the additional TiN layer weakens the signal of the silicides below in the case of sample IC-B. Hence, the observation of the two different formed silicide lattices is likely connected to the presence of the Ti-N layer and the applied temperature treatment. This knowledge is complemented by morphological information from transmission electron microscopy (TEM). Fig. 6.4 compares cross-section TEM images of both samples, including EDX mapping for the elemental composition. The surface of sample IC-A appears much rougher and less ordered when compared to sample IC-B. Therefore, it can be assumed that the formation of TiN on the titanium surface modifies the growth of the deposited silicon.

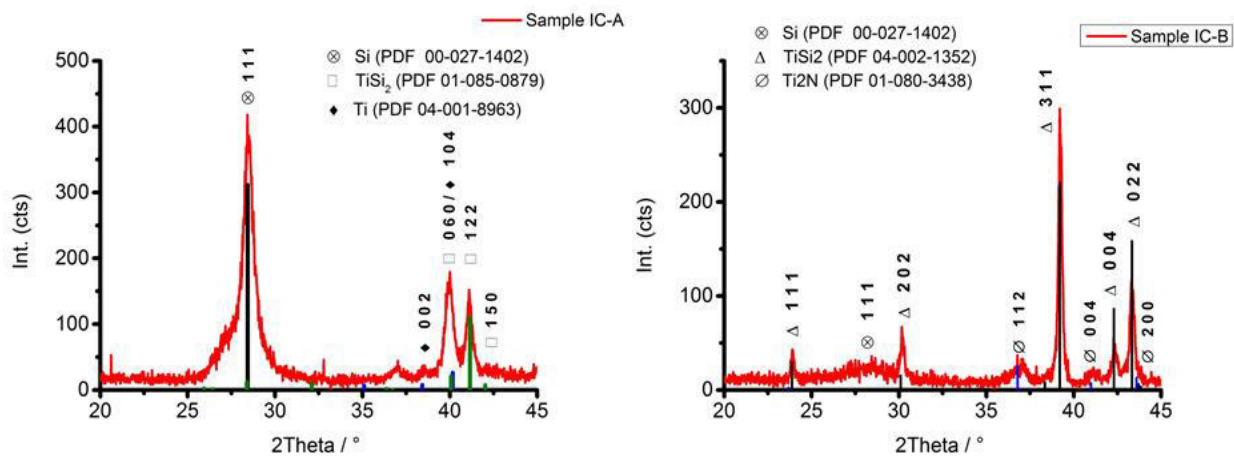


Fig. 6.3: GIXRD patterns of differently treated samples at identical incidence angles in comparison. A y-axis offset has been added to the pattern of IC-A for clarity. The impact of the additional TiN layer on both the crystallinity of the deposited silicon and the phase composition of the intermediate layers can be clearly seen. Note the two crystallographically different orthorhombic TiSi_2 phases appearing in the two patterns (+:*Cmcm*; *: *Fddd*).

Also, the calculated penetration depth of approximately 300 nm fits with the layer thicknesses observed in the microscopy result. GIXRD offers in this case a tool for non-destructive measurement (compared to electron microscopy) of thin layered samples to determine essential differences in structure and morphology on the nm scale.

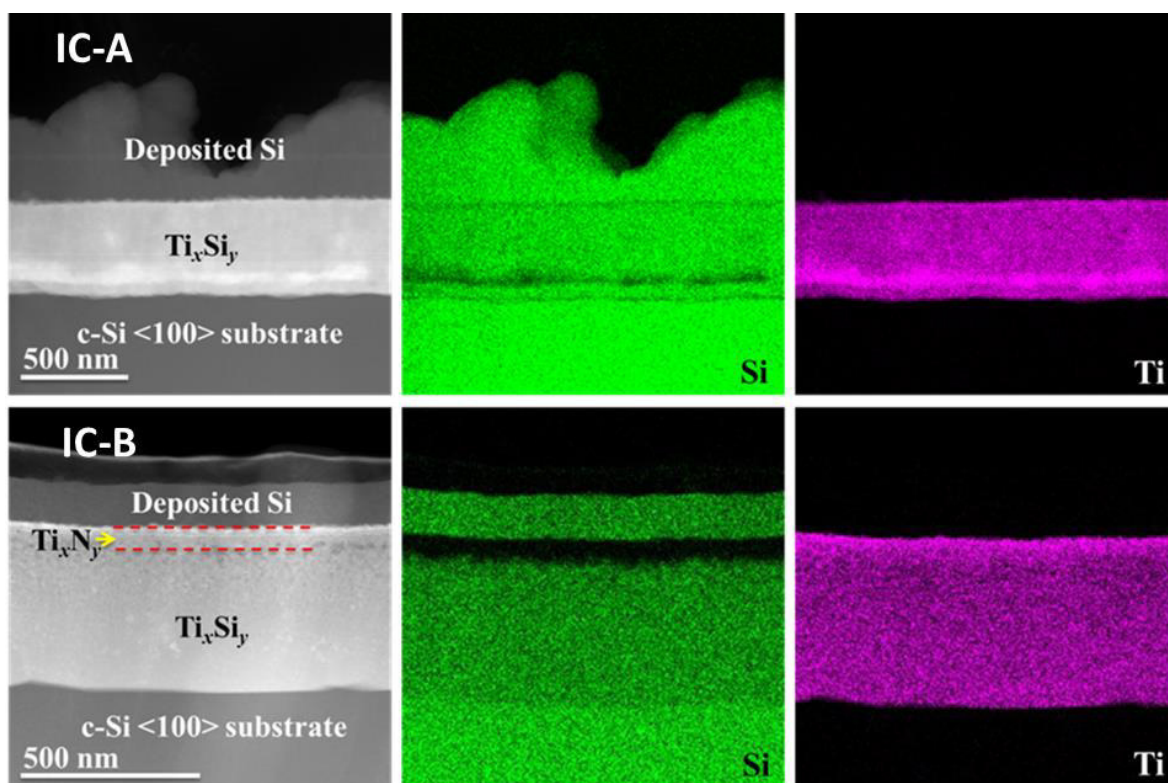


Fig. 6.4: Cross-section TEM images and elemental composition (EDX) of sample IC-A and IC-B. The differences in the layer stacking (TiN) and silicon growth can be seen clearly.

6.2 Surface sensitive reduction

A developed in-house operation mode for Grazing Incidence Diffraction was applied to the field of Cu/ZnO catalysts for the hydrogenation of CO/CO₂^(9,10). The sample was prepared by a controlled co-precipitation with Na₂CO₃ from a Cu_{0.68}/Zn_{0.29}/Al_{0.03} metal nitrate mixture (pH 6.5, 65 °C, 1.5 h ageing time) and subsequent calcination (2 KPM, 330 °C, 3 h) of the hydroxy-carbonate precursor to the corresponding oxides. Afterwards, the sample was pressed into small dense pellets of 1 cm in diameter (2 t pressure) and reduced in hydrogen. In two series of samples, either the reduction temperature or the hydrogen concentration was varied. The aim of this experiment was to investigate the possible impact of brass formation⁽¹¹⁾ on the catalysts and to monitor the different structural states of ZnO from wurtzite as a starting point for the formation of brass. Since the formation of brass in reductive atmosphere starts with the dissolution of Zn in the already reduced copper metal in the surface near regions, a more surface sensitive XRD technique needs to be applied. The used pellet of the Cu/ZnO-based catalysts represents a macroscopic model of an active site consisting of Cu and ZnO. The idea of the experiment was to analyse with surface sensitive GIXRD the beginning of brass formation at/near the surface. Since the reduced samples are sensitive to re-oxidation in air, GIXRD at 0.8° incidence angle was applied in an inert atmosphere (Ar). Brass formation leads to an increase of the Cu lattice parameter and thus to a shift of the peaks to lower angles. This increase of the Cu lattice parameter is a very sensitive descriptor for the determination of the brass formation also semi-quantitative. Fig. 6.5 depicts the observed trend for the first series, in which the hydrogen concentration was kept constant at 20% and the reduction temperature was varied between 250 °C and 500 °C (20% H₂, 80% Ar, dwell-time 1h).

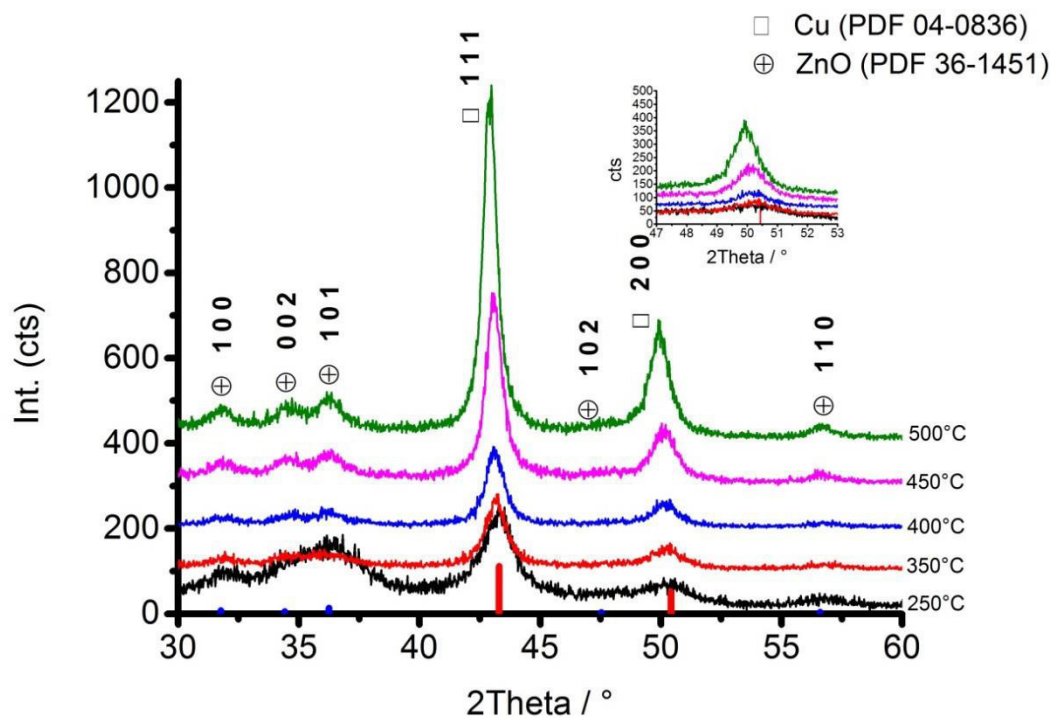


Fig.6.5: Temperature dependent reduction of the Cu/ZnO-based catalyst. The angle of incidence was set to 0.8° for all measurements. The inset displays the shift of a high angle reflection Cu 220.

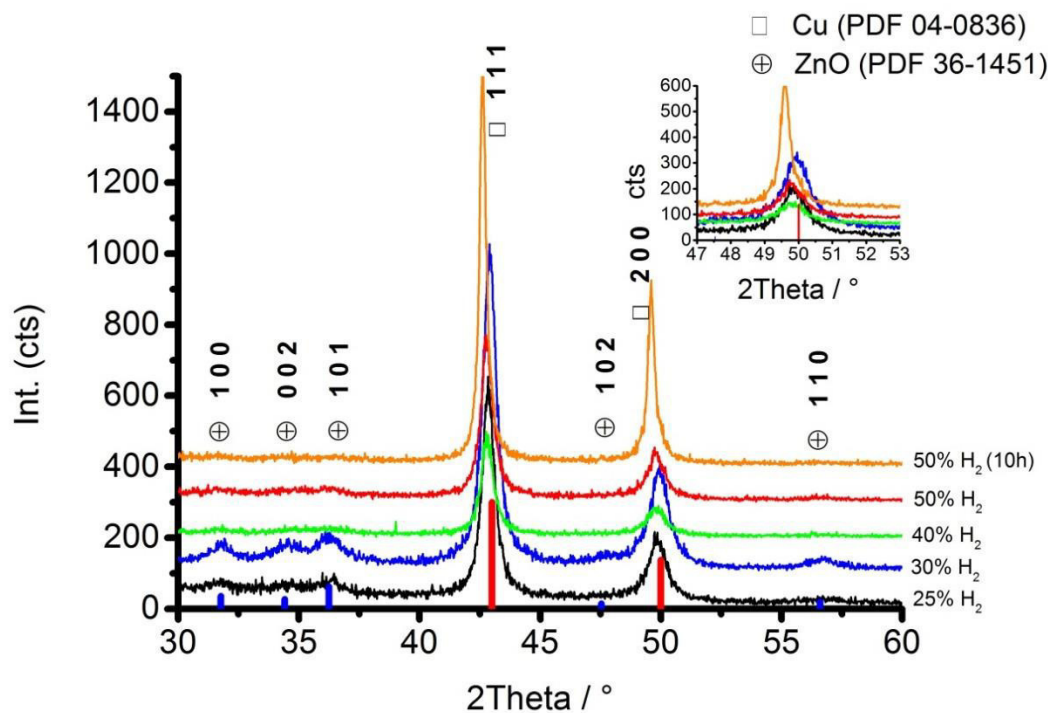


Fig.6.6: Hydrogen concentration dependent reduction. The shift of the Cu 220 peak is visible in the inset. In the last measurement (orange line, 10 h) the ZnO peaks have almost vanished due to brass formation.

To emphasize the observed shift the enlargement of Fig. 6.5 displays a high angle reflection (220) of Cu with increasing reduction temperature. The shifts to lower 2θ values give a clear indication of

brass formation, as the ZnO reflections, in contrast, are not affected by a peak shift. In addition, progressing crystallisation/sintering of ZnO with increasing reduction temperature is evidenced by decreasing peak widths clearly visible between 30-40° 2 θ . In the second series, the temperature was kept at the previous maximum value of 500 °C while the hydrogen concentration was increased to 50%, as shown in Fig. 6.6. In a final experiment, the reduction time was extended from 1 to 10 h (500 °C, 50% H₂). In this series, the intensity of the ZnO reflections strongly decreases and finally vanishes, which can be explained by the consumption of ZnO due to the formation of brass. The ongoing incorporation Zn into the Cu lattice and the final brass formation is again impressively described by the shift of the Cu (111) and (220) reflections. The brass rich character of the sample kept for 10 h at 500 °C in 50 % H₂ was already noticeable by a colour change from black to gold. Fig. 6.7 shows the activity trend in the methanol synthesis reaction for different reduction temperatures prior to the activity test, in which the T and p were constant for all samples at 30 bar and 230 °C. The activity of the catalysts strongly decreases with an increase in the reduction temperature, which gives the first evidence that a possible formation of brass is responsible for the poor methanol activity.

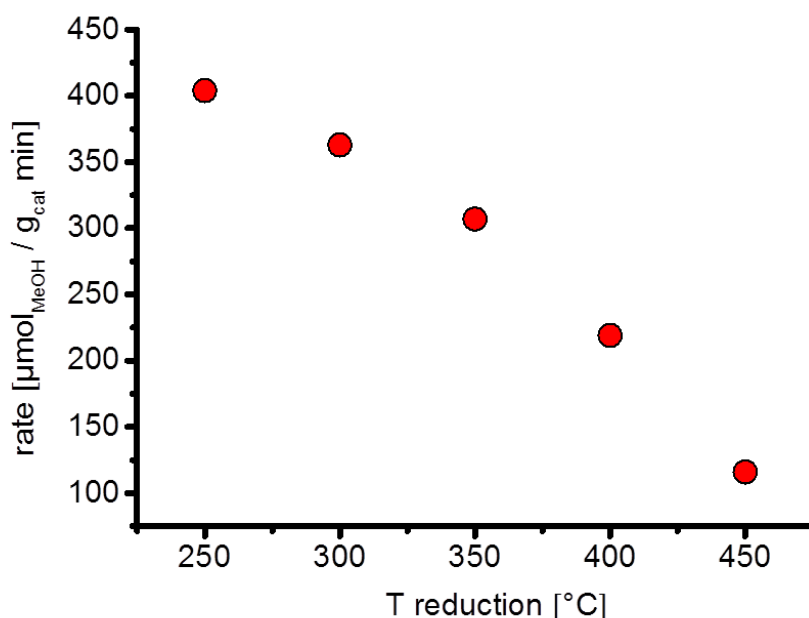


Fig.6.7: Activity data for the conversion to methanol for the temperature variation series. Note the decreasing conversion rate for higher temperatures due to brass formation.

In order to evaluate to what degree the results reflect surface reduction, all samples were also measured in (bulk sensitive) symmetric diffraction mode- parallel beam (PB) geometry. For a more quantitative analysis, the diffraction patterns were fitted with the Rietveld method, though the deviating relative intensities made it necessary to include a “preferred orientation” model for the Cu phase. Fig. 6.7 a&b present the extracted Cu lattice parameter changes as $\Delta a = a_{\text{fit}} - a_{\text{Cu}}$, with the reference value of $a_{\text{Cu}} = 3.6150 \text{ \AA}$ (PDF-04-0836)⁽¹²⁾. The corresponding fit values are summarized in Table 6.1. Fig. 6.7 and Tab 6.1 clearly demonstrate that harsher reduction conditions lead to an increased Cu lattice parameter, thus proving an increase in brass formation. Another general trend is that the GID experiments consistently give slightly higher values than the symmetric measurements,

which is compatible with the expectation that the more surface sensitive GID mode should detect a higher Zn concentration in the brass than the bulk sensitive PB mode. However, the possibility that this systematic difference could be an artefact resulting from the different measurement geometries cannot be strictly ruled out. It should be noted that both measurements for the sample reduced in 30% H_2 consistently show a deviation from the general trend. Whether there was a problem with the measurements due to the sample alignment, or a problem in the sample preparation, remains unclear. Overall, this set of experiments demonstrates that Grazing Incidence Diffraction also has an enormous potential in application to “powder” samples.

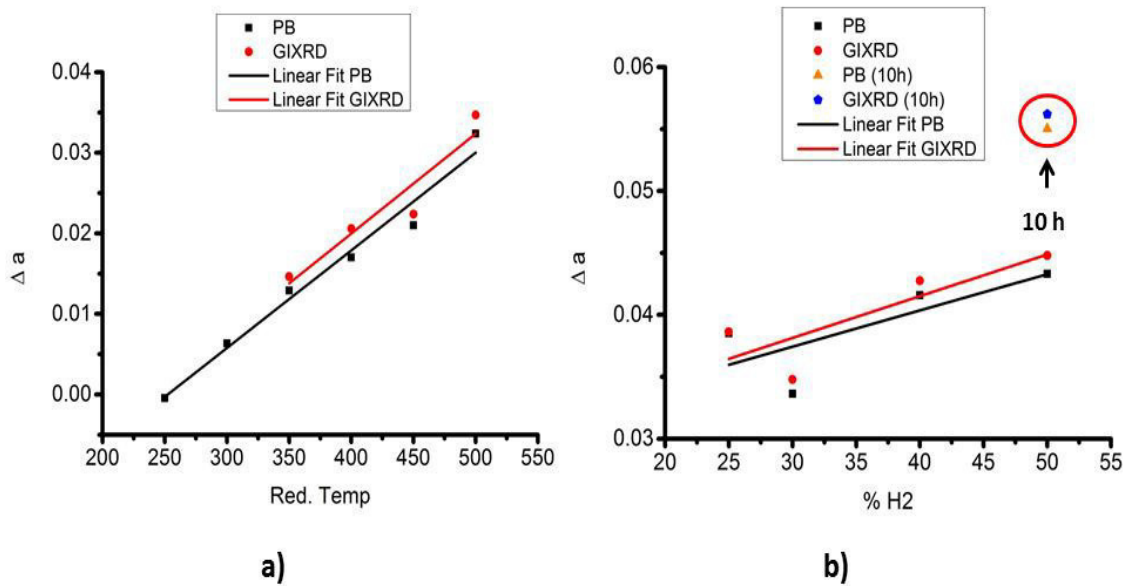


Fig. 6.8: Lattice parameter changes Δa relative to pure copper. a) Increasing reduction temperature. b) Increasing H_2 concentration (last data point: increasing reduction time).

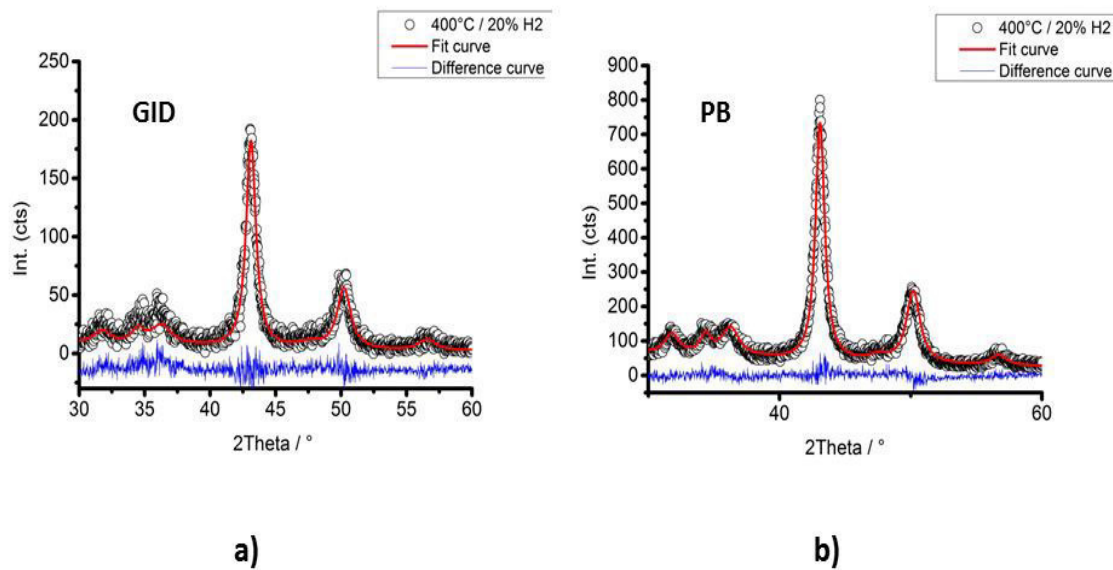


Fig. 6.9: Exemplary fit curves of the 400 °C/20% H_2 treatment. Note the differences between GID (a) and PB (b) measurement fit results. In the GIXRD case, the relative intensities of the ZnO reflections below 40° are not well described by a classical Rietveld refinement.

Tab. 6.1: Summary of fit results from the brass formation experiments for the lattice constant a of Cu.

		Parallel Beam (symmetric)			Grazing Incidence (GIXRD)	
Reduction at 20% H ₂	Red. T (°C)	a (Å)	Error (Å)	wt.% ZnO from Rietveld	a (Å)	Error (Å)
	250°	3.615	0.003	47.6	a)	
	300°	3.621	0.004	50.3	b)	
	350°	3.628	0.004	35.5	3.630	0.004
	400°	3.632	0.002	30.5	3.636	0.003
	450°	3.636	0.001	36.0	3.637	0.002
	500°	3.647	0.001	35.0	3.650	0.001
Reduction at 500 °C	% H ₂	a (Å)	Error (Å)	wt.% ZnO from Rietveld	a (Å)	Error (Å)
	25	3.654	0.001	35.0	3.654	0.001
	30	3.649	0.001	17.3	3.650	0.002
	40	3.657	0.001	21.5	3.658	0.002
	50	3.658	0.001	14.9	3.660	0.002
	50 (10h)	3.670	0.001	13.7	3.671	0.001

a) In contrast to the PB measurement, GIXRD detects the presence of additional, overlapping peaks (Cu₂O?), which severely distort the Rietveld refinement.

b) The GID pattern was not saved properly due to hardware problems.

6.3 Calibration of LPCVD process using X-ray reflectometry

Besides GIXRD, X-ray reflectometry can also be used for process development^(13,14,15). The calibration of an in-house developed LPCVD machine (Low Pressure Chemical Vapour Deposition) was carried out by X-ray Reflectometry. The LPCVD process was developed for coating conductive substrates with silicon by using SiH₄. The task was to relate the deposition time to the obtained layer thickness, i.e. to determine the effective deposition rate. XRR is very suitable for this purpose as it is a reference free method, i.e. it does not need an additional standard for calibration. Furthermore, it is an integral and averaging method, which, besides easier application, is an advantage when compared to, for example, cross-section TEM. However, the actual target samples for the deposition process were Ti foils, which are difficult to measure in XRR due to roughness problems. Thus, an additional silicon wafer was added to each deposition experiment as a reference for X-ray reflectometry measurements. The deposition process was performed with increasing holding times to achieve different thicknesses with each run (1 mbar, 550 °C, 50 sccm SiH₄ + 100 sccm Ar, various t). The critical angle of silicon was found constantly to be $\theta_c = 0.23^\circ$, which corresponds to an average density of 2.6 g/cm³ ($\rho_{lit.} = 2.38 \text{ g/cm}^3$ ⁵). The slightly higher value could result from very thin surface oxide, SiO₂ which may have formed after the samples were taken out of the reactor and exposed to air. A second reason might be found in the deviation from the nominal and effective surface density from bulk values due to the layer growth mechanism. The fit model for the measured curves was based on a double layer model (Si+SiO₂) on top of the Si substrate wafer. Both layers were assumed as abrupt (sharp refractive index) profiles in a Névot-Croce model. Refinement against thickness and

electron density was executed to obtain the thickness values. The top SiO₂ layer was used as buffer layer to model the surface look for higher accuracy in the determination of the Si thickness. Bruker Leptos software was used for data evaluation (V.7.8, 2015). Fig. 6.10 shows well two XRR curves from the series used for the calibration. The resulting calibration curve is depicted in Fig. 6.11, which indicates a very good linear correlation between the layer thickness and the deposition time. The only exception is the last data point which corresponds to the thickest layer. The reason for this deviation is that the thickness of the deposited layer (ca. 400 nm) is already beyond the resolution of the setup which can be estimated to be around 250 nm. Also Cal_E shows already higher error bars due to being close to the resolution limit. Thus the last two data points need to be treated with care even though their fit values look promising. Because the presence of a top SiO₂ layer was assumed in the fit model for the whole series, Fig.6.9 shows two sets of data points, one corresponding to the Si layer only and the other to the total thickness of Si plus SiO₂. Since the SiO₂ layer is significantly thinner than the Si layer, the linear correlation would not change significantly by including SiO₂. In summary, X-ray reflectometry has helped to determine the actual deposition rate of the newly built LPCVD setup and thus to further improve exact sample preparation.

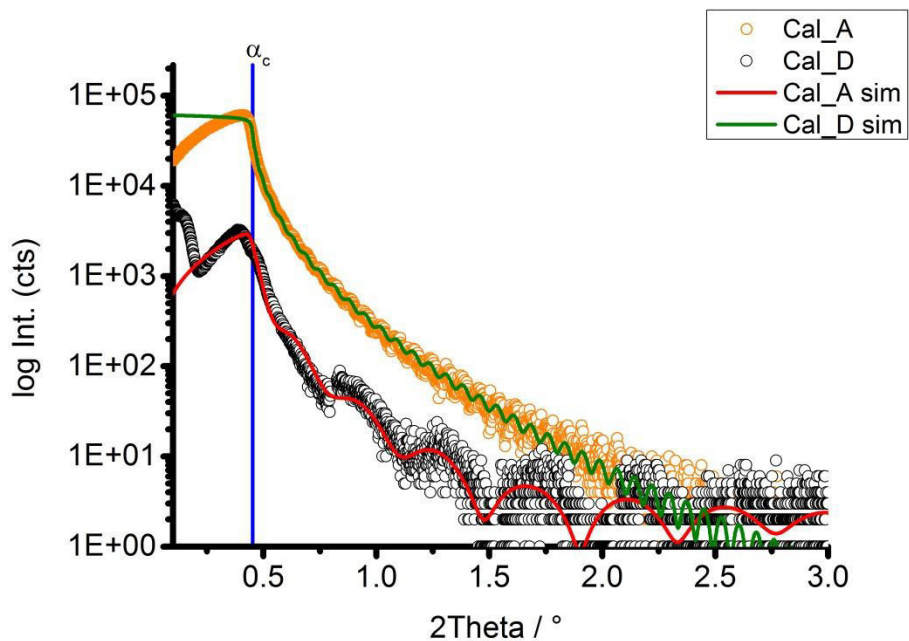


Fig. 6.10: Exemplary reflectometry curves measured for the calibration of the LPCVD silicon deposition process.
Estimated thicknesses: Cal_A: 19 nm., Cal_D: 109 nm.

Tab .6.2: Estimated layer thicknesses of deposited Si and the probable SiO₂ top layer.

	t (Si) (nm)	t (SiO ₂) (nm)	d (Si) (g/cm ³)	d (SiO ₂) (g/cm ³)	χ ²
Cal_A	19.1 ± 0.1	4.4 ± 0.3	2.4 ± 0.1	3.2 ± 0.1	0.030
Cal_B	49.6 ± 0.4	3.1 ± 0.9	2.4 ± 0.1	3.8 ± 0.7	0.012
Cal_C	70.1 ± 1.0	3.6 ± 1.1	2.3 ± 0.1	3.1 ± 0.5	0.011
Cal_D	109.9 ± 1.1	2.0 ± 1.1	2.3 ± 0.1	3.8 ± 0.3	0.012
Cal_E	218.9 ± 3.9	2.3 ± 2.2	2.4 ± 0.1	3.17 ± 0.6	0.011
Cal_F	448 ± 10.0	3.0 ± 3.0	2.4 ± 0.1	2.8 ± 0.5	0.011

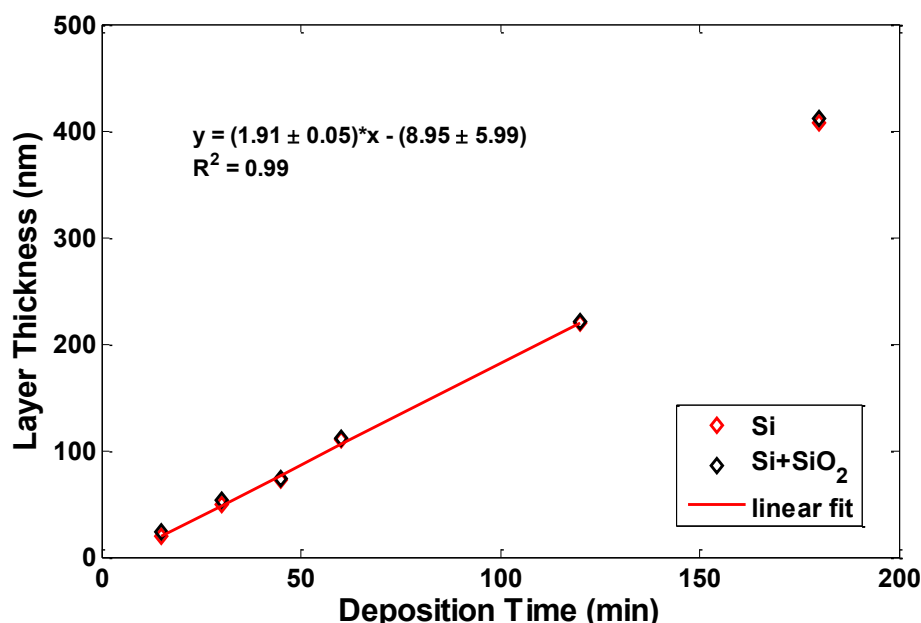


Fig. 6.11: Calibration curve for the LPCVD process of Si. Both assumptions (Si, Si+SiO₂ layer) give a good agreement for the linear fit. Cal_F is an outlier as the thickness exceeds the resolution limit of the setup detection.

6.4 Conclusion

GIXRD, as well XRR, are very powerful tools when compared to standard XRD techniques. The ability to test samples without the need of specific sample preparation (as in electron microscopy) is of great benefit and makes a quick analysis possible. For all three application examples shown here, additional insights not easily obtained using other techniques were produced. For the high-performance Ti-Al alloy, the identity of the major phases in the passivation layer and their stacking sequence was elucidated by variable incidence angle GIXRD. In the second case, some experimental evidence of an earlier brass formation at the surface of a reduced Cu/ZnO powder catalyst was found. Finally, X-ray reflectometry was exploited to calibrate the deposition rate of amorphous silicon in a newly established LPCVD setup.

6.5 References:

- 1) A. Martel, F. Caballero-Briones, A.I. Oliva, R. Castro-Rodríguez, A. Irribarren, P. Bartolo-Pérez, J. L. Peña, *Physica Status. Solidi B* 220 (2000) 261-267.
- 2) P. Colombi, P. Zanola, E. Bontempi, R. Roberti, M. Gelfi, L.E. Depero, *J. Appl. Cryst.* 39 (2006) 176-179.
- 3) C.A. Kaufmann, R. Caballero, T. Unold, R. Hesse, R. Klenk, S. Schorr, N. Nichterwitz, H.-W. Schock, *Sol. Energ. Mat. Sol. Cells* 93 (2009) 859-863.
- 4) K. Vamsi-Krishna, V. Dutta, *Thin Solid Films* 450 (2004) 255-260.
- 5) I.M. Kötschau, H. Schock, *J. Phys. Chem. Solids* 64 (2003) 1559-1563.
- 6) P.K. Barhai, N. Kumari, I. Banerjee, S.K. Pabi, S.K. Mahapatra, *Vacuum* 84 (2010) 896-901.
- 7) R. Krishnan, R. Ramaseshan, T. Mathews, R. Nithya, S. Dash, A.K. Tyagi, B. Raj, *Surf. Eng.* 25 (2009) 218-222.

- 8) G. Martinez, V. Shutthanandan, S. Thevuthasan, J.F. Chessa, C.V. Ramana, *Ceram. Int.* 40 (2014) 5757-5764.
- 9) M. Behrens, F. Studt, I. Kasatkin, S. Kühl, M. Hävecker, F. Abild-Pedersen, S. Zander; F. Girgsdies, P. Kurr, B.-L. Kniep, M. Tovar, R.W. Fischer, J.K. Nørskov, R. Schlögl, *Science* 336 (2012) 893-897.
- 10) F. Meng, Q. Zhang, G. Yang, R. Yang, Y. Yoneyama, N. Tsubaki, *Chem. Eng. J.* 295 (2016) 160-166.
- 11) M.S. Spencer, *Surf. Sci.* 192 (1987) 323-328.
- 12) H.E. Swanson, E. Tatge, *Natl. Bur. Stand. Circ.* 539, Vol. I (1953) 15-16
- 13) A. Kurokawa, Y. Azuma, S. Terauchi, T. Takatsuka, T. Narukawa, A. Takano, S. Mizuno, J. Sameshima, *e-J. Surf. Sci. Nanotechnol.* 14 (2016), 125-130.
- 14) R. Westover, R.A. Atkins, M. Falmbigl, J.J. Ditto. D.C. Johnson, *J. Solid State Chem.* 236 (2016) 173-185.
- 15) D.D.M. Ferreira, A.C. Jakobsen, S. Massahi, F.E. Christensen, B. Shortt, J. Garnæs, A. Torras-Rosell, M. Krumrey, L. Cibik, S. Marggraf, *Proc. SPIE* 9905 (2016) 9905Y-1.

Chapter 7: Summary and final conclusion

The use of iridium as electrode material in the water splitting reaction in PEM electrolyzers gives rise to an enormous pool of structural and mechanistic questions. Regarding the increased catalytic activity in producing oxygen under OER conditions (during continuous potential cycling), especially the electronic structure and the morphology of the resulting active surface became in focus. Applicative aspects, also concerning the possible industrial use of iridium, lead to investigations away from massive iridium samples, e.g. bare Ir foils. In addition to this change in sample type, a very general question was hardly answered: studying the surface dynamics by integral methods. Many attempts have been made already to identify structural key features of the activated iridium surface and to make conclusions about its dependencies. Beside the activity, also the material loss, e.g. dissolution and detachment, are of interest for the further application of iridium as working catalyst. This effect was already paid attention to in the recent literature and demonstrated already the partial instability of the system. Less attention is paid to the changes happening to the iridium metal itself, during transformation into the active oxo-hydroxo surface layer, and connected stability issues. This question set the major intention of the present work and this could be achieved by applying the thin film X-ray techniques: XRR, XRDS and GIXRD. A second important issue arises after the beginning of practical work, to enable in-situ GIXRD measurements. This ultimate goal, connecting measured results under working conditions, became the second big pillar of this thesis. A minor intention, nevertheless worth trying and 3rd pillar, was to apply the GID technique on various sample types outside the common scope (e.g. powder pellets).

The first efforts have been made on establishing an in-situ setup for the use in the home laboratory and have been successful after one year of design and construction work. The test reaction chosen was the oxidation of massive polycrystalline copper in alkaline media, instead of starting with the very complex iridium oxidation. We could achieve a quite high degree of versatility of the cell and demonstrate the working principle for Grazing Incidence X-ray diffraction. For new users we could also provide a short guide for data treatment. A cyclic voltammetry and long-time chronoamperometry treatment revealed the quite unexpected complexity of this reaction. The nanostructured copper surface exhibits well known peaks in the CV, the observed shifts were clarified. During the CA, the oxidation of the Cu surface could only be explained considering cuprite as intermediate. This was connected to in-situ measured GIXRD and could demonstrate the successful operation of our in-situ cell setup. A further use on other interesting systems as well on single crystals would highlight the effort on this fundamental work establishing this capability.

In a second step, a thin film iridium electrode model system was established. The idea to use a Si-wafer substrate originated from the need to have sufficiently smooth surfaces for the application of GIXRD, as well to increase the electron density contrast for a precise XRR study. Pre-testing of bare iridium foils yielded inferior results due to the high surface roughness. The performed test oxidation of an Ir single crystal surface opened the enormous complexity rising with this sample type. Reproduction of the results proved to be difficult as it lead to more than one different state. This showed us that a precise handling of a very broad range of parameters in parallel is necessary. This leads to our decision to stay with an applicable thin film model of the Ir surface. To test our first hypothesis, intrinsic differences in morphology already caused by the deposition method, we used two different preparation types: sputter coating and high-end e-beam evaporation. This new, smooth sample type brought two new possibilities into the arena next to GIXRD: X-ray reflectometry and X-ray diffuse scattering. All together this combination of techniques enabled an almost internal

verification. Reference free XRR probes the electron density, hence crystalline as well as amorphous layers. Examination of the identical electrochemical treatment on two different morphology types revealed our posited statement: the activity in catalytical performance for the OER is already determined by the morphology of the untreated iridium film. Structural flexibility is a prerequisite for higher OER activity. Surface cracks already being present in the untreated sample are likely the reason for higher activity compared to a highly dense Ir layer. A highly dense packed film with smooth surface, appearing well defined in the CV, does take much longer to become in the same way active than a crack-structured, nano-pillar consisting iridium film as formed by simple sputter coating. Strained and dense films like that, tend more likely to get rid of the stress (obtained surface break up) instead of performing in conversion to an oxo-hydroxide layer. The depth-resolved evaluation of the active film revealed the presence of an approximately 8 nm disturbed layer on top of the metallic iridium substrate after the treatment. This is for sure one major highlight, since the XPS spectra indicate the Ir oxidation state just to be changed in a very minor way, whereas the morphology does significantly. The study was supported by SEM, TEM and GIXRD. Crystallographic parameters (from diffraction as well as TEM) showed that the lattice becomes slightly changed as well under the chosen treatment but remains present. The study accomplished the goal and clearly depicts the high surface dynamic, the changing roughness and morphology induced by the treatment being different for both preparation techniques. A connection between the nm-scale fractal changes and the applied current density could be given on an integral scale.

Third, a comparative study concerning the effects of different electrochemical treatments on a constant sample type was conducted to complement the previous results. Three different electrochemical scenarios have been applied to monitor resulting layer structure and morphology: (i) slow speed cyclic voltammetry (CV) (ii) slow speed CV followed by chronoamperometry (CA) and (iii) high speed cycling. All three treatments form a very low dense (absorbing) layer on top of the metallic iridium, indicated by drastically different fractal parameters. The developed two layer model lets us separate the morphologies in a more dedicated way than in the previous section. Data evaluation needed to be done on a very high and detailed level to gain the desired information through XRR and XRD. One of the major differences monitored became the electron density distribution along the probing depth. This comparison demonstrated, that depending on the treatment (CA, CV,...) the final appearance of the oxidized surface is strongly influenced. Supporting information could be gained again by GIXRD, what showed that all three states exhibit also different crystallographic appearance up to complete vanishing of the Ir reflections for high speed cycled samples. This two findings, the strong difference in kinetics by the treatments as well as the direct detection of loss of lattice periodicity (next to a remaining morphology) becomes for sure the second highlight of this work. SEM supported the gained insight in a more pictorial view. A more detailed investigation was done on an e-beam evaporation sample by one cycle of CV followed by a short CA. The analysis of this sample before and after electrochemistry revealed one of the most unexpected results within this work: already after this very soft procedure a significant difference in intensity and width of the Ir 111 reflection over depth was found. After this one cycle the crystal lattice is significantly affected, whereas the morphology remains only slightly changed, which is a fourth highlight found within the iridium electrochemistry. The introduction of a higher defect density or surface reconstruction effects are possible explanations but could not be verified in complete detail. . Nevertheless, this extended surface morphology characterization could demonstrate the already early influence on the Ir morphology and crystal lattice after application of OER- and various electrochemical conditions. Due to the absence of massive bulk iridium, being executed on only a 20

nm thin film, the analysis is very surface near and separates it from the well-known bulk features. Fig.7.1 summarizes in a simplified view the obtained behavior of the different intrinsic morphologies.

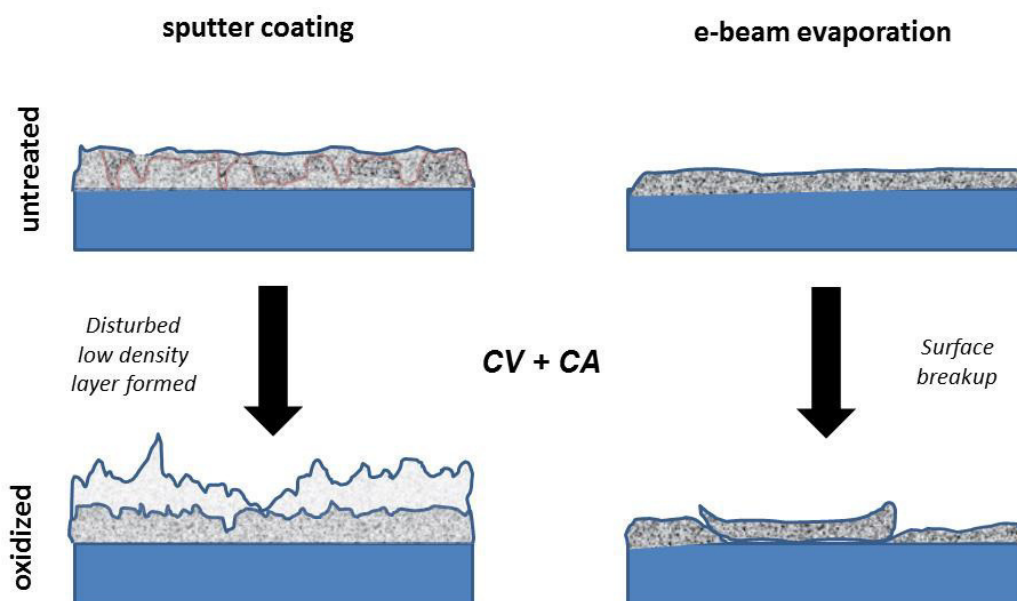


Fig.7.1: Pictorial summary of the electrochemical behavior of sputter coated and e-beam evaporation prepared samples.

Finally, three examples were studied under three different perspectives on GIXRD and XRR. First, a depth resolved qualitative phase analysis on a high temperature alloy was performed. It revealed that the surface composition changes considerably under oxidative atmosphere. The less noble metals, aluminum and yttrium are oxidized and segregate to surface, whereas chromium and zirconium stay almost untouched and form new alloy. In a second example the constant penetration depth of a fixed incidence angle in GIXRD uncovered the differences of silicon growth on two different prepared titanium layer. The introduction of a nitride blocking layer prevents the crystallization of the grown silicon, a finding which was additionally confirmed by TEM. The second application of GIXRD outside the box was concerned with a pressed powder sample of Cu/ZnO catalyst for hydrogenation of CO/CO₂. After reductive treatment with H₂, the surface exhibits a slightly advanced brass formation compared to the bulk. This study used a reduction temperature series on the one hand and a H₂ concentration series on the other hand. The H₂ % series revealed a stronger influence compared to temperature, and the extracted lattice constant, clearly depict the case of alloying to brass. GIXRD contributed with higher intensities gained by the measurement geometry compared to symmetric scans. In the last example XRR was used to calibrate the deposition time of a home build LPCVD machine. Different samples of silicon on a silicon wafer with increasing thickness were evaluated and a clear linear trend of the deposition rate with time could be nicely shown.

The present works contributes to the understanding of oxidized iridium surfaces after being subjected to OER conditions in two ways: First, with the implementation of a model system. Even though it is not completely real-life tailored, the insights gained are highlighting the potential of GIXRD, XRR as well XRDs. It could be illustrated, that iridium surfaces are very dynamic systems under electrochemical transformation. The intrinsic differences, depending on the layer growth,

could be shown to strongly influence the later activity. In contrast, the applied electrochemical conditions also determine the later appearance of the resulting OER active layer. Since the original assumption of kinetic differences could be successfully traced to structural origins, this work has an enormous implication for further structural studies. It can be concluded, that only by the knowledge of the whole “curriculum vitae” of a layer, from the deposition method to the final treatment, the comparability to other systems can be given. As stressed in the upper paragraph the three most important findings for the integral characterization of the dynamical instability of the iridium system are: kinetics, morphology as well the chosen treatments (or combinations of treatments) are very sensitive screws for the OER activity of iridium since each of them alter the morphology of the $\text{Ir}(\text{O})_x(\text{OH})_y$ in a different way. Additionally, by applying thin film diffraction the connection can be made on how strong the influence of a selected current density on the layer morphology actually becomes. The transition from massive bulk iridium to just a few nm thick surface layers offers a new perspective on separating different influences. It has to be noted that this preliminary study was of course hampered significantly by technical issues in some cases. The use of a simple laboratory diffractometer, which is designed as a multi-purpose machine, imposes considerable limitations. For dedicated surface studies, a higher photon flux and a better beam optimization in terms of monochromatization and beam shape would be highly beneficial, and thus it may be expected that corresponding synchrotron studies could lead this type of investigation a completely new performance level. This work also demonstrates the extreme difficulty of using the methods of XRR, XRDS and GIXRD on such a highly dynamic system in the laboratory only. The implementation itself has taken very long, as well as to reach an applicable stage of sample preparation. The data evaluation was also highly iterative and required multiple cycles of development to be applicable for the iridium system. Nevertheless, for the present work many difficulties could be overcome with patience and the extremely carefully chosen conditions for experimental realization. This allowed this study to be executed finally on a very high level.

The second aspect of contributing has not been completely accomplished so far. While the developed in-situ setup is described here specifically for the use with a laboratory diffractometer, a more general application can be envisioned. Even though it was tested in this work only with a simple copper sample, the results are quite promising. Due to this surface sensitive in-situ study, being conducted online and time dependent, the expectations to test it with an Ir sample, possibly with a single crystal sample, gives a very interesting perspective. This would again open the door for an even deeper understanding of surface phenomena.

Appendix I List of sample database numbers (FHI)

Chapter3

Copper sample #26784

Chapter 4

Sample A #22932

Sample B #24516

Sample C #23618

Sample D #24517

Chapter 5

Sample A #24530

Sample B #24851

Sample C #24582

Sample D #24909

Sample E #24547

Sample F #24953

Chapter 6

DLR samples #18466

#18467

#18468

Ti/N-samples #20283

#20285

Cu/ZnO/Al₂O₃ #17980

Si-LPCVD calib. #19573

#19754

#19519

#19520

#19528

Appendix II Information about the author

List of Publications:

- Willinger, E., Tarasov, A., Blume, R., Rinaldi, A., Timpe, O., Massué, C., Scherzer, M., Noack, J., Schlögl, R., Willinger, M.-G., Characterization of the Platinum-Carbon Interface for Electrochemical Applications, ACS Catalysis 7 (2017), 4395-4407
- Pfeifer, V., Jones, T., Velasco Vélez, J., Massué, C., Arrigo, R., Teschner, D., Girgsdies, F., Scherzer, M., Greiner, M., Allan, J., Hashagen, M., Weinberg, G., Piccinin, S., Hävecker, M., Knop-Gericke, A., & Schlögl, R. "The Electronic Structure of Iridium Oxide Electrodes Active in Water Splitting", Physical Chemistry Chemical Physics 18 (2016), 2292-2296
- Frank, B., Xie, Z., Friedel, K., Scherzer, M., Schlögl, R., & Trunschke, A.; Modification of the carbide microstructure by N- and S-functionalization of the support in MoxC/CNT catalysts, Catalysis Science & Technology 6 (2016), 3468-3475
- Pfeifer, V., Jones, T., Velasco Vélez, J., Massué, C., Arrigo, R., Teschner, D., Girgsdies, F., Scherzer, M., Greiner, M., Allan, J., Hashagen, M., Weinberg, G., Piccinin, S., Hävecker, M., Knop-Gericke, A., & Schlögl, R.; The electronic structure of iridium and its oxides, Surface and Interface Analysis 48 (2016), 261-273,
- Pfeifer, V., Jones, T., Wrabetz, S., Massué, C., Velasco Vélez, J., Arrigo, R., Scherzer, M., Piccinin, S., Hävecker, M., Knop-Gericke, A., & Schlögl, R.; Reactive oxygen species in iridium-based OER catalysts, Chemical Science 11 (2016), 6797-6795
- Velasco Vélez, J., Davaasuren, B., Scherzer, M., Cap, S., Willinger, M. G., Guo, J.-H., Schlögl, R., & Knop-Gericke, A., Exploring the incorporation of nitrogen in titanium and its influence on the electrochemical corrosion resistance in acidic media, Surface science 650 (2016), 272-278
- Mette, K., Kühl, S., Tarasov, A., Willinger, M. G., Kröhnert, J., Wrabetz, S., Trunschke, A., Scherzer, M., Girgsdies, F., Düdder, H., Kähler, K., Friedel Ortega, K., Muhler, M., Schlögl, R., Behrens, M., & Lunkenbein, T.; High-Temperature Stable Ni Nanoparticles for the Dry Reforming of Methane; ACS Catalysis 10 (2016), 7238-7248
- Mautner, F., Scherzer, M., Berger, C., Fischer, R., Massoud, S., Synthesis, characterization and luminescence properties of zinc(II) complexes of pseudohalides and nitrite derived from 4-azidopyridine, Inorganica Chimica Acta 425 (2015), 46-51
- Mautner, F., Scherzer, M., Berger, C., Fischer, C., Vicente, R., Massoud, S., Synthesis and characterization of five new thiocyanato- and cyanato-metal(II) complexes with 4-azidopyridine as co-ligand, Polyhedron 85 (2015), 20-26
- Mautner, F., Scherzer, M., Berger, C., Fischer, R., Vicente, R., Massoud, S., Synthesis and characterization of three new 1-D polymeric [M-2(4-azidopyridine)(4)(μ 1,1-N-3)(2)(μ 1,3-N-3)(2)](n) (M = Ni, Co, Cd) complexes, Polyhedron (85), 329-336

- Mautner, F., Berger, C., Scherzer, M., Fischer, R., Maxwell, L., Ruiz, E., and Vicente, R., Different topologies in three manganese- μ -azido 1D compounds: magnetic behavior and DFT-quantum Monte Carlo calculations, Dalton Transactions 42 (2015), 18632-18642